Applications of Optical-Feedback Cavity-Enhanced Absorption Spectroscopy

Ann G. V. Bergin

Wadham College

University of Oxford

A thesis submitted for the degree of

Doctor of Philosophy

Trinity 2013

Declaration of Authorship

I declare that this thesis titled: 'Applications of Optical-Feedback Cavity-Enhanced Absorption Spectroscopy' and the work presented in it are my own. I confirm that the following statements are true.

- This work was done wholly while in candidature for a research degree at this University.
- Where any part of this thesis has previously been submitted for a degree or any other qualification at this University or any other institution, this has been clearly stated.
- Where I have consulted the published work of others, this is always clearly attributed.
- Where I have quoted from the work of others, the source is always given. With the exception of such quotations, this thesis is entirely my own work.
- I have acknowledged all main sources of help.
- Where the thesis is based on work done by myself jointly with others, I have made clear exactly what was done by others and what I have contributed myself.

Ann G. V. Bergin

_____

Signature

_____

Date

Abstract

This thesis presents two contrasting implementations of the optical-feedback cavity-enhanced absorption spectroscopy (OF-CEAS) technique. OF-CEAS combines passive optical-feedback locking of semiconductor lasers with cavity-enhanced absorption spectroscopy, and is well suited to sensitive detection of pressure-broadened trace gases. Chapters 1 and 2 set the work in this thesis in context, by describing the theory and discussing the motivations behind trace gas sensing by tuneable laser spectroscopy in the near- and mid-IR.

Chapter 3 reviews the theory of OF-CEAS, prior to presenting the results of an experimental implementation based on a near-IR DFB diode laser setup following the traditional V-cavity methodology to spatially decouple the optical-feedback beam from the direct back reflection. The capabilities of the system are demonstrated by accurate determination of a self-broadened half-width at half-maximum of a CO_2 transition, and by detection of acetylene in a car exhaust sample.

Chapter 4 describes the design and implementation of the linear cavity methodology for QCL OF-CEAS, which is the significant contribution of this work. Successful OF-CEAS locking with the linear cavity is shown for two different DFB-QCLs, with close operating wavelengths (5.5 and 5.2 µm) but quite different operating powers and facet size. Chapter 5 presents quantitative spectroscopic results from the linear cavity OF-CEAS instrument, using both lasers. Spectroscopy on mixes of N_2O and NO returned sensitivities, quantified by the $\alpha_{\min}$, of 2.7×10^{-8} cm^{-1} in 1 s at 0.28 atm and 2.4×10^{-8} cm^{-1} in 1 s at 0.19 atm respectively. Limited by etalon fringing on the baseline, the $\alpha_{\min}$ compared well with those obtained with V-cavity QCL OF-CEAS instruments. The temporal

stability was investigated by Allan variance calculations and the best minimum detectable concentrations for the linear QCL OF-CEAS instrument were 32 ppm for N_2O (35 s) and 5 ppb for NO (2 s). For NO, this detection limit compares favourably with other mid-IR QCL-based NO sensors, and is sufficient for monitoring NO in polluted urban environments. With the Maxion DFB-QCL, monitoring of NO in air outside the laboratory was attempted, and an air sample drying system benchmarked. Although this experiment proved unsuccessful, it was possible detect trace amounts of NO desorbing from the walls of the gas cell. Over the course of one hour the concentration rose from 3.8 ± 0.7 ppb to 28.4 ± 0.2 ppb, leading to a rate of desorption of $6.76 \pm 0.01 \times 10^{-3}$ ppb s^{-1}. The sensitivity (α_{min}) of these spectra was 7.0×10^{-9} cm^{-1} in 1 s, improved due to the higher mirror reflectivity at the lasing wavelength of the Maxion DFB-QCL, although still limited by etalon fringing. University of Oxford

Acknowledgements

This work was supported by a studentship on the EPSRC grant, "New frontiers in quantitative infra-red to ultraviolet spectroscopy using diode and quantum-cascade lasers" [EP/E019765/1]. I would like to acknowledge my supervisor, Dr Grant Ritchie, and also Prof. Gus Hancock, for the opportunity to work in their group. I would also like to thank my examiners, Dr Meez Islam and Prof. Paul Ewart.

With regard to the science, I would like to acknowledge the help of the following people. Early in my DPhil I was too lazy to write my own LabVIEW programs, and so without Graham Richmond's help I would not have collected any data for Chapter 3. I also need to thank him for buying more than his fair share of beer. The linear cavity QCL OF-CEAS instrument, and therefore Chapters 4 and 5, would not have existed without Damien Weidmann's considerable expertise and enthusiasm, and his patience for explaining every aspect of the experiment to me in the simplest possible terms. Everyone in the PTCL Electronics and Mechanical Workshops built, modified or mended equipment vital for the OF-CEAS experiment. In particular, Kevin, Neville, Phil, Les, and Howard bore the brunt of my questions about that equipment with good humour.

On the non-science side, I'm grateful to my fellow fourth years, Julian, Rich, and Gilly, and also to Dr Katy Langley, for moral support throughout the course of my DPhil. For the past three years, Imogen and Simon have been the best housemates I could have hoped to have. Finally, I would like to thank my Mum and Dad for their continued love and support.

Contents

Nomenclature

CEAS	Cavity-enhanced absorption spectroscopy.
CRDS	Cavity ringdown spectroscopy.
cw	Continuous wave.
DFB-DL	Distributed feedback diode laser.
DFB-QCL	Distributed feedback quantum cascade laser.
DL	Diode laser.
EC-DL	External cavity diode laser.
EC-QCL	External cavity quantum cascade laser.
FMS	Frequency modulation spectroscopy.
FSR	Free spectral range.
FWHM	Full-width at half-maximum.
HWHM	Half-width at half-maximum.
ICOS	Integrated cavity output spectroscopy.
LIV	Light-current-voltage.
ML-CEAS	Mode-locked cavity enhanced absorption spectroscopy.
NICE-OHMS	Noise immune cavity-enhanced absorption spectroscopy.
OA-CEAS	Off-axis cavity-enhanced absorption spectroscopy.
OF-CEAS	Optical-feedback cavity-enhanced absorption spectroscopy.
OF-CRDS	Optical-feedback cavity ringdown spectroscopy.
OF	Optical-feedback.

PAS	Photoacoustic spectroscopy.
PET	Piezoelectric transducer.
QCL	Quantum cascade laser.
SLQW-DFB-DL	Strained layer quantum well distributed feedback diode laser.
TEM_{mn}	Transverse electromagnetic mode, described by a Hermite polynomial with horizontal and vertical nodes m and n.
TE	Thermoelectric.
WMS	Wavelength modulation spectroscopy.

Chapter 1

Absorption Spectroscopy for Trace Gas Sensing

Detection of gases present in trace concentrations has many useful applications, in atmospheric chemistry [1], exploration of other planets [2], clinical diagnostics [3], and is also relevant to fundamental science and photochemistry. Over the past thirty years, in-situ sensing techniques based on tuneable diode laser absorption spectroscopy have been extensively investigated, initially with diode lasers [4] and more recently with quantum cascade lasers [5]. An ideal tuneable diode laser spectrometer has a high sensitivity, high selectivity, and a rapid response rate, preferably in a compact and robust form, at a reasonable cost. Pursuing any one of these features can involve major experimental effort and expense, so it is important to chose an appropriately economic and efficient solution for a given trace gas sensing application.

1.1 Organization of thesis

Chapter 1 and **Chapter 2** contain introductory and review material, on the theory and practicalities of tuneable diode laser absorption spectroscopy, and the physics and applications to spectroscopy of optical cavities. This leads on to

the presentation of a near-IR V-cavity OF-CEAS spectrometer in **Chapter 3**, including a discussion of the important results already derived for OF-CEAS locking of diode lasers to V-cavities.

The significant result of the work presented in this thesis is the successful experimental demonstration of all aspects of OF-CEAS with a QCL coupled to a two mirror linear cavity without suppression of the directly reflected field by optical isolation or a V-cavity. A physical description and experimental evidence of successful OF-CEAS locking with two different DFB-QCLs is the subject of **Chapter 4**. **Chapter 5** presents OF-CEAS spectroscopy results using both lasers, and also describes some measures taken to try and optimize the instrument. **Chapter 6** formally concludes the thesis and outlines some extensions to the linear cavity OF-CEAS technique.

1.2 Quantum basis of absorption spectroscopy

Molecules have unique quantized energy levels, and transitions between these occur when photons are absorbed or emitted, resulting in characteristic spectra. For a single photon transition, the molecular energy level difference, ΔE, necessarily corresponds to the energy of the photon, and they are said to be resonant. For a photon with frequency, ν, and wavelength, λ, these are related via

$$\Delta E = h\nu = \frac{hc}{\lambda}, \tag{1.1}$$

where c is the speed of light in vacuo, and h is Planck's constant. Figure 1.1 shows part of the electromagnetic spectrum: as the wavelength of the absorbed photon decreases and its energy increases, transitions correspond to changes in the vibrational (mid- and near-IR) and electronic energy level (UV-vis).

The intensity of a transition between an initial quantum state $|i\rangle$ and a final quantum state $|f\rangle$, is proportional to the square modulus of the electric dipole

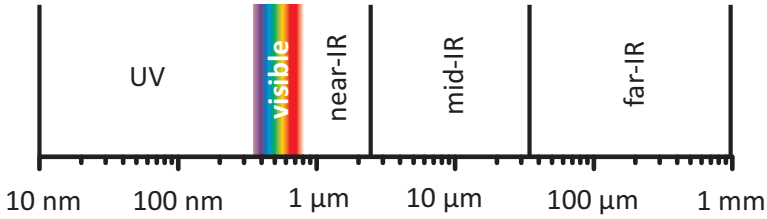

Figure 1.1: The electromagnetic spectrum on a logarithmic wavelength scale from the UV to the far-IR.

transition moment, $\boldsymbol{\mu}_{fi}$ [6], defined as

$$\boldsymbol{\mu}_{fi} = \langle f | \, \boldsymbol{\mu} \, | i \rangle \, . \tag{1.2}$$

This integral is non-zero for allowed transitions. For vibrational transitions considered within the harmonic oscillator approximation, non-zero terms arise in Equation 1.2 when the difference in vibrational quantum number, Δv, is

$$\Delta v = \pm 1. \tag{1.3}$$

IR radiation must be applied to stimulate vibrational transitions, as at room temperature $k_{\mathrm{B}}T$ is much smaller (4×10^{-21} J) than the typical vibrational energy level spacings ($> 10^{-20}$ J) in a molecule. Therefore, most molecules are in the $v = 0$ level and so the fundamental $v = 1 \leftarrow 0$ transitions will dominate. These strongly allowed transitions occur in the mid-IR, between 2.5 and 25 µm [7].

The atomic displacements when a molecule moves, rotates or vibrates can be by defining a set of normal modes. These are derived by associating each atom in the molecule a set of $3N$ normal co-ordinates: N is the number of atoms in the molecule, and this leads to $3N$ degrees of freedom. When the degrees of freedom corresponding to rotation and translation are removed, non-linear molecules have $3N - 6$ normal modes of vibration, while linear molecules possess $3N - 5$ [6].

When mechanical and electrical anharmonicity is considered, mixing of normal

modes is possible and Equation 1.3 is partially relaxed. One effect is that a single photon is able to excite more than one quantum in a given normal mode. These transitions, where $\Delta v = \pm 2, \pm 3, \ldots$, are called overtone transitions. Combination transitions, where a single photon excites more than one normal mode simultaneously, are also made possible by anharmonicity. Overtone and combination transitions of light molecules typically occur in the near-IR from 0.8 to 2.5 µm and are inherently weaker than fundamental transitions, because the simple harmonic oscillator is a good approximation for molecules in the zero point levels and they are formally disallowed by Equation 1.3.

Many rotational energy levels are thermally populated at room temperature, as molecular rotational energy levels are closely spaced and at least two orders of magnitude lower than $k_{\mathrm{B}}T$ (10^{-22} J). As a result, infrared absorption spectra of vibrational molecular transitions consist bands corresponding to rovibrational transitions. The selection rule for rotational transitions in diatomic molecules is $\Delta J = \pm 1$, where J is the rotational quantum number. Transitions with $\Delta J = -1$ form the P-branch of the band, whilst those with $\Delta J = +1$ form the R-branch. Transitions with $\Delta J = 0$ are additionally allowed if the molecule possesses angular momentum parallel to the internuclear axis, and this is known as the Q-branch.

The spectral line intensity, S_{if}, for a rovibrational transition of a single molecule, occurring at a frequency ν_{if}, and a reference temperature of 296 K, is

$$S_{if}(\nu) = \frac{h\nu_{if}}{c}\frac{n_i}{N}\left(1 - \frac{g_i n_f}{g_f n_i}\right) B_{if}, \tag{1.4}$$

in units of [cm^{-1}/(molecule cm^{-2})]. N is the molecular number density. B_{if} is the Einstein coefficient for stimulated absorption, proportional to $|\boldsymbol{\mu}_{fi}|^2$, and describes the rate at which the transition occurs per unit spectral density of the electromagnetic field. The initial and final quantum states have populations n_i and n_f, and statistical weights g_i and g_f [8].

Knowledge of spectroscopic parameters is fundamental to all applications of

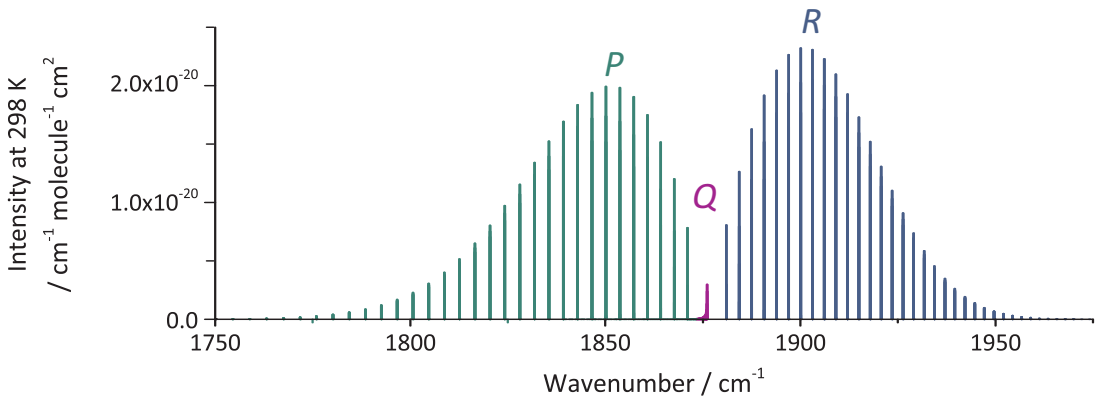

Figure 1.2: Spectrum of HITRAN-listed intensities for the rovibrational transitions comprising the P, Q, and R branches of the fundamental ($v = 1 \leftarrow 0$) vibrational band of NO in its electronic ground state, $^2\Pi_{\frac{1}{2}}$.

trace gas sensing, and several databases exist. The work in this thesis uses the HITRAN molecular spectroscopic database, which contains line-by-line spectroscopic parameters for over forty small molecules of atmospheric relevance [9]. To illustrate the concepts introduced in this section, the HITRAN-listed intensities for the rovibrational transitions comprising the P, Q, and R branches of the $v = 1 \leftarrow 0$ band of NO in its electronic ground state, $^2\Pi_{\frac{1}{2}}$ is shown in Figure 1.2.

1.3 Absorption lineshapes

Spectral absorption profiles do not appear as monochromatic δ-functions, due to a natural linewidth broadening resulting from the uncertainty associated with the quantum states involved in the absorption process [7]. The resulting natural absorption linewidth is much smaller than (a) the linewidth of an unstabilized semiconductor laser, and (b) the linewidth resulting from other broadening mechanisms. For these reasons, specialized techniques must be used to measure the natural linewidth of an absorption profile, e.g. Lamb dip spectroscopy [10].

There are several line broadening mechanisms, and the nature and extent of spectral line broadening depends on both the molecular characteristics and the

environment of the molecule. The spread of a spectral absorption line broadened around ν_{if} is represented by a normalized frequency, temperature, T, and pressure, p, dependent lineshape function, $F(\nu, \nu_{if}, T, p)$ with units of $[1/\text{cm}^{-1}]$, which leads to an absorption cross-section, $\sigma(\nu, T, p)$ with units of $[\text{cm}^2 \text{ molecule}^{-1}]$, defined as

$$\sigma(\nu, T, p) = S_{if}(\nu) F(\nu, \nu_{if}, T, p). \tag{1.5}$$

For pressures around atmospheric pressure (~ 760 Torr) or higher, pressure broadening due to molecular collisions is the dominant contributor to absorption lineshape broadening. Collisions between molecules reduce the lifetime, τ, of the upper state, and lifetime broadening ($\tau \Delta E \approx \frac{h}{4\pi}$) results in a spread of transitions energies, δE [6]. This broadening is homogenous and results in a Lorentzian lineshape, F_{Lrntz}, with the mathematical form

$$F_{\text{Lrntz}}(\nu, \nu_{if}, T, p) = \left[\frac{1}{\pi}\right] \frac{\gamma(p, T)}{\gamma(p, T)^2 + \left[\nu - (\nu_{if} + \delta(p_{\text{ref}})p)\right]^2}, \tag{1.6}$$

where γ is the sum of the air (γ_{air}) and self-broadened (γ_{self}) half-widths at half-maximum, and δ accounts for any pressure shift of the transition frequency. These parameters (γ_{air}, γ_{self}, and δ) are all transition dependent and listed line-by-line (i.e. for a given ν_{if}) in the HITRAN database. The full-width at half-maximum (FWHM) of a pressure broadened line, $\Delta\nu_{\text{Broad}}$, is

$$\Delta\nu_{\text{Broad}} = 2p \left[q\gamma_{\text{self}} + (1 - q)\gamma_{\text{air}}\right], \tag{1.7}$$

where q is the mixing ratio of the analyte [8].

The pressure broadening contribution to the lineshape is smaller than that arising from Doppler broadening in lower pressure environments (< 10 Torr). The Doppler effect shifts the frequency of the transition for each molecule, according to the projection of its velocity along the direction of propagation of the light. For a linear Doppler shift, ν_{if} is decreased for molecules with velocities in the

direction of source of radiation, and increased for those with opposite velocities. For a laser beam propagating along the z-axis, the Doppler shifted absorption frequency, ν_{Dopp}, for a molecule with a velocity component v_z is

$$\nu_{\text{Dopp}} = \nu_{if}\left[1 \pm \frac{v_z}{c}\right]. \tag{1.8}$$

This inhomogeneous broadening results in a Gaussian lineshape, F_{Dopp}, of the form

$$F_{\text{Dopp}}(\nu, \nu_{if}, T) = \frac{1}{\Delta\nu_{\text{Dopp}}} \exp\left[\frac{-4\ln 2(\nu - \nu_{if})^2}{\Delta\nu_{\text{Dopp}}}\right], \tag{1.9}$$

for which the FWHM, $\Delta\nu_{\text{Dopp}}$, is

$$\Delta\nu_{\text{Dopp}} = \frac{2\nu_{if}}{c}\sqrt{\frac{2k_{\text{B}}T\ln 2}{m}}, \tag{1.10}$$

where m is the mass of the molecule in kg [7].

Both broadening mechanisms can make significant contributions to the lineshape in intermediate pressure regimes. A convolution of the Lorentzian and Gaussian lineshapes known as the Voigt lineshape [11, 12], F_{Voigt}, best describes the lineshape in this regime, and has the complex form

$$F_{\text{Voigt}}(\nu, \nu_{if}, T, p) = K(x, y) + \mathrm{i}L(x, y). \tag{1.11}$$

Typically only the real part of this function, $K(x, y)$, is evaluated, as given by

$$K(x, y) = \frac{y}{\pi}\int_{-\infty}^{\infty} \frac{\exp[-\nu^2]}{y^2 + (x - \nu)^2}\,\mathrm{d}\nu, \tag{1.12}$$

where

$$x = \frac{\sqrt{\ln 2}(\nu - \nu_{if})}{\Delta\nu_{\text{Dopp}}} \text{ and } y = \sqrt{\ln 2}\frac{\Delta\nu_{\text{Broad}}}{\Delta\nu_{\text{Dopp}}}. \tag{1.13}$$

1.4 Direct absorption spectroscopy

The simplest direct laser absorption spectroscopy experiment is drawn in Figure 1.3: a laser beam with an initial intensity I_0 passes through an absorbing sample of length L, and the transmitted intensity I is detected. For a homogenous analyte of independently absorbing molecules, the Beer-Lambert law [13, 14, 15] relates these measured quantities to the frequency dependent absorption coefficient, $\alpha(\nu)$:

$$I = I_0 \exp[-\alpha(\nu)L]. \tag{1.14}$$

For the Beer-Lambert law to be valid, the light source must have a smaller linewidth than the absorption profile, and also consist of parallel rays that travel the same distance through the absorbing medium. Lasers are consequently ideal sources for direct absorption spectroscopy. However, given the often high power nature of laser sources, further care must be taken to ensure that the laser beam remains a non-invasive probe and does not chemically change the sample, or cause optical saturation and significantly deplete the population in the lower energy level [7]. The Beer-Lambert law as given in Equation 1.14 is based on the assumption that light extinction occurs only by absorption, and must be modified to include other processes, like scattering of light.

The absorption cross section, $\sigma(\nu, T, p)$, is related to the $\alpha(\nu)$, which has units

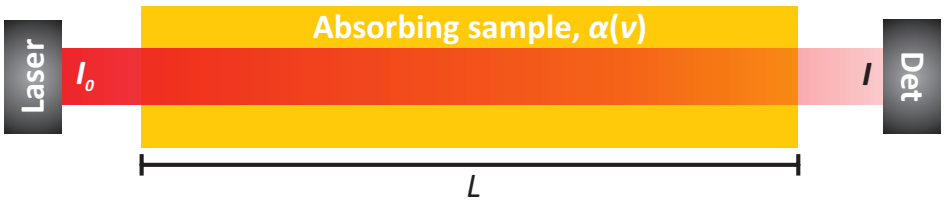

Figure 1.3: Illustration of Beer-Lambert law absorption, where I_0 is the incident intensity on the absorbing sample, I the transmitted intensity, and $\alpha(\nu)$ the absorption coefficient.

of [cm^{-1}], by the concentration, C in [molecules cm^{-3}], of the absorbing sample:

$$\alpha(\nu) = C\sigma\left(\nu, T, p\right). \tag{1.15}$$

The concentration of a given analyte can be retrieved from a recorded transmission profile or an absorption profile in the following way. Integrating Equation 1.15 leads to

$$\int_{-\infty}^{\infty} \alpha(\nu)\,\mathrm{d}\nu = CS_{if}(\nu), \tag{1.16}$$

from which the left-hand side is given by the area underneath a fitted profile, and S_{if} is known for a given transition, e.g. from the HITRAN database. The consequent advantages of direct absorption spectroscopy are that it is simple, species specific, non-invasive and does not require calibration.

There are disadvantages too. Firstly, laser sources with a tuning range covering at least the absorption lineshape of the chosen transition must be available at an appropriate wavelength, and at an affordable price. Secondly, direct absorption spectroscopy ultimately relies on measuring a small signal over a noisy baseline. Typical noise equivalent absorption coefficients, denoted α_{min} and discussed further in Section 1.6, for direct absorption spectroscopy are on the order of 10^{-3} to 10^{-4} cm^{-1} for 1 s integration [16]. Where the species to be detected absorbs weakly (small $\alpha(\nu)$) or is present in a low concentration, more complex techniques may be necessary to enhance the signal to noise ratio.

1.5 Signal enhancement and noise reduction

The form of the Beer-Lambert law (Equation 1.14) immediately suggests two methods of enhancing the absorption signal: increasing $\alpha(\nu)$ by choosing a spectral region with higher intensity transitions, and enhancing the pathlength. Both of these methods are used in the work presented in this thesis.

1.5.1 Spectral region

Strong fundamental vibrational transitions occur in the mid-IR spectral region, this is illustrated for the diatomic molecule nitric oxide (NO) in Figure 1.4. This shows on a log-scale the HITRAN-listed integrated intensities on both wavenumber (cm^{-1}) and wavelength (µm) scales [9] . The transitions in the single mid-IR fundamental vibrational band are up to $\sim$ 1000 times more intense than the overtone transitions in the near-IR.

Mid-IR spectroscopy has been extensively reviewed by Tittel et al. [17], and Figure 1.5 summarizes suitable laser sources for spectroscopy in the near- and mid-IR. These may be categorized as either (a) laser sources based on a gain medium producing mid-IR photons, or (b) those based on non-linear frequency conversion of near-IR photons. Lasers for absorption spectroscopy require a single-mode output (unless special techniques are used [18]), with a tuning range

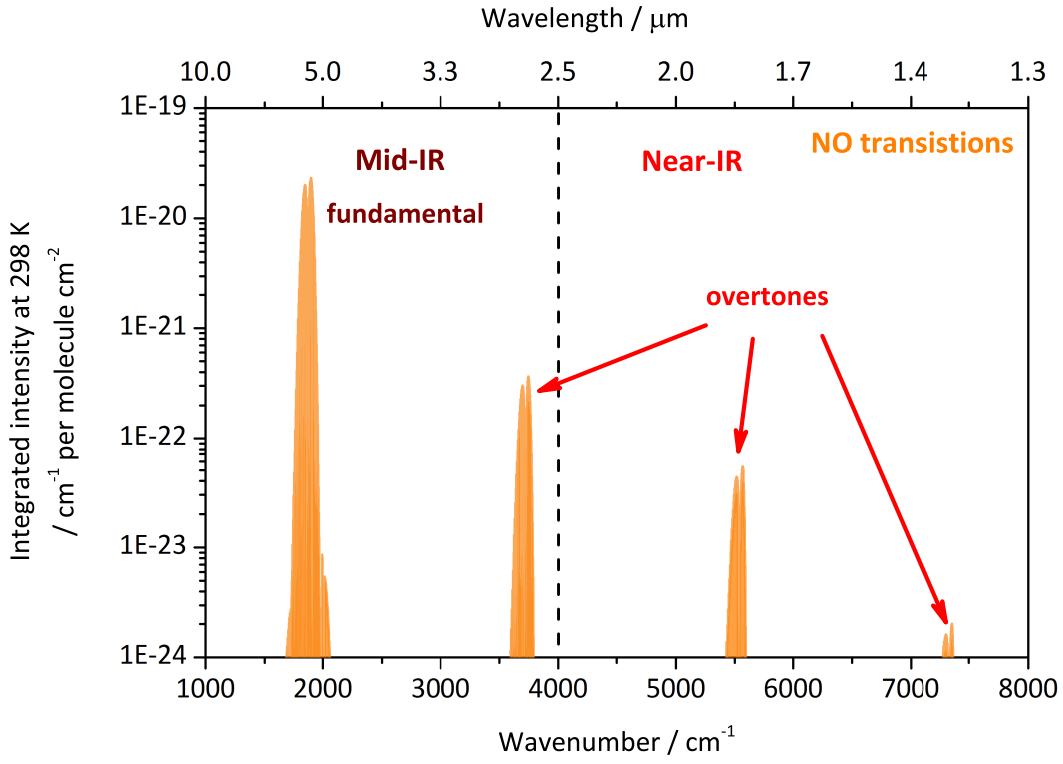

Figure 1.4: HITRAN-listed integrated intensities of NO on a log-scale against wavelength and wavenumber, illustrating the much higher transition intensities of the mid-IR fundamental vibrational band, cf. the near-IR overtone bands.

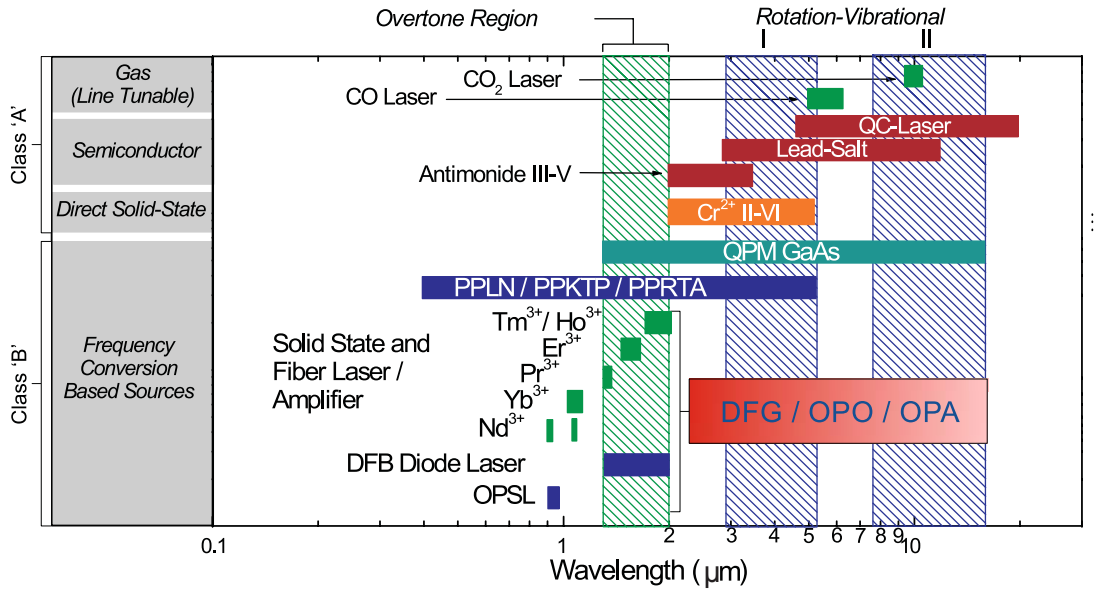

Figure 1.5: Overview of mid-IR laser sources, taken from [17]. QC-laser is quantum cascade laser; QPM is quasi-phase-matched; PPLN/PPKTP/PPRTA are all types of non-linear crystals; DFG is difference frequency generation; OPO and OPA are optical parametric oscillator and amplifier; and OPSL is optically pumped semiconductor laser.

covering the absorption profile, a bandwidth narrower than the measured absorption profile, and a reasonably high power output. Additional desirable features for trace gas sensing instruments include rapid wavelength tuning for high acquisition rates, compactness, thermoelectric cooling and reasonably low cost. For at least twenty years, diode lasers have been able to fulfill these requirements in the near-IR region [19], leading to the development and proliferation of tuneable diode laser absorption spectroscopy.

Unlike diode lasers, some of the older mid-IR sources are particularly unsuited to building small and robust instruments. Continuous wave CO and CO_2 lasers are very high power and narrow linewidth devices, but their usefulness for spectroscopy is limited to transitions near or coincident with the lasing transitions, and they are room-sized and expensive. Difference frequency generation (DFG) is capable of producing cw, and narrow bandwidth light, but such systems are inherently low powered: typically on the order of μW [20], with 15 mW described

as high power [21]. Optical parametric oscillators have high power and a wide spectral range, but are large and complex systems requiring high power pumps, efficient non-linear crystals and produce broad bandwidth light. Mid-IR lead-salt diode lasers have been available since the 1960s, but the severe limitation of these devices was their requirement for cryogenic cooling. This not only placed stringent requirements on the laser housing, but often resulted in short device lifetimes due to extreme temperature cycling [19]. Hence, prior to the invention in 1994 of the quantum cascade laser (QCL) [22] and its subsequent development, access to the mid-IR spectral region for spectroscopy was more difficult than the near-IR.

The lasing wavelength of a diode laser is determined by the bandgap of the semiconductor material from which it is constructed, so extension of the spectral region covered by diode devices is dependent on development of novel semiconductors. Lasing action is particularly difficult to achieve in the small bandgap materials necessary for mid-IR emission, as Auger recombination dominates over radiative recombination of electrons and holes [19]. QCLs by comparison achieve selective mid-IR emission through engineering of the active medium. Very thin layers (a few nm) of semiconductors with alternating refractive indices are deposited via molecular beam epitaxy, creating quantum wells. The energy levels of quantum wells are determined by their thickness [6], consequently so too is the lasing wavelength of a QCL, which may therefore be tuned by adjusting the layer thickness [22].

The invention of QCLs has enabled the production of devices covering a large part of the mid-IR, using existing semiconductors (e.g. InGaAs/InAlAs [22], GaAs/AlGaAs [23]). As was the case for diode lasers, single-mode, continuous wave, thermoelectrically cooled QCLs have been developed, and much experimental effort is now focused on mid-IR tuneable diode laser absorption spectroscopy (see for instance the review by Gmachl and Capasso [24]).

Continuous wave, thermoelectrically cooled distributed feedback QCLs are commercially available from at least two manufacturers in the wavelength range 4 to 16 µm. The work in this thesis uses both diode laser and QCL sources, and these devices are discussed in more detail in the relevant experimental chapters.

1.5.2 Pathlength enhancement

Inspection of the Beer-Lambert law also indicates that the sensitivity of an absorption measurement is increased if the pathlength, L, of the laser beam through the absorbing sample is extended. The obvious limit imposed by the length of the optical table, ~ 1 m, can be circumvented by using mirrors, most simply in the form of a folded optical delay line or multipass cell. Simple types are the two-mirror Pfund and three mirror White cells [25], but for trace gas sensing the most widely used design is that of Herriott [26]. This consists of two spherical mirrors, one of which has a hole for injection and exit of the probe beam. Beam injection with an off-axis alignment results in an elliptical Lissajous spot pattern on the mirrors. Multichannel Herriott cells, with a separate hole for each laser channel, broadband mirror coatings, and astigmatic cells using a greater proportion of the mirror surface have been developed [27]. Multipass cells generally have low pathlength enhancements on the order of ~ 100 m. For Herriott cells in particular, the enhancement is larger for longer mirror spacings and broader diameter mirrors, so long pathlengths can only be achieved by large volume cells.

An alternative method is to contain the absorbing sample within a high finesse optical cavity. This can be either the laser resonator itself, a technique known as intracavity laser absorption spectroscopy (ICLAS), or an external cavity, in which case cavity-enhanced absorption spectroscopy (CEAS) is performed. Typical ICLAS experiments have probed narrowband absorptions superimposed on the broad gain profiles of multimode lasers. Very long pathlength enhancements have been demonstrated with this technique: the longest observed was

70,000 km, achieved using a dye laser. However, the sensitivity enhancement possible for diode laser ICLAS is on the order of km, due to the high internal losses and lower power output of this kind of laser [28]. This level of enhancement is more easily achieved using CEAS, for which diode laser light sources are highly suitable and have been used extensively [29]. The external cavities used are typically formed of very highly reflective dielectric mirrors ($R > 0.999$), with a diameter of 1 inch or less. Cavity-enhanced spectroscopy instruments can have pathlength enhancements on the order of kilometers, while maintaining a small cell volume. These properties make cavity-enhanced forms of spectroscopy ideal for trace gas sensing. The OF-CEAS technique is a form of cavity-enhanced spectroscopy, and a physical description of optical cavities is the subject of Chapter 2, where the techniques of cavity ringdown spectroscopy (CRDS), cavity-enhanced absorption spectroscopy (CEAS) and their variants are introduced.

1.5.3 Noise affecting laser absorption spectroscopy

Technical noise affecting laser absorption spectroscopy can arise from electrical, optical, and mechanical or acoustic sources. Electrical noise can affect laser absorption spectroscopy measurements either by noise on the detected signal, or noise on the laser or system control signals that are converted to optical intensity or frequency fluctuations. Analogue electrical signals are affected by intrinsic noise arising via several mechanisms. Johnson noise is associated with the random thermal motion of electrons, because it is independent of frequency it is also known as white noise. Shot noise arises from the discrete quantum nature of electrons and photons and is also independent of frequency. Shot-noise limited absorption spectroscopy experiment has a noise floor determined by photon arrival at the detector and electron flow in the detector system. Below ~ 100 Hz, Johnson and shot noise are dominated by flicker or $1/f$ noise, which follows a frequency dependency of the form $1/f^n$, where n is between 0.9 to 1.35 [30].

Noise on electrical signals can also come from electrical pickup, radio frequency interference (RFI) and ground loops. Electrical pickup arises either by capacitative coupling between wires, or induction via stray alternating magnetic fields from transformers or wires carrying large AC currents. Minimizing cable length and using effective shielding (e.g. standard coaxial cable) or twisted wire pairs can reduce electrical pickup. Unwanted high-frequency fluctuations of current or charge in a conductor result in an induced electromagnetic wave that cause RFI. Switched power supplies are a notable source of RFI. Potential differences are measured with reference to ground, which is normally assumed to be 0 V. Unless every ground connection is made directly to the zero potential of the earth, these differ for connected instruments and noise may be introduced in the form of ground loops [30]. Acquisition of analogue signals by digitizers can introduce bit-noise, determined by the vertical resolution of the oscilloscope or acquisition card. Normally use of an appropriate amplifier is sufficient to overcome bit-noise.

Reflections between optics results in the formation of etalons and consequent optical frequency dependent sinusoidal variations (fringes) on the baseline. These fringes are a particular problem when their amplitude matches that of the absorption being detected. Etalons may be minimized by using anti-reflection coatings on transmissive optics, tilting plane components, and using wedged components where possible. If the fringes etalons are stable, it might be possible to record and subtract a background spectrum. Otherwise, it may be possible to dither a problematic component along the optical axis faster than the acquisition rate, in order to rapidly change the length of the etalon and smear out the fringing effect.

Mechanical and acoustic noise, which may result in vibrations of optical components, can be reduced by using vibrationally isolated optical tables. Sometimes it may be possible to switch-off troublesome machinery (e.g. vacuum pumps or air-conditioners) while data is collected [30].

1.5.4 Noise reduction techniques

The experimental work in this thesis is based on signal enhancement rather than noise reduction techniques; however, several noise reduction techniques exist and have been used extensively for tuneable diode laser spectroscopy in the near- and mid-IR. Indirect detection schemes, whereby effects caused by absorption rather than absorption itself are measured, have been widely used. These techniques are described as "zero background" as in the absence of an absorber there should theoretically be no signal.

The photoacoustic effect, whereby pulses of laser light induce thermal expansion and contraction of the absorbing medium, producing a pressure wave, was first described by Bell [31, 32] and first applied to detection of the absorbing molecules as photoacoustic spectroscopy (PAS) by [33]. PAS for gas analysis have been reviewed [34, 35]. Instruments based on quantum cascade lasers [36] have been developed. The technique has been enhanced by use of optical-feedback locked power-buildup optical cavities [37, 38] and by the use of quartz-tuning forks [39].

Another technique is Faraday rotation spectroscopy for detection of paramagnetic species [40]. An external magnetic field is applied to the absorbing sample along the direction of propagation of the laser beam, which lifts the degeneracy of the Zeeman components of the transition. Consequently, magnetic circular birefringence is observed as rotation of the polarization plane of the linearly polarized laser radiation. This effect is only strongly observed around absorption lines and is proportional to the concentration of the paramagnetic species. Either the extinction of light through a linear polarizer, or the polarization rotation angle can be detected. The technique is of particular relevance for detecting trace radical species present in the atmosphere (e.g.NO, OH, HO_2), especially as there are no interfering signals from diamagnetic species like CO_2 and H_2O [41].

Another indirect technique is modulation spectroscopy, where the laser fre-

quency is rapidly modulated to produce sidebands either side of the original carrier frequency. There are two distinct regimes: frequency modulation spectroscopy [42] and wavelength modulation spectroscopy [43, 44]. In frequency modulation spectroscopy (FMS) only the first-order side-bands have appreciable magnitude as the modulation frequency ranges from 10s to 100s of MHz, significantly exceeding the laser and the absorption feature linewidths. When no sample is present, there is uniform attenuation of sidebands, and they add up coherently with the carrier and balance each other to produce a beam of constant intensity. However, in the presence of an absorbing or dispersing medium, there is a frequency dependent and therefore asymmetric attenuation of the side-bands, leading to multiple harmonics of the modulation frequency in the detected laser intensity. The strength of absorption determines the magnitude of the harmonics, which may be measured separately using a lock-in amplifier [45].

The other regime is called wavelength modulation spectroscopy (WMS),and is characterized by a low modulation frequency, on the order of (< 1 MHz). For semiconductor lasers, the modulation frequency is therefore smaller than the laser linewidth. Many sidebands are present to a high order, with a small frequency separation resulting in a continuous spectrum. Phase sensitive detection is normally performed at the second harmonic of the modulation frequency as the carrier frequency is scanned across an absorption line. Aside from being zero-background techniques, modulation spectroscopy benefits by moving the detection to higher frequency components, thereby reducing $1/f$ noise. Perhaps the ultimate noise-reduction technique is that of noise-immune cavity-enhanced optical heterodyne molecular spectroscopy (NICE-OHMS), where laser stabilization is used to combine FMS with cavity-enhanced absorption spectroscopy [46].

1.5.5 Optical detectors

The optically sensitive elements of IR detectors are most often based on semiconductor photodiodes, where the energy of the bandgap is engineered to match that of the photon energy. These kind of detectors can be operated in either photovoltaic or photoconductive mode. In photovoltaic mode no bias is applied to the photodiode, restricting the flow of current across the junction. The resulting potential difference is then measured. Signals from photovoltaic detectors must be amplified by a preamplifier close to the photodiode. The preamplifier determines the measurement bandwidth, and photovoltaic detectors are capable of DC to 100 MHz bandwidth. Alternatively, applying a reverse bias to the junction instead enables a flow of current, and this may instead be measured in photoconductive mode. As the reverse bias increases the width of the depletion junction, photoconductive mode results in increased responsivity and also, due to increased capacitance, a faster response time. For the OF-CEAS experiments, photodiode detectors based on room temperature InGaAs operated in photoconductive mode (near-IR) and thermoelectrically cooled HgCdTe operated in photovoltaic mode (mid-IR) were used. The noise equivalent power of a detector, P_{NE}, which has units of [$\mathrm{WHz}^{-1/2}$], is

$$P_{\mathrm{NE}} = \frac{\sqrt{A}}{D^*}, \tag{1.17}$$

where A is the area of the detector and D^* is the wavelength dependent detectivity, in units of [cm $\mathrm{Hz}^{1/2}$ W^{-1}]. D^* must be specified in terms of the detection bandwidth [30].

1.6 Quantifying sensitivity

1.6.1 Noise equivalent absorption coefficient, $\alpha_{\min}$

The sensitivity of a tuneable diode laser absorption spectrometer is ultimately defined by the minimum concentration it can detect for a given analyte. However, the minimum detectable concentration is dependent on the peak cross section, $\sigma(\nu, T, p)$, so techniques that are otherwise identical but conducted in different wavelength regions will result in different sensitivities. A noise equivalent absorption coefficient, $\alpha_{\min}$, is therefore often defined to provide a sensitivity metric that is independent of species and wavelength. The $\alpha_{\min}$ is intended to quantify the smallest absorption detectable over the baseline noise; however, its usefulness as a comparator between instruments and techniques is limited by varying and often unclear definitions. Moyer et al. [47] have briefly reviewed this problem, with particular reference to cavity-enhanced absorption spectroscopy. For this thesis the definition of $\alpha_{\min}$, Equation 1.18, has been chosen to be consistent with their Equation 16, and is always determined for a single scan:

$$\alpha_{\min} = \left[\frac{\Delta P}{P}\right]_{1\sigma} \left[\frac{1}{L_{\text{eff}}}\right] \frac{1}{\sqrt{f_{\text{acq}}}}. \tag{1.18}$$

The parameters are defined as follows. $[\Delta P/P]_{1\sigma}$ is one standard deviation of the residual along a laser scan after fitting the model for a single scan. The second term accounts for the effective pathlength of the absorbing sample, which for cavity-enhanced spectroscopy is given by $L_{\text{eff}} = L/(1-R)$, so $\alpha_{\min}$ is dependent on the mirror reflectivity, R. This is important to note when comparing $\alpha_{\min}$ between near- and mid-IR cavity-enhanced instruments, as the available mirror reflectivity is typically lower at longer wavelengths. f_{acq} is the acquisition bandwidth, which in this work is defined as the reciprocal of the laser scan frequency. The most important reason Equation 1.18 was chosen, is because it is used by other OF-CEAS authors [48, 49].

A common alternative definition of $\alpha_{\min}$ is the standard deviation of an individual data point over time. This is a less rigorous definition of sensitivity, as picking an individual point excludes the influence of stationary etalons that are often a limiting noise source in optical spectroscopy.

1.6.2 Allan variance

The $\alpha_{\min}$ should be always interpreted with caution, not only for the reasons mentioned above, but also because averaging an arbitrary number of spectra to improve $\alpha_{\min}$ eventually becomes unfeasible due to long term frequency drifts. A better way to determine the sensitivity and to quantify the temporal stability of an instrument, is to perform an Allan variance calculation, $\sigma_C^2(t)$, on a parameter retrieved from successive spectra (e.g. the concentration, C) with a known sampling interval, t, [50]. The formula is

$$\sigma_C^2(t) = \frac{1}{2m^2(M-2m+1)} \sum_{j=1}^{M-2m+1} \sum_{i=j}^{j+m-1} \left(C_{i+m} - C_i\right)^2, \tag{1.19}$$

where the index M is the total number of spectra and the index m is the number of averaged spectra. Equation 1.19 is known as the overlapping Allan variance as it takes all possible combinations for a given m [51].

The results of an Allan variance calculation are normally presented as the Allan deviation, $\sigma_C(t)$, as a function of t, on a log-log scale. A plot of this type can be used to identify the dominant type of noise present in the measurement from the gradient of the slope. Initially the slope of Allan deviation decreases as the influence of noise is reduced by averaging more spectra, it then reaches a minimum at the optimum averaging time, before increasing as long term frequency drifts begin to adversely affect the averaging. This method of determining the minimum detectable concentration is rigorous, because the retrieved concentration derives from all of the measured points used to fit the data.

Chapter 2

Physics of Optical Cavities

Since Fabry and Perot first reported their interferometer [52], experimentalists have exploited the physics of optical resonators. The work presented in this thesis makes use of their properties as frequency-selective elements, path-length enhancing optical delay lines, and as optical amplifiers and this chapter presents theory relevant to understanding the physics of these optical cavities.

2.1 Spherical mirror resonators

The simplest optical resonator is formed of two planar partially-reflective elements arranged so that their reflective surfaces are parallel, and is known as a Fabry-Perot etalon [52]. This type of resonator is very sensitive to misalignment: both non-normal ray incidence and non-parallelism of the mirrors will ultimately cause the light ray to follow a path that walks out of the resonator.

Sensitivity to misalignment is greatly reduced for spherical mirror resonators formed of reflectors with concave surfaces. The step-by-step theoretical approach of Saleh and Teich [53] to describe such a resonator, formed by two mirrors with radii of curvature R_1 and R_2, and whose highly reflective dielectric surfaces are separated by a distance L, is summarized in the following section.

2.1.1 Optical conventions

The following standard optical conventions are applied. Optical axes are defined by Cartesian axes such that light propagates along the z-axis; transverse to this are the horizontal and vertical directions, defined respectively as the x- and y-axes. Following Jenkins and White [54], light travels in a positive direction from left to right. Hence, object distances are positive when measured to the left of an optic and image distances are positive when measured to the right. Focal lengths are positive for a converging system ($f > 0$) and negative for a diverging system ($f < 0$), while radii of curvature are positive for convex surfaces ($R > 0$) and negative for concave surfaces ($R < 0$).

2.1.2 Optical ray tracing

Optical ray tracing can be used to determine the geometry required for a light ray to follow a path trapped within a resonator, by ray transfer matrix analysis. The assumptions underlying ray-tracing are that only meridional rays (those that lie in a plane passing through the optical axis) and paraxial rays (those that make small angles with the z-axis) are considered. Within these assumptions, the relationship between the initial, (y_0, θ_0), and final position and slope of the ray, (y_m, θ_m), after m roundtrips around the optical cavity may be considered linear and represented by the following:

$$\begin{bmatrix} y_m \\ \theta_m \end{bmatrix} = \begin{bmatrix} A & B \\ C & D \end{bmatrix} \begin{bmatrix} y_0 \\ \theta_0 \end{bmatrix}. \tag{2.1}$$

The total $ABCD$ matrix is the product of the ray-transfer matrix for each optical component in the system. An optical cavity is a periodic system formed by concatenated identical unit systems. A cavity roundtrip is one unit of the system, and consists of the light ray reflecting off the first mirror, forward propagating a distance L, reflecting off the second mirror, and backward propagating a distance

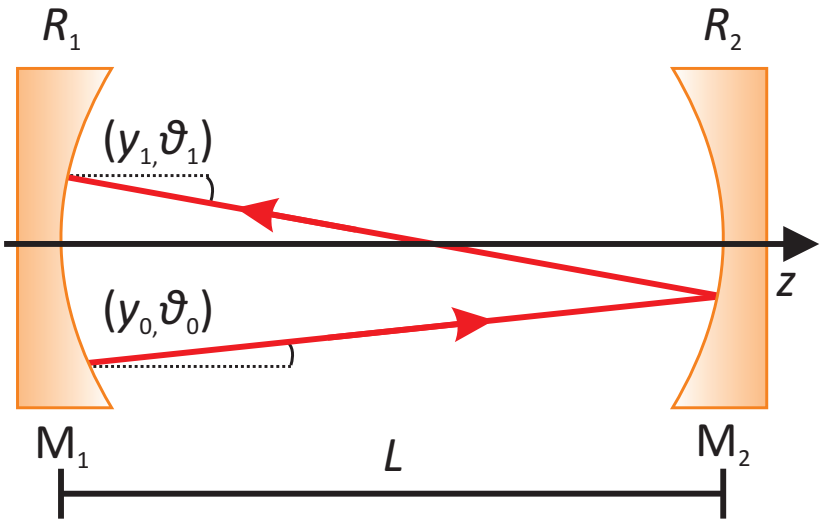

Figure 2.1: A light ray tracing a path through a resonator formed of two mirrors, M_1 and M_2, separated by a distance L, with radii of curvature R_1 and R_2. The ray propagates along the z-axis, according to the paraxial approximation, such that the angle, θ, and consequently the vertical distance, y, from z are small.

L. This is equivalent to light ray propagating forwards through two thin lenses, separated by a distance L, with alternating focal lengths $f_1 = -\frac{R_1}{2}$ and $f_2 = -\frac{R_2}{2}$. A light ray confined within such a resonator is drawn schematically in Figure 2.1. Hence the cavity the roundtrip ray-transfer $ABCD$ matrix is

$$\begin{bmatrix} A & B \\ C & D \end{bmatrix} = \begin{bmatrix} 1 & 0 \\ \frac{2}{R_1} & 1 \end{bmatrix} \begin{bmatrix} 1 & L \\ 0 & 1 \end{bmatrix} \begin{bmatrix} 1 & 0 \\ \frac{2}{R_2} & 1 \end{bmatrix} \begin{bmatrix} 1 & L \\ 0 & 1 \end{bmatrix}. \tag{2.2}$$

For this $ABCD$ matrix, it can be shown that solutions for the position and angle of the ray for Equation 2.1 are

$$y_m = y_{\max} \sin(m\varphi + \varphi_0) \text{ and } \theta_m = \theta_{\max} \sin(m\varphi + \varphi_1), \tag{2.3}$$

where $\varphi = \arccos(b)$, $b = \frac{A+D}{2}$, and $y_{\max}$, $\theta_{\max}$, φ_0, and φ_1 are constants to be determined from initial position and slope of the ray [53]. Rays are confined within the optical cavity when this solution is harmonic, which is the case when φ is real and requires that

$$-1 \leq b \leq 1. \tag{2.4}$$

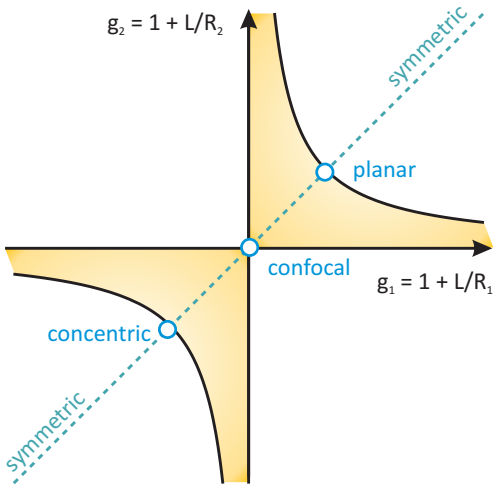

Figure 2.2: Stability diagram for spherical mirror resonator, adapted from Siegman [55]. The horizontal and vertical axes are the parameters g_1 and g_2 respectively; the stable region is yellow, and specific cases are labelled.

This condition is often rewritten as

$$0 \leq g_1 g_2 \leq 1, \tag{2.5}$$

by defining two g-parameters in terms of L, R_1 and R_2:

$$g_1 = 1 + \frac{L}{R_1} \text{ and } g_2 = 1 + \frac{L}{R_2}. \tag{2.6}$$

Figure 2.2 is a graphical depiction of Equation 2.6. The horizontal and vertical axes are the parameters g_1 and g_2 respectively. Stable cavity geometries occur in the shaded yellow region. Symmetric resonators, which have $R_1 = R_2$, lie on the line $g_1 = g_2$. Special cases of symmetric resonators are planar resonators ($R_1 = \infty = R_2$, Fabry-Perot etalon), confocal resonators ($R_1 = L = R_2$), and concentric resonators ($R_1 = L/2 = R_2$) [55].

2.1.3 Gaussian beam optics

Ray tracing optics does not account for the wavelike nature of light. Under the boundary conditions of the spherical mirror resonator, Gaussian beams are the eigensolutions of the Helmholtz wave equation. Consequently, Gaussian beam optics is necessary to describe the spatial intensity distributions and the resonance frequencies of the eigenmodes of an optical cavity.

The transverse intensity, $I(x, y)$, of a circular Gaussian beam propagating along the z-axis is

$$I(x, y) = I_0 \exp\left[-2\frac{(x^2 + y^2)}{(w_x^2 + w_y^2)}\right], \tag{2.7}$$

where I_0 is the intensity amplitude, and w_x and w_y are the horizontal and vertical beam radii. These are further related to the standard deviation, σ_x, of the Gaussian intensity profile by $2\sigma_x = w_x$ in the horizontal direction, and likewise for the vertical direction.

Figure 2.3 shows a Gaussian beam confined within an optical cavity. The Gaussian beam wavefront has a radius of curvature, $R(z)$, which matches the radii of curvature of the cavity mirrors, R_1 and R_2, in the planes of the cavity

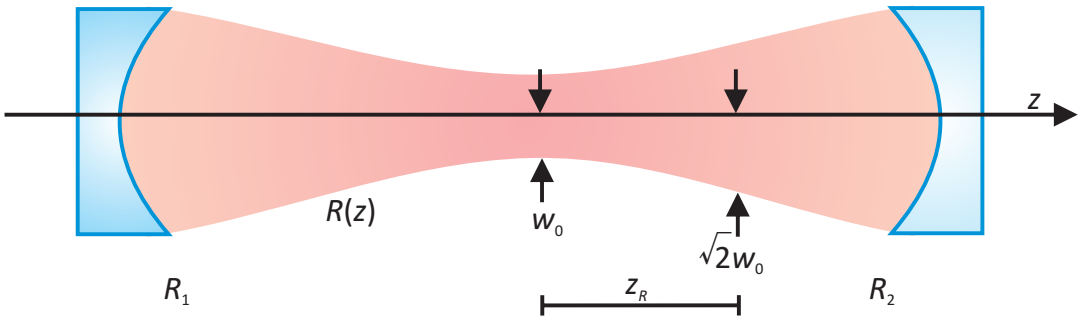

Figure 2.3: Gaussian beam (red) propagating along the z-axis, with beam waist w_0, Rayleigh range z_R and radius of curvature $R(z)$, confined within an optical cavity formed of two mirrors with radii of curvature of R_1 and R_2. [Not to scale.]

mirrors, and therefore the beam retraces itself upon reflection.

$$R\left(z\right) = \left(z - z_0\right)\left[1 + \left(\frac{z_{\mathrm{R}}}{z - z_0}\right)^2\right], \tag{2.8}$$

where z_{R} is the Rayleigh range, the distance at which the beam wavefronts are most curved, and z_0 is the position of the beam waist. The wavefronts are plane at the beam waist, w_0, which is related to z_{R} via the wavelength, λ:

$$w_0 = \left(\frac{\lambda z_{\mathrm{R}}}{\pi}\right)^{1/2}. \tag{2.9}$$

The beam radius, $w(z)$, increases in both directions from w_0, and is defined by

$$\begin{aligned} w^2\left(z\right) &= w_0^2 + \left(\frac{\lambda}{\pi w_0}\right)^2 \left(z - z_0\right)^2 & (2.10)\\ &= w_0^2\left[1 + \left(\frac{z - z_0}{z_{\mathrm{R}}}\right)^2\right], & (2.11) \end{aligned}$$

hence $w(z_{\mathrm{R}})$ is $\sqrt{2}w_0$. From Equation 2.9, it follows that a Gaussian beam is fully described by knowing any two of w_0, z_{R} and λ [53].

The resonance frequencies of a spherical optical resonator are found by considering the phase change of the Gaussian beam, ϕ, as it propagates a distance z:

$$\phi(x^2 + y^2, z) = kz - \zeta(z) + \left(\frac{k\left(x^2 + y^2\right)^2}{2R(z)}\right). \tag{2.12}$$

The first term of Equation 2.12 is the phase of a plane wave: $k = \frac{2\pi\nu}{c}$ is the wavevector, ν is the optical frequency. The second term, $\zeta(z)$, is the Gouy phase retardation accounting for the extra delay of the Gaussian wavefront compared to that of a plane or spherical wave. This takes values from $\frac{-\pi}{2}$ at $z = -\infty$, to $\frac{\pi}{2}$ at $z = \infty$ respectively. The third term accounts for wavefront bending, but on

the beam axis $x^2 + y^2 = 0$, and so ϕ simplifies to

$$\phi(0, z) = kz - \zeta(z). \tag{2.13}$$

As the beam propagates the distance from the first mirror at z_1 to the second at z_2, the phase change is

$$\phi(0, z_2) - \phi(0, z_2) = kL - \Delta\zeta. \tag{2.14}$$

Here $\Delta\zeta = \zeta(z_2 - z_1)$, which is valid because the radius of curvature of the beam wavefront is coincidental to the curvature of the mirrors in the plane of the mirrors. Consequently, the beam necessarily has the same phase at all points on the mirror surface. The phase change for one cavity roundtrip is double this value, and must be an integer multiple of 2π for the Gaussian beam to retrace itself. Given this condition, and defining q as the integer mode index, leads to the following expression for the resonance frequencies, ν_q, of the axial or longitudinal cavity modes:

$$\nu_q = \frac{c}{2L}\left[q + \frac{\Delta\zeta}{\pi}\right]. \tag{2.15}$$

The modes have a frequency spacing, $\Delta\nu_{\mathrm{FSR}}$, commonly referred to as the free spectral range (FSR):

$$\Delta\nu_{\mathrm{FSR}} = \frac{c}{2L}. \tag{2.16}$$

Higher-order eigensolutions other than the Gaussian beam also exist for the spherical mirror resonator. For resonators with rectangular symmetry, these transverse modes have amplitudes described by Hermite polynomials labelled (m, n), where m is a horizontal and n a vertical index corresponding to the number of nodes. These eigensolutions can also be found by solving Maxwell's equations for the boundary conditions of a spherical resonator, and it is from this approach the TEM_{mn} (transverse electromagnetic) nomenclature derives. Simu-

lations of Hermite-Gaussian modes for a symmetrical spherical resonator, with $L = 0.75$ m and $R_1 = 0.5 = R_2$ m, are shown in Figure 2.4, including the fundamental circular Gaussian mode TEM_{00}. Although the wavefront curvature is the same for these higher-order modes, the electric field amplitude distribution and therefore also the intensity is different. The resonance frequencies are also changed, due to the dependence of the Gouy phase retardation on (m, n), but $\Delta\nu_{\mathrm{FSR}}$ is the same. Higher order modes have a greater transverse extent and therefore suffer greater diffraction losses at the resonator mirrors.

The geometric requirement for a stable optical cavity (Equation 2.5) may be rederived within the Gaussian beam approach. From the spherical mirror boundary condition, z_{R} may by written in terms of R_1, R_2 and L:

$$z_{\mathrm{R}}^2 = \frac{-L\,(R_1 + L)\,(R_2 + L)\,(R_1 + R_2 + L)}{R_1 + R_2 + 2L^2}, \tag{2.17}$$

and recasting this equation in terms of the g-parameters defined in Equation 2.6 leads to

$$z_{\mathrm{R}}^2 = \frac{g_1 g_2\,(1 - g_1 g_2)\,L^2}{(2g_1 g_2 - g_1 - g_2)^2}. \tag{2.18}$$

For a confined solution, z_{R} must be real, i.e. ${z_{\mathrm{R}}}^2 > 0$, which is true when $0 \leq g_1 g_2 \leq 1$ (same as Equation 2.5). The Gaussian beam waist may then be conveniently defined in terms of the g-parameters and L:

$$w_0^2 = \left(\frac{\lambda L}{\pi}\right)\sqrt{\frac{g_1 g_2(1 - g_1 g_2)}{(g_1 + g_2 - 2g_1 g_2)^2}}. \tag{2.19}$$

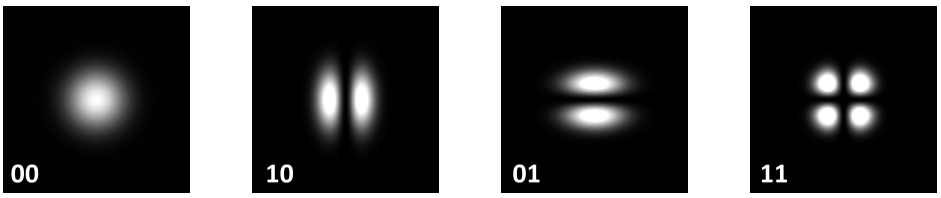

Figure 2.4: Simulations of TEM_{00}, TEM_{10}, TEM_{01}, and TEM_{11} Hermite-Gaussian modes for a spherical mirror resonator.

As can the beam radius on the first and second cavity mirrors:

$$w_1^2 = \left(\frac{\lambda L}{\pi}\right)\sqrt{\frac{g_1}{g_1(1-g_1g_2)}},\; w_2^2 = \left(\frac{\lambda L}{\pi}\right)\sqrt{\frac{g_2}{g_2(1-g_1g_2)}}. \tag{2.20}$$

For a symmetric resonator ($g_1 = g_2$) these reduce to

$$w_0^2 = \left(\frac{\lambda L}{\pi}\right)\sqrt{\frac{1+g}{4(1-g)}}, \tag{2.21}$$

and

$$w_1^2 = \left(\frac{\lambda L}{\pi}\right)\sqrt{\frac{1}{1-g^2}} = w_2^2. \tag{2.22}$$

2.1.4 Non-Gaussian beam quality factor, M^2

The beam waist and standard deviation of non-Gaussian beams with symmetrical intensity profiles can be considered to have a similar relationship to those of Gaussian beams ($w_x = 2\sigma_x$). Based on this assumption, the non-Gaussian analogue of Equation 2.10 is

$$w_x^2(z) = w_{0x}^2 + M_x^4\left(\frac{\lambda}{\pi w_{0x}}\right)^2(z-z_{0x})^2 = w_{0x}^2\left[1+\left(\frac{z-z_{0x}}{z_{\mathrm{R}x}/M_x^2}\right)^2\right], \tag{2.23}$$

in the horizontal direction, and likewise for w_y in the vertical direction. The parameter M^2 is the beam quality factor. Equating coefficients for the second terms of Equation 2.10 and Equation 2.23, leads to a definition of M^2 as the squared ratio of the real to the ideal Gaussian beam waists. This gives $M^2 \geq 1$, with unity representing the case of a Gaussian beam. Because M^2 is related to the far-field half-angle, $\theta_{1/\exp}$, by

$$\theta_{1/\exp} = \frac{M^2\lambda}{\pi w_0}, \tag{2.24}$$

it is a useful measure of beam divergence, relative to that expected of an ideal Gaussian beam. From Equation 2.23 and Equation 2.9 it follows that any beam

with a symmetrical intensity profile is fully described by knowing any three of w_0, z_R, λ, or M^2 [56].

2.1.5 Fourier optics and diffraction loss

The Gaussian beams considered so far have infinite transverse extent. In reality, cavity mirrors have finite apertures and on each reflection some power is lost from the optical cavity due to diffraction, as light leaks out from around the edges of the cavity mirrors. The effect of diffraction is quantified by the Fresnel number, N_F, defined as

$$N_F = \frac{a^2}{\lambda L}, \tag{2.25}$$

where a is the radius of the circular aperture, L is the distance from the aperture, and λ is the wavelength of the incident light. A smaller N_F corresponds to a greater loss per reflection, so diffraction loss is greater at longer λ.

For a symmetrical optical cavity, substitution of Equation 2.22 into Equation 2.25 relates diffraction loss to the beam radius on the mirrors:

$$N_F = \frac{a^2}{\pi w_\mathrm{mirr}^2 \sqrt{1-g^2}}. \tag{2.26}$$

Beams with larger radii (e.g. higher order Hermite-Gaussian modes) therefore suffer greater diffraction losses. Diffraction loss is minimized by mode-matching. For the mid-IR laser beams and optical cavities used in this work, this means that the beam radii on the cavity mirrors is around 10 times smaller than the mirror aperture (1 inch or 25.4 mm), see Section 4.6.3.

2.2 Transmission functions

Optical cavities can be modelled as linear optical systems and the superposition principle may be applied [57]. The frequency dependent electric field transmitted by the optical cavity, $\tilde{E}_0(\omega)$, is the same whether the frequency components in the incident electric field, $\tilde{E}_{\rm inc}(\omega)$, are applied and then summed or summed and then applied [53]. Hence $\tilde{E}_0(\omega)$ and $\tilde{E}_{\rm inc}(\omega)$ are linearly related by a transfer function $\mathcal{H}(\omega)$:

$$\tilde{E}_0(\omega) = \mathcal{H}(\omega)\tilde{E}_{\rm inc}(\omega). \tag{2.27}$$

The signal from the detector is ultimately related to the intensity or power, $I(\omega)$, of light falling on it, which is proportional to the square modulus of the electric field:

$$I(\omega) \propto \left|\tilde{E}(\omega)\right|^2, \tag{2.28}$$

and hence the spectral intensity transmitted by the optical cavity, I_0, is also linearly related to the incident spectral density, $I_{\rm inc}(\omega)$, by a transfer function, $H(\omega)$:

$$I_0 = H(\omega)I_{\rm inc}. \tag{2.29}$$

2.2.1 Without loss

For an optical cavity without losses, the power reflectivity, R, is related to the power transmission, T, of the cavity mirrors by $1 = R + T$. These quantities are related to the electric field reflectivity, r, and transmissivity, t, by

$$R = |r|^2, T = |t|^2. \tag{2.30}$$

The transfer function for a general standing-wave resonator is

$$\mathcal{H}(\omega) = \frac{\tilde{E}_0(\omega)}{\tilde{E}_{\rm inc}(\omega)} = \frac{-t^2 \exp[-{\rm i}\omega t_{\rm r}/2]}{1 - \tilde{g}_r(\omega)}, \tag{2.31}$$

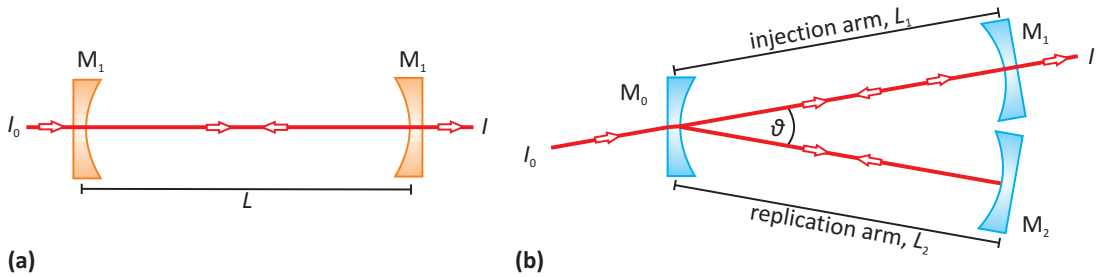

Figure 2.5: Linear and V-cavities, related such that all mirrors, M, are identical, and all cavity arm lengths, L, are equal.

where the numerator expresses transmission of the incident field through the mirror coatings with a phase shift expressed in terms of t_{r}, the cavity roundtrip time. The frequency dependent complex round trip gain, $\tilde{g}_r(\omega)$, depends on the number of reflections required to complete a cavity round trip [55].

Two distinct optical cavity geometries are used in the work presented in this thesis, a two mirror linear optical cavity and a three mirror V-shaped optical cavity. Figure 2.5 depicts a linear and V-shaped cavity related by having identical mirrors and cavity arm lengths. Considering the linear cavity, the field is reflected twice in a roundtrip, leading to:

$$\tilde{g}_{r,\mathrm{lin}}(\omega) = r_2 r_1 \exp[-\mathrm{i}\omega t_{\mathrm{r}}], \tag{2.32}$$

which reduces to

$$\tilde{g}_{r,\mathrm{lin}}(\omega) = r^2 \exp[-\mathrm{i}\omega t_{\mathrm{r}}], \tag{2.33}$$

in the case where the mirrors have identical reflectivity. The electric field in the V-cavity is reflected four times in a roundtrip, instead leading to:

$$\tilde{g}_{r,\mathrm{V}} = r_1 r_0 r_2 r_0 \exp[-\mathrm{i}\omega t_{\mathrm{r}}], \tag{2.34}$$

and for a cavity with identical mirrors this simplifies to:

$$\tilde{g}_{r,\mathrm{V}} = r^4 \exp[-\mathrm{i}\omega t_{\mathrm{r}}]. \tag{2.35}$$

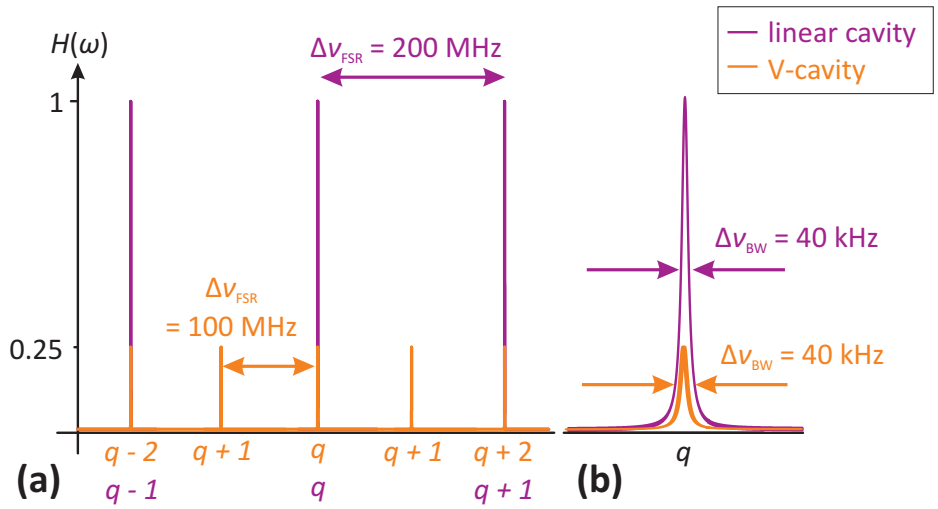

Figure 2.6: (a) Transfer functions, $H(\omega)$, for related linear (purple) and V-cavities (orange) plotted against cavity mode frequency, q; (b) is a magnification around a single mode resonance illustrating the narrow cavity bandwidths.

Combining Equation 2.31 with Equation 2.32 and Equation 2.34, the transfer functions for lossless linear and V-cavities can be derived. For a linear cavity the expression is

$$H_{\mathrm{lin}}(\omega) = \left[\frac{I_0}{I_{\mathrm{inc}}}\right]_{\mathrm{lin}} = \frac{T^2}{(1-R)^2 + 4R\sin^2(\omega t_{\mathrm{r}}/2 - \theta)}, \tag{2.36}$$

where $\theta = \arg(-r)$. This is the standard result for a Fabry-Perot etalon, and has been derived by Lehmann and Romanini [57] using the superposition approach. For a V-cavity

$$H_{\mathrm{V}}(\omega) = \left[\frac{I_0(\omega)}{I_{\mathrm{inc}}(\omega)}\right]_{\mathrm{V}} = \frac{T^2}{(1-R^2)^2 + 4R^2\sin^2(\omega t_{\mathrm{r}}/2 - \theta)}. \tag{2.37}$$

as derived by Morville and Romanini [58, 59].

For comparison purposes, the transfer functions for linear and V-cavities were calculated using R (0.9994) and L (75 cm) (i.e. the parameters for the linear cavity OF-CEAS system described in Chapter 4) and are drawn in Figure 2.6. $H(\omega)$ is a periodic function of frequency, where the period corresponds to the frequency spacing of the axial cavity mode frequencies, which have index q. This

is the FSR (Equation 2.16) and is 200 MHz for the linear cavity and 100 MHz for the V-cavity, which is twice as long. The finesse of the linear resonator, $\mathcal{F}_{\mathrm{lin}}$, is

$$\mathcal{F}_{\mathrm{lin}} = \frac{\pi R^{1/2}}{1-R}, \tag{2.38}$$

which is the standard result for a Fabry-Perot or a spherical resonator [53]. The finesse of the V-shaped cavity, $\mathcal{F}_{\mathrm{V}}$, is

$$\mathcal{F}_{\mathrm{V}} = \frac{\pi R}{1-R^2}, \tag{2.39}$$

equivalent to a result derived for a tilted confocal cavity by Laurent et al. [60]. This means that for a given mirror set the finesse is higher for the linear (~ 5000) than the V-cavity (~ 2600). Both cavities have narrow bandwidth resonances due to the high reflectivity of the mirrors and the correspondingly high finesse. The bandwidth of the resonances at FWHM is

$$\Delta\nu_{\mathrm{BW}} = \frac{\Delta\nu_{\mathrm{FSR}}}{\mathcal{F}}. \tag{2.40}$$

which is the same for both cavities, c. 40 kHz. The height of the maxima for the transmission function of the linear cavity are given by

$$H_{\mathrm{max,lin}} = \left[\frac{I_0}{I_{\mathrm{inc}}}\right]_{\mathrm{max,lin}} = \frac{T^2}{(1-R)^2}. \tag{2.41}$$

For a lossless linear optical cavity the expected transfer function maximum at cavity resonance is unity, i.e. all light incident on the cavity is transmitted. The maxima for the V-cavity are given by:

$$H_{\mathrm{max,V}} = \left[\frac{I_0}{I_{\mathrm{inc}}}\right]_{\mathrm{max,V}} = \left[\frac{T}{(1-R^2)}\right]^2 \approx \left[\frac{T}{2(1-R)}\right]^2. \tag{2.42}$$

For a lossless V-cavity the maximum transmission is a quarter of that for an

equivalent linear cavity [58].

2.2.2 With loss

Real optical cavities are subject to losses, A, such that $1 = R + T + A$. These may be divided into two categories: those that are frequency independent over the bandwidth of the input radiation and mirror coatings, and those that are frequency dependent. Frequency independent losses arise from scattering by molecules or aerosols in the intracavity medium, absorption and scattering in the mirror substrates, and diffraction around the mirror edges (Section 2.1.5). For the optical cavities used in this work, these effects are negligibly small compared to the frequency dependent absorption losses caused by analyte gases.

Measurement of frequency dependent absorption losses form the basis of the cavity-enhanced absorption spectroscopy techniques. R is frequency dependent in the presence of a medium absorbing within the bandwidth of the incident field and each frequency component, ω, can be considered separately within the superposition approach to give a roundtrip attenuation factor

$$R_{\text{eff}}(\omega) = R(\omega)\exp[-\alpha(\omega)L], \tag{2.43}$$

where $\alpha(\omega)$ is the frequency dependent molecular absorption co-efficient and L is the mirror separation in the optical cavity. If an absorber is present in the intracavity medium then $H_{\text{max,lin}}$ is

$$H_{\text{max,lin}} = \left[\frac{I}{I_{\text{inc}}}\right]_{\text{max,lin}} = \left[\frac{T\exp[-\alpha L/2]}{(1 - R\exp[-\alpha L])}\right]^2, \tag{2.44}$$

and $H_{\text{max,V}}$ is

$$H_{\text{max,V}} = \left[\frac{I}{I_{\text{inc}}}\right]_{\text{max,V}} = \left[\frac{T\exp[-\alpha L/2]}{(1 - R^2\exp[-2\alpha L])}\right]^2. \tag{2.45}$$

2.3 Cavity-enhanced spectroscopy

As discussed in Section 1.5.2, the Beer-Lambert law indicates that the sensitivity of an absorption measurement is increased if the pathlength, L, is extended. Using optical cavities, this concept has been applied to spectroscopy in two main forms: cavity ringdown spectroscopy, where the measurement is made in the time domain, and cavity-enhanced absorption spectroscopy, where the measurement is made in the amplitude domain.

2.3.1 Cavity mirrors

The mirrors used in cavity-enhanced forms of spectroscopy have power reflectivity coefficients, R, typically greater than 0.999 [29] and in extreme cases greater than 0.99999 (i.e. losses less than 1 ppm) [61]. Highly reflective mirrors of this type were originally developed for use in laser resonators. They are formed of alternating layers of two different dielectric materials (material 2 and material 3), of thickness h_2 and h_3, and refractive indices n_2 and n_3, deposited by ion sputtering on to a substrate, material 4, in vacuo [29]. The alternating layers fulfil the quarter-wave condition, such that the the optical distances in each material, i.e. n_2h_2 and n_3h_3, are each equivalent to $\lambda/4$.

The reflectivity of a stack of dielectric layers of any thickness can be shown to be:

$$R = \frac{\text{intensity reflected}}{\text{intensity incident}} = \left| \frac{Z_{\text{in}} - Z_{\text{air}}}{Z_{\text{in}} + Z_{\text{air}}} \right|^2, \tag{2.46}$$

from which it is clear that high reflectivity can be achieved by an extreme impedance mismatch between the input, Z_{in}, and air, Z_{air}. For quarter-wave layers, Z_{in} is related to the impedances of the dielectric layers, Z_j, and the total number of layers, p, by $Z_{\text{in}} = (Z_2/Z_3)^{2p} Z_4$ and these ratios of impedances are simply proportional to the refractive indices of the materials. Highly reflective mirrors are typically formed of an odd number of dielectric layers, with the layer

of highest refractive index as the first and last layers [62]. (Equally, a surface can be anti-reflection coated using a multilayer structure impedance matched to air.) A field reflected from such a mirror necessarily undergoes a phase shift of π upon reflection [63], and this is discussed further in Section 4.5.1.

2.3.2 Cavity ringdown spectroscopy

The concept behind cavity ringdown spectroscopy (CRDS) originally arose from the need to measure the reflectivity of very low loss dielectric laser cavity mirrors [64, 65]. A pulse of light is injected into an optical cavity, and decays over a timescale orders of magnitude longer than the cavity roundtrip. The cavity ringdown time, τ_0, is defined as the time taken for the circulating intensity circulating, $I(t)$, to decay to exp[−1] of its initial value, I_0:

$$I(t) = I_0 \exp - [t/\tau_0]. \tag{2.47}$$

Hence τ_0, typically on the order of several µs, is retrieved from experimental data by fitting an exponential function to the intensity decay recorded at the end of the pulse. The ringdown time is related to the mirror reflectivity, R, in the following way. After m cavity roundtrips in time t, the circulating intensity, I_m, is:

$$I_m = I_0 R^{2m} = I_0 \exp[2m \ln R]. \tag{2.48}$$

For the linear cavity in Figure 2.5 the cavity roundtrip time is $t_\mathrm{r} = 2L/c$, and the number of roundtrips is therefore $m = t/t_\mathrm{r}$. Substituting these expressions into Equation 2.48 leads to

$$I(t) = I_0 \exp [ct \ln R/L], \tag{2.49}$$

and by comparison of Equation 2.47 with Equation 2.49, τ_0 is

$$-\tau_0 = \frac{L}{c \ln R}. \tag{2.50}$$

As $R \to 1$, Equation 2.50 may be simplified by taking the first term of the Taylor expansion of $\ln R$, resulting in

$$\tau_0 = \frac{L}{c\,(1-R)}. \tag{2.51}$$

When an absorber is present in the intracavity medium, the ringdown time is reduced and is related to the absorption coefficient, $\alpha(\nu)$, of by

$$\tau = \frac{L}{c\,[(1-R)+\alpha(\nu)L]}. \tag{2.52}$$

This enables the observed ringdown time to be transformed into an absorption, and consequently by stepping the laser frequency over an absorption profile, and recording the τ_0 at each step, an absorption spectrum may be recorded. Because the measurement is made in the time rather than the intensity domain, CRDS benefits not only from pathlength enhancement but is also immune to laser intensity noise, which does not affect the decay rate.

CRDS was first implemented by O'Keefe and Deacon using a pulsed dye laser [66]. This form of CRDS has an acquisition time limited by the pulse repetition rate. The light pulse will have a broad linewidth covering several cavity longitudinal modes. Not only does this reduce the intensity coupled into each mode, reducing the signal-to-noise ratio, but each mode has a slightly different decay rate. This results in a multi-exponential decay and makes it more difficult to accurately retrieve τ_0 [29]. These problems led to the development of cw-CRDS [67]. This form of the technique can achieve faster acquisition rates, by rapid on and off switching of the laser, and also single cavity mode excitation due to the narrower linewidth of a cw laser. Combining the technique with a cw-diode laser also makes possible more compact instruments. Initial implementation of cw-CRDS extinguished the cw-light in order to generate a pulse by using an optical switch [67], which may be combined with locking the laser frequency to that

of the cavity [68], or by rapid detuning of the optical cavity length [69].

CRDS has been widely applied to the detection of trace gas species, and also extended to other problems as detailed in the recent book edited by Berden and Engeln [29]. Its applications to atmospheric chemistry have been reviewed by Brown [70]. CRDS instruments are available commercially from Los Gatos, Tiger Optics and Picarro, with the last company's instruments being widely used for atmospheric CH_4 monitoring [71]. NASA is developing a cw-CRDS instrument for future deployment on Mars for in-situ sensing of CH_4 [72].

2.3.3 Cavity-enhanced absorption spectroscopy

A simpler form of cavity-enhanced spectroscopy is cavity-enhanced absorption spectroscopy, where the optical cavity is continually illuminated by a cw laser and the transmitted intensity recorded. This removes the need for optical switches and fast data acquisition, while maintaining the advantages of high sensitivity.

CEAS relies on measuring a small signal above the baseline noise. A dominant contribution to the baseline noise arises from the frequency-filtering effect of the optical cavity that converts laser intensity fluctuations into frequency fluctuations. CEAS schemes fall broadly into two categories: those that try to remove this effect (ICOS and OA-CEAS), and those that lock the laser frequency to that of the optical cavity modes (OF-CEAS, NICE-OHMS, ML-CEAS).

Integrated cavity output spectroscopy (ICOS) relies on simultaneously exciting very many high order TEM_{mn} cavity modes, to suppress fringing on the baseline. The simplest method of achieving this is to rapidly sweep the laser while monitoring the cavity transmission with a relatively slow detector or to rapidly dither the cavity length. However, the non-uniform mode excitation inherent to this method causes the coupling efficiency of the laser beam into the cavity to vary, leading to cavity output intensity fluctuations. This also causes the transverse spatial output to change, which becomes particularly problematic with small area

detectors. More sophisticated off-axis alignment schemes overcome this problem. The beam incident on the cavity is injected such that it folds along a complex trajectory similar to that of a beam in a Herriott cell, closing on itself after N cavity round trips [73]. This results in a reproducible beam trajectory in the cavity, so as the laser frequency passes through resonance with successive groups of degenerate cavity modes, leading to uniform mode excitement.

Given the division of the power of the input laser radiation between so many modes, the optical power leaking out of the cavity is very low for the non-resonant schemes of ICOS and OA-CEAS, resulting in a low signal-to-noise ratios. High order TEM_{00} modes also have large beam radii on the cavity mirrors, so diffraction losses are increased. This problem is exacerbated when using diode lasers, as these have a relatively large linewidth compared to that of the optical cavity, so very little light is coupled into the cavity.

Certain schemes have instead been developed to exploit the resonant properties of optical cavities, in order to overcome these difficulties. Arguably the technique of optical-feedback cavity-enhanced absorption spectroscopy (OF-CEAS), pioneered by the groups of Romanini and Morville [59], has proven most relevant to tuneable diode laser spectroscopy. Two versions of this scheme are implemented in this work and the technique is discussed further in Section 2.4.2

There are two other notable resonant cavity techniques: noise-immune cavity-enhanced optical heterodyne molecular spectroscopy (NICE-OHMS) [46], and mode-locked CEAS (ML-CEAS) [74]. ML-CEAS was also pioneered by the group of Romanini, and works on the principle that if the laser repetition rate of a mode locked laser is in an integer ratio with the cavity $\Delta\nu_{\mathrm{FSR}}$, then the resonances of the laser frequency comb correspond to those of the cavity. Field instruments have been demonstrated for measuring atmospherically important radicals at marine boundary layers in France [75] and Antarctica [76]. Although they have the benefit of being broadly tuneable, mode-locked lasers are prohibitively expensive.

The ultimate cavity-enhanced technique is that of NICE-OHMS, which is most simply thought of as cavity-enhanced frequency modulation spectroscopy (CE-FMS). The laser is stabilized by the Pound-Drever-Hall method and CE-FMS is performed, this ensures that all parts of the modulation triplet are equally transmitted and enhanced by the optical cavity. NICE-OHMS has demonstrated the best ever $\alpha_{\min}$ of 1×10^{-14} cm^{-1} in 1 s, using an Nd:YAG laser [46]. EC-DL [77], DFB-DL [78], and QCL [79] NICE-OHMS instruments have all been demonstrated, although with a reduced $\alpha_{\min}$ of around 10^{-10}. The reason for this is the increased difficulty in locking of the laser frequency to that of a cavity mode, particularly if the laser linewidth exceeds that of the cavity as is the case for diode lasers, and this leads to a stringent need for high bandwidth feedback loops (a few MHz), and isolation from vibrations [80]. Efforts to miniaturize NICE-OHMS are on-going, most promisingly with fibre-laser based instruments [81]. However, a field-ready NICE-OHMS instrument is yet to be demonstrated.

2.4 Optical-feedback locked cavity-enhanced spectroscopy

For semiconductor lasers, an alternative to electronic locking schemes is to passively self-lock the laser by returning an appropriate fraction of phase controlled optical-feedback into the laser gain medium. An optical-feedback self-locking scheme based on a high finesse optical cavity was described by Laurent et al. [60] and Dahmani et al. [82] in the late 1980s. However, it was not until 2001 that this scheme was combined with cavity-enhanced diode laser absorption spectroscopy (CEAS) by Romanini and Morville [58, 83].

2.4.1 OF-CRDS

The initial implementation was a cw optical-feedback cavity ringdown spectroscopy (OF-CRDS) scheme. This methodology arose out of a need for efficient and reliable coupling of diode lasers (typical linewidth on the order of MHz) to high finesse optical cavities (∼kHz) for cw-CRDS. Ringdown events are observed by rapidly switching (kHz) the diode laser current above and below threshold with a square wave modulation. When switched above threshold, the diode laser frequency undergoes a rapid frequency down chirp due to heating of the laser chip. As the chip reaches thermal equilibrium, the frequency chirp slows and the laser frequency tunes until it matches that of a cavity resonance. Efficient and rapid injection of light into the cavity then occurs, which also results in the return of optical-feedback to the laser. By virtue of this injection seeding, the laser frequency locks to that of the cavity mode for a time period much longer than the cavity ringdown time ($\sim \tau_0$). There is also a laser linewidth narrowing effect. The end of the square pulse switches the laser current below threshold, extinguishing the light incident on the cavity and allowing a ringdown transient to be recorded.

This self-locked scheme had several advantages over other cw-CRDS schemes. The coupling efficiency of the diode laser to the narrow bandwidth of the cavity modes is vastly increased, due to the linewidth narrowing and frequency stabilization resulting in larger signals. The self-locking results in rapid injection and therefore a fast acquisition rate of several kHz. No fast optical switch (e.g. an acousto-optic modulator) is required for extinguishing the laser beam. The original scheme had no active stabilization of the optical-feedback phase, but the same group later extended the technique to include this [84]. The OF-CRDS technique has also been implemented by Orr-Ewing and coworkers for detection of aerosols [85, 86].

2.4.2 OF-CEAS

Most implementations of OF-locked cavity-enhanced absorption spectroscopy have been based on the optical-feedback cavity-enhanced absorption spectroscopy technique (OF-CEAS), also developed by the group of Romanini and Morville [59]. This version of the technique instead measures the intensity transmitted by the cavity, relaxing the need for the fast acquisition and synchronization systems required to capture cavity ringdown transients. As the cavity-coupled diode laser frequency is tuned by varying the injection current it locks to successive axial cavity mode frequencies. Accordingly, the temporal cavity transmission consists of an envelope of peaks, whose frequency spacing corresponds to the free spectral range, $\Delta\nu_{\mathrm{FSR}}$, of the optical cavity. When an absorber is introduced to the cavity, this yields a cavity-enhanced absorption spectrum with a self-calibrating relative frequency scale.

OF-CEAS has several advantages over other demonstrated CEAS schemes. Using a resonant TEM_{00} alignment, and locking the laser frequency to those of the cavity modes, results in a very high and reproducible cavity coupling rate and a correspondingly large signal-to-noise ratio. This alignment also results in a much smaller beam radius on the cavity mirrors, leading to reduced diffraction losses and the prospect of very small cell-volumes if small diameter mirrors are used. Although OF-CEAS has a requirement for active control of the phase of the returning feedback (see Section 4.7), the speed of the control loop is such that user-friendly LabVIEW based systems are adequate [48, 49, 87, 88, 89], this would not be possible using an electronic locking scheme.

Consequently, OF-CEAS is a robust and sensitive technique, well-suited to the measurement of trace gases in the pressure broadened regime, combining high sensitivity with a experimental setup, arguably more simple than that of diode laser CRDS or NICE-OHMS. The inventors of the technique (the group of Romanini, Morville and their collaborators) have applied several variants of the OF-CEAS

technique to a wide range of gas sensing problems They have used instruments based on near-IR diode lasers coupled to V-shaped optical cavities for air-borne real-time measurement of atmospheric methane [90], laboratory measurements of CO_2 isotopologues [91], and breath analysis faster than a single respiratory cycle [92]. They have extended the technique to use visible blue [93] and red [84] EC-DLs, a vertical external cavity surface emitting laser [94], and also quantum cascade lasers [49, 88]. They hold a patent for the OF-CEAS technology [95], which has been developed into a commercially available instrument [96]. Currently, they are building an OF-CEAS instrument into the tip of an ice-core drill to measure methane isotopologues in gas bubbles trapped in Antarctic ice [97] as part of a major climate research initiative. An interesting ring-cavity variant was demonstrated by Hamilton et al. [87] using a visible diode laser. Hamilton and Orr-Ewing have also built V-cavity QCL OF-CEAS [48, 98]. DFB-DL V-cavity OF-CEAS was also demonstrated by Baran et. al. [99], and it is on these results that the next chapter builds. More significantly, Chapters 4 and 5 present a novel linear cavity variant using a QCL, some of which was published as [89].

Chapter 3

Near-IR Diode Laser V-cavity OF-CEAS

This chapter introduces the technique of optical-feedback cavity-enhanced absorption spectroscopy (OF-CEAS) and presents experimental results of a near-IR V-cavity implementation that follows the form of the first reported instrument [59]. Prior to the experimental work, the chapter begins by describing operation of diode lasers relevant to tuneable diode laser absorption spectroscopy, before a review of the theory relevant to understanding the OF-CEAS self-locking scheme is given. The experimental setup is introduced, and the instrument is applied to investigating the spectroscopy of carbon dioxide (CO_2) and sensing of acetylene (C_2H_2).

3.1 Diode lasers

Following Schawlow and Townes' 1958 proposal for extending maser techniques into the infrared and visible regions [100], the first working laser was built in 1960 [101]. Diode lasers were demonstrated soon after by several groups [102, 103, 104, 105]. The two primary advantages of diode lasers are their compact size ($\ll$ 1 cm) and the ability to directly tune their frequency by modulating

the injection current [106]. The application of these advantages to optical fibre telecommunications drove the development of diode lasers based on InGaAsP, emitting in the 1.1 to 1.6 µm wavelength range that is optimally transmitted by silica optical fibres [19]. These properties of diode lasers are also relevant to spectroscopy, as this wavelength range coincides with the near-IR spectral region, where many small molecules have weak overtone and combination bands.

3.1.1 Diode laser operation and waveguiding

The simplest diode is formed at a junction of *p*-type and *n*-type doped semiconductors. Applying a forward bias causes electrons and holes in the depletion region around the junction to recombine radiatively, emitting photons with an energy defined by the semiconductor bandgap. The reverse process (production of electron and hole pairs via photon absorption) also occurs until a critical voltage is reached, at which the rate of photon emission exceeds that of absorption, and population inversion is achieved [19]. A laser diode is formed by polishing the crystal facets perpendicular to the *pn*-junction plane to form an optical cavity. This most simple diode laser (a homostructure) is highly inefficient and several improvements are necessary to define the gain medium and thereby confine both the charge carriers and the optical mode.

Vertical confinement results from the use of *p*-*p*-*n* double heterojunction structures. In this scheme, the *p*-type active region has a smaller bandgap than the *p*- and *n*-type cladding layers. This causes sharp drops in energy at both the conduction band at the *p*-*p* junction and the valence band at the *p*-*n* junction, trapping the charge carriers and better defining the thickness of the gain medium. The optical mode is confined as a result of the necessarily higher refractive index of the active region compared to the cladding materials [19].

The optical mode is horizontally confined by either the width of the optical gain region (gain guided) or by a inclusion of a waveguide structure of rela-

tively higher refractive index. This can be formed by a ridge waveguide (weakly index guided) or a buried heterostructure (strongly index guided). Although more difficult to fabricate, index guided lasers offer superior confinement to gain guided lasers and therefore better lasing efficiency. With these improvements, heterostructure index guided lasers offer cw rather than pulsed operation, at lower threshold currents (10s of mA rather than $\sim$ 1 A), leading to better wall-plug efficiency, easier temperature control, and increased device lifetimes. Typical dimensions of such a diode laser are 1000 by 500 by 200 µm (length, width, height), with a waveguide width of 2 µm [19].

3.1.2 Multiple quantum well diode lasers

The lasing wavelength of a diode laser structure can be fine tuned by building in multiple quantum wells. If the thickness of the active layer approaches the de Broglie wavelength ($\sim$ 28 nm in GaAs [107]) then the density of states occupied by carriers is no longer dependent on carrier energy, but becomes quantized and defined by a series of quantum wells. This further confines the charge carriers and therefore has the added benefit of reducing the threshold current [19].

3.1.3 Single mode operation

The gain spectrum of diode lasers is typically far broader than the axial cavity mode spacing of the Fabry-Perot (FP) type cavity produced by polishing the semiconductor crystal facets, Agrawal and Dutta calculated a factor of 4 for a particular InGaAsP FP-DL structure [19]. Such FP-DLs therefore emit on more than one axial mode, with mode-hops occurring with temperature induced shifts of the gain peak. Lasers of this type cannot be used for OF-CEAS, where smooth tuning over pressure broadened absorption profiles, i.e. around 0.5 cm^{-1}, is required.

One method of fabricating a single mode device is to build a distributed

feedback (DFB) grating into the laser structure. The grating structure is formed by alternating the thickness of one layer (e.g. the waveguide ridge) to produce a periodic variation of refractive index. Consequently, the forward and backward propagating beams are coupled by feedback from backward Bragg scattering and mode selection occurs according to the Bragg condition:

$$\lambda_k = \frac{2\Lambda}{k}, \tag{3.1}$$

where λ_k is the lasing wavelength selected by the grating period, Λ, and k is the order of Bragg diffraction induced by the grating. DFB-DLs do not mode hop with temperature change, but instead tune around λ_k due to temperature induced changes in the refractive index of the grating. For diode lasers, this results both from Joule heating of the grating associated with increased current flow and also changes in carrier density. The tuning extent will greatly depend on the DFB-DL structure, but is typically around 0.1 $\mathrm{cm^{-1}\,K^{-1}}$, leading to a continuous tuning range of 5 $\mathrm{cm^{-1}}$ [19]. High power DFB-DL devices (power output from several tens to hundreds of mW) are widely commercially available in the near-IR, both from specialist manufacturers like Nanoplus and also the likes of Thorlabs and Newport.

An alternative method of achieving single-mode operation is to couple an FP-DL to an external cavity formed by a diffraction grating to create an external cavity diode laser (EC-DL). EC-DL devices use a diffraction grating to partially reflect light back into the FP-DL, in a strong optical-feedback regime. The effect of the optical-feedback can be modelled as a wavelength dependence of the reflectivity of the laser facet facing the external cavity, consequently different longitudinal modes of the external cavity have different losses. Mode selection therefore occurs on the mode with the lowest loss closest to the peak of the gain profile. Such devices are wavelength tunable by altering the angle of the diffraction grating and have very broad (up to 200 $\mathrm{cm^{-1}}$) tuning ranges, although not

necessarily without mode-hops [19]. Commercial EC-DL systems are available across the near-IR, for instance from Sacher Lasertechnik who offer systems over most of the range from 370 to 1770 nm.

3.1.4 Diode laser linewidth

In addition to proposing the concept of a laser, Schawlow and Townes also proposed a formula to predict the intrinsic laser linewidth [100]. Laser emission consists of both stimulated and spontaneous emission, and the latter causes both amplitude and phase noise. This noise is manifest as a broadening of the laser linewidth, as the instantaneous laser frequency, ν, is the time derivative of the net phase. The Schawlow-Townes formula predicts a Lorentzian distribution around the lasing frequency, ν, with a FWHM $\Delta\nu_{\mathrm{ST}}$, related not only to the FWHM of a given laser mode, but also inversely proportional to the laser power, P_{las}. This model was found to accurately describe the intrinsic linewidths of lasers based on discrete transitions [55].

Later experiments performed by Fleming and Mooradian showed that diode lasers have a linewidth, $\Delta\nu_{\mathrm{DL}}$, 50 times greater than predicted by the Schawlow-Townes formula [108]. This observation was explained by Henry [109], who proposed a diode laser linewidth broadening parameter, β, that corrects the Schawlow-Townes linewidth by a factor of $(1+\beta^2)$, to account for the coupling of amplitude and phase noise. The resulting modified Schawlow-Townes equation for a diode laser operating on a single longitudinal mode is [110]:

$$\Delta\nu_{\mathrm{DL}} = \frac{v_{\mathrm{grp}}^2 h\nu \alpha_{\mathrm{cav}} \alpha_{\mathrm{mirr}} n_{\mathrm{sp}}}{4\pi P_{\mathrm{las}}} \left(1+\beta^2\right) = \Delta\nu_{\mathrm{ST}} \left(1+\beta^2\right). \tag{3.2}$$

Here v_{grp} is the group velocity, defined as the ratio of photon flux to photon density; the photon energy of the lasing transition is $h\nu$; α_{cav} and α_{mirr} are loss factors associated with the laser cavity and mirrors; and n_{sp} is the spontaneous emission factor (or population inversion parameter). β describes the relationship

between gain, G, refractive index, η, and carrier (electron and hole) density, N:

$$\beta = -2k \left. \frac{\mathrm{d}\eta}{\mathrm{d}N} \right/ \frac{\mathrm{d}G}{\mathrm{d}N} , \tag{3.3}$$

where k is the wavevector. As η and G are related to the real and imaginary parts of the laser gain medium susceptibility, changes in either of these quantities cause changes in the other, described by the Kramers-Kronig relations [53]. Diode lasers operate on interband transitions with asymmetric gain spectra, resulting in a carrier density dependence of the refractive index. Spontaneous emission therefore results not only in an instantaneous phase changes, but also in a delayed phase changes mediated by carrier density fluctuations inducing changes in the gain.Typical measured values of β for diode lasers lie in the range 2 to 8 Osiski and Buus [111].

3.2 Diode lasers and optical-feedback

3.2.1 Rate equations

Lang and Kobayashi have derived a rate equation for the evolution of the electric field, E_{las}, within a semiconductor laser resonator subject to optical-feedback, that satisfies Maxwell's equations [112]. Assuming that the semiconductor's response to the electric field is dominated by fast intraband scattering processes, and that the device oscillates on a single longitudinal mode of the laser cavity (reasonable

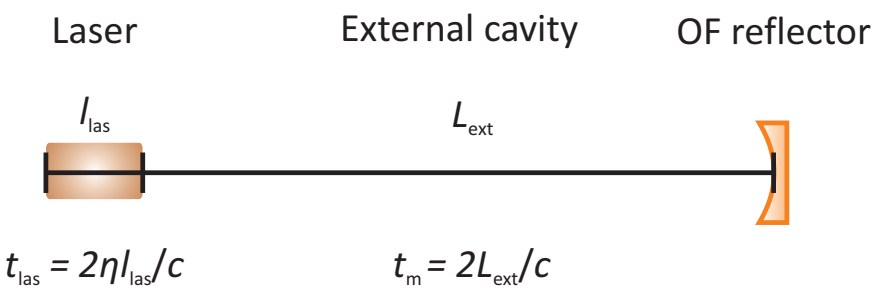

Figure 3.1: Schematic of a reflector supplying optical-feedback to a semiconductor laser, showing optical lengths and roundtrip times for each part of the system.

for a DFB device), results in

$$\frac{\mathrm{d}E_{\mathrm{las}}}{\mathrm{d}t} = \left[\mathrm{i}\frac{\eta_{\mathrm{mode}}}{\eta_{\mathrm{grp}}}(\omega - \Omega)\right] E_{\mathrm{las}}(t)\exp[\mathrm{i}\omega t + \phi(t)] + \frac{1}{2}(G - \Gamma)(1 - \mathrm{i}\beta)\exp[\mathrm{i}\omega t + \phi(t)] + \kappa E_{\mathrm{las}}(t - t_m)\exp[\mathrm{i}\omega(t - t_m) + \phi(t - t_m)], \quad (3.4)$$

where ω is the lasing frequency, Ω is the free-running laser frequency, and ϕ is the phase. The net rate of stimulated emission is the gain, G, and Γ is the photon decay rate, which is the inverse of the photon lifetime in the laser cavity. The parameter η_{mode} is the mode refractive index, and η_{grp} the group index corresponding to η_{mode}; β is the diode laser linewidth broadening parameter. Rate equations for the amplitude, A, and phase, ϕ, respectively of E_{las} may derived from the first and second terms of Equation 3.4, via $E_{\mathrm{las}} = A\exp[-\mathrm{i}\phi]$.

The third term describes the effect of optical-feedback returned to the laser medium by a reflector, as depicted in Figure 3.1. The roundtrip delay time between the output laser facet and the external optical-feedback reflector, t_m, is given by $t_m = \frac{2L_{\mathrm{ext}}}{c}$, where L_{ext} is the length of the effective external cavity. The feedback coupling rate, κ, is

$$\kappa = \frac{1}{t_{\mathrm{las}}}\left[\frac{1 - R_{\mathrm{las}}}{\sqrt{R_{\mathrm{las}}}}\right]\sqrt{f_{\mathrm{ext}}}, \quad (3.5)$$

where t_{las} is the roundtrip time in the laser cavity. This is related to the length of the laser cavity, l_{las}, by $t_{\mathrm{las}} = \dfrac{2\eta_{\mathrm{mode}}l_{\mathrm{las}}}{c}$. R_{las} is the laser cavity facet reflectivity co-efficient, and f_{ext} is the fraction of output power that returns to the laser cavity.

Systems where optical-feedback is reflected from a mirror [112], an optical fibre [113], and a high finesse optical cavity [60, 82] have all been studied. From Equation 3.4, the change in the lasing gain, ΔG, and frequency, $\Delta\omega$, due to

optical-feedback are given by

$$\Delta G = -2\kappa \cos(\omega t_m), \tag{3.6}$$

$$\Delta\omega = (1+\beta^2)^{1/2}\kappa \sin(\omega t_m + \arctan\beta), \tag{3.7}$$

from which it is apparent that in the absence of optical-feedback (i.e. $\kappa = 0$), both ΔG and $\Delta\omega$ take the values of the free running laser.

3.2.2 Sensitivity to optical-feedback

For optical-feedback to influence the semiconductor laser behaviour, the rate of returning photons, κP where P is photon number, must greatly exceed the rate of spontaneous emission, ρ_{spt}:

$$\kappa P \gg \rho_{\text{spt}}. \tag{3.8}$$

Substituting Equation 3.5 in to the above expression, and setting $\frac{(1-R_{\text{las}})}{\sqrt{R_{\text{las}}}} \approx 1$, leads to the following condition for the necessary fraction of output power, f_{ext}, that must be returned to the gain medium in order to influence the laser behaviour:

$$f_{\text{ext}} \gg \left[\frac{\rho_{\text{spt}} t_{\text{las}}}{P}\right]^2. \tag{3.9}$$

Noting that the reciprocal of t_{las} is the longitudinal mode spacing of the laser, $\Delta\nu_{\text{mode}}$, and that $\frac{\rho_{\text{spt}}}{P}$ is roughly equal to the diode laser linewidth, $\Delta\nu_{\text{DL}}$, enables recasting of Equation 3.9 as:

$$f_{\text{ext}} \gg \left[\frac{\Delta\nu_{\text{DL}}}{\Delta\nu_{\text{mode}}}\right]^2. \tag{3.10}$$

Equations 3.9 and 3.10 imply that reduced spontaneous emission rates, higher laser output powers, narrower laser linewidths, and shorter laser cavities all result in greater sensitivity to optical-feedback [19].

3.2.3 Optical-feedback regimes

Tkach and Chraplyvy [114] experimentally identified five operating regimes for single mode diode lasers subject to optical-feedback. These were later theoretically investigated by Schunk and Petermann [115], who related the laser linewidth with optical-feedback, $\Delta\nu_{\mathrm{OF}}$, to that without, $\Delta\nu_{\mathrm{DL}}$, by

$$\begin{aligned} \Delta\nu_{\mathrm{OF}} &= \frac{\Delta\nu_{\mathrm{DL}}}{[1 + C\cos(\omega t_m + \arctan\beta)]^2} \\ &= \frac{\Delta\nu_{\mathrm{ST}}\,[1+\beta^2]}{[1 + C\cos(\omega t_m + \arctan\beta)]^2}, \end{aligned} \tag{3.11}$$

where the feedback parameter, C, is defined as

$$\begin{aligned} C &= \kappa t_m (1+\beta^2)^{1/2} \\ &= \frac{L_{\mathrm{ext}}}{\eta l_{\mathrm{las}}}\left[\frac{1-R_{\mathrm{las}}}{\sqrt{R_{\mathrm{las}}}}\right]\sqrt{f_{\mathrm{ext}}}(1+\beta^2)^{1/2}. \end{aligned} \tag{3.12}$$

Each feedback regime is characterized by the number of solutions existing for Equations 3.6 and 3.7 given a particular value of C. By Equation 3.12, the operating regime therefore depends on the length of the external optical cavity L_{ext}, the extent of returned power, f_{ext}, and also the refractive index and facet reflectivity of the diode laser. As L_{ext} may be related to the roundtrip time of the optical feedback field, C is also related to the phase of the optical-feedback field.

Regime I is characterized by $C < 1$, either because f_{ext} is small ($< 10^{-8}$), or L_{ext} is short. Under these conditions a single solution of Equation 3.7 exists, and the laser linewidth is either broadened or narrowed, depending on the feedback phase (i.e. L_{ext}). Increasing f_{ext} ($\sim 10^{-8}$ to 10^{-6}) or L_{ext} eventually leads to $C > 1$, defined as Regime II. For this regime, multiple solutions exist for Equation 3.7, with the number of solutions increasing as C increases. The frequency gap between solutions is approximately given by the free spectral range of the

external cavity, and broadening of the laser linewidth is observed as the laser hops between modes corresponding to the minimum linewidth.

As f_{ext} is increased to around $\sim 10^{-6}$ to 10^{-3} and L_{ext} is on the order of ~ 1 m, Regime III is reached and the feedback phase converges to $[2\pi - \arctan\beta]$. The laser frequency ceases to mode hop, and Equation 3.11 simplifies to

$$\Delta\nu_{\text{OF}} = \frac{\Delta\nu_{\text{ST}}\,[1+\beta^2]}{[1+C]^2}, \tag{3.13}$$

indicating maximum linewidth narrowing is achieved. This is the regime in which successful diode laser OF-CEAS locking occurs. As an approximate rule of thumb, for Regimes I through III the optical-feedback is "weak" as $f_{\text{ext}} \lesssim 10^{-3}$ [19].

Regime IV is the so-called coherence-collapse regime and occurs in diode lasers subject to "strong" optical-feedback, $f_{\text{ext}} \gtrsim 10^{-3}$. In this regime, competition between the mode with the narrowest linewidth (i.e. $\omega t_m = 2\pi - \arctan\beta$ in Equation 3.11) and the mode with the minimum threshold gain ($\omega t_m = 0$ in Equation 3.6) causes frequency fluctuations and a large linewidth broadening. By inspection of Equation 3.11 and Equation 3.6, these modes are only different when the linewidth broadening parameter is non-zero.

Regime V is the extended cavity operation regime, with $f_{\text{ext}} > 10^{-1}$. In this regime the laser operates as a long cavity laser with a short active region. If the external cavity is frequency-selective (i.e. contains a diffraction grating) then the laser operates on a single longitudinal mode with linewidth narrowing for all optical-feedback phases. This is the regime in which EC-DL devices operate, and linewidth reduction is typically on the order of a factor of 10, from 100 MHz to 10 MHz [19].

3.2.4 Diode laser V-cavity OF-CEAS

Both Dahmani et al. [82] and Laurent et al. [60] showed that returning weak optical-feedback to a diode laser from a tilted confocal cavity can bring about

both frequency locking and linewidth narrowing in the late 1980s. However, optical-feedback diode laser self-locking was not combined with cavity-enhanced diode laser absorption, by placing an absorbing gas sample in the cavity used to lock the laser until 2004 by the group of Romanini and Morville [83].

3.2.5 Frequency locking

Laurent et al. used a tilted confocal cavity as an OF reflector and a schematic of their setup is drawn in Figure 3.2 (a), for this arrangement the returning feedback fraction is

$$f_{\mathrm{ext,V}} = \alpha_{\mathrm{OF}} R(1-R)^2 \left[R^4\right]^m, \tag{3.14}$$

where α_{OF} is an attenuation factor, R and T are the reflectivity and transmission of the cavity mirrors, and m is the number of cavity roundtrips. This expression corresponds to transmission of the light field through the first cavity mirror, m roundtrips around the cavity, an extra reflection to follow the path back to the laser, and transmission through the first cavity mirror.

The reason for using a tilted confocal cavity was to decouple the two possible optical-feedback fields: the intended cavity reflected field, and the undesirable field reflected from the dielectric coating of the first cavity mirror. This is also the reason why Morville et al. used a V-cavity, as the fields follow the same paths, as shown in Figure 3.2 (b). By this simple geometric argument, Equation 3.14 is therefore also applicable to the case of a V-cavity, as the field follows the same path. Hence the feedback coupling rate for a V-cavity may be defined as:

$$\kappa_{m,\mathrm{V}} = \frac{1}{t_{\mathrm{las}}} \left[\frac{1-R_{\mathrm{las}}}{\sqrt{R_{\mathrm{las}}}}\right] \left[\alpha_{\mathrm{OF}} R(1-R)^2 R^{4m}\right]^{1/2}, \tag{3.15}$$

as originally derived by Laurent et al. for a tilted confocal cavity. Taking the time independent solution for Equation 3.4, after separating the real and imaginary parts an expression for the change in the lasing gain, ΔG, and frequency, $\Delta\omega$,

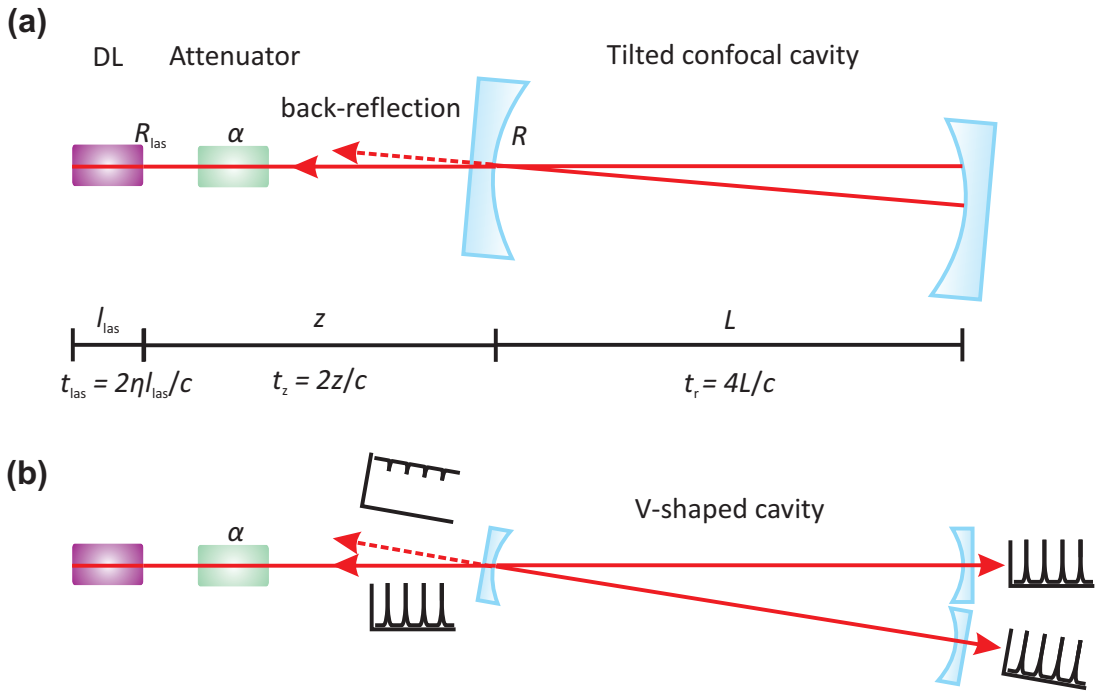

Figure 3.2: (a) Schematic of the confocal high finesse cavity OF reflector and (b) the equivalent V-cavity arrangement. DL is the diode laser; $R_{\rm las}$ is the laser facet reflectivity; R is the cavity mirror reflectivity; and $l_{\rm las}$, z and L are the optical distances in the laser resonator, between the laser output facet and the cavity mirror, and along the cavity arm lengths. The small insets are sketches of the transmission function at each of the four possible ports. After [59, 60].

due to optical-feedback are obtained in terms of Ω, $\kappa_{\rm m}$ and β:

$$\Delta G = -2\sum_{m=0}^{\infty} \kappa_{\rm m} \cos(\omega t_m), \tag{3.16}$$

$$\Delta\omega = (1+\beta^2)^{1/2} \sum_{m=0}^{\infty} \kappa_{\rm m} \sin(\omega t_m + \arctan\beta) = \Omega - \omega, \tag{3.17}$$

which are the analogues of Equation 3.6 and Equation 3.7 summed over the number of cavity roundtrips.

From inspection of Figure 3.2, the total optical-feedback delay time is

$$t_m = t_z + (m + \tfrac{1}{2})t_{\rm r}, \tag{3.18}$$

where t_z is the laser to cavity roundtrip time, and $t_{\rm r}$ is the cavity roundtrip time. Substituting Equation 3.18, together with Equation 3.15, into Equation 3.17 leads

to an expression for the cavity-coupled laser frequency, ω:

$$\omega = \Omega - K_{\mathrm{V}} \left[\frac{\sin[\omega\left(t_z + \frac{t_{\mathrm{r}}}{2}\right) + \arctan\beta] - R^2 \sin[\omega\left(t_z - \frac{t_{\mathrm{r}}}{2}\right) + \arctan\beta]}{1 + \frac{4R^2}{(1-R^2)^2}\sin^2[\frac{\omega t_{\mathrm{r}}}{2}]} \right], \quad (3.19)$$

where K_{V} is

$$K_{\mathrm{V}} = (1+\beta^2)^{1/2}\sqrt{\alpha_{\mathrm{OF}}}\frac{c}{2\eta l_{\mathrm{las}}}\left(\frac{1}{2}\right)\frac{\mathcal{F}_{\mathrm{V}}}{\mathcal{F}_{\mathrm{las}}}. \quad (3.20)$$

Here $\mathcal{F}_{\mathrm{V}}$ is the V-cavity finesse, and $\mathcal{F}_{\mathrm{las}}$ the finesse of the diode laser resonator. Expressed in terms of optical distances instead of roundtrip times, Equation 3.19 is

$$\omega = \Omega - K_{\mathrm{V}} \left[\frac{\sin[\frac{2\omega}{c}(z+L) + \arctan\beta] - R^2 \sin[\frac{2\omega}{c}(z-L) + \arctan\beta]}{1 + \frac{4R^2}{(1-R^2)^2}\sin^2[\frac{2\omega L}{c}]} \right]. \quad (3.21)$$

Figure 3.3 is a schematic representation of Equation 3.21, illustrating the static frequency behaviour of the cavity coupled laser frequency as it coincides with three resonances (ω_q and $\omega_{q\pm1}$) of the high finesse cavity. Without optical-feedback (gray line), ω tunes continuously, and is equal to the free-running laser frequency, Ω. With optical-feedback (black line), around the cavity resonances ω locks to ω_q (horizontal regions), within a bandwidth defined by that of the cavity resonances. The ω predicted by Equation 3.21 shows hysteresis during up- and downward tuning. This is not observed experimentally, and the purple (upwards frequency tuning) and green arrows (downwards frequency tuning) indicate the frequency jumps avoiding the regions of negative slope. For OF-CEAS, Figure 3.3 also shows that the locking range (orange line) must be less than one FSR of the cavity for the laser to sequentially lock to every mode. This locking range is proportional to the attenuation of the optical feedback, $\sqrt{\alpha_{\mathrm{OF}}}$.

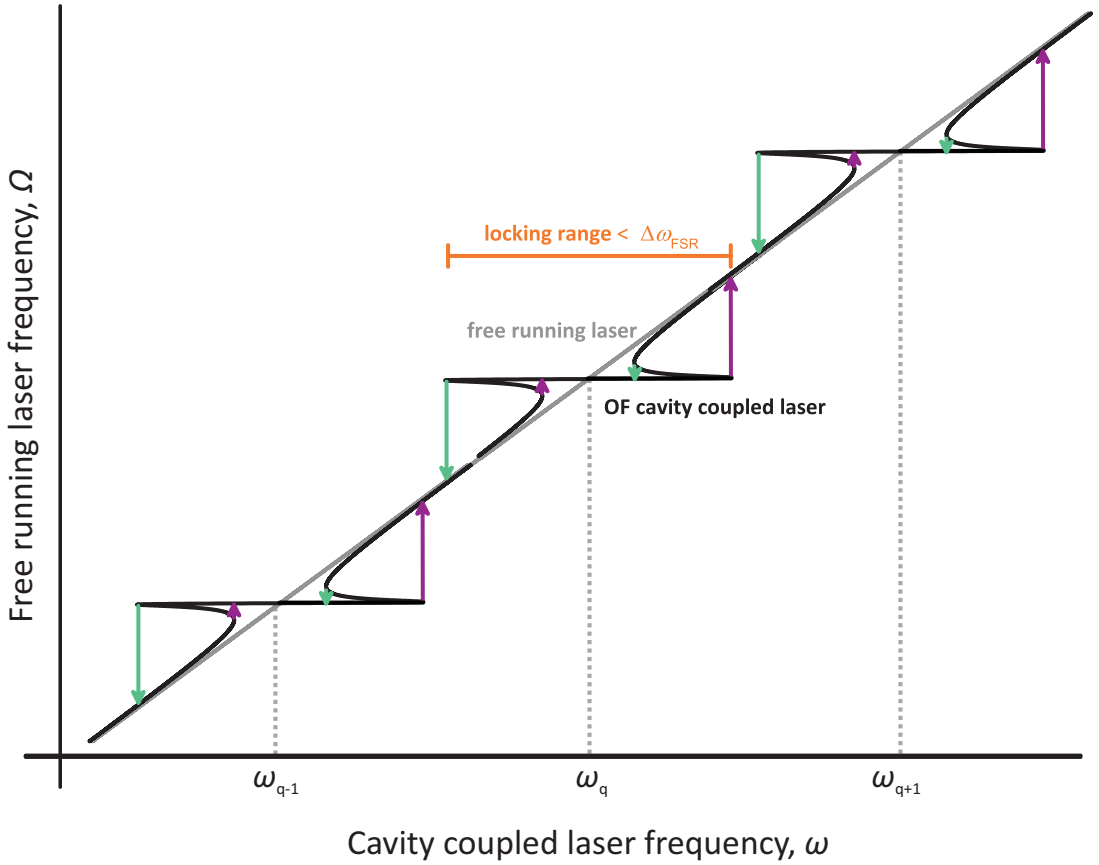

Figure 3.3: Static frequency behaviour of the cavity coupled laser frequency (ω, black) as it coincides with three cavity resonances, $\omega_{q\pm1}$, compared to that of the free running laser (Ω, gray). Purple (upward tuning) and green (downward tuning) arrows indicate frequency jumps avoiding regions of negative slope. The orange line denotes the locking range for OF-CEAS.

3.2.6 Phase matching

Optical feedback returns to injection seed the laser only when the cavity coupled laser frequency, ω, is in resonance with the frequency of a longitudinal cavity mode, ω_q; this is apparent from the transfer function of the V-cavity, Section 2.2. Consequently frequency locking of the free running laser frequency, Ω, only occurs at successive cavity modes: i.e. $\Omega = \omega = \omega_q$. The phase, ϕ_q, of the optical-feedback field reflected from the cavity must match that of the emitted field at the laser facet This must be true for all longitudinal modes, each of which has a different number of field oscillations along z, and can be achieved by controlling z. The phase, ϕ_q, is related to the cavity mode frequency, ω_q, and roundtrip delay

time, t_m by

$$\phi_q = \omega_q t_m, \tag{3.22}$$

which can alternatively be given in terms of the distances traversed by the optical-feedback field:

$$\phi_q = \frac{2\omega_q}{c}\left[z + (2m + L)\right]. \tag{3.23}$$

The phase difference between successive modes, $\phi_{q+1} - \phi_q$, must be an integer multiple, k, of 2π, for constructive interference:

$$\phi_{q+1} - \phi_q = \frac{2\left(\omega_{q+1} - \omega_q\right)}{c}\left[z + (2m + L)\right] = 2\pi k. \tag{3.24}$$

In this expression, $\omega_{q+1} - \omega_q$ is simply the cavity free spectral range ($\frac{2\pi c}{4L}$, cf. Equation 2.16). With some working, Equation 3.24 can be rearranged to:

$$z = L\left[2(k - m) - 1\right], \tag{3.25}$$

implying that z must be set to an odd integer multiple of L in order to have phase matching for all longitudinal modes at the laser facet.

3.2.7 Linewidth narrowing

The OF-CEAS locking scheme also causes laser linewidth narrowing. The phase matching criterion (Equation 3.25) corresponds to maximum linewidth narrowing given by Equation 3.11. Laurent et al. showed that this becomes:

$$\Delta\nu_{\mathrm{OF,V}} = \frac{\Delta\nu_{\mathrm{ST}}\left[1 + \beta^2\right]}{\left[1 + \sqrt{\alpha_{\mathrm{OF}}}\dfrac{L_{\mathrm{ext}}}{\eta l_{\mathrm{las}}}\dfrac{\mathcal{F}_{\mathrm{V}}}{\mathcal{F}_{\mathrm{las}}}(1 + \beta^2)^{1/2}\right]^2}, \tag{3.26}$$

and as the second term in the denominator is $\gg 1$ this is further reduces to:

$$\Delta\nu_{\mathrm{OF,V}} \approx \frac{\Delta\nu_{\mathrm{ST}}}{\alpha_{\mathrm{OF}}\left[\frac{L_{\mathrm{ext}}}{\eta l_{\mathrm{las}}}\frac{\mathcal{F}_{\mathrm{V}}}{\mathcal{F}_{\mathrm{las}}}\right]^2}, \tag{3.27}$$

implying the effect of optical-feedback is to remove the dependence of the diode laser linewidth on β [60]. For the typical values for the diode laser in this thesis (given in Table 3.1), this suggests a linewidth reduction factor of 4×10^5.

3.2.8 Absorption coefficient from the cavity output signal

In direct absorption spectroscopy, the Beer Lambert law (Equation 1.14) relates the transmitted intensity if there were no sample, I_0, and the absorption attenuated intensity I, to the frequency dependent absorption coefficient, $\alpha(\nu)$. For cavity-enhanced absorption spectroscopy, the following relation is derived [116]:

$$\frac{I_0}{I} = \frac{1-(R\exp[-\alpha(\nu)L])^2}{(1-R^2)\exp[-\alpha(\nu)L]}, \tag{3.28}$$

where R is the mirror reflectivity and L the arm length of the optical cavity. (Note that a V-cavity has a total length of $2L$.) An approximation in the limit of small absorption ($\alpha(\nu) \to 0$) and high mirror reflectivity ($R \to 1$) results in a version of the Beer-Lambert law, with an effective pathlength $L_{\mathrm{eff}} = L/(1-R)$:

$$\frac{I_0}{I} = 1 + \frac{\alpha(\nu)L}{1-R}. \tag{3.29}$$

For OF-CEAS, the frequency locked diode laser is monochromatic with respect to the cavity resonances and the appropriate relationship between I_0 and I is instead derived by taking the ratio of the cavity transfer functions without (Equation 2.42) and with (Equation 2.45) an absorber present (Section 2.2). For the

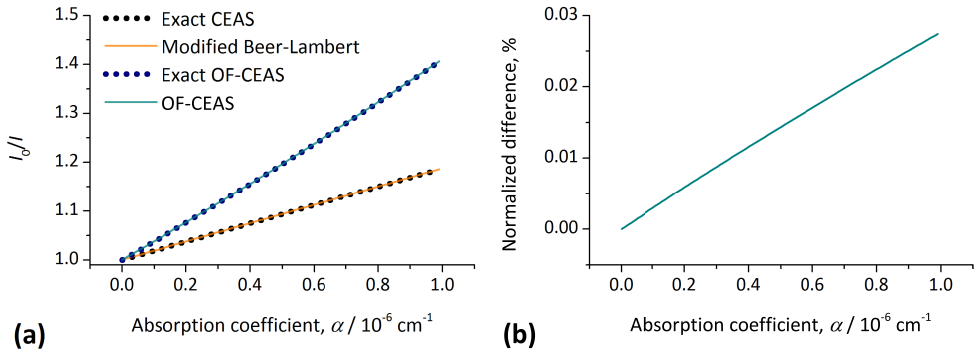

Figure 3.4: Panel (a) compares Equation 3.28 (black dots), Equation 3.29 (orange line), Equation 3.30 (blue dots), Equation 3.31 (turquoise line); (b) shows that for the work in this chapter, values of the absorption coefficient are sufficiently small that the approximations made to derive Equation 3.31 are valid.

V-shaped cavity, this leads to

$$\frac{I_0}{I} = \frac{(1 - R^2 \exp[-2\alpha(\nu)L])}{(1 - R^2)\exp[\frac{-\alpha(\nu)L}{2}]}, \tag{3.30}$$

which in the limit of small absorption and high mirror reflectivity simplifies to

$$\frac{I_0}{I} = \left[\frac{\alpha(\nu)L}{(1 - R)} + 1\right]^2. \tag{3.31}$$

Equation 3.31 has been derived by Motto-Ros et al. [117] and Hamilton et al. [87]. The equivalent expression for a linear cavity built with equivalent mirrors and the same cavity arm length is the same, and is derived in Section 5.1.2 and Appendix A.

Figure 3.4 (a) shows Equations 3.28, 3.29, 3.30 and 3.31 simulated for values of $\alpha(\nu)$ ($\sim 10^{-6}$ cm^{-1}), R (0.9995) and L (150 cm^{-1}) matching the experimental values in this chapter. The validity of the approximations in the derivation of Equation 3.31 was determined by calculating the %-difference between the exact and approximate values and normalizing. The approximations are in excellent agreement with the exact expressions. Plotted in Figure 3.4 (b) there is a difference of less than 0.03%, given the absorption cross sections expected in this

chapter. The relation used for OF-CEAS shows a further advantage over CEAS, as the dynamic range is much wider than that of CEAS.

3.3 Experimental

3.3.1 Diode laser

The diode laser was a strained layer quantum well distributed feedback diode laser (SLQW-DFB-DL) [LD6204, Marconi-Caswell]. The manufacturer measured the wavelength to be 6525 cm^{-1} (1532 nm) and the linewidth to be 1.36 MHz at 25 °C. The laser was housed in a commercial mount [Thorlabs, TCLDM9] with an integrated thermoelectric (TE) cooling element for temperature controlled operation. Custom temperature and current controllers [PTCL Electronics] were used, the current controller was based on a low-noise design by Libbrecht and Hall [118]. Typically, the laser was operated at around room temperature (20 °C) with an injection current of $\sim$ 200 mA, leading to an output power of $\sim$ 30 mW, commensurate with the manufacturer's specification. The laser frequency was scanned over transitions of interest by applying a symmetrical linear current ramp using a function generator [TTi, TG1010A], and was calibrated using a wavemeter [Burleigh, WA-1000].

3.3.2 Optics and V-cavity

The V-cavity OF-CEAS setup is shown schematically in Figure 3.5. The diode laser beam was focused by a series of three lenses [Thorlabs, AR coated $R < 0.25\%$] and steered into the optical cavity by two turning mirrors. The second of these turning mirrors defined the injection angle into the optical cavity and was mounted on a gimbal mount to decouple adjustment of horizontal and vertical tilt, for effective adjustment. The V-shaped optical cavity was symmetrical, with equal injection and replication arms of 75 cm and total length of 150 cm, leading to a

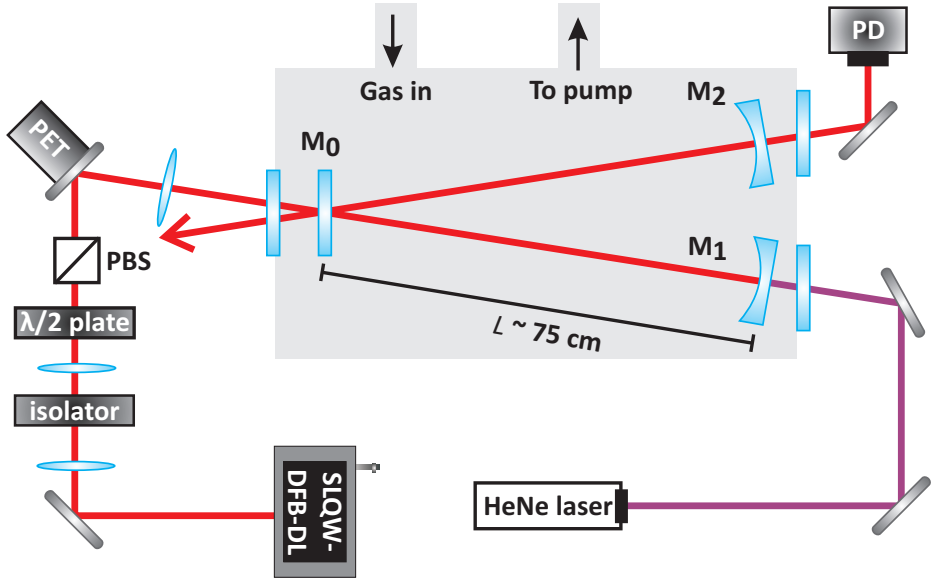

Figure 3.5: Schematic of the diode laser V-cavity OF-CEAS setup. SLQW-DFB-DL is the diode laser, $\lambda/2$ is a half-wave plate, PBS is a polarizing beam splitter, PET is a piezoelectric transducer and PD is the photodiode detector. The windows of the cell are unlabelled and the mirrors are labelled M.

$\Delta\nu_{\mathrm{FSR}}$ of 0.003 cm^{-1} (100 MHz, Equation 2.16). The angle between the cavity arms was (2°), to maintain the high reflectivity of the folding mirror despite non-normal incidence of the laser beam. The mirror set comprised a plane folding mirror (M_0) with lower reflectivity [Newport, 10CM00SR.70T, $R > 0.9995$]. The mirrors at the end of the injection (M_1) and replication arms (M_2) were of higher reflectivity [Newport, 10CM00SR.70F, $R > 0.9997$], and had a 1 m radius of curvature. This arrangement is equivalent to a folded spherical mirror resonator, and met the stability criterion defined by Equation 2.5.

Alignment of the invisible near-IR beam to the optical cavity was enabled by overlapping a counter-propagating red HeNe laser beam, injected into the replication arm of the optical cavity. The cavity mirrors were held in high-precision mounts [Newport, Ultima100-A] with locking screws added to the adjusters, which were secured once the alignment was finalized. The spatial output of the beam transmitted by the cavity was observed using a near-IR camera [Electronviewer Micronviewer 7290A] and the alignment adjusted for dominant excitation of TEM_{00}. Light leaking out of the cavity was focused on to a InGaAs

photodiode [Thorlabs, DET410], set up so that the response time was around a hundredth of the cavity ringdown time.

3.3.3 Effect of V-cavity geometry on odd and even longitudinal modes

The odd and even longitudinal modes of the symmetrical V-cavity have, respectively, an antinode and a node at the surface of the folding mirror. The scattering and absorption losses in the dielectric stack of the folding mirror are dependent on the electric field amplitude, and consequently, there is a mode-by-mode alternation effect in the cavity output signal of a V-shaped cavity, such that the folding mirror has reduced reflectivity for the odd set of modes [59]. Within a highly reflective dielectric stack, the amplitude of the electric field decays exponentially, so consideration of the top layer is most important for scattering losses. For practical cavity mirrors, scattering is caused by surface roughness and adsorbed dirt, and as such, a dirtier folding mirror results in a larger alternation effect between the transmitted power for odd and even modes [119].

There is a further more subtle effect. If the cavity arm lengths are not equal, there is an additional sinusoidal baseline modulation imposed on each set of modes. This is because the position of the antinodes and nodes of the odd and even fields shift relative to the true centre of the cavity as a function of optical frequency. The period of oscillation is related to the displacement of the folding mirror with respect to the true cavity centre, and the oscillations for odd and even modes are in quadrature [59].

3.3.4 Optical-feedback control

Both the phase and power of the optical-feedback returned to the SLQW-DFB-DL were controlled. Feedback attenuation optics were necessary to reduce the locking range of the laser, including a Faraday optical isolator [OFR, IO-D-1550]

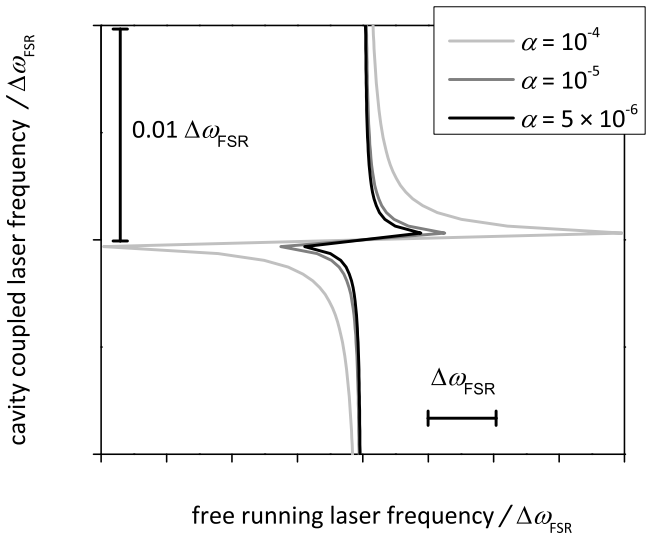

Figure 3.6: Simulations of the SLQW-DFB-DL locking frequency based on parameters in Table 3.1

providing approximately -40 dB isolation and with $> 96\%$ forward transmission. (The OF-CEAS instrument of Morville [58], also used a multiple quantum well DFB-DL and required an isolator.) Additionally a variable attenuator, comprising a half-wave plate [Thorlabs, AHWPO5M-1600, AR coated $R < 0.5\%$] and a polarizing beam splitter [Newport, 05FC16PB.9, AR coated $R < 1\%$] was used. To illustrate the need for optical-feedback attenuation, the frequency locking range of the laser was simulated for several different attenuation values, using Equation 3.21 and the parameters listed in Table 3.1.

The results are shown in Figure 3.6. With only the optical isolator, α_{OF} is around 10^{-4}, and with the addition of the half-wave plate on maximum attenuation, α_{OF} is roughly 10^{-5}. Noting that the locking range is proportional to

Parameter	Value	Source
β, laser linewidth broadening parameter	3	[111]
η, refractive index of laser gain medium	3.5	[120]
l_{las}, length of laser	1000 µm	[19]
$\mathcal{F}_{\mathrm{las}}$, finesse of laser cavity	3	[19]
$\mathcal{F}_{\mathrm{V}}$, finesse of V-cavity	4000	from measured τ_0
$\Delta\nu_{\mathrm{FSR}}$, free spectral range of V-cavity	100 MHz	from measured L

Table 3.1: Parameters used to estimate the SLQW-DFB-DL locking range.

$\sqrt{\alpha_{\mathrm{OF}}}$, both of these cases show a locking range greater than one $\Delta\nu_{\mathrm{FSR}}$ of the cavity. A reduced α_{OF} on the order of 5×10^{-6} brings the locking range to within the required range of $< \Delta\nu_{\mathrm{FSR}}$. The additional attenuation is likely to arise from imperfect spatial matching of the optical-feedback beam back into the laser facet.

The phase of the optical-feedback was manually adjustable. First, for coarse adjustment the laser was mounted on a translation stage. For fine adjustment, the turning mirror immediately before the cavity was mounted on a PET, which could be altered manually. For the V-cavity OF-CEAS system, there was no active phase adjustment, and all data was acquired as single scans.

3.3.5 The gas cell

The cavity was enclosed in a cell to enable studies of gas mixtures. This comprised an aluminium box, with internal dimensions of 110 by 230 by 940 mm and a consequent (large) sample volume of ~ 24 L. The internal base of the box had an optical board, to which the cavity mirror mounts were attached. The cell had three windows [CVI, IF-2025-C], corresponding to the positions of the three cavity mirrors in order to let light in and out of the cell. These were an anti-reflection coated ($R < 0.5\%$) and wedged (0.5°) to prevent the formations of etalons in the fused silica substrate. The gas cell had standard KF inlets and outlets for connections to gas lines, and was evacuated by a rotary pump. Pressure was monitored using both a 10 Torr and an atmospheric pressure meter [Ceravac, CTR 90].

3.3.6 Data acquisition

The cavity output signal was acquired by a digitizer card [Gage, Compuscope 1450] controlled by a custom LabVIEW program, written by Graham Richmond. To make full use of the dynamic range of the digitizer card, the cavity output signal was amplified and a DC offset applied. With the 14-bit vertical resolution

of the card this resulted in a volt-resolution of 0.6 mV. A horizontal resolution of 200 kSamples s^{-1} was found to adequately sample the profiles of the peaks in the cavity output signal.

3.4 Results

3.4.1 Optical-feedback locking

Successful optical-feedback locking of the SLQW-DFB-DL frequency, brought about by an appropriate optical-feedback power and phase is shown in Figure 3.7. A linear current ramp of 6 mA was applied to the laser with a frequency of 6.7 Hz, whilst the cavity output signal (a) was recorded. The SLQW-DFB-DL is seen to lock to around 40 cavity modes over the course of the scan, leading to power

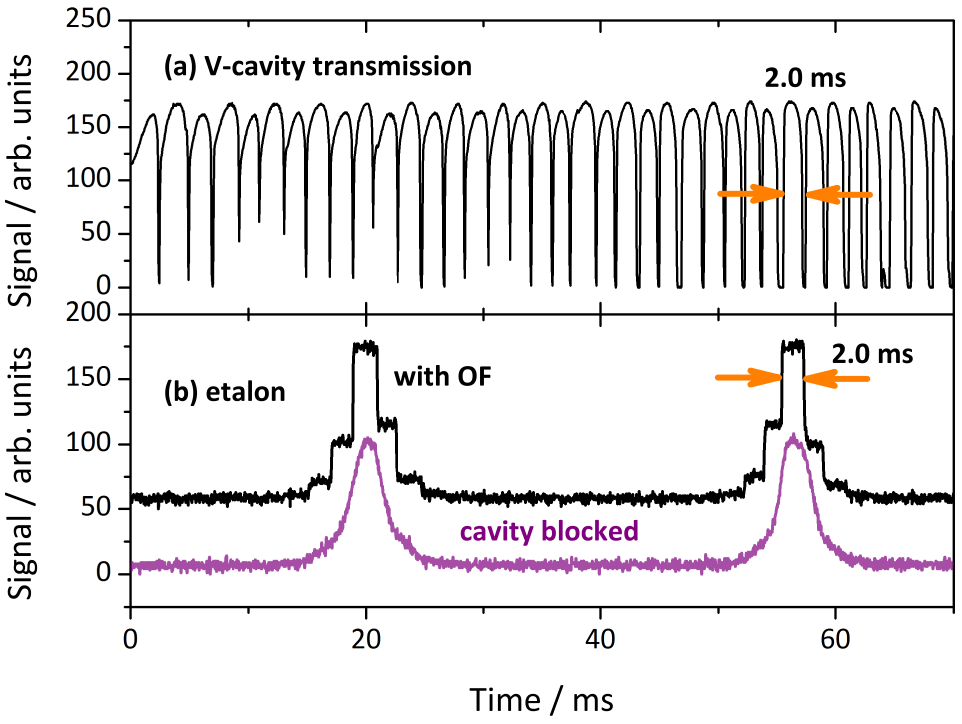

Figure 3.7: V-cavity laser locking illustration, showing simultaneous transmission of (a) the high finesse V-cavity, and (b) the low finesse etalon aligned in the split beam path, both without (purple) and with (black) OF from the cavity. Traces in (b) are offset for clarity.

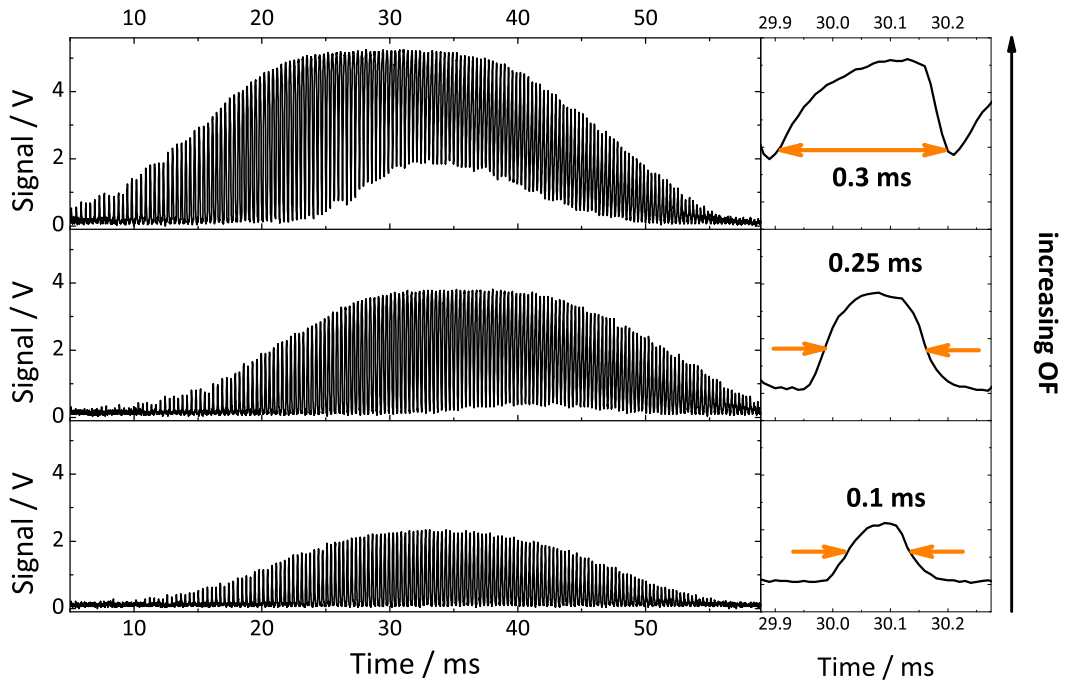

Figure 3.8: Illustration of the effect of increasing the laser and optical-feedback power on the cavity output signal and frequency locking range of the laser.

modulation of the detected signal. The alternation effect between odd and even modes, discussed in Section 3.3.3, is clearly visible. The 2.0 ms locking time, estimated using the mode FWHM, is much longer than the several µs of the nominal cavity ringdown time, τ_0 .

At the same time, the transmission through a low finesse etalon [Melles Griot, 2 GHz FSR], aligned in the additional beam path created by the polarizing beam splitter, was recorded on a second detector. This is shown as the black trace in Figure 3.7 (b), and the etalon fringes display steps exactly corresponding to the 2.0 ms frequency locking time of the laser. For comparison the trace in purple was recorded under the same conditions with a beam block between the laser and the cavity; here the etalon fringes are smooth as the laser frequency tunes continuously.

Applying a much wider (30 mA) scan, the effect of the variable OF attenuator was investigated, and the results are presented in Figure 3.8. From bottom to

top, the half-wave plate was rotated so that the power incident on the cavity increased and the attenuation of optical-feedback decreased. Not only did the cavity output signal increase, but so did the FWHM of the modes (from 0.1 ms to 0.3 ms), expected given the dependence of the locking range on $\sqrt{\alpha_{\mathrm{OF}}}$.

3.4.2 Spectroscopy of CO_2

The V-cavity OF-CEAS spectrometer was used to determine the self-broadened half-width at half-maximum (HWHM), γ_{self}, for the $Q(46)e$ transition in the $(11^12) \leftarrow (00^00)$ combination band of CO_2. This transition, which is centered at 6528.137 cm^{-1}, and has an S_{if} of 6.049×10^{-27} $\mathrm{cm}^{-1}/(\mathrm{molec\ cm}^{-2})$ and a Doppler width of 0.0121 cm^{-1} at the experimental temperature of 296.15 K. This transition is relatively distant from other from other CO_2 transitions, so it could reasonably be fitted as a single absorption line using a simple routine, and very weakly absorbing so $\alpha(\nu)$ was small and Equation 3.31 valid. Pure carbon dioxide [BOC, > 99.995%] was let into the cell in 10 Torr increments from 50 to 120 Torr and the cavity output signal recorded.

The SLQW-DFB-DLwas scanned over the transition by applying a linear current ramp of 5.3 mA with a frequency of 5.62 Hz. An example of the cavity output signal exhibiting absorption by 110 Torr of CO_2, is shown in Figure 3.9. This gave a scan width covering 44 modes, equivalent to ~ 0.2 cm^{-1}. The FWHM

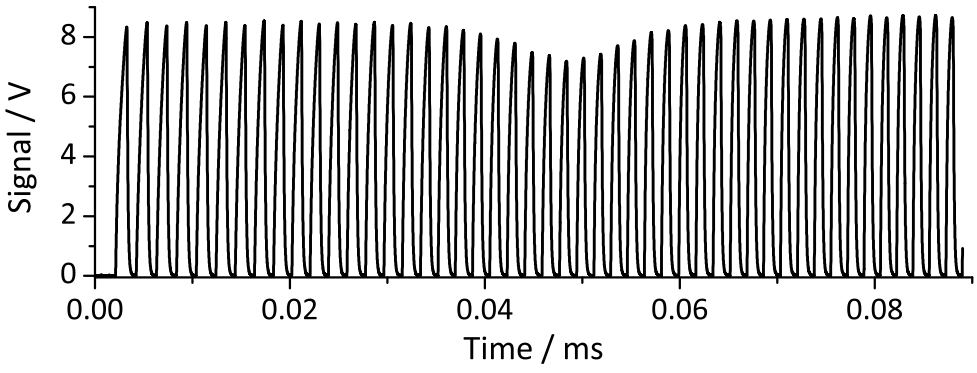

Figure 3.9: Example V-cavity OF-CEAS cavity output signal exhibiting absorption by CO_2.

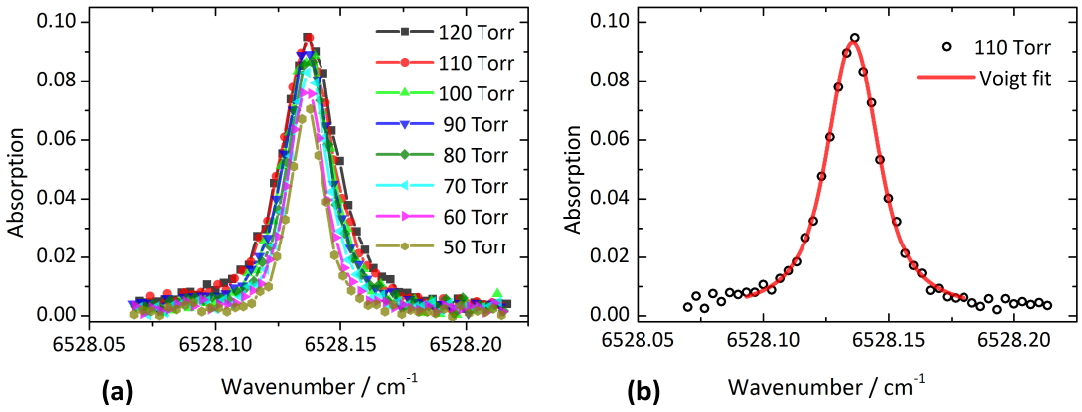

Figure 3.10: (a) OF-CEAS absorption spectra for the self-broadened pressure series of the $Q(46)e$ transition in the $(11^12) \leftarrow (00^00)$ band of CO_2 and (b) example Voigt profile fit to an absorption spectrum of 110 Torr of CO_2.

of each mode is about 0.7 ms, around 100 times longer than the nominal cavity ringdown time expected for this mirror set. The alternation effect of odd and even modes is small (> 70 mV, less than 1% of the transmitted intensity).

Frequency-calibrated absorption spectra were obtained from the cavity output signal. The transmission maxima, $I(\nu)$, were identified using a MATLAB routine and their positions mapped on to a relative frequency scale defined by the FSR of the cavity (~ 0.003 cm^{-1}). The frequency scale was made absolute by assigning transitions using the HITRAN database [9]. Data for odd and even modes were separated and a linear baseline, I_0, fitted to each separately by excluding the absorption feature. The resulting absorption profiles for the self-broadened pressure series are shown in Figure 3.10 (a).

Voigt profiles (Equation 1.11) were fitted to the resulting absorption spectra using the OriginPro built in fitting function. The Doppler FWHM was fixed and all other fitting parameters (the vertical offset, the horizontal frequency shift, the area underneath the curve and the Lorentz FWHM) were allowed to float. In order to determine γ_{self} the retrieved Lorentz FWHM were collated and plotted as a function of pressure. The resulting distribution is plotted in Figure 3.11, where the error bars correspond to the fitting error on the Lorentz

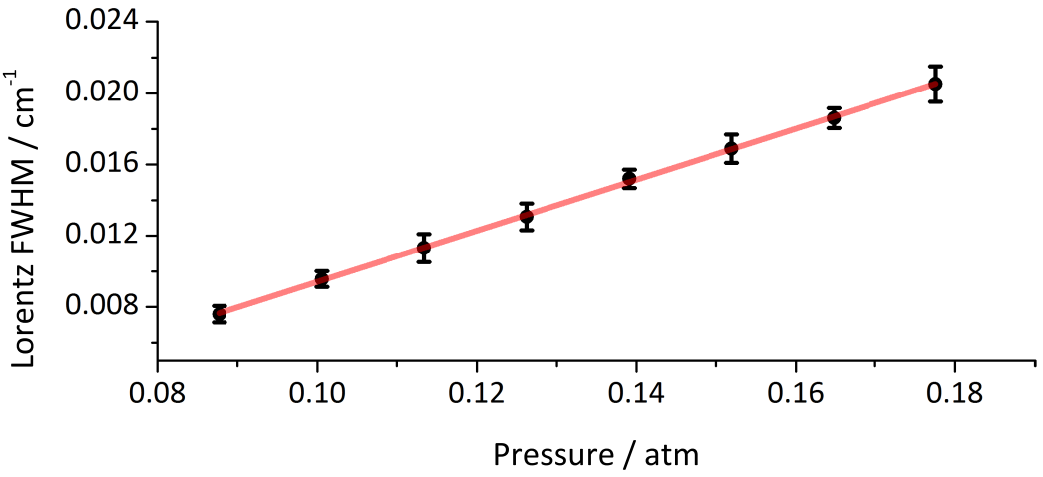

Figure 3.11: Lorentzian FWHM versus pressure to calculate the pressure broadening coefficient for the $Q(46)e$ transition in the $(11^12) \leftarrow (00^00)$ band of CO_2

FWHM. A line was fitted to this distribution, with the least-squares fit directly weighted by the error. The slope was halved to obtain a HWHM and gave γ_{self} as 0.072 ± 0.002 cm^{-1} atm^{-1}. This is within 4% of the theoretical HITRAN listed value (0.075 cm^{-1}), which is generally found to be within 1% of experimentally determined values [121].

At the same time, the sensitivity of the V-cavity OF-CEAS instrument was investigated. The cavity output signal was instead recorded for laser scans free from absorption features and the noise equivalent absorption coefficient (α_{min}) calculated from these traces, which represent the baseline above which absorption features must be measured. The analysis of the cavity output signal followed that described in the previous section, and the identified transmission maxima for the separated odd (blue) and even (red) modes are plotted against a relative frequency scale in Figure 3.12, which also displays the fitted linear baselines. The noise on the traces is dominated by a sinusoidal baseline variation and intensity fluctuations. As the sinusoidal baseline variation is in quadrature for the odd and even sets, it is most likely attributable to inequality of the cavity arm lengths, i.e. the spectral ripple described in Section 3.3.3. The intensity fluctuations are likely to arise from phase fluctuations of the optical feedback field that lead to

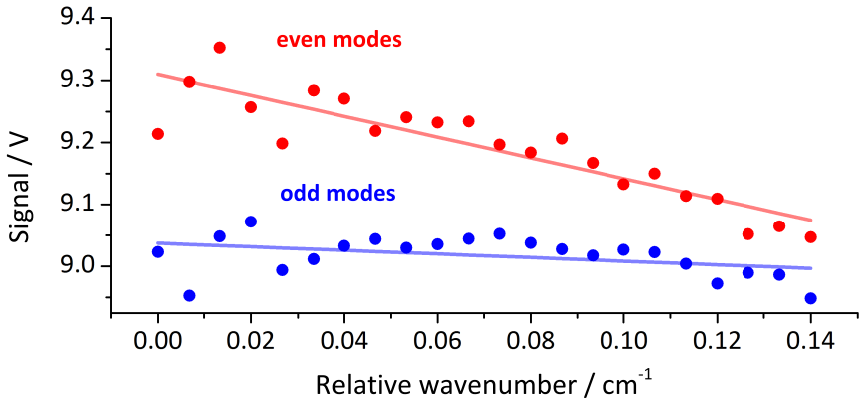

Figure 3.12: Identified and separated peak maxima of the cavity output signal in the absence of absorption features, to estimate α_{min}. The set of odd modes is blue, while the even modes are red.

non-optimal injection seeding of the laser. This disturbs the linewidth narrowing and frequency locking and, the resulting frequency fluctuations of the laser lead to cavity transmission amplitude fluctuations.

Equation 3.31 was used to transform the cavity output signal into an absorption coefficient in order to calculate the α_{min}. The identified peak maxima were $I(\nu)$, while the linear baseline was I_0. The cavity length, L, was known and the mirror reflectivity, R, was calibrated by measuring the cavity ringdown time. The cavity ringdown time for a linear cavity was derived in Section 2.3.2. Although not immediately obvious, the V-shaped cavity in Figure 2.5 has the same cavity ringdown time, τ_0, as the linear cavity shown in the same figure. The cavities have identical mirrors and cavity arm lengths, and so although two additional reflections are required to complete a roundtrip in a V-cavity, the time taken to complete a roundtrip is also doubled, as $t_{\text{r}} = \dfrac{c}{4L}$, and these two effects cancel each other out [58]. The τ_0 was measured following the approach of [83], the laser current was rapidly modulated (798.5 kHz) by a square wave, switching it above and below threshold. Several successive ringdown events recorded on the falling edge of the ramp, leading to τ_0 of 6.0 ± 0.3 µs and a mirror reflectivity of 0.99958 ± 0.00002. Taking one standard deviation of the noise equivalent absorption coefficients across the laser scan results in a α_{min} of 9×10^{-9} cm^{-1} in 1 s for

the set of even modes (red) and 8×10^{-9} cm^{-1} in 1 s for the set of odd modes (blue).

3.4.3 Acetylene detection

To illustrate its trace gas sensing capability, the V-cavity OF-CEAS spectrometer was used to detect acetylene (C_2H_2) in a gas sample collected from a car exhaust. Acetylene is a volatile organic compound (VOC) and pollutant and its presence in the troposphere is due almost entirely to human activity, primarily burning of fossil fuels and biomasses [122]. Coupled with its relatively long local atmospheric lifetime of 5 weeks [123], this suggests that acetylene could be used as a tracer of polluted air masses. Acetylene mixing ratios are measured hourly using gas chromatography mass spectrometry (GCMS) as part of the UK automatic hydrocarbon monitoring network [124]. The GCMS instruments measure 27 different hydrocarbons and have a detection limit of 70 ppt for acetylene, with preconcentration [125]. The mean mixing ratio in central London is 9 pbb, with occasional pollution events leading to concentrations of up to 90 ppb. The average concentration in rural Oxfordshire is much lower, at around 2 ppb [124]. Aside from environmental and atmospheric studies, sensitive, rapid and specific detection of acetylene is relevant to the petrochemical industry, where acetylene is an impurity in flows of ethene gas [126].

For this experiment, car exhaust fumes were sampled using an evacuated glass bulb with a volume of ~ 1 L by placing its inlet into the exhaust pipe of the car and opening the inlet tap. The engine of the petrol car was run under conditions similar to those used during the hydrocarbon emissions test in a UK Ministry of Transport (MOT) test, stationary and with engine revs [127]. An aerosol filter [Swagelok, SS-4FWS-05] was fitted to the sampling bulb to block particulates that may otherwise have caused additional intracavity losses by scattering the beam.

For these OF-CEAS measurements, a different set of mirrors with a higher finesse was used. The mirror set consisted of one of the previously used high reflectivity Newport mirrors and two others [Layertec, 106940, $R > 0.9999$], again with a 1 m radius of curvature. This cavity also met the stability criterion (Equation 2.4). In order to retrieve the concentration from the recorded absorption spectrum, the mirror reflectivity was calibrated by a ringdown measurement, recorded immediately after the cavity transmission signal. The resulting τ_0 was 12.0 µs, leading to an increased average mirror reflectivity of 0.99998, commensurate with the specification. Unfortunately, the optical surfaces of these mirrors were dirty due to extensive previous use, and this resulted in a large alternation effect, of around 200 mV or 10% of the signal. Additionally, the alignment of the cavity was much harder to maintain when letting gases in and out of the gas cell, even with the mirror mounts locked.

The $P(11)e$ acetylene transition in the (10100) $\leftarrow$ (00000) combination band, which occurs at 6529.179 cm^{-1}, was chosen for monitoring purposes as the most intense acetylene transition within the operating range of the laser: at the experimental temperature of 294.15 K, S_{if} was 1.171×10^{-20} cm^{-1}/(molec cm^{-2}). To record a spectrum, 50 Torr of car exhaust sample were let into the OF-CEAS cell, and the laser was scanned over the transition. The cavity output signal for a single scan was analysed and fitted with a Voigt profile, as described in Section 3.4.2, with the vertical absorption scale transformed into an absorption coefficient using Equation 3.31, the resulting spectrum is presented in Figure 3.13. Using the area underneath the fitted profile, the returned mixing ratio of acetylene was 661 ± 9 ppb, where the error accounts for the uncertainty in the temperature, ringdown calibration and the pressure. A previous study of sources of atmospheric acetylene found an average mixing ratio of 100 ppb from vehicle exhausts, suggesting that the concentration retrieved here is at least of the correct order of magnitude [122]. From the standard deviation of the residuals to the

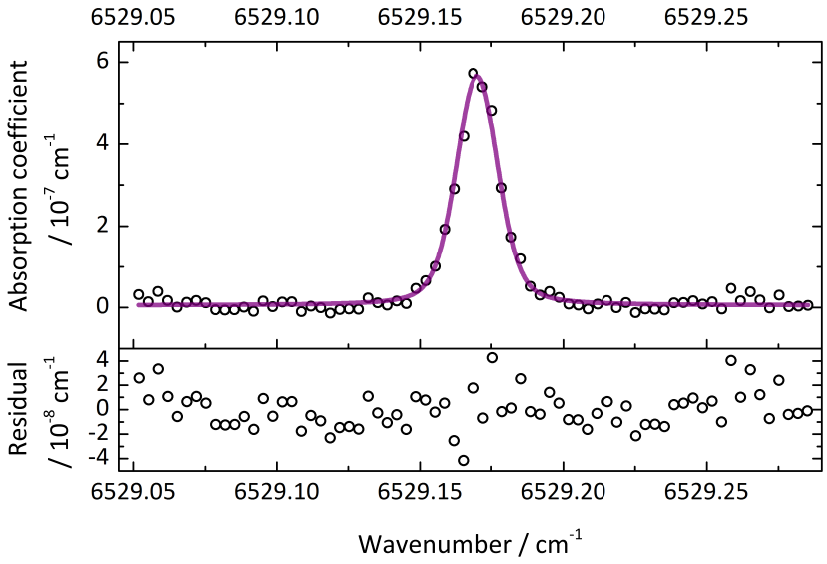

Figure 3.13: Absorption spectrum of car exhaust gas mix, showing the $P(11)e$ transition in the (10100) ← (00000) band of acetylene.

fit, the α_{min} was determined to be 6×10^{-9} cm^{-1} in 1 s, which corresponds to a detection limit of 10 ppb in 1 s at 50 Torr.

This part of the near-IR is the best spectral region for acetylene sensing by absorption spectroscopy. Acetylene does have fundamental vibrational bands in the mid-IR, but the symmetry of the molecule means only two are IR active. Their intensities are on the same or only one order of magnitude better than the transition studied in this work: the lower reflectivity of mirrors and reduced responsivity of detectors in the mid-IR mean that measurements in that region are unlikely to result in lower detection limits, especially with the cavity-enhanced techniques necessary for high-sensitivity atmospheric detection. The lowest detection limit for acetylene has been recorded using a near-IR diode laser cw-CRDS instrument, operating close to the region of this work at 6565.62 cm^{-1} (1523 nm). This lab-based sensor could detect mixing ratios as low as 340 ppt in 70 s acquisition time, without sample preconcentration, and the instrument was used to conduct a monitoring campaign in central Helsinki. To achieve this level of performance, the instrument had an extremely high cavity finesse of 390, 000,

equivalent to a τ_0 of 215 µs [128].

3.5 Summary

The sensitivity of the instrument presented in this chapter was limited by the sinusoidal baseline variations arising from the inequality of the cavity arm lengths, and the temporal stability was severely hindered by the lack of active phase matching. As such, the near-IR V-cavity OF-CEAS spectrometer and the analysis routine presented in this chapter are far from optimized, and are consequently some way off the best reported performance (a $\alpha_{\min}$ on the order of 10^{-11} cm^{-1} in 1 s) of the best reported near-IR OF-CEAS instrument [117].

The major criticism of the analysis routine is that transmission spectra of both even and odd modes were transformed into absorption spectra using a ringdown measurement resulting from only one mode set. A widely deployed method of simplifying the analysis is to set the laser cavity distance (z) to an even integer multiple of L. This has the effect of phase-matching every other longitudinal mode at the laser facet, Equation 3.25. Although this halves the spectral sampling resolution, the added advantage is that the locking range is increased to $2\Delta\nu_{\mathrm{FSR}}$, allowing a faster scan rate in order to obtain the same FWHM for each mode and thereby reducing $1/f$ noise [59].

The complications inherent in using a V-cavity could be avoided by using a simple two mirror linear cavity. Quantum cascade laser (QCL) OF-CEAS has already been demonstrated using the V-cavity methodology, but the entirely different nature of QCL structure and transitions suggest they respond differently to optical-feedback. This may allow the use of a simple linear cavity without the need for optical isolation for suppression of the field directly back-reflected from the dielectric coating of the first mirror. There would also be the added benefit of working in the mid-IR and therefore accessing strong fundamental transitions.

Chapter 4

Developing Mid-IR Linear Cavity QCL OF-CEAS

4.1 Motivation

Several aspects of the OF-CEAS technique make it highly suited both to studies of fundamental spectroscopy and sensing with mid-IR QCLs, and the technique has already been successfully demonstrated for spectroscopy of N_2O, CO_2 and H_2O [88], and applied to detection of CH_4 and N_2O in air [48] and formaldehyde [49]. There are several advantages of OF-CEAS compared to ICOS, OA-CEAS and CRDS specific to working in the mid-IR. CRDS with a cw-QCL requires either optics (e.g. an acousto-optic modulator (AOM), currently only available as a custom mid-IR optic [129]) or electronics to rapidly shutdown the laser [130], in addition to the fast acquisition and synchronization systems required to capture the cavity ringdown signal. OF-CEAS has the potential to deliver commensurate sensitivity without these requirements. Implementations of the more sophisticated OA-CEAS have been preferred over ICOS for mid-IR instruments, in order to have reproducible cavity mode coupling and spatial output. OA-CEAS relies on exciting very many high order cavity modes, in order to suppress the frequency-filtering effects of the optical cavity. Given the division of

the power of the input laser radiation between so many modes, this results in the average optical power leaking out of the cavity being very low; in the mid-IR this can be close to the noise equivalent power of TE-cooled photodiodes. The output is also spatially diffuse leading to increased diffraction losses, which are greater at longer wavelengths (Equation 2.25). This leads to a requirement for large-area cryogenically cooled detectors and custom large diameter cavity mirrors (2 inches). Consequently, mid-IR OA-CEAS typically results in a pathlength gain on the order of 1000 or less [131, 132, 133, 134], unless a great deal of effort and expense is put into counteracting these factors [47].

In contrast, the TEM_{00} alignment and frequency locking inherent to OF-CEAS result in highly optimized coupling of light into the optical cavity and pathlength gain is easily on the order of kilometres. This leads to an increased signal-to-noise ratio, with a cavity output signal orders of magnitude larger than the noise equivalent power of TE-cooled mid-IR detectors. The spatial profile of the beam is also reduced, decreasing diffraction losses and enabling the use of smaller area mirrors. This last feature means that very small volume gas cells can be used.

4.1.1 Alternatives to V-cavity OF-CEAS

Aside from the V-cavity, which was described in Chapter 3, several alternative designs for locking diode lasers to high finesse cavities using optical-feedback have been demonstrated. Like the V-cavity, they are all designed to suppress optical-feedback from the directly back-reflected field returning into the laser gain medium, and are shown in Figure 4.1. Successful diode laser OF-CEAS schemes based on (e) and (f) have been demonstrated, while the others have been demonstrated as optical-feedback locked power-buildup cavities. None of the schemes in Figure 4.1 has been successfully implemented for QCL OF-CEAS. The power build-up schemes (a) through (d) use a linear cavity and polarization-based optical isolation from the direct back-reflected field. Perhaps the most

subtle scheme is that of (a) and (d), where the birefringent properties of the dielectric cavity mirrors are used as polarization selective optics in conjunction with a quarter-wave plate ($\lambda/4$). The intracavity field experiences a small change in polarization on every reflection, and consequently the field reflected from the cavity and the direct back reflection have different polarizations. This effect has

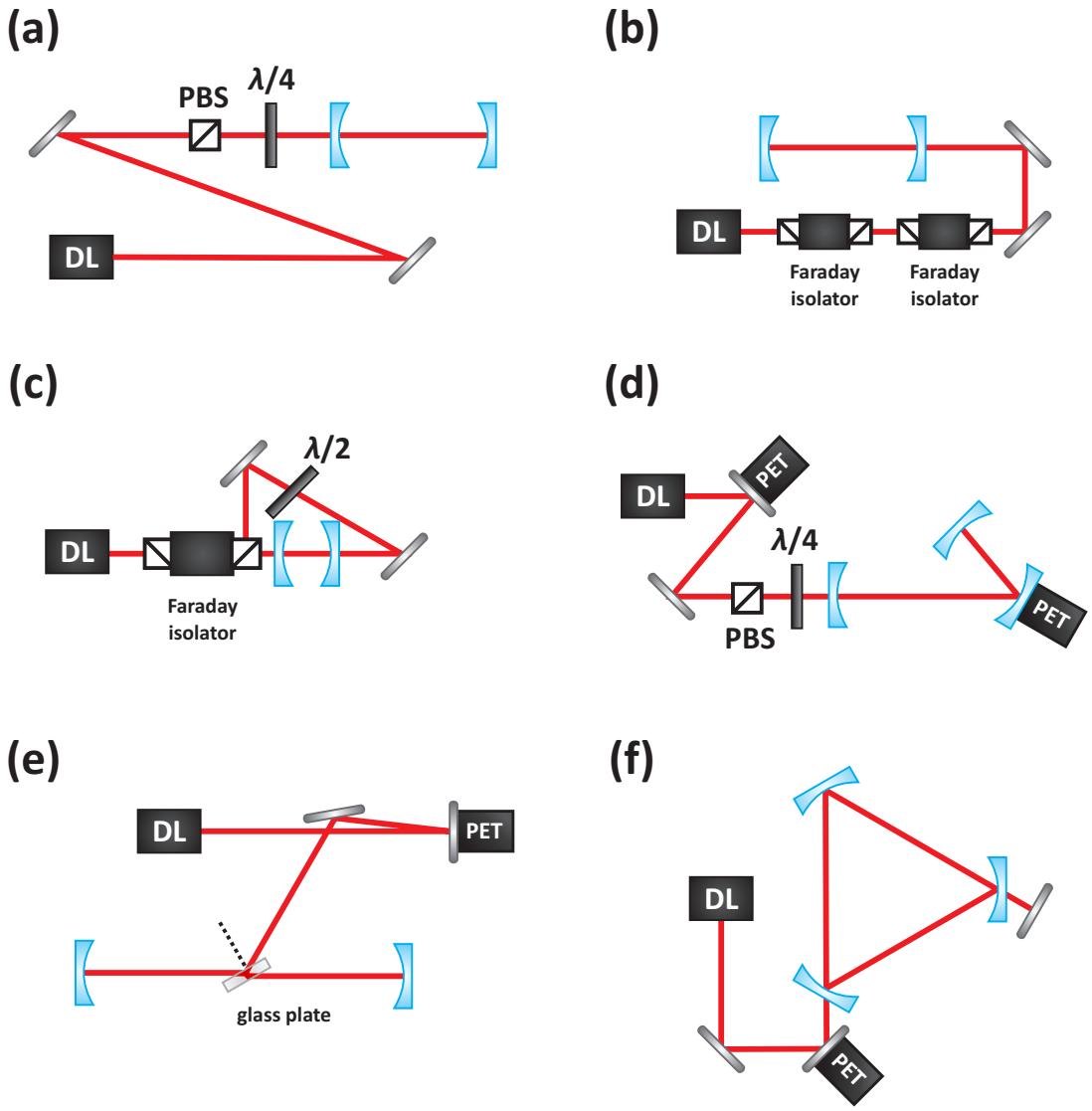

Figure 4.1: Alternatives to the V-shaped or tilted cavity for diode laser OF-locking: PET is piezoelectric transducer; DL is diode laser; PBS is polarizing beam splitter; and $\lambda/2$ and $\lambda/4$ are half- and quarter-wave plates. Linear cavities with optical isolation have been built using (a) [135] and (d) [136] birefringent properties of the optical cavity mirrors; and (b) [37, 137] and (c) [138] using Faraday rotators between crossed polarizers. Panel (e) is the Brewster angle cavity developed by Motto-Ros [139] and panel (f) is the ring cavity developed by Hamilton et al. [87].

been used in (a) to measure the birefringent properties of cavity mirrors [135], and in (d) as a power build-up cavity scheme to focus a beam of Cs atoms [136]. Hamilton investigated this latter scheme for linear cavity diode laser OF-CEAS. Because the birefringence of cavity mirrors is often very small, and not always a reliable feature of mirror coatings, such a scheme was found to be unfeasible for robust OF-CEAS [140].

Other schemes have used linear cavities with Faraday rotator based isolators. Sometimes more than 60 dB isolation is required, and this has been achieved by placing two Faraday isolators in series. Shown in (b), this scheme has been used by the group of Hippler for both OF-enhanced photo-acoustic spectroscopy (PAS) and Raman spectroscopy [37, 137]. A more nuanced scheme is that of (c), where a half-wave plate was used to rotate the polarization of the optical-back field, enabling its selective attenuation. This scheme was used by Dixon et al. [138] to enhance second harmonic generation by placing a non-linear crystal in the power-buildup cavity.

Those schemes proven to work for OF-CEAS (e and f) have both used alternative cavity arrangements. The first example is that of the two mirror cavity with a Brewster-angle optic at its centre, Figure 4.1 (d), allowing cavity injection without transmission through a cavity mirror [84, 117]. The drawback of this scheme is that if the optical surfaces of the intracavity optic are dirty, then the absorption and scattering losses for odd and even modes will differ and an alternation effect will arise, as for a V-cavity (Section 3.3.3). For mid-IR implementations, the low absorption and high surface quality required of the intracavity optic is likely to lead to a need for a costly custom optical component.

Ring-cavity OF-CEAS (f) was developed by Hamilton et al. [87] using a visible diode laser. The travelling-wave nature of the modes of a ring-cavity, coupled with a three mirror design, ensures that the direct back-reflection does not follow the path of the incoming beam. To provide optical-feedback, a retroreflector was

placed behind one of the cavity mirrors, allowing control of the feedback coupling rate without the need for transmissive optics, increasing the light incident on the cavity and reducing the number of components between which etalons could occur. This approach did not work successfully with a QCL [48], as the retroreflector was not able to provide a sufficiently large feedback coupling rate to bring about locking for OF-CEAS (see Section 4.5).

4.1.2 Linear cavity QCL OF-CEAS?

Use of a V-cavity, or one of the alternative forms presented in the previous section, have been considered necessary for OF-CEAS because the high reflectivity of the cavity mirror means that the feedback coupling rate, κ, of the direct back-reflected field is likely to be high. A diode laser subject to such "strong" feedback is likely to operate in the coherence collapse regime and exhibit unstable behaviour.

A thorough search of the literature reveals a single paper describing a diode laser successfully locked to a linear cavity without optical isolation [141]. The authors attributed the success of their scheme to mode-mismatching between the spatial output of the laser and that supported by the cavity, which spatially filtered the direct back reflection. An attempt to apply this scheme to OF-CEAS with a diode laser proved unsuccessful [140]. This chapter presents the first successful two mirror linear cavity OF-CEAS experiment, crucially with a QCL rather than a diode laser. The stable frequency response of QCLs to "strong" optical-feedback, combined with the requirement to phase match the optical-feedback field to the emitted field at the laser facet, makes this experiment possible and these factors are discussed further in Sections 4.5 and 4.5.1.

There are several advantages to using a linear cavity. All modes have a node at each mirror, so there is no alternation effect, and there is no introduction of sinusoidal baseline oscillations from mismatch of cavity arm lengths (Section 3.3.3). One less mirror is required and this reduces cavity losses; theoretically by a fac-

tor of four compared to the V-cavity, see Figure 2.6. More light is transmitted through the cavity on to the detector (increasing the signal-to-noise ratio) and more optical-feedback is returned to the QCL (beneficial given QCL response to optical-feedback, see Section 4.5).

4.2 Historical development of QCLs

The first QCL was demonstrated in 1994 [22], based on an intersubband lasing transition. Capasso has described this breakthrough as ending the "bandgap slavery" of semiconductor laser wavelengths [142]. The idea of intersubband lasing transitions between very thin layers of alternating semiconductor materials was proposed in 1970 by Esaki and Tsu [143] and expanded to include pumping by resonant tunnelling by Kazarinov and Suris [144] the following year. However, only the realization that the lower state of the laser transition must be emptied on a timescale much shorter than the lifetime of the upper state, and the subsequent development of both the theory and the material engineering techniques to favour this process, enabled the first working QCL to be demonstrated [142].

Part of the gain medium of the first demonstrated QCL is schematically illustrated in Figure 4.2. The laser had a GaInAs/AlInAs active region, grown by molecular beam epitaxy on lattice matched InP. The active region had three quantum wells, each of which were separated by a multilayer digitally graded alloy injector-relaxation region. Applying a forward bias, an electron tunnels through the 4.5 nm thick AlInAs barrier into the $n = 3$ energy level, on a time scale of 0.8 ps. This electron undergoes a diagonal radiative transition to $n = 2$, producing a photon whose energy is defined by the width of the first quantum well of the active region, which has a thickness of 0.8 nm and therefore a lasing wavelength of 4.2 µm. A diagonal transition was chosen to reduce spatial overlap between the upper and lower levels of the lasing transition, increasing the lifetime of the upper state, to favour population inversion. Finally, a rapid relaxation from

$n = 2$ to $n = 1$ via phonon resonance occurs. Optimization of these processes was engineered into the material by selecting the thicknesses of the second and third quantum wells to be 3.5 and 2.8 nm respectively, in order to have excellent spatial overlap, leading to fast relaxation on a time scale of 0.6 ps. Tunnelling through the barrier into the next active region also occurs on a fast timescale of 0.2 ps, again favouring population inversion. The optical phonon relaxation time between $n = 3$ and $n = 2$ is estimated to be 4.3 ps, making it a relatively unfavoured process. By tunnelling through the injector-relaxation regions, a single electron cascades through a concatenated series of these discrete active regions (25 for this laser) producing one photon in each. Additional cladding layers act as a waveguide, confining radiation propagating parallel to the active region. The ridge of the waveguide was 12 µm wide and formed by etching. The end facets were cleaved to produce a Fabry-Perot type laser cavity, resulting in a waveguide length of 500 µm. This QCL had a peak power of 8 mW in pulsed operation.

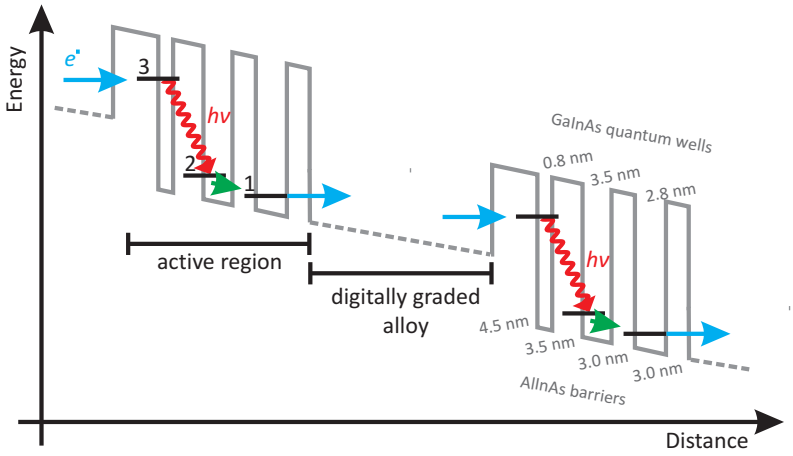

Figure 4.2: The three quantum well intersubband diagonal transition lasing scheme of the first reported QCL, adapted from [22].

4.2.1 Continuous wave, room temperature, and single-mode operation

This first demonstrated QCL was pulsed and required cryogenic cooling. Operating at a temperature of 10 K, the laser threshold current was 850 mA. By Joule's first law, this means that approximately 7 W of power had to be dissipated. Cryogenic cooling shortens laser chip lifetimes and reduces reliability, because of extreme temperature cycling. Additionally, pulsed QCL sources are not suitable for OF-CEAS. Not only would the bandwidth of the pulse excite more than one longitudinal mode simultaneously, but pulsed QCLs also have an inherent frequency chirp associated with the laser pulse, with a typical rate of 0.005 cm^{-1} ns^{-1} (150 MHz ns^{-1}), which further prevents a sufficient intensity build-up in any given cavity mode [132]. The development of vertical lasing transitions, based on active regions with two quantum wells where the upper and lower levels of the lasing transition are in the same well, led to both continuous wave devices that did not exhibit a frequency chirp [146], and room temperature operation QCLs [145]. Vertical lasing transitions are less sensitive to layer interface roughness and impurities, resulting in a narrower gain spectrum and a lower threshold current [147].

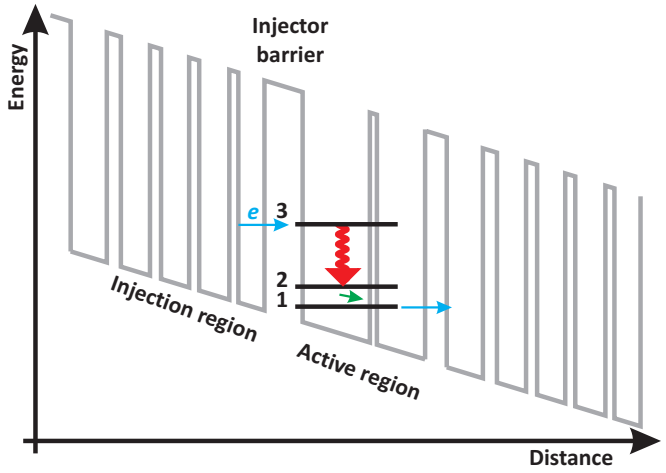

Figure 4.3: The two quantum well structure of the first vertical transition room temperature QCL, adapted from [145].

For room temperature operation, several further improvements were made to the gain region. The multilayer relaxation-injector region was redesigned with thinner layers. This better confined the wavefunction inside the active region and minimized the probability of electron escape from the upper level of the lasing transition into the injector-relaxation region. The barrier between the two quantum wells in the active region was also made thinner, resulting in increased optical phonon emission and a shorter tunneling escape time, both strengthening the population inversion. Finally, the injector region and the injection barrier were redesigned to increase tunneling. With a wavelength of 8.5 µm, this QCL was the first ever mid-IR semiconductor laser to operate at room temperature, an important advance on lead-salt diode laser technology [145].

Single mode operation DFB devices were demonstrated in 1997, by including a corrugated grating on the surface of the ridge waveguide [148]. This led to the first demonstration of QCL absorption spectroscopy in 1998, where a pulsed room temperature DFB-QCL was applied to wavelength modulation spectroscopy of N_2O at 8 µm [149]. Alpes Lasers SA was the first company to commercialize QCL technology, and cw room temperature DFB-QCLs became available in 2004 [150].

4.2.2 Further recent developments relevant to tuneable QCL absorption spectroscopy

Other recent developments relevant to tuneable QCL absorption spectroscopy include efforts to extend the wavelength region covered by QCL devices, widening the tuning range of single mode devices, and improving wall plug efficiency. The QCLs described above were based on GaInAs/AlInAs on lattice matched InP, and QCLs using this material system cover the wavelength region 3.4 to 24 µm [24]. Extension of the QCL methodology to other material systems has extended this range. A major development was the demonstration of THz QCL devices

based on the AlGaAs/GaAs material system [151]. The shortest reported QCL wavelength (2.9 µm) was achieved using a InAs/AlSb QCL [152]. Additionally, theoretical proposals for QCLs based on GaN/AlGaN or GaN/InGaN for THz and near-IR QCL have been given [153, 154].

Wall-plug efficiency is primarily being addressed by improving fabrication methods and understanding of the more developed InP substrate QCL technology [155, 156]. Additionally, the concept of a cascaded lasing transition, where the electron undergoes two consecutive transitions and emits two photons of the same energy in a single active region has been demonstrated [157], a concept that also results in improved QCL efficiency.

An area of development with particular relevance to tuneable laser absorption spectroscopy is an on-going effort to broaden the wavelength tuning ranges of single mode devices. EC-QCLs have been demonstrated [158, 159] and are commercially available from Daylight Solutions, but rely on mechanical tuning of the wavelength, which is inherently less robust than current or temperature tuning of DFB devices. Alternative devices include: a super structure grating array of five single-mode distributed feedback quantum cascade lasers fabricated monolithically on a single chip (tuning range of 86 cm^{-1}) [160]; novel hairpin shaped laser cavities for Fabry-Perot devices (tuning range of 15 cm^{-1}) [161, 162]; and also QCLs including a distributed Bragg reflector (tuning range of 63 cm^{-1}) [163].

Many of the developments described above have resulted from the major Mid-InfraRed Technologies for Health and the Environment (MIRTHE) interdisciplinary research programme supported by the National Science Foundation in the USA [164]. The existence and continued support of this scheme by the US government demonstrates the strategic importance of QCL based sensing technology.

4.3 QCLs used in this work

Two different QCLs, from two different manufacturers [Alpes Lasers SA and Maxion, now part of Thorlabs] were used to implement linear cavity QCL OF-CEAS. Both were cw DFB-QCLs with lasing wavelengths near 5.5 µm and 5.2 µm, within the high reflectivity bandwidth of the same cavity mirror set. Consequently the same optical setup was used for both of the lasers.

4.3.1 QCL housing and temperature control

During operation, a QCL generates several W of heat and therefore requires specialized housing for heat dissipation and temperature control in order to have stable frequency operation. A mount was devised for this purpose at the Rutherford Appleton Laboratory (RAL), and a labelled design is shown in Figure 4.4. Both QCL chips were purchased as "chip-on-carrier" (NS submounts) from the manufacturers, and were similarly housed. The submount was held on a Cu heatsink, attached to the cold junction of a Peltier element for thermoelectric cooling. The hot junction of the Peltier element was attached to another Cu heatsink that formed the back of the laser mount, and this contained internal channels through which water was circulated for cooling. Thermal contact between the heatsink and the QCL submount was maximized using a small amount

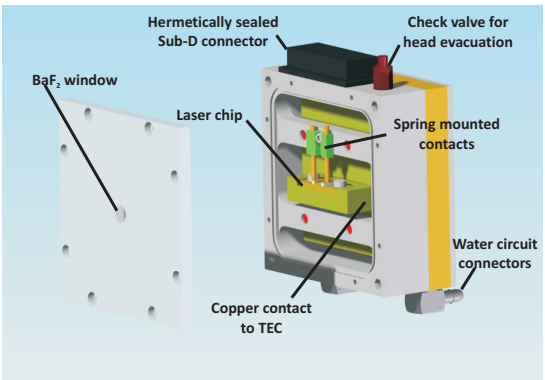

Figure 4.4: The QCL custom housing, courtesy of RAL.

of thermal contact grease [Apiezon N].

When operated, the QCLs were cooled to temperatures ranging from 9 to −30 °C. To prevent condensation or crystallization of water on the QCL chips, the main section of the mount was hermetically sealed and evacuated to better than 5 Torr with a small diaphragm pump [KNF, various models]. The QCL facets were positioned as close as possible to the exit window to minimize the spatial extent of the beam prior to the collimation optic. For the Alpes laser a BaF_2 window was used, while for the Maxion laser a CaF_2 window was used instead [both Crystran, diameter 6.85 mm, thickness 0.5 ± 0.1 mm].

The lasers were thermoelectrically cooled (TEC) by a Peltier element positioned at the back of the heat sink. The temperature was monitored by a thermistor positioned on the copper block itself. Two similar custom temperature controllers were used [PTCL Electronics, design by Neville Baker], setup so that the thermistor reading was linear over the operating range. Electrical contact between the hermetically sealed DB-9 connector for the temperature controller, current source (discussed in Section 4.4) and the laser submount was made with spring loaded contact pins, positioned once the QCL chips had been secured in the mount. Commercial housing systems are now readily available and custom housing offered no particular advantage for the linear cavity QCL OF-CEAS development system, (see [87, 98] for a V-cavity QCL OF-CEAS system built with such components). However for historical reasons, the Alpes laser was already mounted in a custom housing prior to commencing the QCL OF-CEAS experiment and the Maxion laser was similarly mounted for ease of integration into the setup.

4.3.2 Alpes DFB-QCL

Linear cavity QCL OF-CEAS was first implemented with an Alpes Lasers cw DFB-QCL [sbcw395]. The specified LIV characteristics are plotted in Figure 4.5.

Typically, this laser was operated at −15 °C and had an output power of 3 mW. The specified emission spanned 1818.7 cm^{-1} at 10 °C to 1829.5 cm^{-1} at −30 °C, corresponding to wavelengths close to 5.5 µm. The laser was previously used in a different experiment, and its linewidth measured to be 16 MHz [166]. During the course of this other experiment, the laser was accidentally submerged in water leaking into the housing from the cooling unit. The laser was returned to Alpes and cleaned by them. The laser performance after this incident was not noticeably worse or different to the specifications, indicating a (perhaps unexpected) degree of robustness of the laser chip to harsh conditions.

Microscope images were taken of the laser at the Central Laser Facility at RAL, to determine the size of the facet into which optical-feedback must be refocused for successful OF-CEAS. An example image is shown in Figure 4.6 (a). The Alpes DFB-QCL is an index guided laser, and two laser ridges are visible on the top surface of the semiconductor substrate. Surfaces deposits resulting from the water submersion may explain the varying contrasts across the surface of the semiconductor substrate. The speckles of extreme contrast (blue) are most likely

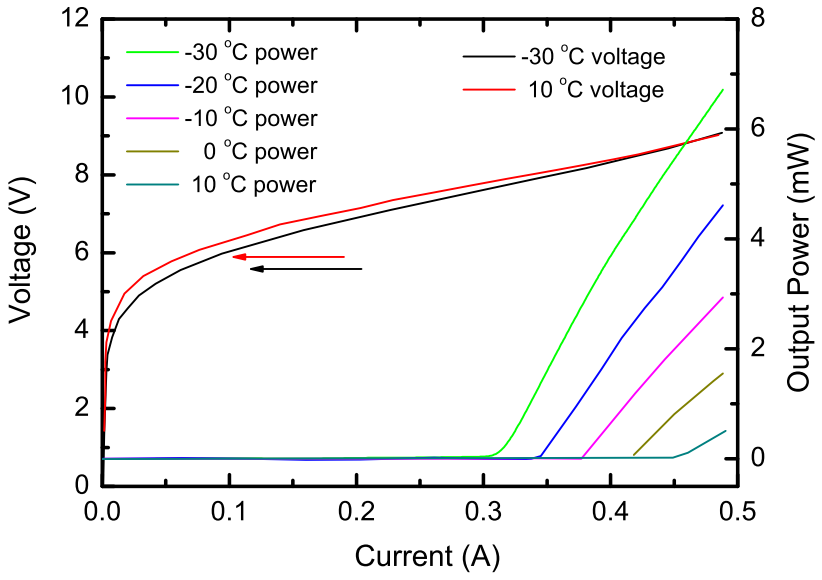

Figure 4.5: Specified voltage and average power against current for the Alpes DFB-QCL. For clarity, voltage curves are only shown for 10 and −30 °C.

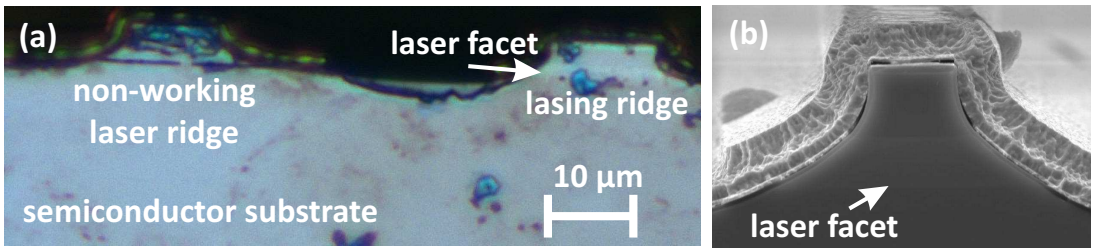

Figure 4.6: (a) microscope image of the Alpes QCL; (b) microscope image from Alpes User Manual [165].

to be dirt, as these kind of structures have not been observed in microscope images of other QCLs used at RAL. The ridge on the left-hand side is contaminated with this material, and hence is a non-lasing ridge. The lasing ridge is on the right hand side. Due to the varying contrasts it is not immediately obvious, but a brighter stripe is visible across the lower part of the ridge, and this corresponds to the lasing facet, with a horizontal and vertical dimension of approximately 10 µm and 1 µm respectively. For comparison, panel (b) shows a microscope image from the Alpes Lasers User's Manual [165]. Although this image has no scale information, the position and low contrast between the active and cladding regions correlate with those in (b).

4.3.3 Maxion DFB-QCL

The second laser with which linear cavity OF-CEAS was implemented was a Maxion cw DFB-QCL [M575AY]. Maxion specified an output power of 150 mW at 30 °C. Measurements (performed by James Kirkbride) of the voltage and average power of the Maxion DFB-QCL mounted in the custom housing are plotted against current for several operating temperatures in Figure 4.7. Unfortunately, the temperature controller was not able to operate at 30 °C, so a direct comparison with the specification was not possible. The measured output power at 9 °C is considerably lower than 150 mW. This is probably due to poor thermal contact between the QCL heatsink and the cold junction of the Peltier. Typi-

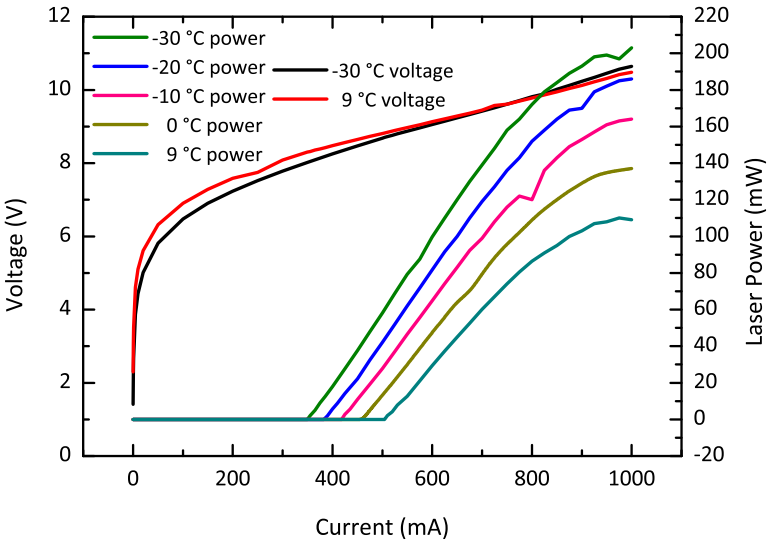

Figure 4.7: Measured voltage and average power against current for the Maxion DFB-QCL. For clarity, voltage curves are only shown for 10 and −30 °C.

cally, this laser was operated at temperatures such that the output power was on the order of 100 mW. Although the laser linewidth of this particular laser has not been measured, Lamb dip spectroscopy was used to determine the linewidth of a very similar[a] Maxion DFB-QCL [M575AH] [167]. That laser had a slightly higher output power (250 mW) and a linewidth of 0.80 ± 0.06 MHz. The emission wavenumber was measured using an FTIR spectrometer [Perkin Elmer, Spectrum 100] and spanned 1883 cm^{-1} at 9 °C to 1890 cm^{-1} at −30 °C, corresponding to wavelengths close to 5.2 µm. The dips in the laser power in Figure 4.7 are due to water absorptions.

Maxion helpfully supplied the design specification for the device. This information is confidential to Maxion and has been removed from the electronic copy of this thesis.

[a]Both of these lasers were manufactured to meet a particular custom specification regarding output power and lasing wavelength for a different experiment. The M575AH had a wavelength range around 5 cm^{-1} away from the specification, while the M575AY used in this work was the final device that fully met the specification.

4.4 Current sources

4.4.1 Intrinsic QCL linewidth

The intersubband lasing transitions in a QCL lead to a symmetrical gain spectrum with no variation of the refractive index at the gain peak. Correspondingly, the linewidth broadening parameter β was predicted to be zero [22] and has subsequently been measured to be close to zero [110, 146, 168, 169], and between -0.5 and 2 strongly dependent on injection current [170, 171]. The increase with injection current has been explained by the increase in carrier densities in both the upper and lower lasing levels leading to a change in the susceptibility. The negative β is physically possible, and arises from the high threshold current compared to diode lasers, which results in significant self-heating.

The low values of β suggests that the intrinsic linewidth of a QCL should be described by the Schawlow-Townes equation. Yamanishi et al. [172] reformulated the Schawlow-Townes equation based on the characteristic parameters of QCL gain media, and predicted a narrower intrinsic linewidth. This due to the (engineered) short lifetime of the upper state of the laser transition, which is much shorter than the spontaneous emission lifetime, and results in a high ratio between the rates of stimulated to spontaneous emission. Intrinsic linewidths of less than 1 MHz [173, 174] have been measured for unstabilized DFB-QCLs. Frequency stabilized QCLs have realized linewidths of 12 kHz [175] (by locking to a narrow absorption feature) and 5 Hz (Pound Drever Hall method) [79].

4.4.2 Effective QCL linewidth

In practice, it is difficult to reach the intrinsic linewidth due to technical noise on the injection current supplied to the QCL, and this results in an effective laser linewidth. For stable frequency operation and narrow effective linewidths, the QCL current source needs to have low current noise and good DC stability.

Previous experimental investigations into QCL OA-CEAS, indicated that the commercial current source [ILX Lightwave, LDX 3232] introduced a significant amount of technical noise on to the laser current. As a result, consecutive scans of the injection current were displaced relative to each other in optical frequency, on the order of the Doppler width of the studied CH_4 transitions ($\sim$ 100 MHz) [133]. This is undesirable, as the laser linewidth limits the spectral resolution of non-stabilized QCL absorption spectroscopy experiments. To reduce the effective QCL linewidth, two alternative current sources were investigated and compared to the ILX Lightwave. These were a custom made controller, and a commercial controller from Wavelength Electronics that became available just after the custom device had been developed. The essential characteristics of the different sources are compared in Table 4.1.

The custom controllers were devised and built by Phillip Hurst in the PTCL Electronics Workshop, and based on a diode laser current source by Libbrecht and Hall [118]. Two versions of this controller were tested, a prototype device and a mark I device (Mk I), pictured in Figure 4.8, based on the same circuitry and components but to some extent miniaturized for the Mk I. High specificity was possible with these custom devices. As there was no stringent space constraint, the PTCL Electronics controllers was made out of larger but lower-noise components than the commercial ILX device. Electronic pickup was reduced by minimizing connections. The injection current cables were soldered directly to

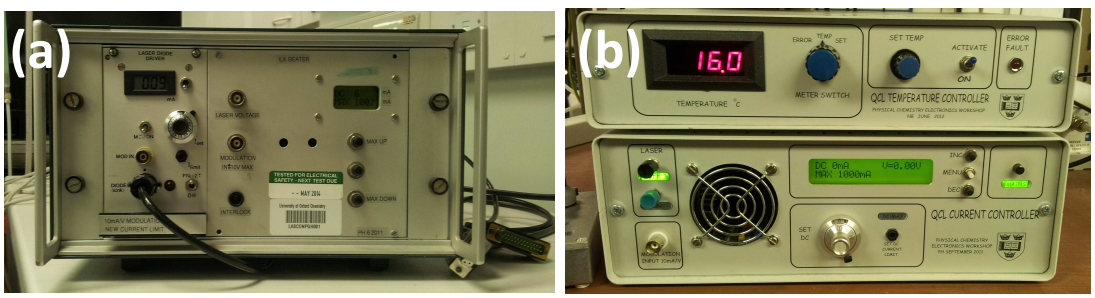

Figure 4.8: The PTCL Electronics (a) prototype and (b) Mk I current sources. The temperature controller is on top of the current controller in (b).

Current source	Current range / A	Modulation bandwidth / MHz
ILX Lightwave	0 to 4	DC to 0.25
Wavelength Electronics	0 to 1.5	DC to 2
PTCL Electronics	0 to 1	DC to 3

Table 4.1: Comparison of current range and modulation bandwidths of the QCL current sources.

the electronics board, although a D-plug was use for the connection to the QCL mount. The power supply in the prototype device was outside the controller chassis, and significantly shielded in the Mk I, to reduce mains noise at 50 Hz and its harmonics. An added benefit of the Libbrecht and Hall design was the ability to directly modulate the laser at much higher frequencies, opening up the possibility of performing wavelength modulation spectroscopy at much higher frequencies, thereby reducing the effect of $1/f$ noise.

At around the same time that the PTCL Electronics controllers were completed, Wavelength Electronics commercialized current sources developed at Pacific Northwest National Laboratory (PNNL) [176, 177]. Several models are available, and the model chosen for testing was the QCL1500, able to supply up to 1.5 A and therefore appropriate for the QCLs involved in the test. A key difference between the Wavelength Electronics source and the others, is that it requires an external power supply. For the tests conducted here, a linear power supply was used [ISO-TECH]. An added advantage of the Wavelength Electronics devices is that they have the necessary interfaces for easy integration with a LabVIEW VI or other control device. The tests involving the Wavelength Electronics source were performed at the Rutherford Appleton Laboratory.

4.4.3 Tests on dummy load resistors

The current controllers were first tested on "dummy loads" (resistors mounted on heatsinks) simulating a QCL. Two tests were carried out on the DC current

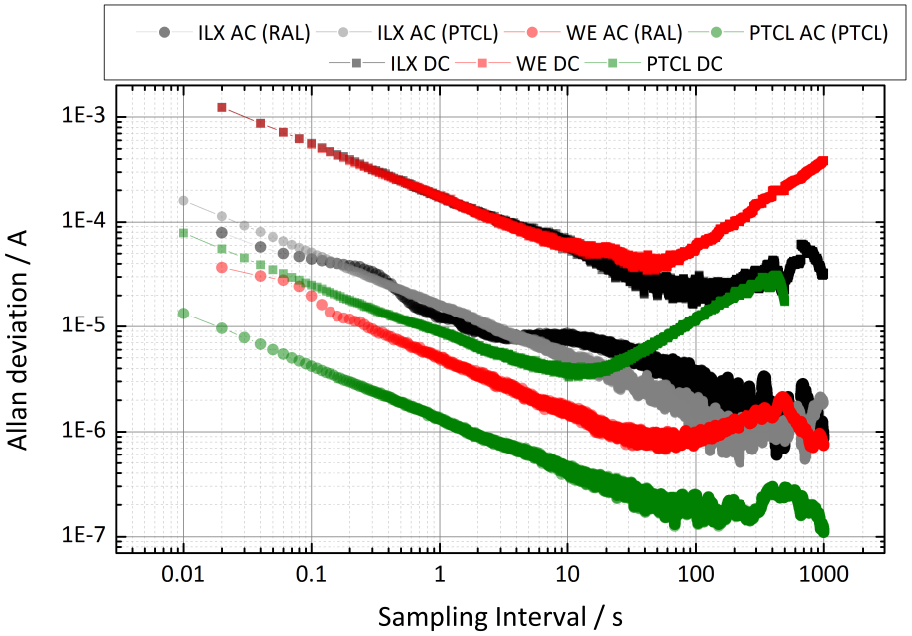

Figure 4.9: Allan deviation of the current controllers supplying (400 mA) to dummy loads, to determine temporal stability. Recorded both in DC mode (squares) and AC mode (circles) for the ILX Lightwave (black), Wavelength Electronics (red) and PTCL Electronics Mk I (green) sources.

supplied by each controller: a test of temporal stability and a frequency analysis.

For the temporal stability test each device was connected to a load and operated at a DC current of 400 mA. The two sources tested in the PTCL (the PTCL Mk I and an ILX Lightwave) were connected to a 25 Ω load, while those tested at RAL (Wavelength Electronics and another ILX Lightwave) were connected to a 10 Ω load. The voltage across the load was recorded for 30 minutes, both in DC mode and AC mode, and overlapping Allan variances were performed on these time series to determine the temporal stability. The results of this test are presented as Allan deviations of the supplied current in Figure 4.9.

The Allan deviations recorded in AC mode for the ILX devices in the PTCL and at RAL are broadly in agreement. From the traces recorded in DC mode, the PTCL Electronics Mk I is seen to have superior DC stability by one order of magnitude, up to a sampling interval of 10 s. This is again true for the traces recorded in AC mode, which represent the high frequency noise present on the DC signal. In turn, the Wavelength Electronics device is seen to perform better than

the ILX Lightwave device. These results suggest that the increased specificity of the Wavelength Electronics and PTCL Electronics Mk I sources significantly improved on the DC stability possible with the ILX Lightwave source.

A spectral analysis of the frequencies present in the current signal supplied by the ILX Lightwave and PTCL Electronics prototype devices to the 10 Ω load was performed using a swept-tuned superheterodyne spectrum analyser [Agilent 4395A]. In simplified terms, the spectrum analyser attenuated and then mixed the input signal with a signal from a local oscillator. Due to the nonlinearity of the mixer, its output consisted of the two original signals, their harmonics, and the sums and differences of the original frequencies and their harmonics. This signal was then passed through a scanning bandpass filter, and the power at each frequency recorded [178].

The resulting spectra are presented in Figure 4.10, where the upper panels (a)

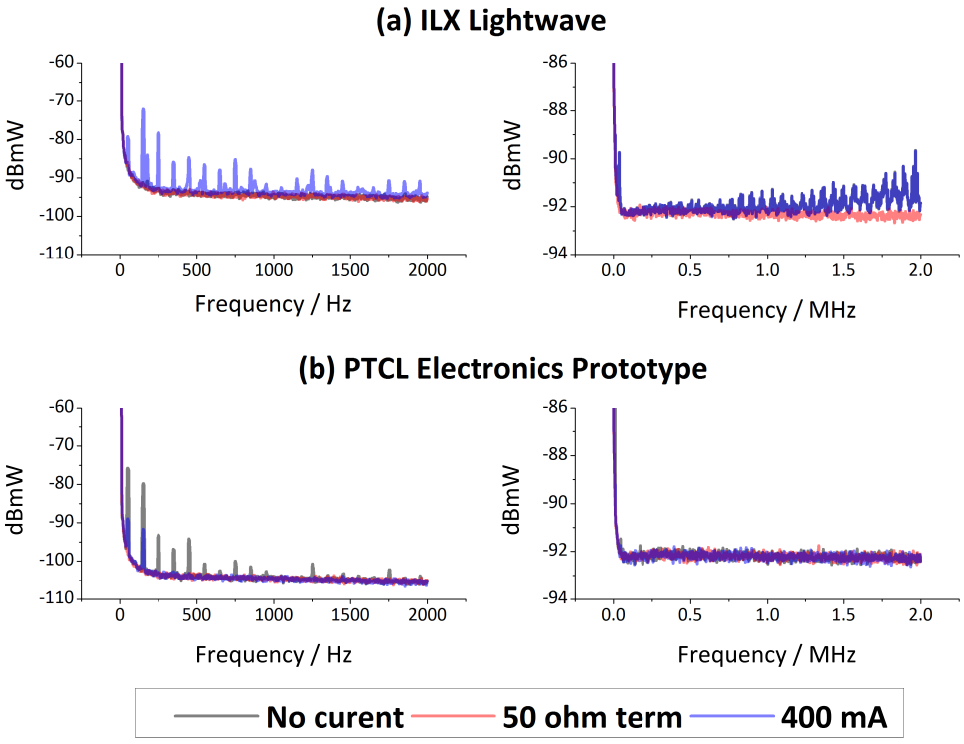

Figure 4.10: Power frequency spectra for (a) the ILX Lightwave and (b) for the PTCL Electronics prototype current controllers. Left-hand panels present low frequency spectra at high resolution bandwidth (10 Hz); righthand panels present high frequency spectra with lower resolution bandwidth (300 Hz).

show data for the ILX Lightwave and the lower panels (b) for the PTCL Electronics prototype. For each device power-frequency spectra of the noise floor (50 Ω termination, red), the device connected but not supplying any current (black), and the device supplying 400 mA DC (blue), were recorded. The spectra on the left-hand side investigate low frequencies (0 to 2 kHz) with a high resolution bandwidth (10 Hz). When supplying current both devices have spikes in the power spectrum above the noise floor corresponding to mains frequency (50 Hz) and its harmonics.

Towards higher frequencies the PTCL Electronics prototype has fewer power spikes and they have smaller amplitudes, suggesting that the use of a linear power supply may have reduced the effect of mains frequency noise. Although it seems that the PTCL Electronics prototype displays these spike when supplying "0 mA", this is actually because the minimum current that could be supplied by the prototype device was 8 mA. The panels on the right show investigations of high frequencies (0 to 2 MHz) with a lower resolution bandwidth (300 Hz). When supplying current, the ILX Lightwave controller displays many power spikes of increasing magnitude above the noise floor; in contrast the PTCL Electronics prototype spectrum looks very clean.

4.4.4 Measuring the effective QCL linewidth

The centre of a narrow (i.e. Doppler broadened) CH_4 transition was used as a frequency marker to estimate the effective laser linewidth achieved using the ILX Lightwave, PTCL Electronics Prototype and Mk I current controllers. These experiments used a different cw DFB-QCL [Alpes, sbcw835], similarly mounted and collimated to the previously described Alpes DFB-QCL. The laser had a frequency range from 1212 to 1223 cm^{-1} ($\sim$ 8.2 µm) at temperatures from 30 to −30 °C, and an output power of around 35 mW for the conditions under which the experiment was conducted.

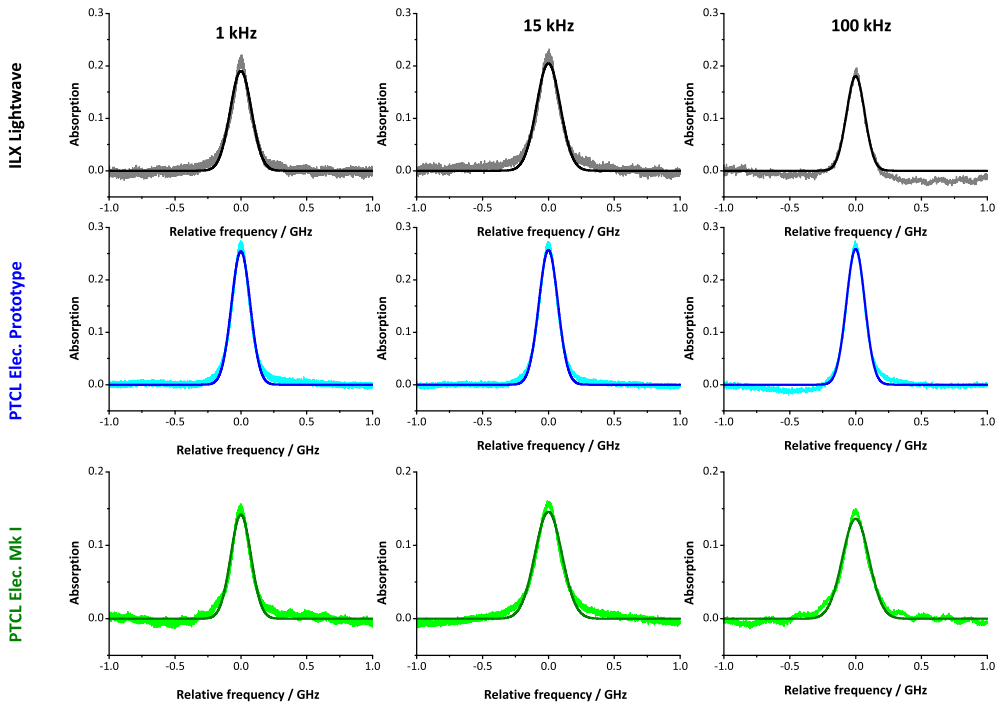

Figure 4.11: Examples of the CH_4 absorption spectra fitted with Gaussian profiles for each current controller (ILX Lightwave, PTCL Electronics Protoype, and PTCL Electronics Mk I) at each tested scan rate (1, 15 and 100 kHz).

A 10 cm long glass sample cell with BaF_2 windows, containing a low pressure of CH_4 (4.5 Torr), was placed in the collimated beam path. The laser was repeatedly scanned over the $(12, F2, 8) \leftarrow (13, F1, 3)$ CH_4 transition in the v_4 vibrational band[a] centered at 1218.63 cm^{-1} [9], with a linear current ramp. Laser scan frequencies of 1, 15 and 100 kHz were investigated. A Ge etalon [500 MHz FSR] was used as an optical frequency standard. The optically immersed photovoltaic HgCdTe detector [VIGO, PVMI-3TE-10.6] had a time constant of ≤ 3 ns, and the detector preamplifier had a bandwidth of 20 MHz. Around 150 traces were acquired by a digital oscilloscope [LeCroy, WaveSurfer 434] with a bandwidth of 400 MHz. The recorded transmission spectra were each fitted with a function incorporating a Gaussian profile and a linear baseline, for which all parameters were allowed to float. The relative frequency positions of the mean of

[a]For the v_4 band of CH_4, in which one vibrational quantum of the triply degenerate T_2 deformation mode is excited, the quantum numbers (J, C, α) correspond to rotation, rovibrational symmetry, and an index for the α^{th}-state described by the same J and C [179].

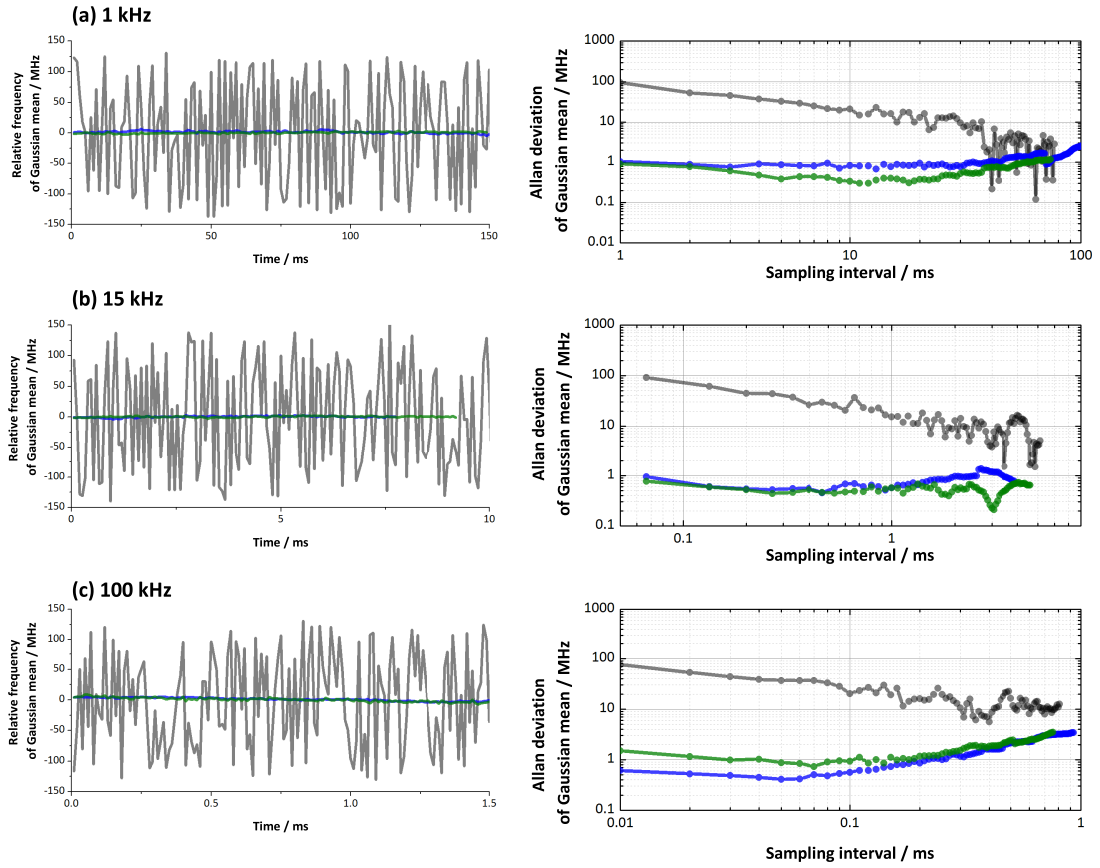

Figure 4.12: Time series (left-hand side) and corresponding Allan deviations (right-hand side) for the mean of the Gaussian profiles fitted to the spectra.

the profiles were collected.

Example fitted absorption spectra for each controller at each test scan frequency are shown in Figure 4.11. Further analysis of the data is presented in Figure 4.12 as time series and Allan deviations calculated from those time series, and as histograms in Figure 4.13, to estimate the effective laser linewidth.

The time series show that the relative frequency positions had much wider frequency excursions (~ 100 MHz) for the ILX Lightwave than for the PTCL Electronics devices (~ 1 MHz). Correspondingly, the Allan deviation of the transition centre for the ILX Lightwave is around two orders of magnitude larger than the PTCL Electronics devices. The slopes of log-log Allan deviation plots for the ILX Lightwave are all between -1 and $-\frac{1}{2}$, suggesting a white-noise dominance. The slopes of the corresponding plots for the PTCL devices initially have slopes

close to 0, suggesting a dominance of $1/f$ noise, before increasing due to frequency drifts.

In Figure 4.13, the left-hand panels show the histograms for all three devices. At all scanning frequencies, the ILX Lightwave (grey) produced an effective laser linewidth with a profile independent of the optical frequency that is around 100-times larger than those of the PTCL Electronics devices. The histograms (magnified in the right-hand panel) of the Gaussian mean for the PTCL Electronics sources have much narrower Gaussian distribution, and were fitted as such and the FWHM used to estimate the effective laser linewidths. Scanning at 1 kHz, the Mk I device (green) resulted in a slightly narrower effective linewidth than the prototype (blue), 3 ± 1 compared to 6 ± 2 MHz. Faster scan rates reduce $1/f$ noise, and both devices performed better at 15 kHz, with similar effective linewidths of 3 ± 1 MHz. However, at 100 kHz, both devices resulted in a broadened effective laser linewidth, 9 ± 3 MHz for the Mk I and 9 ± 4 MHz for the prototype.

The Wavelength electronics current source could not be included in these tests. However, a report on an early version of this controller by Myers et al. [177], suggests that significantly better performance could be expected, as the authors obtained an effective linewidth of less than 150 kHz estimated in a similar way.

The significant performance improvement demonstrated by the PTCL current controller has contributed to the successful implementation of QCL experiments based on multipass cells, cavity-enhanced absorption spectroscopy, and wavelength modulation spectroscopy [180, 181], and also studies of Lamb dip spectroscopy [167].

The OF-CEAS locking scheme brings about laser linewidth narrowing, so the effective linewidth is determined by the cavity bandwidth rather than the current controller. However, there is some evidence to suggest that the performance improvements offered by the PTCL and Wavelength Electronics current sources

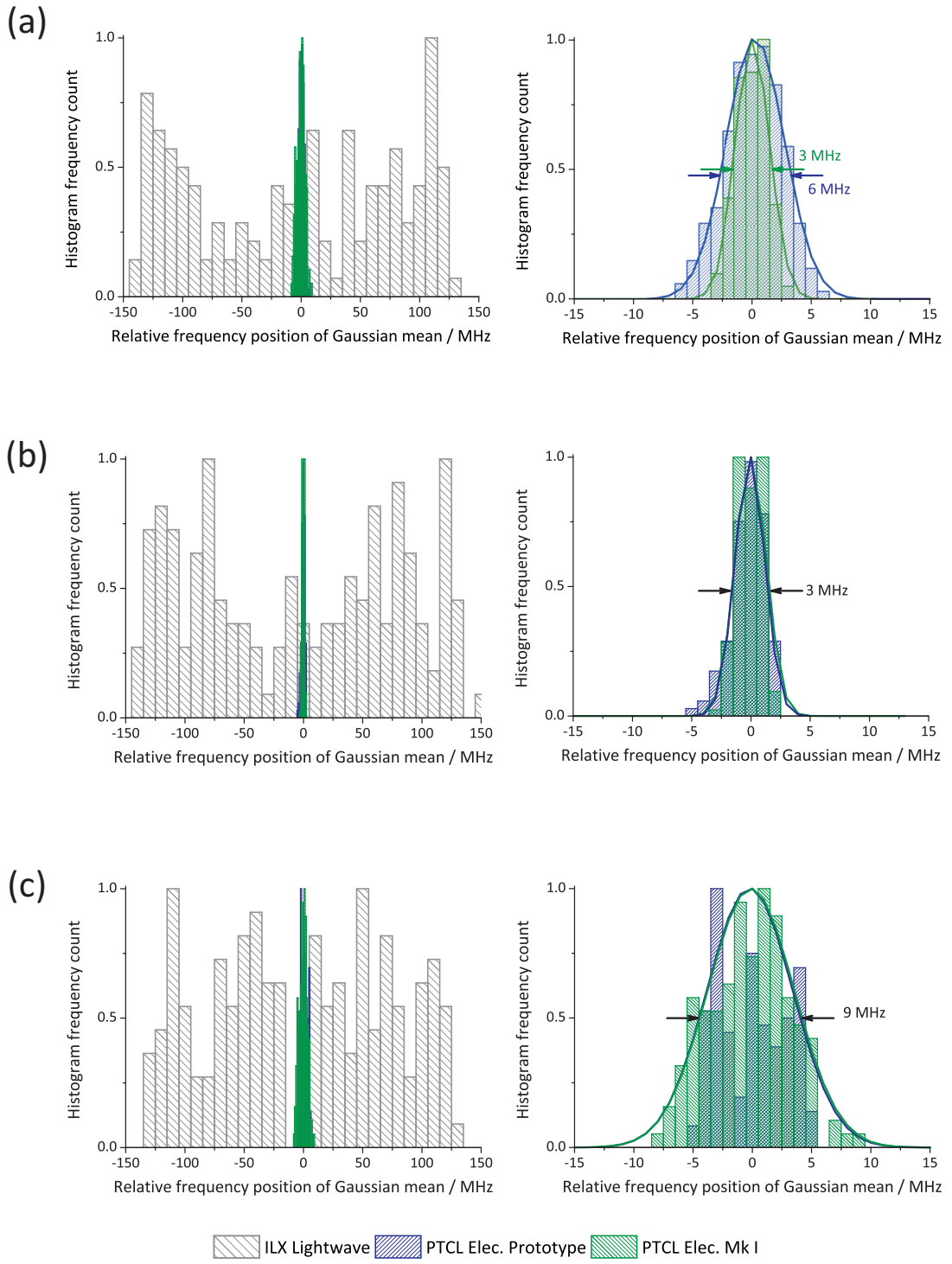

Figure 4.13: Histograms of the Gaussian mean position used to estimate the effective laser linewidth, for scanning frequencies of (a) 1 kHz, (b) 15 kHz, and (c) 100 kHz. The distributions for all three devices are shown in the left-hand panels; the righthand panels present magnifications of the narrower PTCL Electronics device distributions.

are also important for OF-CEAS. The QCL OF-CEAS spectrometer reported by Hamilton and Orr-Ewing [48] used the ILX Lightwave current controller. They later developed their instrument to use a Wavelength Electronics device instead, and found a improvement on the stability of the cavity intensity build up [182]. The work on the linear cavity QCL OF-CEAS experiment was begun prior to the availability of the PTCL Electronics Mk I controller. Although there were other aggravating factors at this early stage of development, most notably very significant water absorption of the intracavity beam in air at atmospheric pressure as the cavity was not enclosed in a gas cell, it was difficult to obtain any cavity output signal with the linear cavity when using the ILX Lightwave controller. Contrastingly, a reasonably large cavity output signal and successful OF-CEAS locking under the same conditions with the PTCL Electronics Mk I was possible, and is presented in Section 4.10.

4.5 Optical-feedback response of QCLs

The response of QCLs to optical-feedback contrasts markedly with that of diode lasers: this section makes clear what those differences are and how they make possible linear cavity QCL OF-CEAS. QCLs are found to be less sensitive to optical-feedback than diode lasers. There are two reasons for this. First, it is difficult to reinject light back into the QCL gain medium, because the QCL waveguide dimensions are below the diffraction limit. For instance, Brownsword and Weidmann [183] calculated by ray-tracing that for their EC-QCL, only $23 \pm 8\%$ of the light from the external cavity returned to the QCL gain medium, when diffraction limited optics were used. Second, the intersubband nature of the QCL lasing transition leads to zero or close to zero values of the linewidth broadening parameter (as discussed in Section 4.4). This has important consequences for the response of QCLs to optical-feedback. The relations for frequency locking (Equation 3.7) and linewidth narrowing (Equation 3.11), derived for coupling of

a diode laser to a V-cavity, both scale with $\sqrt{1+\beta^2}$, implying that an increased optical-feedback coupling rate, κ, is required to bring about a given level of frequency locking or linewidth narrowing for a QCL. This is evidenced by the fact that although all diode laser implementations of OF-CEAS, save that of the ring-cavity, have required significant optical-feedback attenuation, none of the reported QCL OF-CEAS instruments have.

QCL linewidth and frequency are found to be more stable under conditions of optical-feedback than those of diode lasers. The coherence collapse regime (defined as Regime IV in Section 3.2.3), occurring in diode lasers at high levels of feedback, is caused by interactions between the mode with the narrowest linewidth and the mode with the minimum gain. These laser modes are only different when the linewidth broadening parameter is non-zero [115]. Consequently, the coherence collapse phenomenon was not predicted to occur in QCLs, and has not been observed [184, 185]. Reference [185] is a very recent paper comparing the effects of strong optical-feedback on a diode laser, a mid-IR DFB-QCL [Alpes, similar to the laser used in this work] and a THz QCL, both theoretically and experimentally. The optical-feedback reflector was a metallic mirror. Experimentally, the authors found that the mid-IR and the THz QCLs were stable to optical-feedback coupling rates of $\kappa \sim 10^{-2}$, two orders of magnitude greater than that of the diode laser. Using a linear stability analysis, they were further able to show that for QCLs with $\beta < 2$, multimode instabilities are not predicted to occur. There are no reports of a QCL having $\beta > 2$, confirming that stable performance in the presence of strong optical-feedback is an intrinsic property of QCLs.

4.5.1 Phase of reflected field

Successful OF-CEAS locking requires that the phase of the optical-feedback field matches that of the laser emission field at the laser facet, E_{inc}. For the linear

cavity, there are two fields contributing to optical-feedback, the cavity reflected field, $E_{\text{out}} \exp(\mathrm{i}\phi_{\text{out}})$, and the field directly back-reflected from the dielectric mirror coating, rE_{inc}. (Optical-feedback from the mirror substrate is neglected, as there is only around 20 % reflection from the plane ZnSe at normal incidence.) Here r is given by $|r| \exp \mathrm{i}\delta$, where δ is the phase change on reflection from the dielectric mirror. A schematic of this situation at the mirror coating of the first cavity mirror is drawn in Figure 4.14.

High reflectivity dielectric mirrors were introduced in Section 2.3.1. The mirror is composed of an odd number of layers of alternating refractive index (only three are shown in Figure 4.14) deposited on a substrate, in this case ZnSe. The order of refractive indices is $n_{\text{air}} < n_2 < n_{\text{ZnSe}} < n_3$. rE_{inc} undergoes a phase change of π every time it reflects off a material of higher refractive index. Given the quarter-wave thickness of the layers there is an additional phase change of π for every layer twice traversed during a reflection. Consequently, reflection from any layer of the dielectric mirror results in δ equal to an odd integer multiple of π. rE_{inc} is therefore always in antiphase with $E_{\text{out}} \exp(\mathrm{i}\phi_{\text{out}})$ and as a result, if the laser to cavity distance is adjusted to satisfy the phase matching criterion for a linear cavity (Equation 4.9, derived in the next section), then rE_{inc} does not have the correct phase to injection seed on every mode of the external optical

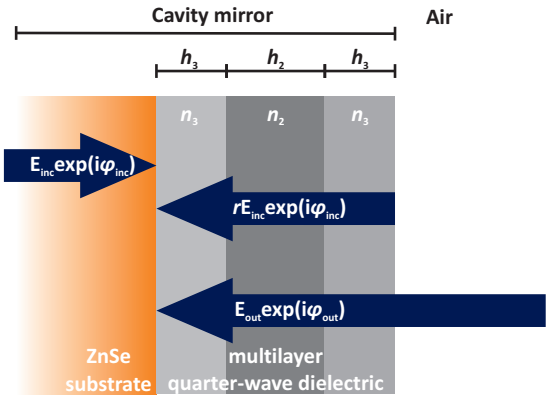

Figure 4.14: Schematic of a high reflectivity dielectric mirror, based on a ZnSe substrate, and with alternating layers of material with refractive indices n_2 and n_3. The electric fields relevant to the beams in the linear cavity OF-CEAS experiment are shown.

cavity. Evidence for this effect is presented in Section 4.11.

4.5.2 Frequency locking

An equation describing the change in frequency due to optical-feedback, $\Delta\omega$, equal to the laser frequency subject to optical-feedback, ω, minus that of the free running laser frequency, Ω, was derived for a diode laser coupled to a V-cavity in the previous chapter. The analogous expression for frequency locking of a QCL to a linear cavity may be derived in the following way, again starting from the Lang and Kobayashi equation (Equation 3.4). The situation is schematically depicted in Figure 4.15. At the laser facet, only the cavity reflected field has the correct phase to injection seed the QCL, so only this field need be considered. The feedback coupling rate, $\kappa_{m,\mathrm{Lin}}$, is given by:

$$\kappa_{m,\mathrm{Lin}} = \frac{1}{t_{\mathrm{las}}}\left[\frac{1-R_{\mathrm{las}}}{\sqrt{R_{\mathrm{las}}}}\right]\left\{\left[\alpha_{\mathrm{OF}}R(1-R)^2R^{2m}\right]^{1/2}\right\}, \tag{4.1}$$

where, as before, t_{las} is the roundtrip time in the laser gain medium, R_{las} is the power reflectivity of the laser facets, R is the cavity mirror reflectivity, and α_{OF} is an attenuation factor. The roundtrip time for the cavity reflected field is $t_m = t_z + mt_{\mathrm{r}}$, where t_z is the roundtrip time between the laser facet and the first cavity mirror, t_{r} is the cavity roundtrip time, and m is the number of cavity roundtrips. Substituting the t_m and $\kappa_{m,\mathrm{Lin}}$ into Equation 3.7 results in:

$$\Delta\omega = (1+\beta^2)^{1/2}\frac{1}{t_{\mathrm{las}}}\left[\frac{1-R_{\mathrm{las}}}{\sqrt{R_{\mathrm{las}}}}\right]\left[\alpha_{\mathrm{OF}}R(1-R)^2\right]^{1/2} \sum_{m=0}^{\infty} R^m \sin\left(\omega t_z + m\omega t_{\mathrm{r}} + \arctan\beta\right). \tag{4.2}$$

Having evaluated the sum in Equation 4.2, the details of which are given in Appendix A, and collected together the constants as the quantity K_{lin}, $\Delta\omega$ for

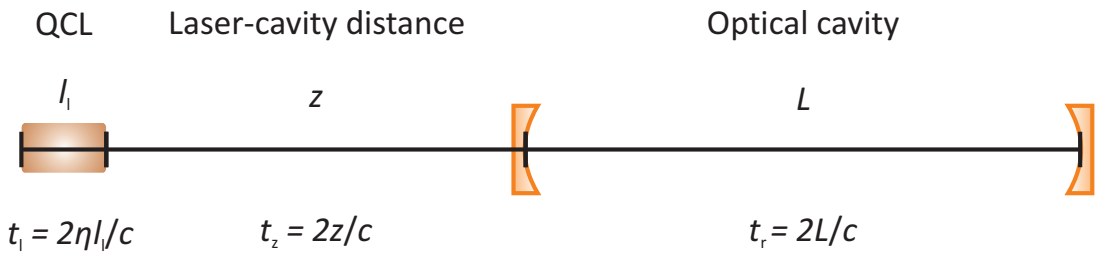

Figure 4.15: High finesse linear cavity OF-reflector.

the linear cavity is

$$\Delta\omega = K_{\text{lin}} \left[\frac{\sin[\omega t_z + \arctan\beta] - R\sin[\omega(t_z - t_r) + \arctan\beta]}{1 + \frac{4R^2}{(1-R^2)^2}\sin^2[\frac{\omega t_r}{2}]} \right]. \tag{4.3}$$

with

$$K_{\text{lin}} = (1+\beta^2)^{1/2}\sqrt{\alpha_{\text{OF}}}\frac{c}{2\eta l_{\text{las}}}\frac{\mathcal{F}_{\text{lin}}}{\mathcal{F}_{\text{las}}}, \tag{4.4}$$

where $2\eta l_{\text{las}}$ is the optical distance in the laser gain medium, $\mathcal{F}_{\text{lin}}$ is the finesse of the linear cavity, and $\mathcal{F}_{\text{las}}$ the finesse of the laser cavity, both given by Equation 2.38. $\Delta\omega$ may also be expressed in terms of the optical distances (i.e. the laser to cavity distance z and the cavity length L see Figure 4.15):

$$\Delta\omega = K_{\text{lin}} \left[\frac{\sin[\frac{2\omega z}{c} + \arctan\beta] - R\sin[\frac{2\omega}{c}(z-L) + \arctan\beta]}{1 + \frac{4R^2}{(1-R^2)^2}\sin^2[\frac{2\omega L}{c}]} \right]. \tag{4.5}$$

The phase matching criterion for the linear cavity, such that the phase of cavity reflected field matches that of the emitted field at the laser facet is also derived in the same way as that for the V-cavity (Equation 3.25). When in resonance with the frequency of a cavity mode, ω_q, the laser frequency, ω, locks to the cavity mode frequency and has a phase given by:

$$\phi_q = \omega_q t_m \tag{4.6}$$

$$= \frac{2\omega_q}{c}[z + mL]. \tag{4.7}$$

The phase difference between all successive modes must be an integer multiple, k, of 2π, in order that all modes have a node at the laser facet:

$$2\pi k = \phi_{q+1} - \phi_q = \frac{2\left(\omega_{q+1} - \omega_q\right)(z + mL)}{c}. \tag{4.8}$$

As before, $\omega_{q+1} - \omega_q$ is simply the cavity free spectral range, (2π times Equation 2.16) and the following relation by be arrived at:

$$z = L(k - m). \tag{4.9}$$

For optical-feedback at the laser facet both k and m are integers, and consequently Equation 4.9 implies that z must be set to an integer multiple of L in order that all modes have the same phase at the laser facet.

4.6 Optical design

4.6.1 Mid-IR beam profiling

QCL beam profiling was used extensively while designing and building the linear cavity QCL OF-CEAS setup: for measuring the beam quality factor (M^2), for collimation, and to determine the beam waist to be mode matched into the optical cavity. Two beam profiling devices were used for this purpose. When necessary, images from both cameras were fitted using a MATLAB routine using a least squares approach to model 2D elliptical Gaussian profiles [186].

The first was a pyroelectric array camera [Pyrocam III, Spiricon now part of Ophir Photonics], with a 12.4 by 12.4 mm active area and a pixel size of 85 by 85 µm. The surface charge of a pyroelectric crystal changes with heating by absorption of radiation, and this change is detected in order to produce an image. Such devices are inherently AC, and continuous wave light incident on the sensor array must be chopped more rapidly than thermal relaxation time of the crystal [30].

The second camera [DataRay, WinCamD FIR2-16] had a 10.3 by 13.7 mm long wave infrared microbolometer array [ULIS] with a pixel size of 35 by 35 µm. The resistance of bolometric materials is very temperature dependent, and can be continually measured as absorbed radiation heats the sensor [30]. The 50 mW cm^{-2} saturation threshold quoted by the manufacturer was easily exceeded, even with the lower output power Alpes DFB-QCL(3 mW), and hence careful monitoring of the laser power density was required to ensure that the beam did not saturate (or burn) the sensor. A high operating temperature and a current very close to threshold were chosen to minimize the output power. Optical-feedback can reduce the threshold current of a QCL by up to a few mA (see Section 4.11), and for this reason a minimal tilt was carefully maintained to avoid reflections from the window of the camera returning into the QCL and causing increases in power

that could damage the sensor. For the Maxion laser, it was additionally necessary to use a 1.0 optical density Ge-substrate neutral density filter [Edmund Optics, 64-355] to attenuate the laser power. This was mounted as close as possible to the laser to avoid imaging reflections of the beam.

4.6.2 Collimation

Both the Alpes and Maxion QCL beams were collimated by a lens external to the laser housing. In both cases the same Pb-chalcogenide aspheric lens [Thorlabs, C036TME-E] was used; this had a 4 mm focal length, a 0.56 numerical aperture, and was AR coated ($R < 1\%$). The QCL chip was mounted in its housing, and the housing fixed to the optical table so that the emitted beam was referenced to the axes defined by the optical table.

The microbolometer array was brought as close as possible to the collimation lens and its height adjusted to centre the beam on the sensor. This defined the working height for the optical system; for the Alpes DFB-QCL laser this was 145 mm, while for the Maxion DFB-QCL this was 140 mm. The camera was translated away from the laser along the z-axis defined by the optical table, and the beam aligned through the centre of the collimation lens by adjusting the horizontal and vertical micrometers of the translation stages on the laser housing. Finally, the z-position of the collimation lens was adjusted, so that it was close to 4 mm away from the laser output facet, accounting for the optical distance in the output window. The successful result of a collimation procedure for the Maxion DFB-QCL is shown in Figure 4.16. The microbolometer images present example beam profiles on the same scale at distances from the output window of (a) 100 mm, (b) 610 mm, and 1410 mm, although (b) was taken during a different collimation procedure to (a) and (c). The laser is clearly emitting on a TEM_{00} mode, although the beam profile is arguably some way away from the expected elliptical Gaussian. This could in part be due to a distortion of the

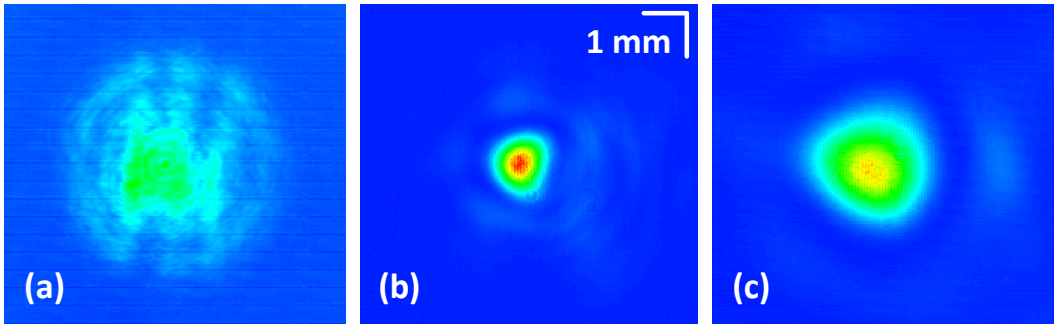

Figure 4.16: Collimated Maxion QCL beam at (a) 100 mm, (b) 610 mm, and 1410 mm from the output face of the BaF_2 window on the laser mount.

intensity distribution caused by tilting the camera. The laser beam exhibits the natural divergence of a Gaussian beam. The effects of diffraction around the approximately circular aperture of the CaF_2 window are visible. For (a) these have the form of Fresnel ripples typical of near-field diffraction. For (b) and (c) the diffraction pattern is better described as an Airy-disk pattern, as expected for Fraunhofer diffraction in the far field [55]. The non-uniform intensity of the diffraction ring is likely to arise from imperfections in and around the edge of the CaF_2 window.

4.6.3 Optical cavity design

The optical cavity mirrors were purchased from Los Gatos optics and all came from the same coating batch. They had a diameter of 1 inch and the highly reflective dielectric mirror coating was deposited on 5 mm thick ZnSe substrates. The specified radius of curvature was −500 mm, giving a focal length, f_{mirr}, of 250 mm.

The cavity length, L, was chosen to be close to 750 mm in order to fulfil several criteria, which Figure 4.17 graphically illustrates for possible values of L from 10 cm to 1 m. First, for the specified radii of curvature, a 750 mm cavity length is a stable geometric configuration (Equation 2.5). Second, as shown on the blue right-hand axis, the free spectral range is 200 MHz, resulting in an adequate

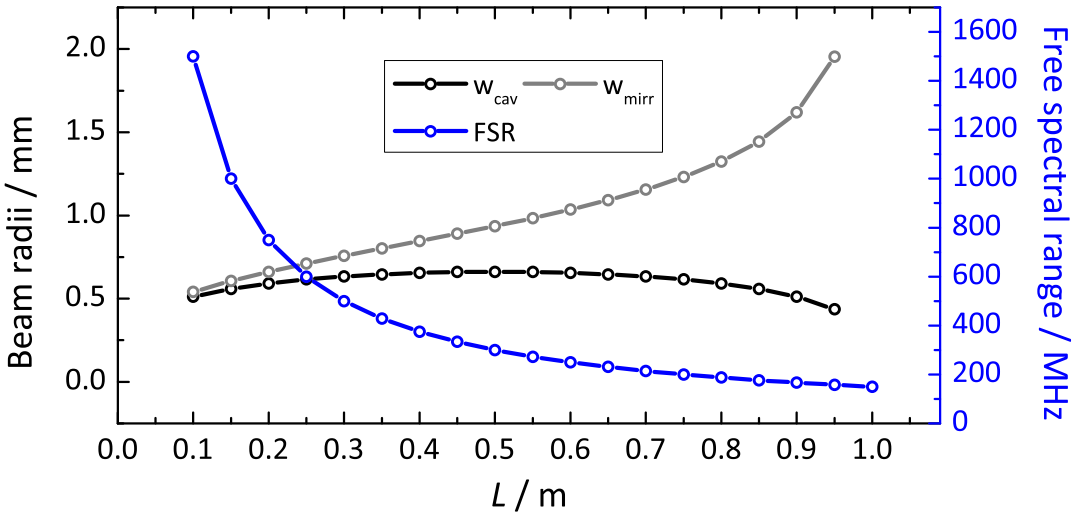

Figure 4.17: Beam radius on mirrors (grey, left-hand axis), beam waist (black left-hand axis), and cavity free spectral range (blue right-hand axis) as functions of L.

spectral sampling resolution for pressure broadened absorption profiles. Another consideration is the beam radius on the mirrors (w_{mirr}) and at the centre of the cavity (w_{cav}, the beam waist), shown on the black left-hand axis. For L equal to 750 mm, the beam radius on the mirrors is ~ 1.2 mm, i.e. about a tenth of the mirror surface, so diffraction loss is negligible. Finally, for a linear cavity, the OF-CEAS locking phase-matching criterion (Equation 4.9) mandates that the laser to cavity distance to be an integer multiple of L; this distance must also be long enough to allow room for the mode matching scheme.

4.6.4 Mode matching

The collimated QCL beam was mode matched to the optical cavity. This optimized both the coupling of the light into the cavity and also the reinjection of optical-feedback into the QCL gain medium. A simple scheme was devised, based on the approach of Self for the focusing of spherical Gaussian beams, where input and output Gaussian beam waists are images and objects of the focusing optic

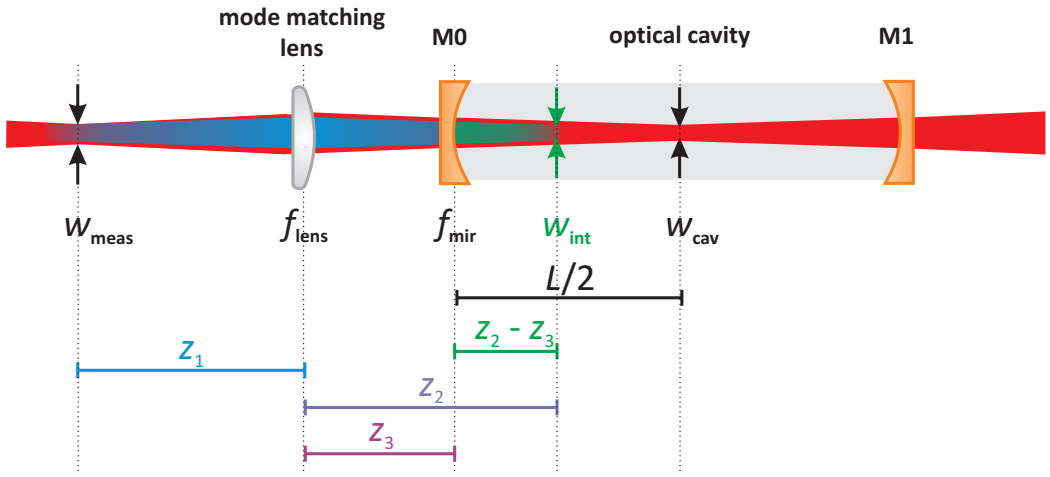

Figure 4.18: Schematic of the optics in the mode matching scheme, known parameters are labelled in black.

[187]. The Gaussian beam analogue of the geometric thin lens equation is

$$\frac{1}{f} = \frac{1}{z_{\text{obj}} + \left[(z_R/M^2)^2/(z_{\text{obj}} - f)\right]} + \frac{1}{z_{\text{img}}}, \tag{4.10}$$

where f is the focal length of the optic, z_{obj} is the object distance, z_{img} is the image distance, z_{R} is the Rayleigh range, and M^2 is the beam quality factor. The magnification is given by

$$\gamma = \frac{w_{\text{img}}}{w_{\text{obj}}} = \left[1 - [z_{\text{obj}}/f]^2 + \left[z_R/(M^2 f)\right]^2\right]^{-1/2}. \tag{4.11}$$

Figure 4.18 schematically illustrates the scheme: known parameters are labelled in black. The collimated QCL beam was focused by a off-axis parabolic mirror (OAPM) to a waist, w_{meas}, measured using the microbolometer array. Equation 2.19 was used to calculate the cavity beam waist, w_{cav}, which for the symmetrical linear cavity was $L/2$ from the surface of mirror M1. A lens of focal length f_{lens} was chosen to image w_{meas} into the cavity and form a waist at $L/2$. This corresponds to mode matching of the cavity TEM_{00} eigenmode.

Given the known parameters and using Equation 4.10, Equation 4.11 and the definition of z_{R} (Equation 2.9) for each optic in the mode matching system results

in a series of simultaneous equations that can be solved to determine z_1 and z_3. The details of this calculation are given in Appendix B.

A planoconvex CaF_2 with 150 mm focal length [Thorlabs] was chosen as the mode matching lens. This lens did not have an anti-reflection coating, because none was available for this off-the-shelf optic at 5 µm. The chosen off-axis parabolic mirror [Edmund Optics] had an effective focal length of 152.4 mm. The mode matching calculations for z_1 and z_3 were carried out separately for horizontal and vertical directions. These were averaged, then and adjusted to account for the optical distances in the mode matching lens and the first cavity mirror. The results of this calculation for the Maxion DFB-QCL setup are given in Table 4.2; the results for the Alpes DFB-QCL setup were similar.

Parameter / mm	$w_{\mathrm{meas},x}$	$w_{\mathrm{meas},y}$	w_{cav}	z_1	z_3
	0.178	0.163	0.590	250	167

Table 4.2: Mode matching parameters for Maxion DFB-QCL setup.

4.6.5 Beam quality factor

For the Alpes DFB-QCL, an attempt was made to calculate M_x^2 and M_y^2 from measured beam waists. Beam profiling was used to find w_{meas} and w_{int} and the magnification of the mode matching lens calculated. Then using Equation 4.11 and Equation 2.9, M^2 was calculated and found to be 1.2 ± 0.3 horizontally and 1.9 ± 0.6 vertically. The large errors are dominated by the difficulty in accurately locating the beam waist positions, as the beam waist was only around 5 pixels wide on the microbolometer array, and this process was not repeated for the Maxion laser.

4.6.6 Alignment

The path of the invisible mid-IR beam was marked by aligning two irises in the direct beam line (length c. 150 cm), along which the QCL was collimated. This

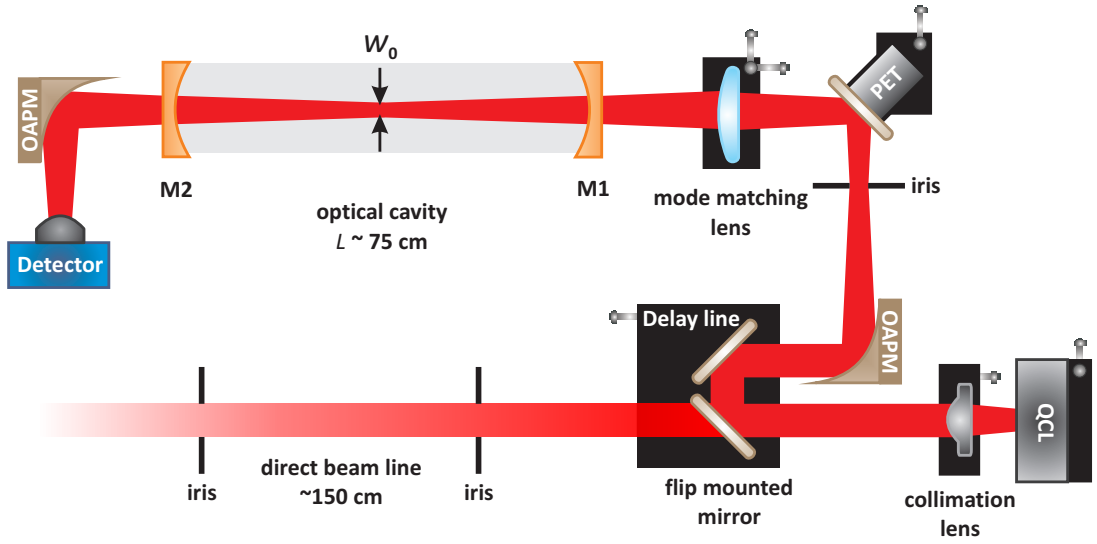

Figure 4.19: Schematic of the linear cavity QCL OF-CEAS optical setup, not to scale. OAPM is an off-axis parabolic mirror, PET is a piezoelectric transducer.

allowed a co-propagating red laser beam [HeNe] to be overlapped with the QCL beam to aid alignment. The optical setup is shown schematically in Figure 4.19. Two turning mirrors, the first mounted on a flip mount to maintain access to the direct beam line, were fixed to a translation stage to form a delay line. This enabled coarse tuning (c. ± 3 cm) of the laser-cavity distance. The focusing OAPM was aligned and, using the microbolometer array, the beam waist located and an iris placed at this position to act as a spatial filter. The turning mirror immediately before the cavity was fixed in a gimbal mount [Thorlabs, GM100] to decouple θ_x and θ_y adjustment, and on a translation stage in x, for effective adjustment of the injection angle of the beam into the cavity. The beam was aligned so that the axis of the optical cavity continued to follow a path referenced to the axes of the optical table.

The high finesse optical cavity was aligned by monitoring the red alignment laser. Reflections back to the alignment laser were made visible by fixing a white card to its front panel, with a pinhole through which the emitted beam passed. The mode matching lens, mounted on 3D micrometer adjusters, was inserted into the beam and aligned. The cavity mirrors were held in custom bellows assemblies

allowing two axis rotation. Mirror M_2 was inserted first and its position and angle adjusted to align the reflection back on to the incoming beam. Mirror M_1 was inserted second and aligned similarly. The diverging beam transmitted through M_2 was imaged on to the detector [VIGO, PVI-2TE-6] by an OAPM. The effective area of the detector was increased to 1 mm^2 by a hyperhemispherical immersion lens.

4.7 Active phase control

Active phase control of the optical-feedback was achieved through matching the laser to cavity distance to the length of the optical cavity on a wavelength scale. This was accomplished by mounting the turning mirror immediately before the optical cavity on a piezoelectric transducer (PET), the actuation of which was controlled by an error signal based on the phase-dependent cavity transmission peak asymmetry. The error signal was produced by a LabVIEW program.

The PET [Piezomechanik, HPSt 150/20-15/35] was a ring-actuator and had a total stack length of 40.5 mm. A custom high voltage amplifier supplied a control voltage, V_{PET}, to the PET. Described by Equation 4.12, V_{PET} comprised a variable DC offset, V_{DC}, with a manually adjustable range from 0 to nearly 10 V, and the error signal from the LabVIEW program, V_{lock}, which were both subject to a constant gain of 15:

$$V_{\mathrm{PET}} = 15\,[V_{\mathrm{DC}} + V_{\mathrm{lock}}]\,. \tag{4.12}$$

Hence, V_{PET} spanned a range 0 to 150 V, allowing displacements of the PET from 0 to 50 µm, i.e. up to ten times the laser wavelength.

To estimate the magnitude of the displacement required to correctly adjust the phase, a cavity transmission peak was monitored whilst V_{DC} was manually adjusted to correct its asymmetry. It was found that adjusting V_{DC} by about 1 V was sufficient. This is equivalent to a change in V_{PET} of 15 V and, by approxi-

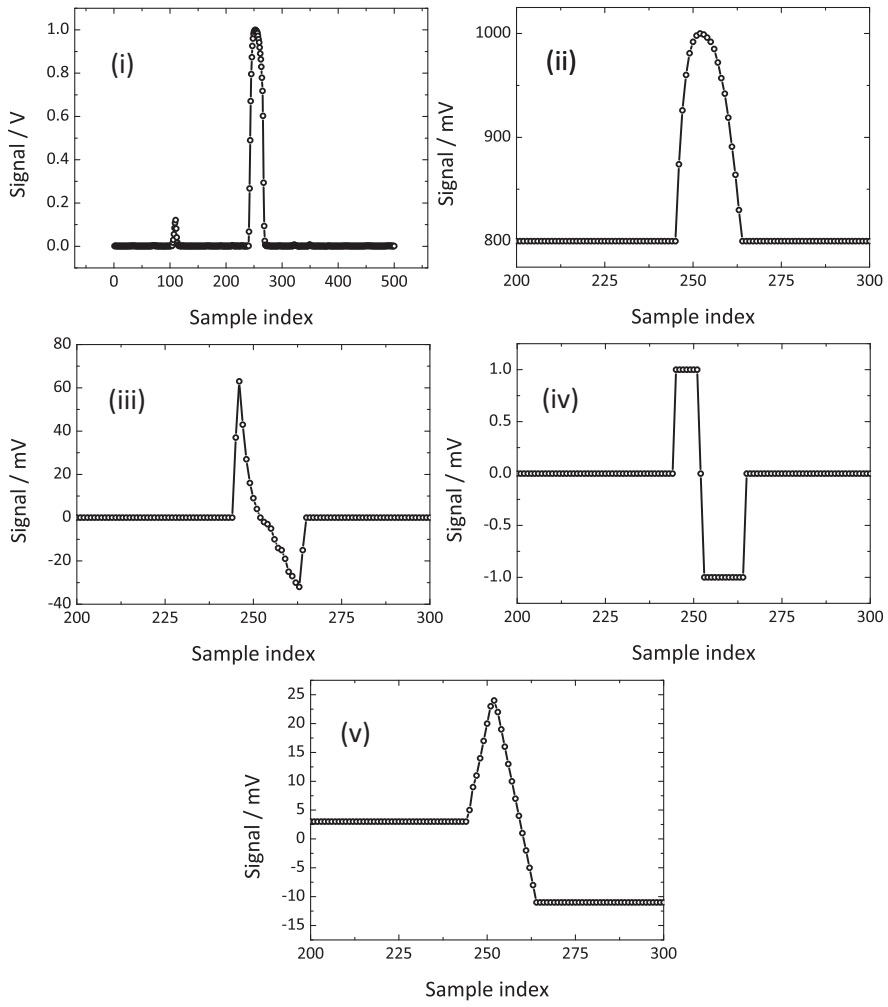

Figure 4.20: Locking scheme signals. The cavity transmission signal peak is: (i) normalized; (ii) clipped; (iii) differentiated; (iv) saturated; and (v) integrated, in order to produce an error signal.

mating the PET response as linear, corresponds to a displacement of around one wavelength (5 µm).

The cavity transmission signal was digitized by a PC card [National Instruments, DAQ card PCI-1610] and the analysis for the error signal performed by a PC running a custom LabVIEW program. The program was triggered by the TTL pulse accompanying the laser current ramp, so a correction voltage was generated and applied to move the PET once every scan, typically every 0.1 to 0.2 s. The vertical resolution of the card was 16-bit. The horizontal resolution was set to ensure adequate sampling (20 or more data-points) across cavity transmission

peaks.

Figure 4.20 shows how the asymmetry of a cavity transmission peak was analysed in order to produce an error signal. The cavity transmission signal over a whole up or down ramp was captured and then cut so that the program analysed 1 to 10 cavity transmission peaks. These were (i) normalized relative to the maximum intensity, to prevent the system responding to fluctuations in the mode height. The resulting signal was (ii) clipped so that only the top 20 % of the signal was analysed, as the asymmetry information is contained in this top part of the signal. Additionally, the lower part of the signal also contains lower intensity cavity transmission peaks corresponding to higher order cavity TEM_{mn} modes, to which the error signal should not respond.

The cleaned signal was subsequently (iii) differentiated and then (iv) saturated, prior to (v) integration to produce an error signal, similar to the method of Ohshima and Schnatz [188]. The mean value of the integrated signal over the sampling indices was then transformed into the correction voltage, V_{lock}. For cavity transmission signals taken from laser down ramps, a polarity correction (multiplication by -1) was applied. This accounted for whether the QCL was scanned from low to high frequency (on the up ramp) or vice-versa (the down ramp), as this results in an opposite phase change requiring the PET to be moved in the opposite direction. An appropriate gain was then applied, in order to produce a PET displacement of one wavelength or less. V_{lock} was applied to the PET via Equation 4.12.

4.8 Data acquisition

Data were acquired by the DAQ card and recorded for post processing and fitting. Two adjustments were found to be necessary for low noise acquisition. First, signals from the detector were acquired in differential mode, in order to reject common-mode voltages. Having made this change, it was necessary to exchange

the switched power supply that came with the detector for a linear power supply [PTCL Electronics]. This was found to be much less noisy.

4.9 The gas cell

The cavity mirrors formed the windows of the gas cell, and were held in bellows assemblies connected by a 1 inch diameter stainless steel tube. The bellows assemblies allowed limited and coupled x- and y-adjustment and each had a quarter inch stainless steel inlet or outlet tube welded to it.

The cell was evacuated by a rotary pump, and analyte and inert broadening gases added via quarter inch stainless steel tubing. An aerosol filter [Swagelok, SS-4FWS-05] fitted to the gas inlet blocked particles of diameter greater than 0.5 µm from entering the cell. A capacitance manometer (Leybold Vakuum, Ceravac CTR 90), working in the atmospheric range, was used to monitor pressure. This pressure meter was calibrated against a Hg-manometer.

4.10 Linear cavity OF-CEAS locking

The OF-CEAS locking scheme, first developed by Morville et al. [59] for a diode laser and already demonstrated for V-cavity QCL OF-CEAS [48, 49, 88], was found to work successfully when either the Alpes or the Maxion DFB-QCL was coupled to the linear cavity, as the following results demonstrate.

4.10.1 With the Alpes DFB-QCL

The three cavity output signals shown in Figure 4.21 were an early indication that OF-CEAS locking was working successfully with a linear cavity. All panels show an up- (0 to 100 ms) and a down-ramp (100 to 200 ms) of the symmetrical triangular current ramp supplied to the Alpes DFB-QCL, with an amplitude of 44.5 mA and a frequency of 5.15 Hz. This current scan tuned the laser frequency

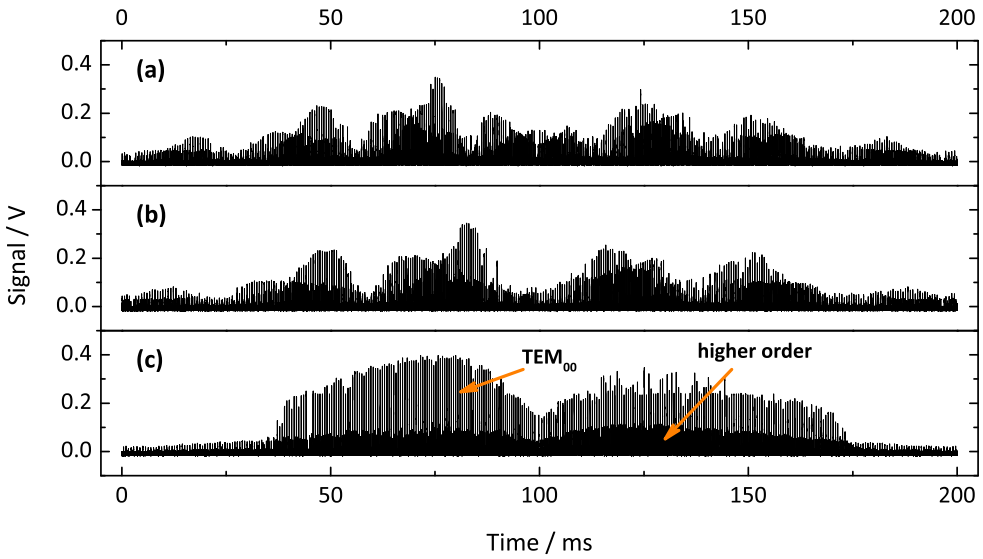

Figure 4.21: Early indication of successful optical-feedback response of the Alpes DFB-QCL coupled to the linear cavity. Panels (a) through (c) show the cavity output signal as the position of the optical delay line is optimized for phase matching at the laser facet.

over more than 100 longitudinal cavity modes, i.e. > 0.6 cm^{-1}. The traces show an OF-CEAS type cavity output signal that is far from optimized, but responded as expected to adjustment of the phase matching parameters, i.e. moving the delay line and the PET. At this stage in the development of the instrument, the optical cavity was not enclosed and was therefore open to lab air: for this reason, strong pressure broadened water absorptions significantly attenuated the signal.

Despite this interference, the cavity output signals in Figure 4.21 display fringing indicative of power modulation as the laser frequency locks to successive modes of the optical cavity. The optical-feedback phase dependence of the amplitude and symmetry of the power modulation peaks was investigated by scanning the position of the optical delay line and manually adjusting the position of the PET-mounted turning mirror. As expected, these parameters were very sensitive to changes in the laser-cavity distance, which determined the optical-feedback phase. From (a) through (c) the position of the delay line was optimized. All of the traces display locking to both TEM_{00} and higher order modes, as the cavity alignment and mode-matching were not optimized at this stage. The delay was

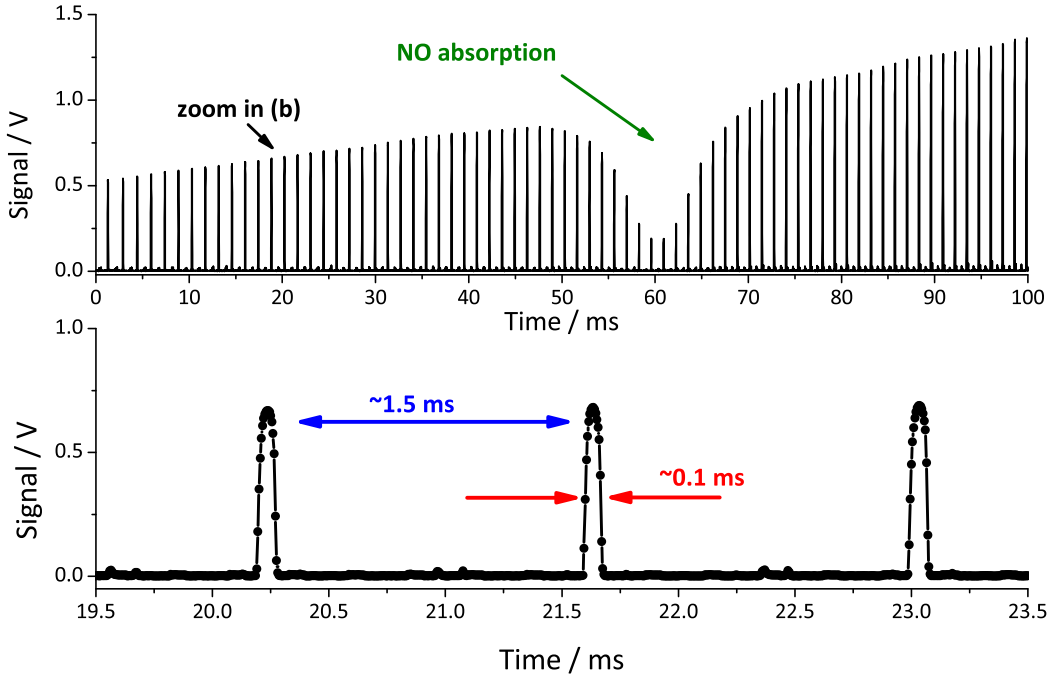

Figure 4.22: The fully optimized OF-CEAS cavity output signal acquired for (top) one up-ramp of the Alpes DFB-QCL, exhibiting absorption by NO, and (bottom) a magnification of this signal around 20 ms.

not well-positioned in (a) and (b), and this leads to a non-optimal optical-feedback phase causing these traces to display several beat-group envelopes of longitudinal modes for each transverse mode. The delay was optimally positioned in (c), and each transverse mode forms a single envelope of longitudinal modes.

Several further steps were taken to improve the cavity output signal and Figure 4.22 (a) shows the cavity output signal for the fully optimized instrument. The cavity alignment, including the mode-matching, was fine-tuned and locking to modes other than TEM_{00} was minimized. The optical cavity was enclosed in a gas cell, with the windows formed by the cavity mirrors. This allowed the intracavity medium to be evacuated by a rotary pump, reducing the water concentration from c. 1 % to a few hundred ppm, and enabled the observation of absorptions from analyte gas mixtures at pressures lower than atmospheric pressure. In this case, a trace amount of NO was let into the cell and broadened to

around 200 Torr by N_2 [BOC, Oxygen-free N_2]. Any effects from air currents in the intracavity medium would also have been reduced. The laser was scanned over an NO absorption profile by applying a linear current ramp of 20 mA with a frequency of 4.95 Hz; Figure 4.22 shows only the up-ramp.

For this optimized system, over the 100 ms of the up-ramp, the Alpes DFB-QCL is seen to lock to 60 successive longitudinal cavity modes leading to power modulation of the detected signal. This represents the typical maximum range of the laser frequency scan. Wider scans resulted in a reduction of the fraction of returned optical-feedback, as the laser frequency tuned more quickly, such that locking was not maintained. The peak-power increases as the QCL power increases over the course of the up-ramp. The magnified section in Figure 4.22 (b), demonstrates successful feedback locking to three successive modes. The locking time, estimated using the mode FWHM is 120 µs, much longer than the cavity ringdown time, τ_0. In the $\sim$ 1.5 ms spent between locking to cavity resonances, the cavity output signal is very small.

4.10.2 With the Maxion DFB-QCL

Figure 4.23 is the analogue of Figure 4.22 for the Maxion DFB-DL, and again shows successful optical-feedback locking. This laser could be operated over a wider range of currents, and therefore a more extensive linear current ramp covering a wider frequency scan could be applied than for the Alpes DFB-QCL. Additionally, the higher power of the laser meant that a sufficient locking range could be achieved with a scan rate double that applied to the injection current for the Alpes laser. The laser frequency was scanned over a pair of weak NO transitions, by a linear current ramp of 45 mA with a frequency of 10.0 Hz. Compared to the Alpes DFB-QCL, the FWHM of the power modulation peaks is widened (350 µs), with about the same time between locking events. The peak to peak time gap is around 0.6 ms. An increased frequency locking range is expected,

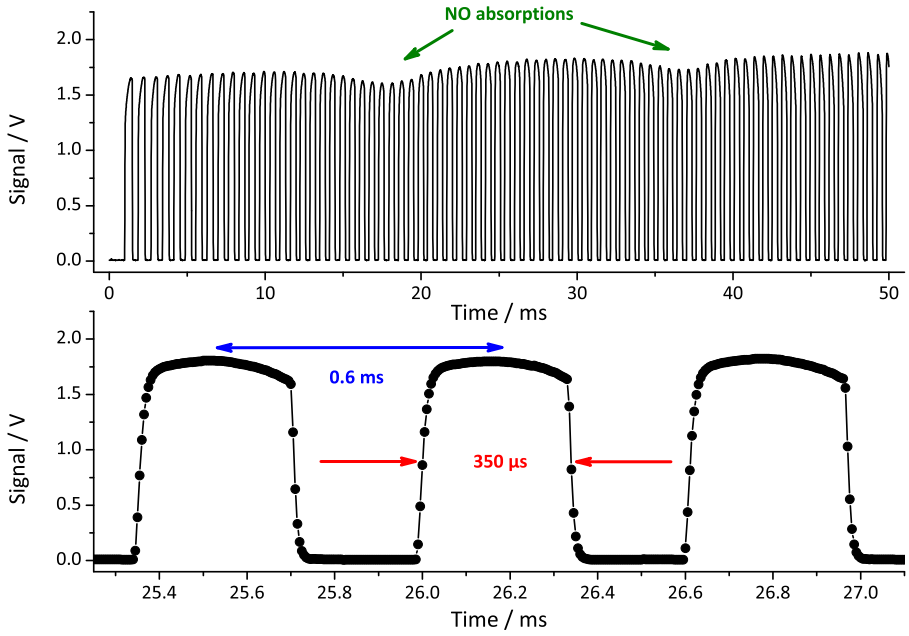

Figure 4.23: The fully optimized OF-CEAS cavity output signal acquired for (top) one up-ramp of the Maxion DFB-QCL, exhibiting weak absorptions by NO, and (bottom) a magnification of this signal around 26 ms.

as Equations 3.10 and 3.9 suggest the Maxion laser should be more sensitive to optical-feedback, due to its higher power output and (resulting) narrower intrinsic linewidth.

The low power output of the Alpes laser (~ 3 mW), further diminished by water absorption in the open-air beam path, precluded the use of a beam splitter. This was possible with the Maxion laser (~ 100 mW), and several interesting optical-feedback effects were investigated. First, fine adjustment of the optical cavity alignment was investigated for the Maxion DFB-QCL by simultaneously recording the temporal cavity output on the detector and the spatial output on the microbolometer array, using a wedged CaF_2 beam splitter. The results of this investigation are presented in Figure 4.24, where the order follows the experimental sequence from top to bottom. The contour plots share the same horizontal, vertical and normalized intensity scales. The ripple-effect on the contour plots arise from reflections between the camera window and the beam splitter at any point in the beam path. The line plots do not all represent cavity transmission

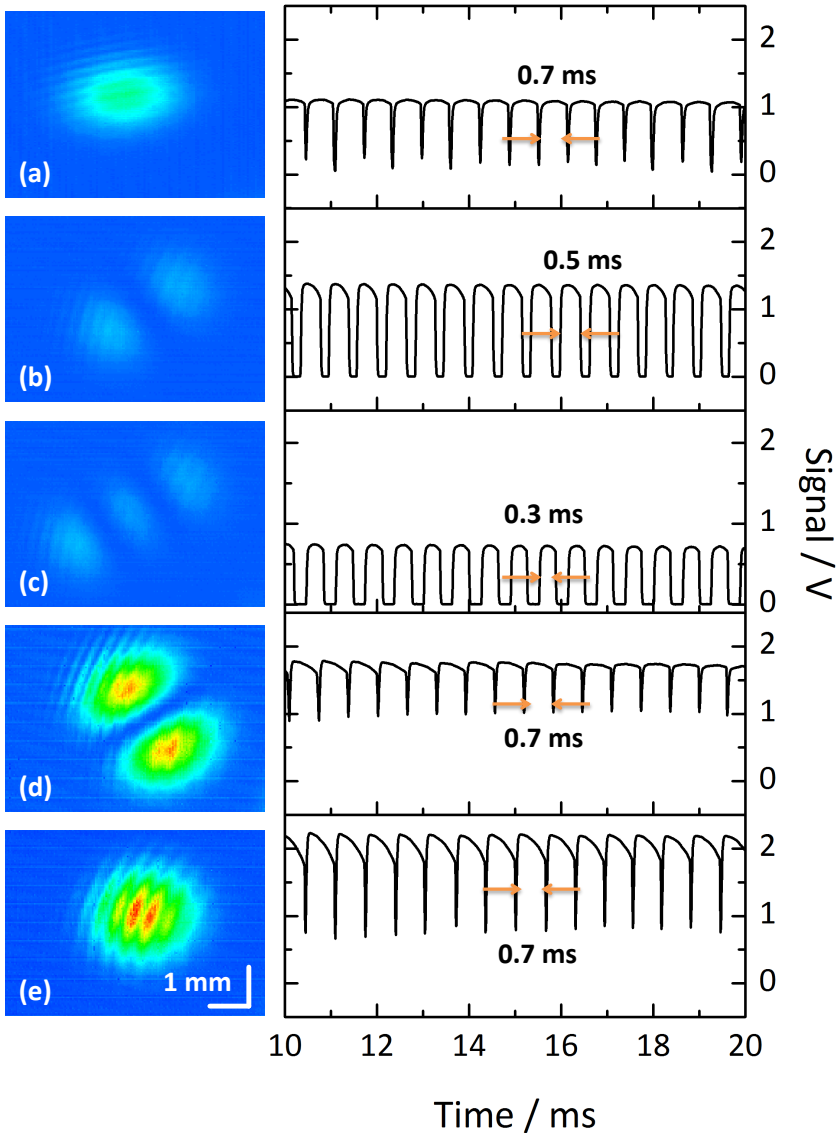

Figure 4.24: Simultaneous measurements of the temporal cavity output on the detector (line plots) and the spatial output on the microbolometer array (contours, all scales the same).

with optimal phase.

Having followed the coarse alignment procedure, contour plot (a) shows a major contribution from a TEM_{00} mode, though the low intensity and ellipticity of the image both suggest significant contributions from higher order modes. Micrometer adjustment of the beam injection into the cavity using the translation stage resulted in alignment to mostly higher order (b) TEM_{10} and (c) TEM_{20} modes. These appear to be rotated relative to the axes defined by the optical

table. Because the QCL chip, and consequently the QCL beam, the optical cavity axis, and the microbolometer array shared these axes, this suggests that the cavity mirrors introduced an astigmatism. Further evidence for this is that upon adjusting the tilt of the first cavity mirror between recording panels (c) and (d), this rotation 'flipped'. This effect has previously been observed for the spatial output of both near-IR [29] and mid-IR optical cavities [133] illuminated with diode and QCL sources respectively.

For the temporal cavity transmission on the detector, (a) through (c) show a decrease in laser locking period, estimated using the FWHM of the cavity transmission peaks, from 0.7 to 0.5 to 0.3 ms. This decreasing series follows an expected decrease in the fraction of returned power, f_{ext}, as the mode order increases and therefore the transverse spatial extent of the mode increases.

Panel (d) shows alignment to an intense TEM_{10} mode and (e) the final alignment to an intense TEM_{00} mode. Compared to (a), (e) is much more intense and circular, suggesting a much higher proportion of TEM_{00} character. For both of these modes the locking period correspondingly increases back to 0.7 ms, due to the predominant alignment to low order modes and greater f_{ext}. It is perhaps surprising that there is not a large difference between these two modes, because the TEM_{10} mode has a node at its centre. When using the Maxion QCL, sometimes extremely good alignments were realized that resulted in very high levels of optical-feedback returning to the laser, such that the required $\Delta\nu_{\mathrm{FSR}}$ locking range was exceeded. The attenuation of the beam by the CaF_2 beamsplitter was found to be adequate to reduce the locking range.

4.11 QCL threshold current reduction by optical-feedback

Lasing action of a semiconductor laser occurs when photon gain exceeds photon loss during a laser cavity round trip. This happens when the rate of photon production, by either spontaneous or stimulated emission, is faster than the photon loss rate, by waveguide absorption or transmission through the laser facets. The laser threshold current, I_{Th}, is the injection current at which this condition is fulfilled. Injection seeding by optical-feedback increases the photon number density in the gain medium, and causes further stimulated emission, thereby reducing the laser threshold current.

Osmundsen and Gade [189] have derived Equation 4.13, to describe the optical-feedback reduced laser threshold, $I_{\mathrm{OF,Th}}$, in terms of the laser longitudinal mode spacing, $\Delta\nu_{\mathrm{las}}$, the photon lifetime in the laser gain medium, τ_{p}, the reflectivity of the laser facets, R_{las}, and the attenuation coefficient of the optical-feedback, α:

$$I_{\mathrm{OF,Th}} = I_{\mathrm{Th}} \left\{ 1 + 2\Delta\nu_{\mathrm{las}}\tau_{\mathrm{p}} \ln \left[\sqrt{R_{\mathrm{las}}} \left(\frac{1 + \sqrt{R_{\mathrm{las}}}\sqrt{\alpha}}{\sqrt{R_{\mathrm{las}}} + \sqrt{\alpha}} \right) \right] \right\}. \tag{4.13}$$

This equation was based on a steady state approximation of optical-feedback returning from an external reflector to a diode laser, and as multiple reflections were considered, it should be a good approximation for the coupled optical cavity case.

Hamilton made an experimental observation of this effect, using a 7.8 µm Alpes DFB-QCL coupled to a V-shaped optical cavity, optimally arranged for an OF-CEAS experiment [98]. A short linear current ramp was applied to the laser, with the current initially below threshold, and the laser output power was monitored simultaneously with the output of the optical cavity. Below threshold, no laser light was incident on the detector except at optical cavity resonant frequencies, where a significant power enhancement was observed, due to optical-feedback

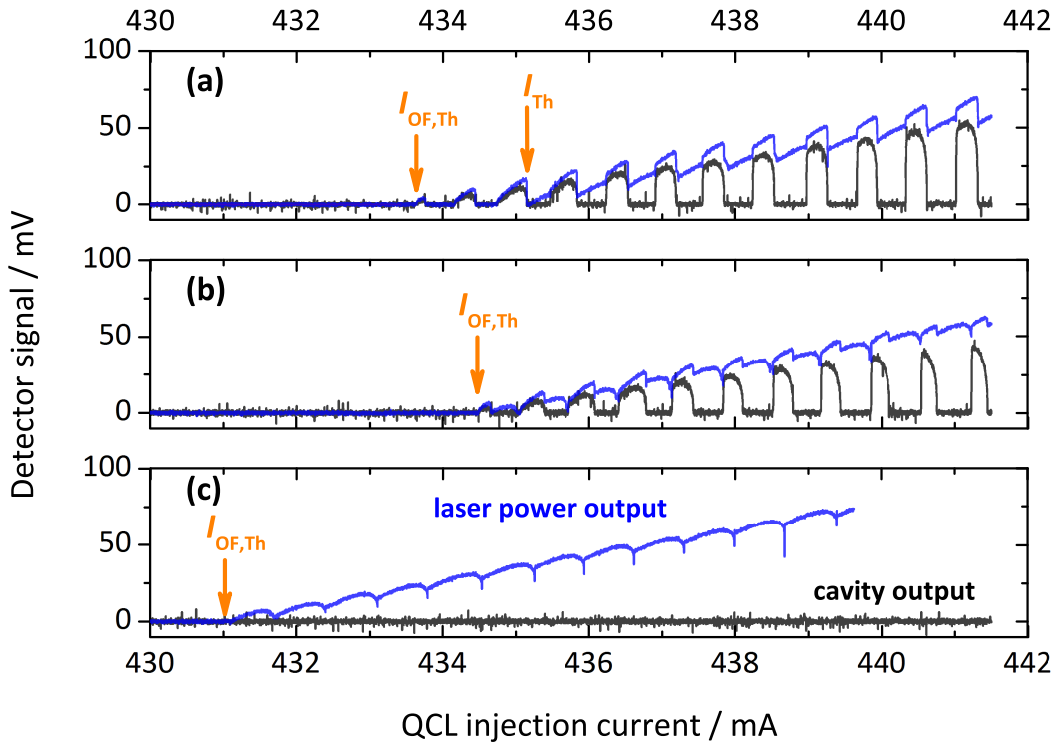

Figure 4.25: Optical-feedback threshold current reduction investigation: (a) fully optimized alignment and optical-feedback phase with annotation showing the threshold current reduction; (b) after phase detuning; (c) after altering the injection angle.

from the V-cavity lowering the threshold current by around 3 mA.

A similar experiment was performed with the Maxion DFB-QCL coupled to the linear cavity, and the results are presented in Figure 4.25. The beam was divided with a beam splitter in the path to the laser, and the laser power output signal (blue) monitored on a second detector [VIGO, PVMI-10.6], simultaneously with the cavity output signal (black). The analogous result to Hamilton's is shown in Figure 4.25 (a), and is commensurate with his results, with the laser displaying a (slightly smaller) threshold reduction from 435 mA of around 2 mA when on resonance with the cavity modes . To obtain this result, the cavity alignment and the optical-feedback phase were both optimized.

Three other cases were also investigated: blocking the optical cavity, altering the angle of injection of the beam into the cavity, and detuning the optical-feedback phase. With a beam block between the first cavity mirror and the laser,

no significant optical-feedback injection seeded the QCL gain medium, and no threshold current reduction was observed. A very minimal adjustment of the injection angle (moving the translation stage by a few µm) resulted in a non-optimal cavity alignment and no cavity output signal was observed Figure 4.25 (c). Despite this, the laser output power signal displays an even more marked threshold reduction (almost 4 mA), and power modulations. Estimating the frequency scale of trace (c) by the cavity fringes in (a), the free spectral range is almost the same. This suggests that this trace displays the effect of optical-feedback from the direct back reflection from the first cavity mirror surface, which forms an effective optical cavity with the laser facet, as previously documented by [184]. The further decrease in threshold compared to the cavity coupled case is likely due to the increased optical-feedback (i.e. f_{ext}), given the very high reflectivity of the cavity mirror.

This is confirmed by Figure 4.25 (b), where although the cavity was optimally aligned, the optical-feedback phase was slightly detuned by manually adjusting the position of the PET. This is evidenced by the asymmetry of the cavity output signal power modulation peaks. Here the laser power output signal follows (a) when on resonance with the cavity modes, and instead follows a behaviour similar to (c) in between. From this investigation, it is clear that when the linear optical cavity is optimally aligned, and the optical-feedback phase correctly adjusted for injection seeding by the cavity reflected field, the behaviour of the QCL is not significantly affected by optical-feedback from the direct back reflection off the first cavity mirror.

4.12 Summary

This chapter has demonstrated the viability of linear cavity QCL OF-CEAS locking, without suppression of the direct back-reflection from the dielectric coating of the first cavity mirror. These results have been explained by arguing that

QCLs are frequency stable to "strong" optical-feedback regimes, and that the phase matching criterion cannot simultaneously be met for both the cavity reflected and direct back-reflected fields. Full development of the linear cavity OF-CEAS instrument was presented, including tests to determine the performance of a custom low noise current driver for QCLs against the commercial alternative. Active phase control of the optical-feedback was implemented, based on a LabVIEW program controlling the position of a PET. Successful OF-CEAS locking was demonstrated for both the Alpes and Maxion DFB-QCLs, which had different characteristics, most notably a factor of 30 difference in operating power. The next chapter presents spectroscopy results using the linear cavity QCL OF-CEAS instrument.

Chapter 5

Mid-IR Linear Cavity QCL OF-CEAS

This chapter presents the spectroscopic results of the linear cavity OF-CEAS instrument, obtained by analysing both the Alpes and Maxion DFB-QCL OF-CEAS transmission spectra, some of which were presented in the previous chapter. The results in Sections 5.2.2 and 5.2.3 were published as [89]. Some attempts at optimizing the linear cavity QCL OF-CEAS instrument are also described.

5.1 Data acquisition and analysis

The DFB-QCLs were scanned over transitions of interest by applying a symmetrical triangular current ramp. Data were acquired by the DAQ card (described in Section 4.7) and recorded for post processing and fitting. Frequency-calibrated transmission spectra were obtained from the cavity output signal by identification of the transmission maxima, $I(\nu)$, the positions of which were mapped on to a relative frequency scale, ν, defined by the $\Delta\nu_{\mathrm{FSR}}$ of the cavity. A global fitting routine was used, based on the approach described in [190]. This routine had the major advantage of including multiple absorption lineshapes in the fit, which enabled the analysis of multi-component mixtures. This is particularly impor-

tant in this spectral region (5.2 to 5.5 µm) where there are many strong water absorptions.

5.1.1 Fitting routine

The fitting algorithm builds a forward model, $F(\mathbf{x})$, representing the expected signal recorded by the OF-CEAS instrument. $F(\mathbf{x})$ is constructed from known experimental parameters (the cavity length, the total pressure, and the calibrated mirror reflectivity) and spectral information (line position, intensity, pressure broadening, and parameter temperature dependence) from the HITRAN database [9]. The state vector $\mathbf{x}$ represents the retrieved fitting parameters (either mirror reflectivity or concentration, frequency shift, baseline slope and offset). These are related to the measurement vector, $\mathbf{y}$, representing the measured data (i.e. the spectrum), and the error associated with the uncertainty in the measurements, ϵ:

$$\mathbf{y} = F(\mathbf{x}) + \epsilon. \tag{5.1}$$

Retrieval of $\mathbf{x}$ such that the forward model accurately describes $\mathbf{y}$ is performed by an optimal estimation that minimizes χ^2:

$$\chi^2 = [\mathbf{y} - F(\mathbf{x}_n)]\mathbf{S}_\epsilon^{-1}[\mathbf{y} - F(\mathbf{x}_n)]^{\mathrm{T}} + [\mathbf{x}_a - \mathbf{x}_n]\mathbf{S}_a^{-1}[\mathbf{x}_a - \mathbf{x}_n]^{\mathrm{T}}. \tag{5.2}$$

This optimization is an iterative process for various solutions $\mathbf{x}_n$. Each step locally linearizes the outcome and converges to a point where χ^2 reaches a minimum, by reducing the quadratic spread between the measurement vector, $\mathbf{y}$, and the forward model with solutions $\mathbf{x}_n$, weighted by the uncertainty in the measurements $\mathbf{S}_\epsilon$. This is further constrained by minimizing the difference between the solutions $\mathbf{x}_n$ and a set of a priori values $\mathbf{x}_a$, weighted by the errors on these a priori values, $\mathbf{S}_a$. The optimization works within the assumption that the uncertainty in the parameters have a normal distribution and was developed by Rodgers [191].

The fitting routine was programmed to return: the concentration or concentrations of single analytes or mixtures; a frequency shift accounting for small differences between the assigned and fitted frequency scales; and the parameters for a linear or quadratic baseline, accounting for constant transmission losses and the power modulation of the QCL during frequency tuning. Laser power attenuation due to intracavity absorption reduced optical-feedback [88] was found to be negligible ($\ll 1\%$), so no correction was made for this effect. Molecular absorption lineshapes were modelled as Voigt profiles.

5.1.2 Absorption coefficient from transmission spectra

As for the V-shaped cavity, the relationship between the absorption coefficient, $\alpha(\nu)$, the mirror reflectivity, R, and the ratio of the transmission of a linear cavity with, I, and without absorbing losses, I_0, is given by Equation 3.31, and this was used for the model. The validity of this expression for linear cavity OF-CEAS is not immediately obvious. The derivation now given for a linear cavity follows that of [48, 90]. The ratio of the transfer functions for a linear cavity without (Equation 2.41) and with (Equation 2.44) an absorber present is:

$$\frac{I_0}{I} = \frac{(1 - R\exp[-\alpha(\nu)L])^2}{(1-R)^2\exp[-\alpha(\nu)L]}. \tag{5.3}$$

By re-arranging Equation 2.50 to give $R \approx \exp[-L/c\tau_0]$, and substituting this into Equation 5.3 leads to:

$$\frac{I_0}{I} = \frac{(1 - \exp[-L/c\tau_0]\exp[-\alpha(\nu)L])^2}{(1-\exp[-L/c\tau_0])^2\exp[-\alpha(\nu)L]}. \tag{5.4}$$

Within the limit of small absorption, $\exp[-\alpha(\nu)L] \approx 1$ in the denominator, yielding:

$$\frac{I_0}{I} = \frac{(1 - \exp[-L/c\tau_0]\exp[-\alpha(\nu)L])^2}{(1-\exp[-L/c\tau_0])^2}. \tag{5.5}$$

Re-arranging this expression and taking the natural logarithm to make $\alpha(\nu)L$ the subject gives:

$$-\alpha(\nu)L = (L/c\tau_0) + \ln\left\{1 - \sqrt{\frac{I_0}{I}}\,(1 - \exp[-L/c\tau_0])\right\}, \tag{5.6}$$

which may be further simplified using the approximation:

$$\ln\left\{1 - \sqrt{\frac{I_0}{I}}\,(1 - \exp[-L/c\tau_0])\right\} \approx -\frac{L}{c\tau_0}\sqrt{\frac{I_0}{I}}. \tag{5.7}$$

Re-arranging yields an expression for the absorption coefficient in terms of τ_0:

$$\alpha(\nu) = \frac{1}{c\tau_0}\left(\sqrt{\frac{I_0}{I}} - 1\right), \tag{5.8}$$

which may also be expressed in terms of the mirror reflectivity R, by using Equation 2.50:

$$\alpha(\nu) = \frac{(1-R)}{L}\left(\sqrt{\frac{I_0}{I}} - 1\right). \tag{5.9}$$

Equation 5.9 is simply a rearrangement of Equation 3.31. This derivation has shown that the relation between $\alpha(\nu)$, and the measured cavity parameters is the same as that for a V-shaped cavity, because τ_0 is the same for linear and V-shaped cavities with the same arm length, i.e. L see Figure 2.5. Alternatively, the linear cavity may be considered as a V-cavity in the limit where than angle between the arms tends to zero.

Given the assumptions in the derivation, Equation 3.31 is an approximation in the limit of small $\alpha(\nu)$. The validity domain of Equation 3.31 was therefore tested. For this work, the maximum values of $\alpha(\nu)$ were on the order of 1×10^{-5} cm^{-1}, and comparison of Equation 3.31 with the exact expression (Equation 5.3) resulted in an overestimation of 0.1 %.

5.2 Linear cavity OF-CEAS with the Alpes DFB-QCL

Spectroscopic measurements of H_2O, N_2O, and NO were undertaken using linear cavity OF-CEAS with the Alpes DFB-QCL. The laser was scanned over transitions of interest by applying a symmetrical triangular current ramp of c. 20 mA with a frequency of c. 5 Hz, corresponding to scanning over 60 to 80 cavity modes.

5.2.1 Spectroscopy of H_2O and N_2O isotopologues

One of the first examples of a spectrum recorded using the linear cavity OF-CEAS instrument is depicted in Figure 5.1, this shows a single transmission spectrum recorded in 0.2 s. The gas mix comprised a calibrated 2 % mix of N_2O in N_2 [CK Gas], diluted to 2.42 ± 0.02 ‰ with further N_2 [BOC, Oxygen-free nitrogen]. Additionally, the mix also contained H_2O, from molecules desorbing from the cell walls and from the dilutant N_2 which was not dried. Studied at a total pressure of 0.423 atm, this mix resulted in pressure broadened absorption lineshapes covering several $\Delta\nu_{\mathrm{FSR}}$ of the cavity.

None of the absorptions visible in Figure 5.1 are due to the primary isotopologue of the absorbing molecule: absorptions A and C arise from transitions in

Label	Isotope	Position / cm^{-1}	S $\mathrm{cm}^{-1}/(\mathrm{molec\ cm}^{-2})$	Transition
A	$H_2{}^{18}O$	1821.834	1.047×10^{-22}	(532) ← (423) in (010) ← (000)
B	$N_2{}^{18}O$	1821.971	4.234×10^{-25}	$P(22)e$ in (110) ← (000)
C	$H_2{}^{18}O$	1822.094	3.399×10^{-23}	(523) ← (414) in (010) ← (000)

Table 5.1: Line-by-line HITRAN data for H_2O and N_2O isotopologue transitions in Figure 5.1 [9]. Quantum numbers for H_2O are $(J'', K_a'', K_c'') \leftarrow (J', K_a', K_c')$, where K_a and K_c are projections of the total angular momentum, J, on the a- and c-molecular rotational axes in the upper (double prime) and lower states (single prime), and then by (v_1, v_2, v_3), where v_1 is the vibrational quanta in the symmetric stretch, v_2 the number in the bend, and v_3 the number in the asymmetric stretch.

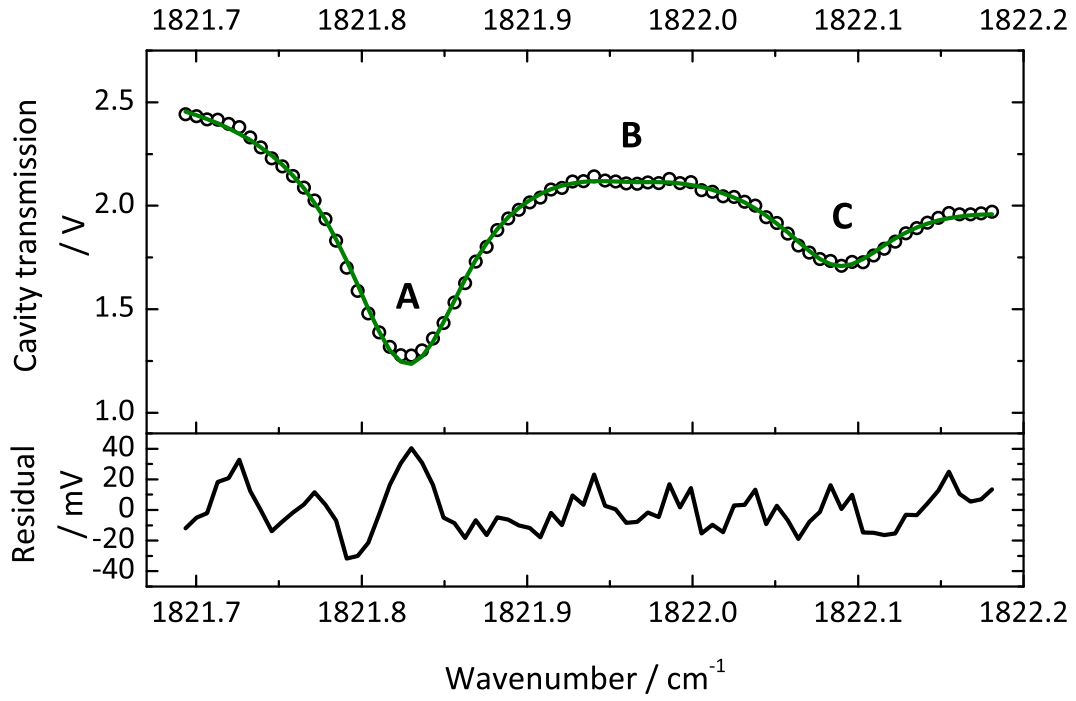

Figure 5.1: Linear cavity OF-CEAS transmission spectrum of $H_2{}^{18}O$ (A and C) and $N_2{}^{18}O$ (B), showing experimental data (dots), fitted model (solid lines), and residual (lower plots).

the in the fundamental bending mode of the $H_2{}^{18}O$ water isotopologue, while absorption B is the $P(22)e$ transition in the (110) $\leftarrow$ (000) combination band of $N_2{}^{18}O$. The HITRAN-listed positions and intensities of these lines are given in Table 5.1.

The mirror reflectivity, R, was calibrated by recording several hundred ring-down measurements, and the fitting routine was programmed to return the concentrations of H_2O and N_2O, the frequency shift, and linear baseline offset and slope ($I_0 = a + b(\nu)$). However, there was a discrepancy between the expected (2.42 ± 0.02 ‰) and retrieved concentration (1.45 ± 0.03 ‰) of N_2O. Instead, the expected concentration was used to recalibrate the mirror reflectivity. This lead to a mirror reflectivity of 99.90 ± 0.01, and a corrected residual water concentration of 570 ± 5ppm.

By Equation 3.31, the sensitivity as defined by $\alpha_{\min}$ for this spectrum was

3.2×10^{-8} cm^{-1} in 1 s, limited by etalon fringing clearly visible on the residual in Figure 5.1. There is also a marked W-shaped residual over the middle of H_2O absorption A. This shape is characteristic of collisionally narrowed lineshapes. This effect is expected for H_2O, where the wide spacing of rotational energy levels (c. 300 cm^{-1}) inhibits collisional broadening [192], and there is experimental evidence of collisional narrowing for H_2O at these pressures in this region [193]. However, the large number of fitting parameters required for this multi-species spectrum precluded further investigation of more appropriate spectral lineshapes. Nonetheless, this spectrum demonstrates the ability of the linear cavity OF-CEAS instrument to probe the weaker absorptions associated with non-primary isotopologues.

5.2.2 Spectroscopy of N_2O

Figure 5.2 shows an example transmission spectrum of an N_2O absorption, again from a single scan recorded in ~ 0.2 s. The N_2O absorption comprised 3 unresolved transitions with a combined intensity of 2.3×10^{-24} cm^{-1}/(molec cm^{-2}) at 296 K, which are given in Table 5.2. In order to obtain a pressure broadened absorption lineshape, covering around 10 cavity $\Delta\nu_{\mathrm{FSR}}$, a total pressure of 0.28 atm of a 1.8 ± 0.1 % N_2O in N_2 gas mix was used. This mix was again formed by further dilution of the calibrated mix mentioned in the previous section. Again, the mirror reflectivity was calibrated based on the N_2O concentration of the gas mix. This yielded a mirror reflectivity, R, of 99.931 ± 0.006 %, where the error corresponds to estimates of the uncertainties in the mixture calibration, pressure measurement and data fitting, and is consistent with the manufacturer's specified value. In particular, given the high J-states of the N_2O transitions, uncertainty resulting from how well the temperature was known was high. The corresponding noise-equivalent absorption coefficient, α_{min}, was 2.7×10^{-8} cm^{-1} for 1 s averaging by Equation 1.18.

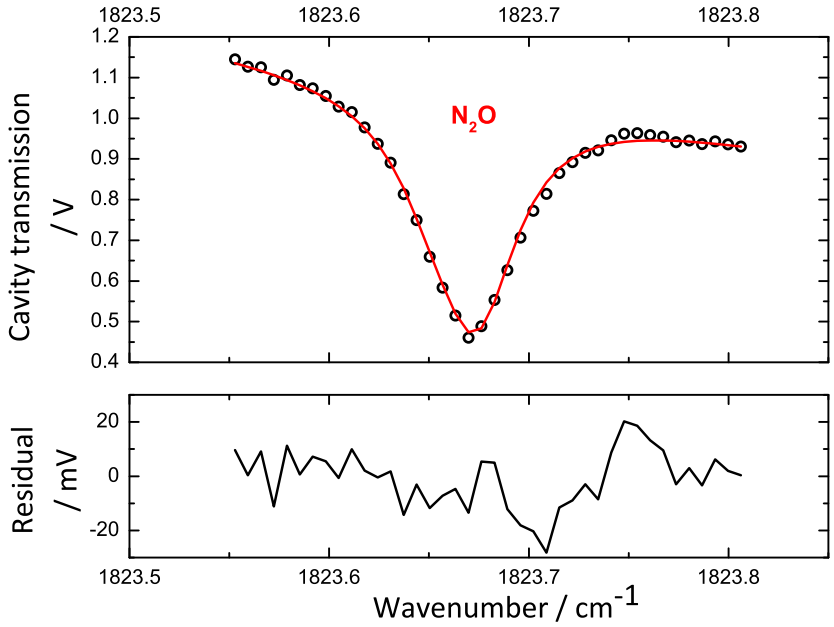

Figure 5.2: Linear cavity OF-CEAS transmission spectrum of N_2O, showing experimental data (dots), fitted models (solid lines), and residuals (lower plots).

Isotope	Position / cm^{-1}	S / $cm^{-1}/(molec\ cm^{-2})$	Transition
$^{14}N_2{}^{18}O$	1823.652	4.4×10^{-25}	$P(20)e$ in (110) ← (000)
$^{14}N_2{}^{16}O$	1823.670	1.6×10^{-24}	$P(61)e$ in (110) ← (000)
$^{14}N_2{}^{16}O$	1823.675	2.9×10^{-25}	$P(55)e$ in (120) ← (010)

Table 5.2: The N_2O transitions comprising the absorption in Figure 5.2

5.2.3 Spectroscopy of NO

Figure 5.3 shows a spectrum of the unresolved Λ-doublet of the $P(14.5)$ transition in the $v = 1 \leftarrow 0$ band of NO. The combined intensity of the transitions contributing to this absorption is 5.5×10^{-20} $cm^{-1}/(molec\ cm^{-2})$ at 296 K. The markedly decreasing baseline is due to the wing of an intense H_2O transition 3.8×10^{-20} $cm^{-1}/(molecule\ cm^{-2})$ centered at 1825.20 cm^{-1}, around 1 cm^{-1} from the centre of the NO transition. The spectrum, came from a single scan recorded in ∼ 0.2 s, with trace NO in the cell broadened by N_2 to 0.19 atm. The α_{min} was 2.4×10^{-8} cm^{-1} (1 s), in close agreement with that obtained for N_2O.

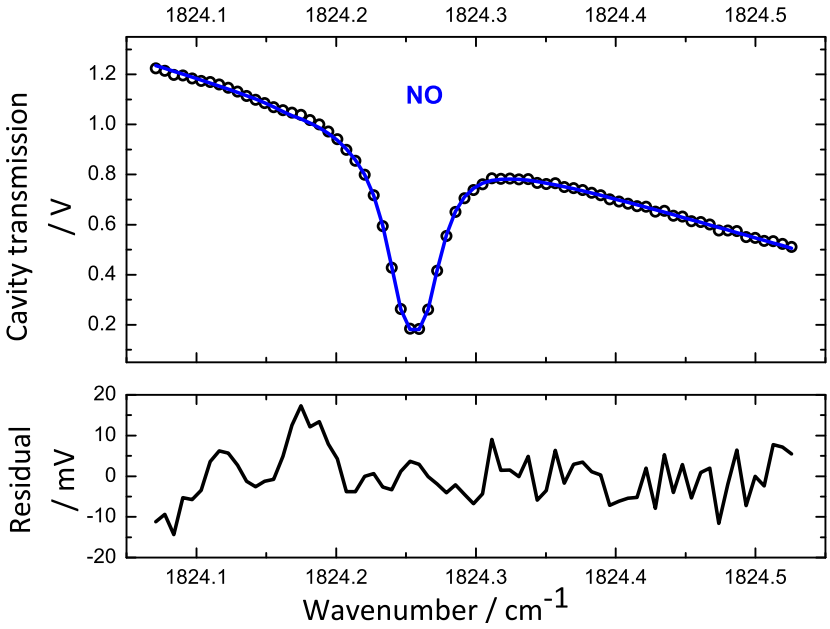

Figure 5.3: Linear cavity OF-CEAS transmission spectrum of NO, showing experimental data (dots), fitted models (solid lines), and residuals (lower plots).

5.2.4 Sensitivity

The noise equivalent power of the detector was 2.9 nW, calculated using Equation 1.17 given a specified detectivity of 3.5×10^9 cm $Hz^{1/2}$ W^{-1} at 5.5 µm, an effective area of 0.1 cm^2, and a sampling bandwidth of 10 kHz. The specified responsivity was 9430 $V\,W^{-1}$ and therefore the noise equivalent voltage was 0.03 mV. The bit noise on the acquisition system was measured, and found to be five times larger (0.15 mV) and therefore represented the detection limit of the system. The bit noise equivalent α_{min} is 5.1×10^{-9} cm^{-1} in 1 s, indicating that nearly a factor of five could be gained in sensitivity, by use of an appropriate low-noise amplifier. For the spectra presented in Figures 5.1, 5.2 and 5.3 the minimum detectable absorption coefficient was limited by etalon fringes on the transmission signal, causing a sinusoidal baseline variation. This effect is attributable to reflections between the immersion lens on the detector and the exit cavity mirror, further investigated in Section 5.3.3.

With the caveats discussed in Section 1.6, the sensitivities obtained can be

compared with those of the previously reported V-cavity QCL OF-CEAS instruments, using the $\alpha_{\min}$. Hamilton and Orr-Ewing [48] reported an $\alpha_{\min}$ of 5.5×10^{-8} cm^{-1} in 1 s, with a mirror reflectivity of 0.999652(4) at 7.8 µm. The existing results of the linear cavity setup already represent better sensitivity than this, despite a lower mirror reflectivity. The best reported QCL OF-CEAS sensitivity was recently obtained by Gorrotxategi-Carbajo et al. [49], and was 1.6×10^{-9} cm^{-1} in 1 s with a mirror reflectivity of 0.9998 at 5.6 µm, and a fitting routine including a sinusoidal baseline to account for etalons arising within the cavity mirror substrates. With equivalent mirrors, which could certainly be obtained from LohnStar Optics given the overlap of the spectral regions of this work and [49], the $\alpha_{\min}$ obtained in this work would be improved to 6×10^{-9} cm^{-1} (1 s). Hamilton and Orr-Ewing also obtained their mirrors from LohnStar, who specialize in coating mid-IR optics and may therefore produce higher quality coatings than Los Gatos. No QCL OF-CEAS instrument has yet reached the same level of sensitivity ($\alpha_{\min}$ of 3×10^{-10} cm^{-1} in 1 s) as the best near-IR instrument [117], because the higher quality of available mirror coatings in the near-IR typically results in $R > 0.9999$.

5.2.5 Temporal stability

The temporal stability of the linear cavity OF-CEAS instrument was also investigated. Overlapping Allan variance calculations [51] were carried out on concentration time series, with a total duration of 200 s derived from $\sim$ 1000 spectra of the same analyte gas mixture sampled at 0.2 s intervals. Figure 5.4 shows log-log plots of the Allan variance (left) and deviation (right) for monitoring N_2O from Section 5.2.1 (green) and Section 5.2.2 (red), and NO from Section 5.2.3. A typical optimal averaging period was 2 s as shown for the top Allan plot for N_2O (red) and NO (blue). This typical performance is inferior to those reported by both Hamilton (200 s) [48], and Gorrotxategi-Carbajo et al. (12 s, on formalde-

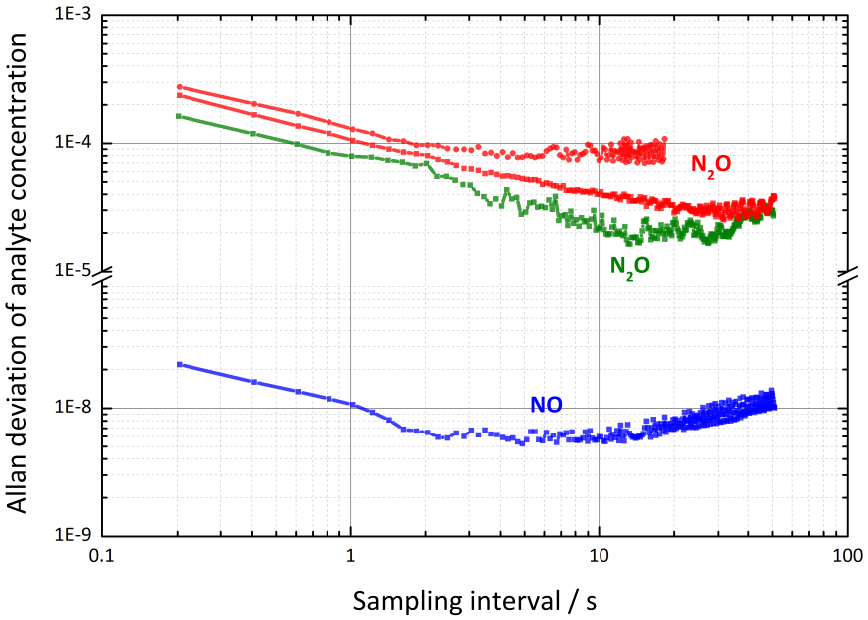

Figure 5.4: Log-log Allan deviation plots for returned concentration of N_2O (green squares and red circles), and NO (blue triangles).

hyde) [49]. However, on occasion the system was stable enough to average for 10 s N_2O (green) or 35 s, as evidenced by the lower Allan plot for N_2O (red). The concentration time series used to produce the red N_2O traces come from two measurement series performed one after the other on the same gas sample, and experimental investigations into the source of this effect are presented in Section 5.2.5. The Allan variance plots all have initial gradients close to -1 indicating white noise behavior. From the Allan variance minima, the best minimum detectable concentrations for the linear QCL OF-CEAS instrument are 32 ppm for N_2O (35 s) and 5 ppb for NO (2 s). (The accuracy of concentration retrieval was better for the red N_2O trace as there was a single absorption to fit. Hence this is taken as the minimum detectable concentration, as opposed to the green N_2O trace where multiple lines were fitted.)

The detection limit for N_2O is reported to quantify instrument stability. N_2O is a greenhouse gas and is also implicated as an ozone-layer depleter [194]. As such, it has already been the subject of detection for two of the three other reported OF-CEAS spectrometers. The instrument developed by Hamilton and

Orr-Ewing obtained a minimum detectable concentration of 2 ppb for N_2O, measuring a transition in the band corresponding to the symmetric stretch ($P(12)$ in 1_0^1), with an intensity ten thousand times greater than the overtone and combination bands it was possible to probe in this study. Additionally, the group of Gorrotxategi-Carbajo et al. obtained a detection limit of 15 ppb working at 4.8 µm (asymmetric stretch) in earlier QCL OF-CEAS work [88].

These are the first reported OF-CEAS spectra of NO, and the detection limit already obtained indicates a potential application for monitoring in polluted urban environments. For example, the 2011 Defra Air Quality data show NO concentrations at the Oxford city centre monitoring station varied from 7 to 4000 ppb, with a mean of 500 ppb [124].

5.2.6 Accuracy of concentration retrieval

For the N_2O data presented in Figure 5.4, the time series of returned fitting parameters are shown in Figure 5.5 (2 s stability) and Figure 5.6 (35 s stability). These measurement series were performed one after the other on the same sample, under the experimental conditions described in Section 5.2.2. The returned fit-

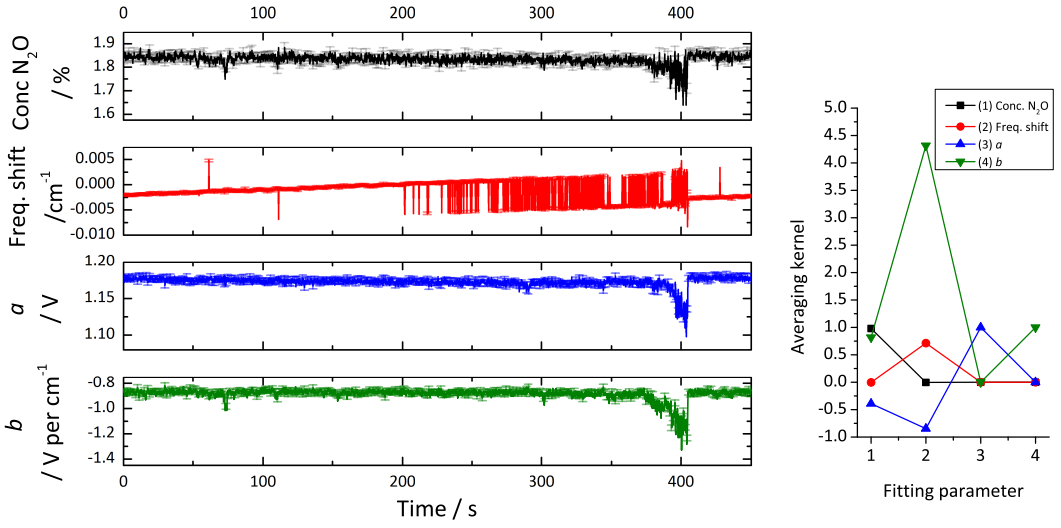

Figure 5.5: Times series of fitting parameters for the N_2O spectra data with 2 s stability from Figure 5.4 and averaging kernels.

ting parameters were the concentration of N_2O (black), the frequency shift (red) required to correct the fitted profile to the HITRAN determined position, the offset, a (blue), and slope, b (green), of the linear baseline, and the 1σ uncertainty (error bars) on these parameters. To determine cross-talk between the fitting parameters and get an idea of the accuracy of concentration retrieval, the previously described fitting program was used to determine averaging kernels, and these are presented alongside the time series. For a perfect instrument (no noise, 100% information content) for which a perfect retrieval has been performed on the signal, the averaging kernel is the identity matrix, indicating zero cross-talk between fitting parameters [195].

For the 35 s stability data, there is reduced correlation between all parameters compared to the 2 s stability data, most notably between the frequency shift and the baseline slope. The correlation for the 35 s stability data is most likely caused by the fact that the linewidth is large compared to the extent of the scan, so there is less information from which to recover accurate baseline information. Additionally, it is worth noting that a frequency shift of around 0.006 cm^{-1} corresponds to one $\Delta\nu_{FSR}$ of the optical cavity.

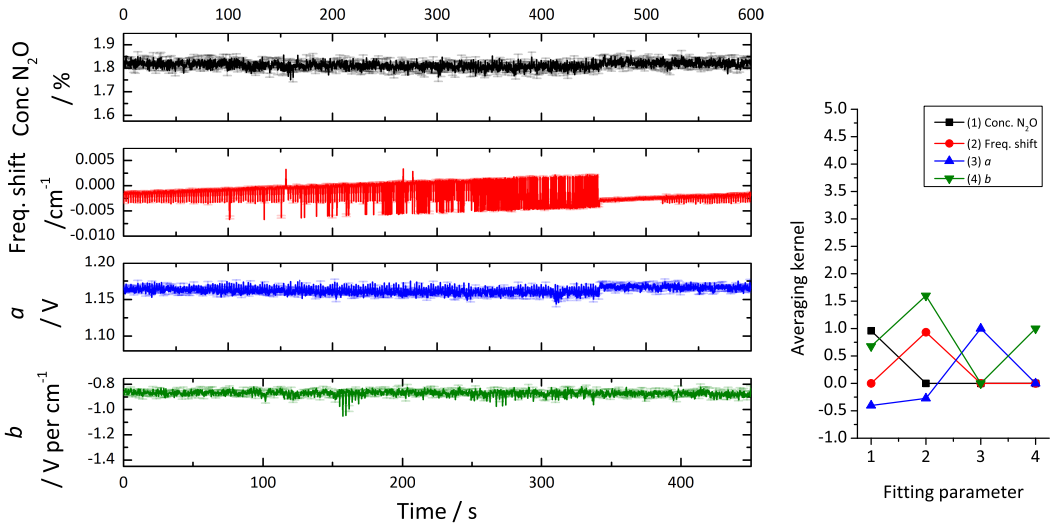

Figure 5.6: Times series of fitting parameters for N_2O spectra data with 35 s stability from Figure 5.4, and correlation weightings.

5.2.7 Temperature controller

The temperature controller was investigated as a potential cause of the identified temporal instability. The controller was changed to a newer model, initially based on exactly the same circuit as the older model, but housed in a casing that allowed easier addition of a front panel port for monitoring the control voltage supplied to the QCL mount, through an isolation amplifier. First, the fine tuning of the control circuit was investigated. The control voltage was monitored, while the QCL temperature was set to a constant value (−15 °C) and small adjustments to the proportional, integral and differential gains, made until no oscillation was visible above the noise on the signal as viewed on an oscilloscope (70 mV) on a timescale of greater than 5 minutes, much longer than the required stability time. The differential gain was removed as a result of this investigation, as the goal of the circuit was long term temperature stability, which fast reactions to temperature fluctuations could counteract. The relationship between control voltage and the reading from the thermistor in the QCL mount was then determined and found to be linear within the temperature operating range of the laser 9 to −15 °C, as expected. From this calibration, the temperature change equivalent to noise of 70 mV was found to be 1 °C. Figures given in the manufacturer's specification sheet, indicate that a 1 °C temperature change results in a laser frequency shift of 26 times the $\Delta\nu_{\mathrm{FSR}}$. From Figures 5.5 and 5.6, the laser frequency shifts returned by the fitting program were much smaller than this, sometimes up to 2 $\Delta\nu_{\mathrm{FSR}}$, but more often less than one. This shows that, as expected, the QCL temperature control did not respond to the 70 mV noise, as the response time (governed by heating and cooling of the large Cu block) is likely to be around 1 s. This suggests that over the course of several minutes the temperature was stable to better than 0.1 °C, and that the temperature controller an unlikely source of the temporal instability.

This conclusion was further corroborated by direct sampling of the signals

supplied by the temperature controller to the QCL mount. The voltage across the thermistor was directly sampled and monitored on an oscilloscope, essentially by expanding the D-connector and directly adding a BNC connection. Upon inspection, this signal did not show signs of instability that could correspond to the identified limitation. This same investigation was repeated for the volt-signal supplied by the current controller, which was also excluded as a source of the temporal instability.

5.3 Results using the Maxion DFB-QCL

The Peltier element in the custom housing for the Alpes DFB-QCL developed a fault, and consequently experiments were continued using a Maxion DFB-QCL. In addition to other differences, already described in Section 4.3.3, this laser had a wider operating range between the threshold and the maximum current which could be applied. Consequently, typical linear current scans of 100 mA were applied, resulting in wider frequency scans covering more than 100 modes of the optical cavity. A system for removal of the etalons limiting the sensitivity of the instrument was investigated, before detection of atmospheric NO was attempted.

5.3.1 Improvements to the gas cell

Given the slight adjustments to the collimation, alignment and mode matching scheme required by changing the laser, the opportunity was taken to make some improvements to the gas cell. Previously, the cell had not been isolated from movement of the taps to the vacuum pump and gas sample inlet, and without extremely delicate handling this caused significant misalignment of the optical cavity during routine gas handling. This situation was improved by bolting the taps via bulkhead unions [Swagelok, SS2507-400-61] to structures that were fixed to the optical table. This simple step significantly improved the stability of the optical alignment with respect to gas handling. During this process, all

connections in the gas lines to and from the cell were leak tested and, where necessary, tightened: this improved the base pressure of the cell (from a reading of 3 Torr to 0 Torr on the atmospheric pressure meter). Improved pumping reduced the amount of residual water that remained after pumping down.

5.3.2 Alignment stability

Although alignment of the optical cavity to TEM_{00} was straightforward, and stable on the short time scales required for measuring, it was not stable from day to day. The instability of the alignment can be attributed to the poor quality of the mirror mounts. The ball at the end of the adjustment screws on these mounts all ended on plane surfaces: true kinematic mounts have three different types (trihedral hole, V-shaped slot, and a plane surface) in order to prevent undesired motion [30]. This resulted in significant difficulty in maintaining the alignment from day to day. This problem was much worse for the Maxion DFB-QCL than for the Alpes DFB-QCL, and this can be attributed to the smaller facet size of the Maxion DFB-QCL. Economic constraints prevented the redesign of the gas cell.

5.3.3 Baseline etalon removal

All of the spectra presented in Section 4.3.2, had a sensitivity (quantified by the α_{min}) limited by a sinusoidal baseline variation arising from etalon fringing. The etalon with the largest amplitude fringes arose from reflections between the exit cavity mirror and the hyperhemispherical Ge-immersion lens on the detector. The shape of the immersion lens made it impossible to totally prevent all reflections by tilting the detector.

From inspection of successive scans, the FSR and frequency position of the etalon was observed to be stationary with respect to the frequency scan of the laser. Consequently, a simple means of dithering the detector along the optical

axis was investigated. The intention was that the detector would have been dithered over a length range such that the sinusoidal fringe pattern was translated by a whole period on a time scale faster than the laser scan, smearing out the effect of the etalon and therefore improving the sensitivity. A small PET, with a similar specification but a shorter stack length ($\sim$ 10 mm) than the one used for phase control, was aligned against the back of the detector. The PET was connected to a high voltage power supply [Burleigh, Amp. Driver PZ-150F, maximum 10 kHz modulation amplitude] that provided a 35 V signal, to which a programmable function generator [TTi, TG1010A] added a sinusoidal modulation with an amplitude of $\sim$ 25 V. The dithering speed achievable with the small PET was limited by the large mass of the detector ($\sim$ 500 g) and it was not possible to dither faster than the laser scan (10 Hz). Instead, a slow (1 Hz) dithering regime was investigated as a means of removing the effect of the etalon having averaged several successive scans together. Given the amplitude of the modulation and the properties of the PET, this corresponded to a maximum displacement of around 1 µm. Moving the detector this distance along the optical axis had a negligible effect on the intensity of the detected cavity transmission.

For these experiments, the Maxion DFB-QCL was operated at 9.0 °C and scanned over two water transitions by applying a current ramp of 100 mA. The transitions were in (010) $\leftarrow$ (000) band, corresponding to the bending vibration, close to 1885.3 cm^{-1}. The species with the more intense transition was $H_2{}^{16}O$ and had an intensity of 2.97×10^{-22} $cm^{-1}/(molec\ cm^{-2})$, whilst the less intense was an $H_2{}^{18}O$ isotope transition (1.65×10^{-23} $cm^{-1}/(molec\ cm^{-2})$). Around 500 transmission spectra (scan index) were recorded both with and without dithering. The scan covered 125 modes (mode index) and were fitted using the method described in Section 4.8. A single example fitted spectrum and residual are shown in Figure 5.7. To investigate the effect of dithering, contour plots of the residuals for each scan were first investigated. These are the top contour plots in Figure 5.7,

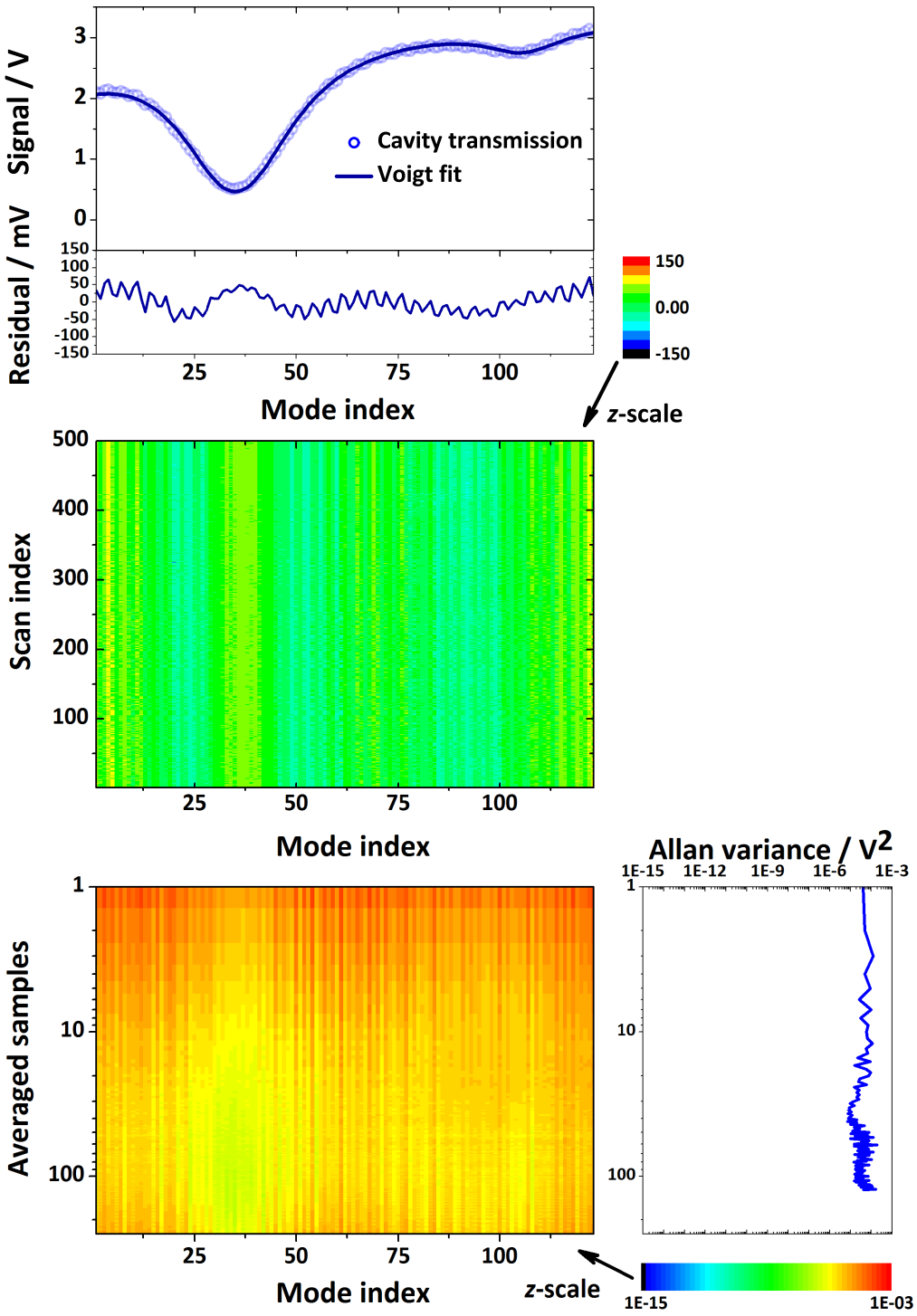

Figure 5.7: Results without dithering. Top plot is an example fitted transmission spectrum and residual. Top contour plot shows the residual for every scan. Bottom contour plot shows the mode-by-mode Allan variance for the residual, side plot is an example Allan variance.

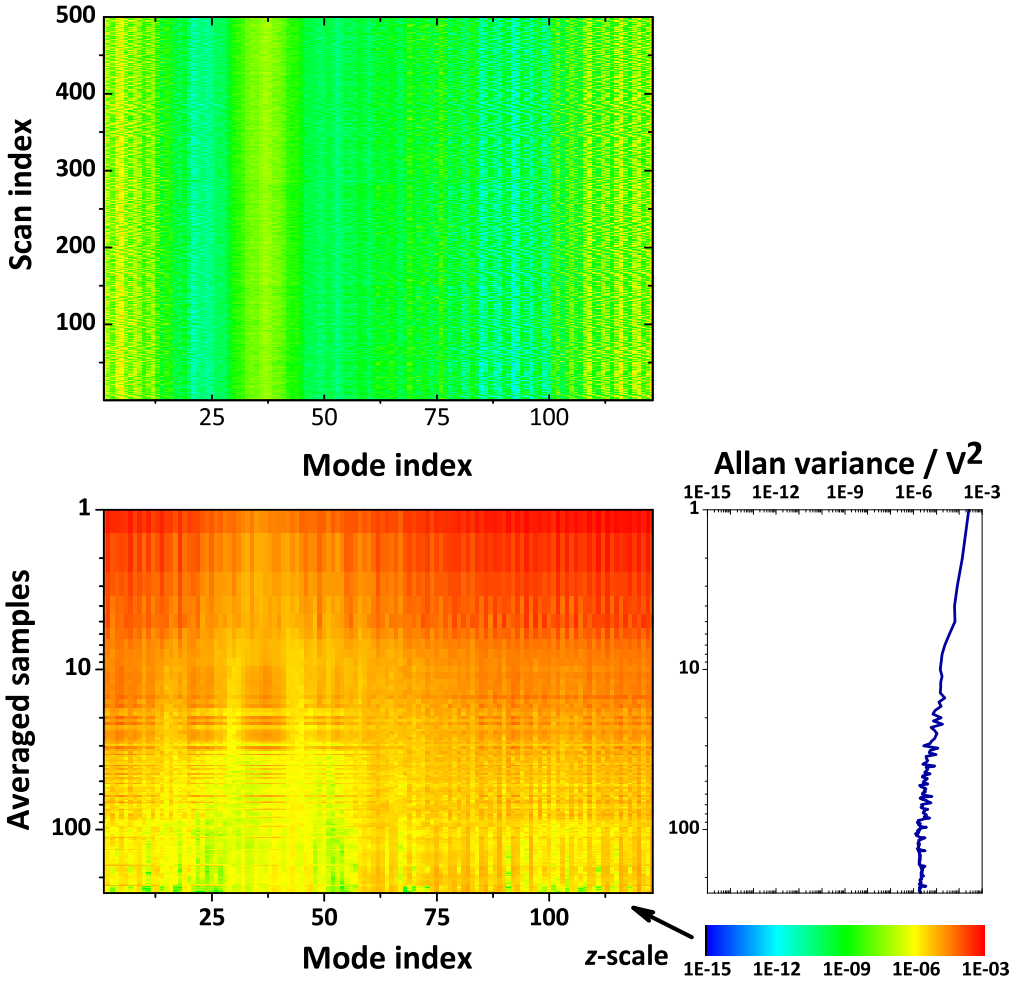

Figure 5.8: Results with dithering. Top contour plot shows the residual for every scan. The effect of changing the etalon length is clearly visible. Bottom contour plot shows the mode-by-mode Allan variance for the residual, side plot is an example Allan variance.

which shows the results without dithering, and Figure 5.8, which shows the results with dithering. Without dithering, the etalon is visible as a sinusoidal alternation, particularly between modes 55 and 80 where transmission is high. With dithering, the etalon is seen to move position relative to the absorption features, as the detector is dithered. (The other major feature visible in both residual contour plots is the W-shape at the centre of the more intense transition, visible from modes 25 and 50, this could be an indication of collisional narrowing as discussed in Section 5.2.1.)

The second analysis performed on the residuals was a overlapping Allan variance calculation, which was carried out per mode. Dithering the detector artificially introduces a drift, and consequently the minimum of the Allan variance should occur after fewer averaged samples in the dithered case. These are presented as the bottom contour plots, for which the contour scale is logarithmic; example single Allan variance plots are also shown. As the Allan variance minima occur in roughly the same place with or without dithering, dithering is shown to not be effective in smearing out the etalon.

5.4 Attempt at measuring atmospheric NO with linear cavity OF-CEAS

The potential of linear cavity QCL OF-CEAS instrument for detection of atmospheric NO was already demonstrated using the Alpes DFB-QCL in Section 5.2.3. The detection limit on the transitions studied with the Alpes DFB-QCL was 5 ppb in 2 s; the integrated intensity of the lines within the range of the Maxion DFB-QCL is slightly larger, although on the same order of magnitude, suggesting that an even better detection limit could be achieved. Trace gas detection of NO is relevant to both atmospheric chemistry and human breath analysis.

5.4.1 Motivation for trace gas detection of NO

NO is present as a trace species in both the troposphere and the stratosphere. Natural sources include forest fires, anaerobic processes in soil, and electrical storms; whilst the primary anthropogenic source is combustion of fossil fuels [194]. As such, detection of trace amounts of NO is of significant importance for studies of atmospheric chemistry and combustion processes [196]. The main tropospheric reactions of NO are summarized in Figure 5.9; the key points are that the joint chemistry of NO and NO_2 plays a major part in the formation and destruction of tropospheric O_3, and that the daytime and nighttime chemistries are different. Photolysis of NO_2 dominates in daylight, and this leads to the production of tropospheric O_3 by reaction of NO with peroxy radicals (HO_2 or RO_2, where R is some organic functional group). At nighttime, the reaction of NO with O_3 to form NO_2 dominates instead. These processes leads to the production of photochemical smog, as NO concentrations build up overnight and further increase due to emissions during the morning rush-hour, eventually leading to the production of O_3, which together with NO and NO_2 are considered tropospheric pollutants.

Consequently NO concentration is measured hourly at recording sites through-

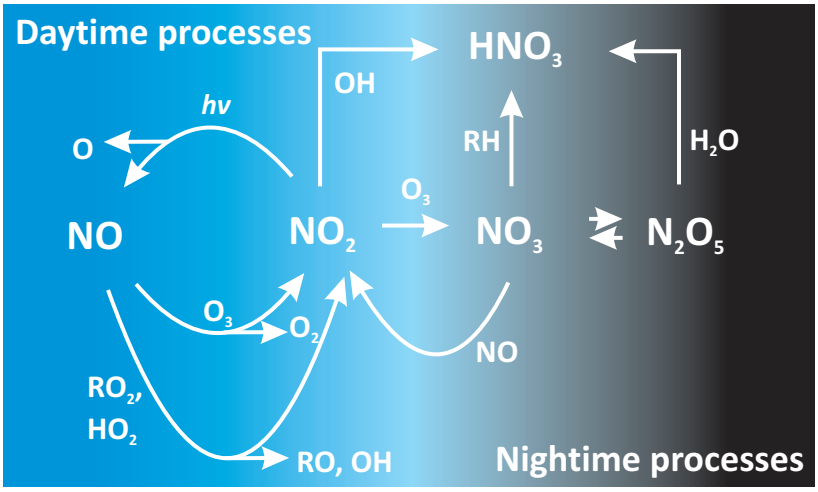

Figure 5.9: Day- and night-time reactions of NO.

out the UK, as part of the air quality monitoring scheme [124]. These measurements are made indirectly by a chemiluminescent analyser. The reaction of NO with O_3 follows two possible pathways, one of which results in electrically excited $NO_2(^2B_{1,2})$, the relaxation of which produces chemiluminescence. The lower detection limit of the analyser is 7 ppb [125].

NO also has an important physiological role: it is produced by the human body, and plays a role in signalling mechanisms for blood flow and neurotransmission [197]. Endogenous NO was first detected in exhaled human breath in 1991 [198]. Increased levels in asthmatics ($\sim$ 60 ppb) relative to non-asthmatics ($\sim$ 30 ppb) were reported by Alving et al. [199], and linked to bronchial inflammation. Exhaled NO has since been extensively studied, first using chemiluminescent analysers and more recently with mid-IR QCL spectroscopy.

The fundamental vibrational transition of NO has a bandhead at around 5.2 µm, a region in which suitable QCLs and detectors have been available for around a decade [197]. As early as 2001, Menzel et al. obtained a detection limit of 3 ppb using a Herriott cell, and 16 ppb by OA-CEAS, with a liquid nitrogen cooled DFB-QCL. To date, the lowest detection limit for NO by a QCL based sensor was based on OA-CEAS, and achieved 0.7 ppb in 1 s [200]. Other investigators have achieved detection limits suitable for sensing of NO in breath by various methods. These include combining WMS and a Herriott cell for sub-ppb detection [201, 202]; 4.9 ppb in 1 s with quartz-enhanced PAS [203]; 4.5 ppb in 1 s with Faraday modulation spectrometry [204]; and 1 ppb in 4 s with ICOS [205].

5.4.2 Drying air samples

Measuring atmospheric NO above the significant H_2O absorptions at 5.2 µm is challenging, as atmospheric H_2O concentrations are roughly on the order of 1 % [194]. The effect of residual H_2O remaining in the cell was already shown in Section 5.2.1. Air samples were dried to minimize the H_2O concentration present

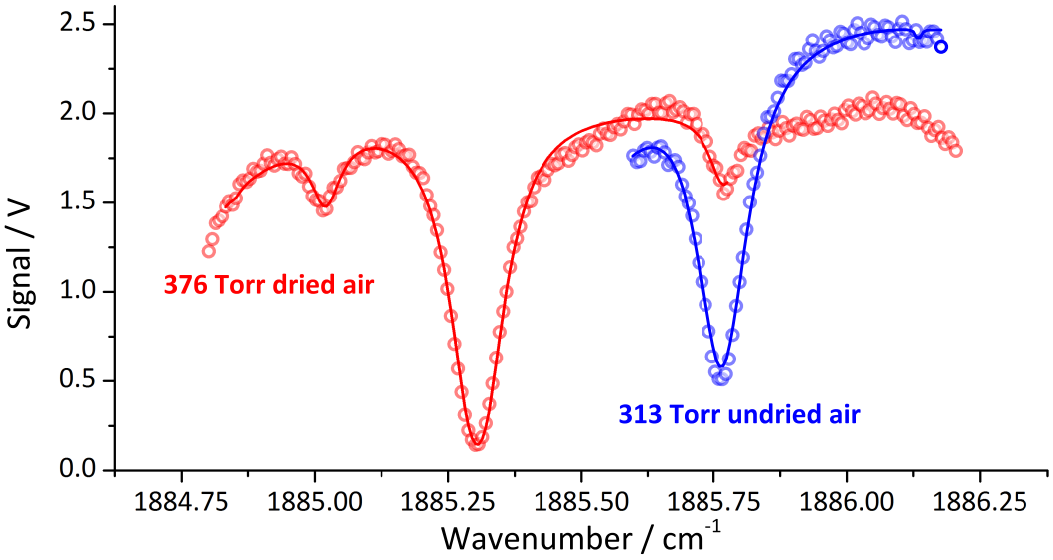

Figure 5.10: Examples of OF-CEAS transmission spectra of air samples containing H_2O with (red) and without (blue) drying using the Nafion tubing.

and thereby reduce the interference of H_2O absorptions. This was accomplished by admitting air samples into the cell via a length of tubing permeable to H_2O but not other molecules [Permapure Nafion, DM-060-24-COMP2, 0.060 outer diameter, 24 inch length compression fittings]. The tubing was held in a sealed container of desiccant [Sigma Aldrich, 3 Å molecular sieves], and the H_2O in the air sample equilibrated with the water in the desiccated container, drying the air sample. According to the manufacturer, the tubing was not permeable to or absorbent of NO, so there should not have been a significant loss of the intended analyte.

The effectiveness of the drying was benchmarked by recording OF-CEAS spectra of the water transitions studied in Section 5.3.3, and fitting them to retrieve the H_2O concentration, as shown in Figure 5.10. Without drying (blue) the H_2O concentration was found to be $0.480 \pm 0.002\%$. With drying (red) this was reduced to 290 ± 10 ppm, i.e. by around a factor of 17.

5.4.3 Attempt at measuring atmospheric NO

For NO trace gas sensing with the Maxion DFB-QCL, of the transitions within the range of the laser the $R(3.5)$ in $v = 1 \leftarrow 0$ band of NO was chosen, because of its high intensity and distant position from interfering water absorptions. The HITRAN listed lines comprising this transition are given in Appendix C. In order to access this transition, the Maxion DFB-QCL frequency was operated at 9.0 °C, and scanned over the chosen transition by a c. 45 mA linear current ramp with a frequency of c. 10 Hz. This resulted in a scan covering 70 $\Delta\nu_{\mathrm{FSR}}$ of the optical cavity. A length of 1/4 inch teflon tubing sampled air taken from outside the laboratory where the linear cavity OF-CEAS instrument was located on the 4th floor of the Physical & Theoretical Chemistry Laboratory. This experiment was attempted on a number of days, at variety of hours over the course of May 2013, but no atmospheric NO was observed. For comparison, NO concentrations recorded as Defra air quality monitoring data in Oxford for May 2013 are shown in Figure 5.11, using a conversion factor of 1 $\mu g\,m^{-3} = 0.8$ ppb at 293 K and 101.3 kPa [124]. The Oxford St Aldates data comes from a roadside location close

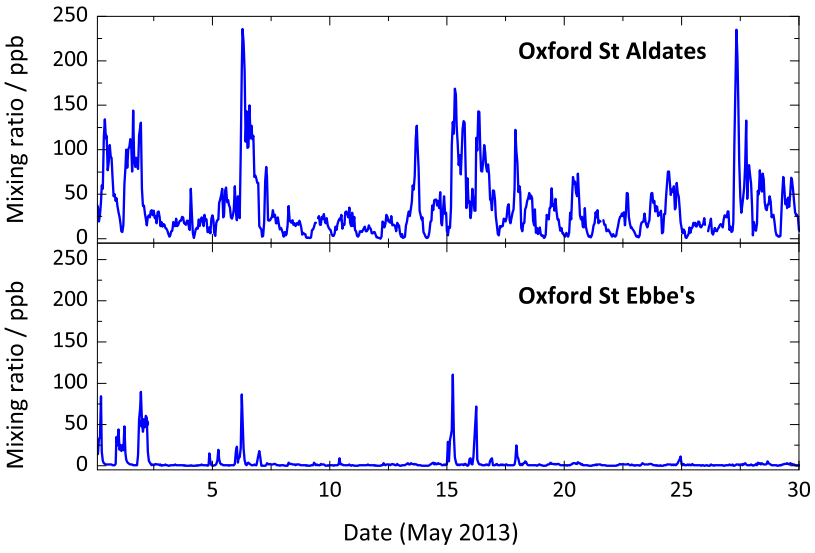

Figure 5.11: Defra air quality data showing the NO concentration for the monitoring sites in Oxford during May 2013.

to a bus terminus, while Oxford St Ebbes is suburban, located to the southwest of the St Aldates site. The science site, where the OF-CEAS instrument was located, is to the northwest of the Oxford St Aldates site, and given the prevailing southwesterly wind in Oxford, the expected NO concentration of the air around the science site could be expected to be at the same levels as Oxford St Ebbes or less. Had the atmospheric measurement campaign been conducted in the winter, when daylight hours are reduced, detection of NO would have been highly probable. Additionally, it is likely that NO molecules in the air samples were adsorbed by the teflon tubing; in future, this could be investigated by instead using coated glass tubing. Given the previously demonstrated detection limit, there is no doubt that if the OF-CEAS instrument had been closer to sources of pollution atmospheric NO would have been observed.

5.4.4 Desorption of NO and H_2O

During the course of the attempted measurements on atmospheric air samples, after a sample had been left in the gas cell for around 20 minutes absorption signals from trace concentrations of NO were in fact observed. Unfortunately the gas cell had been exposed to samples of pure NO during other experiments, and so the likely origin of the trace NO was molecules desorbing from the walls of the gas cell. Cleaning the mirrors and bellows assemblies with alcohol, and using a new clean connecting tube between the mirror mounts did not eliminate the appearance of these absorptions. Instead, the desorption of NO from the gas cell walls was investigated. A total pressure of 218 ± 4 Torr of N_2 [BOC, Oxygen-free N_2, dried by the Nafion tubing] was let into the gas cell. Spectra were recorded of this static sample every 5 minutes for just over 1 hour. Examples fitted spectra, with a time gaps of around 5 minutes, are shown in Figure 5.12.

The concentration of NO was retrieved in the following way. The mirror reflectivity, R, was calibrated by ringdown measurements, taken immediately

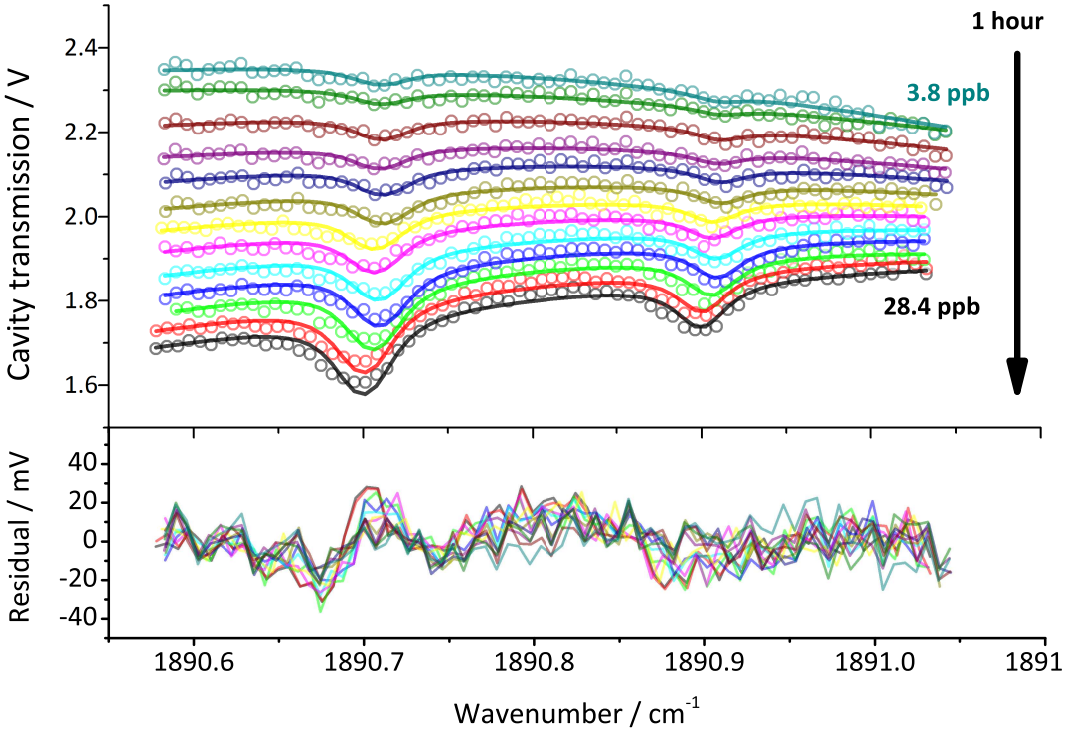

Figure 5.12: Example transmission spectra taken during the investigation of NO desorbing from the cell walls. There is a time gap of about 5 minutes between each spectrum: a fit to the first spectrum returned a concentration of 3.8 ± 0.7 ppb, which increased to 28.4 ± 0.2 ppb for the last.

after the conclusion of this time series: τ_0 was determined to be 6.00 ± 0.01 µs, leading to a R of 0.99957 ± 0.00007. The spectra were fitted using the previously described algorithm. This was programmed to return the concentration of NO, the concentration of H_2O, the frequency shift, and parameters for a quadratic baseline (offset, slope and quadratic components). For these spectra, fitting of the baseline proved challenging, especially as to the left-hand side it is seen to be affected by a strong neighboring H_2O absorption, which increases over time as H_2O also desorbs from the cell walls. Attempts to use a linear baseline resulted in a poor fit.

For all spectra, there was significant cross-talk between the concentration and the baseline fitting parameters, particularly for the early spectra when the concentration of NO was low, for which the frequency shift was also highly correlated. Consequently, for the lower concentrations the required frequency shift was of the

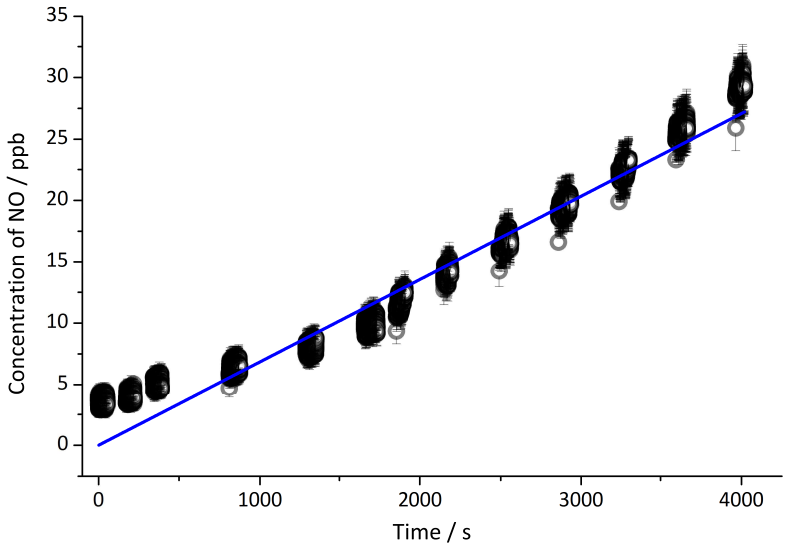

Figure 5.13: Linear fit using first order desorption kinetics to the retrieved NO concentrations.

same order of magnitude as the 1σ uncertainty on this parameter. The fit to the first spectrum shown in Figure 5.12 returned a concentration of 3.8 ± 0.7 ppb. After one hour, desorption led to an increased concentration of 28.4 ± 0.2 ppb. The α_{min} for these spectra was 7.0×10^{-9} cm^{-1} in 1 s, still limited by etalon fringes. This sensitivity is better than that reported for spectra taken using the Alpes DFB-QCL, as the wavelength of the Maxion DFB-QCL is closer to the centre of the wavelength range of the high reflectivity dielectric mirrors.

The concentration results were concatenated and are plotted, together with an estimate of the errors resulting from uncertainty in the pressure and the fitting error in Figure 5.13. The desorption of NO from the walls of the gas cell was modelled as a first-order rate process:

$$\begin{aligned} \frac{\mathrm{d}[\mathrm{NO}]_{\mathrm{ads}}}{\mathrm{d}t} &= -k_{\mathrm{ads}}[\mathrm{NO}]_{\mathrm{ads}} \\ [\mathrm{NO}]_{\mathrm{ads}} &= [\mathrm{NO}]_{\mathrm{ads},0} \exp\left[-k_{\mathrm{ads}}t\right], \end{aligned} \tag{5.10}$$

where $[\mathrm{NO}]_{\mathrm{ads}}$ is the concentration of adsorbed NO at time t, $[\mathrm{NO}]_{\mathrm{ads},0}$ the initial adsorbed concentration, and k_{ads} the first order rate constant. By conservation

of matter, the concentration of gaseous NO, $[NO]_{gas}$, is $[NO]_{ads,0} - [NO]_{ads}$, and therefore:

$$[NO]_{ads} = [NO]_{ads,0}(1 - \exp[-k_{ads}t]), \tag{5.11}$$

which at early t, such that $k_{ads}t \ll 1$, may be simplified to a linear relation:

$$[NO]_{gas} = [NO]_{ads,0}k_{ads}t \tag{5.12}$$

Fitting a line with an intercept at the origin to the desorption data in Figure 5.12, leads to a value for $[NO]_{ads,0}k_{ads}$ of $6.76 \pm 0.01 \times 10^{-3}$ ppb s^{-1}.

5.5 Summary

This chapter has presented the quantitative spectroscopic results of the linear cavity OF-CEAS setup, using both the Alpes and Maxion DFB-QCLs. With the Alpes DFB-QCL, early initial spectra of $H_2{}^{18}O$ and $N_2{}^{18}O$ transitions demonstrated the capability of the technique for probing weak absorptions associated with non-primary isotopologues. The performance of the linear cavity OF-CEAS instrument was benchmarked by spectroscopy of N_2O. Described by the α_{min}, the sensitivity of the N_2O spectra at 0.28 atm was 2.7×10^{-8} cm^{-1} in 1 s. The spectral region around the lasing wavelengths of both of the lasers coincided with the fundamental vibrational transition of NO at around 5.2 µm, and the NO spectra are in fact the first reported using OF-CEAS. Spectroscopy of an NO mix was also studied with the Alpes DFB-QCL, and at a pressure of 0.19 atm an α_{min} of 2.4×10^{-8} cm^{-1} in 1 s was achieved, commensurate with the result for N_2O. Limited by etalon fringing on the baseline, the α_{min} was shown to compare well with values obtained using V-cavity QCL OF-CEAS instruments previously reported by others. Investigations of the temporal stability led to the best minimum detectable concentrations for the linear cavity Alpes DFB-QCL OF-CEAS instrument to be 32 ppm for N_2O (35 s) and 5 ppb for NO (2 s). This compared

favourably with other mid-IR QCL-based NO sensors, and to be sufficient for monitoring NO in polluted urban environments.

A detector dithering system for removal of the sensitivity-limiting etalon was investigated with the Maxion DFB-QCL. Further experiments with this laser included an attempt to monitor NO in air samples collected from outside the laboratory. Although this atmospheric campaign was unsuccessful, trace amounts of NO were instead detected desorbing from the walls of the gas cell. The retrieved concentrations rose from 3.8 ± 0.7 ppb to 28.4 ± 0.2 ppb over the course of one hour. These concentrations were modelled with a limited degree of success by first order desorption kinetics, and a rate of desorption of $6.76 \pm 0.01 \times 10^{-3}$ ppb s^{-1} was determined.

Chapter 6

Conclusions and Future Work

6.1 Formal conclusion

This thesis has presented two contrasting implementations of the optical-feedback cavity-enhanced absorption spectroscopy (OF-CEAS) technique, which combines passive optical-feedback locking of semiconductor lasers with cavity-enhanced absorption spectroscopy. With an appropriate feedback rate, optical geometry, and phase of the optical-feedback field, as the laser frequency is continuously tuned by varying the injection current it locks to successive axial cavity mode frequencies. Accordingly, the temporal cavity transmission consists of a single envelope of peaks, whose frequency spacing corresponds to the free spectral range (FSR) of the optical cavity. When an absorber is introduced to the cavity, this yields a cavity-enhanced absorption spectrum with a well-defined frequency scale, making OF-CEAS well suited to sensitive detection of pressure-broadened trace gases.

Chapter 3 presented a near-IR OF-CEAS instrument, based on a strained layer quantum well distributed feedback diode laser (SLQW-DFB-DL) centered at 1532 nm (6525 cm^{-1}). This setup closely followed the form of the first reported OF-CEAS instrument [59], and used the well-established V-cavity methodology to spatially decouple the field reflected by the cavity from the direct back-reflected

field from the dielectric coating of the first cavity mirror. This instrument was first used to accurately measure the self-broadened half-width HWHM, γ_{self}, of the $Q(46)e$ transition in the $(11^12) \leftarrow (00^00)$ combination band of CO_2. The obtained value, 0.072 ± 0.002 cm^{-1} atm^{-1}, was within 4% of that given by HITRAN. Second, the near-IR V-cavity instrument was used to detect acetylene present in a sample of car exhaust gas, determining a concentration of 661 ± 9 ppb. This system lacked active phase control. Thermal and mechanical drifts of either the cavity length or the laser to cavity distance therefore resulted in a temporal stability effectively on the order of a single scan (around 0.1 s), and this precluded averaging of spectra. The instrument was also subject to the usual complications inherent to the V-shaped cavity. Most notably, the maxima of the peaks in the cavity output signal displayed the usual intensity alternation locking to odd and even modes, and imposed on top of this effect, a spectral ripple arising from slight differences in the length of the injection and replication cavity arms.

The significant results of this work were presented **Chapters 4 and 5**, in which linear cavity OF-CEAS without suppression of the directly reflected field was demonstrated for the first time. This new methodology was made possible by use of a mid-IR quantum cascade laser (QCL). This spectral region coincides with the intense fundamental vibration bands of many small molecules, and the recent development of QCLs has initiated intensive research efforts into gas sensors capable of selective and sensitive measurements. These include V-cavity OF-CEAS instruments, as the limited spatial extent of the TEM_{00} alignment, linewidth narrowing and frequency locking characteristic of OF-CEAS go some way to overcoming some of the difficulties of working in the mid-IR (i.e. increased diffraction losses, smaller area and cryogenically cooled detectors, fewer off-the-shelf optics available at a higher cost) that can preclude the realization of gains in detection sensitivity afforded by the more intense absorptions. **Chapter 4** demonstrated that further consideration of the response of QCLs to optical-feedback, could in

fact allow the use of a linear cavity for OF-CEAS, without suppression of the direct back-reflection from the dielectric coating of the first cavity mirror. This result has been described as "surprising"[a] and also "impossible"[b], as such an experiment has not been successfully performed with a diode laser. QCLs are more stable to "strong" regimes of optical-feedback. First, it is more difficult to reinject optical-feedback into the gain medium of a QCL because the waveguide dimensions are below the diffraction limit. Second, the intersubband nature of the lasing transition leads to near-zero values for the laser linewidth broadening parameter, β. This both precludes the existence of a coherence collapse regime, and means that an increased feedback coupling constant is required to bring about a given level of OF-CEAS locking. These literature results were complemented with an argument suggesting that, due to the nature of reflection from a highly reflective stack of dielectric thin films, the cavity reflected field and that directly back-reflected from the dielectric mirror coating would be in anti-phase. Consequently, adjustment of the laser cavity distance such that the phase matching condition was met for the cavity reflected field led to no significant effect on the QCL behaviour by optical-feedback from the direct back-reflection. Experimental evidence confirming this effect was presented, as part of an investigation into optical-feedback reduction of the Maxion QCL threshold current.

Successful OF-CEAS locking was shown for two different DFB-QCLs, from two different manufacturers that had quite different characteristics, but had close operating wavelengths, within the high reflectivity bandwidth of the same cavity mirror set. The first was an Alpes laser operating at 5.5 µm, with an output power of 3 mW, and a measured facet size of 10 µm by 1 µm. The second was a high power Maxion laser operating at 5.2 µm, with an output power of around 100 mW, and a specified facet size of 5.8 µm by 2 µm. Full development of the linear cavity OF-CEAS instrument was presented. This included benchmarking

[a] Reviewer's comment for [89]

[b] Personal communication between Grant Ritchie and Daniele Romanini.

the performance of a low noise current driver for QCLs against the commercially available alternatives. It was found that the PTCL Electronics device represented a significant performance improvement over that of the previously used ILX Lightwave commercial device, reducing the effective laser linewidth in a direct absorption spectroscopy measurement from several hundred MHz to a few MHz. Active phase control of the optical-feedback was implemented by matching the laser to cavity optical distance to the length of the optical cavity on a wavelength scale, using a turning mirror mounted on a piezoelectric transducer (PET) and a LabVIEW program. Design and mode matching of the optical cavity was described, and for the Maxion laser an investigation into cavity alignment presented.

Chapter 5 presented quantitative spectroscopic studies using the linear cavity OF-CEAS setup with both the Alpes and Maxion DFB-QCLs. With the Alpes DFB-QCL, early initial spectra of $H_2{}^{18}O$ and $N_2{}^{18}O$ transitions showed the ability of the sensitive linear cavity OF-CEAS instrument to probe the weak absorptions associated with non-primary isotopologues. The linear cavity OF-CEAS instrument performance was benchmarked by spectroscopy of N_2O. Quantified by the α_{min}, the sensitivity of the N_2O spectra at 0.28 atm was 2.7×10^{-8} cm^{-1} in 1 s. There was a particular emphasis on the spectroscopy and detection of NO, as the spectral region around 5.5 µm coincides with the fundamental vibrational transition of NO, and the presented NO spectra are in fact the first reported using OF-CEAS. Consequently, spectroscopy of an NO mix was also studied, and at 0.19 atm an α_{min} of 2.4×10^{-8} cm^{-1} in 1 s was achieved. Although limited by etalon fringing on the baseline, the α_{min} compared well with those obtained with V-cavity QCL OF-CEAS instruments [48, 49, 88]. The temporal stability was investigated, and typical stability was around 2 s, determined by the Allan variance minimum. This typical stability is inferior to those reported for other OF-CEAS instruments; however, on occasion the system was stable enough to average for a

respectable 35 s. Consequently the best minimum detectable concentrations for the linear QCL OF-CEAS instrument was 32 ppm for N_2O (35 s) and 5 ppb for NO (2 s). This compares favourably with other mid-IR QCL-based NO sensors, especially given the relatively limited instrument development, and is sufficient for monitoring NO in polluted urban environments. The Maxion DFB-QCL was used to attempt monitoring of NO in air outside the laboratory, and an air sample drying system benchmarked. Although this campaign was unsuccessful, it was possible detect trace amounts of NO desorbing from the walls of the gas cell, from 3.8 ± 0.7 ppb to 28.4 ± 0.2 ppb over the course of one hour. These concentrations were modelled with a limited degree of success by first order desorption kinetics, and a rate of desorption of $6.76 \pm 0.01 \times 10^{-3}$ ppb s^{-1} was determined.

These results demonstrate the high suitability and relevance of linear cavity QCL OF-CEAS as an in-situ trace gas sensing technique. Already a second linear cavity OF-CEAS system, based on an 8.2 µm DFB-QCL [Alpes Lasers SA], has been demonstrated using the methodology and LabVIEW program described in this thesis. Significant development of the "proof-of-principle" instrument presented in this thesis is certainly a worthwhile enterprise, first by overcoming some of the limitations of the existing instrument, and then perhaps by taking steps towards producing an instrument capable of field deployment.

The $\alpha_{\min}$ was limited by etalon fringing, caused by reflections between the exit cavity mirror and the immersion lens on the detector. A simple detector dithering system to remove this etalon was investigated, and shown to not provide a performance improvement. An improved instrument could instead use a non-immersed detector, which could be tilted to prevent reflections: use of such a small area detector is likely to be feasible for OF-CEAS, due to the high intensity and limited spatial extent of the cavity output, afforded by the TEM_{00} alignment and frequency locking in OF-CEAS. Having done this, an order of magnitude in sensitivity ($\alpha_{\min}$) could be gained by use of a low noise amplifier, in order to

overcome the detection limit currently determined by bit-noise on the detector (5.1×10^{-9} cm^{-1} in 1 s).

The temporal instability represents a significant hindrance to reliable instrument performance and achievement of even lower detection limits by averaging spectra. Although the control signals supplied to the QCL from the temperature and current controllers were ruled out, it proved to be beyond the scope of this work to determine the possible electrical, mechanical or acoustic noise source. Measures to isolate the system from these sources of noise could include use of low noise power supplies or batteries, and further steps to prevent transmission of vibration along gas handling lines. The gas handling could also be improved by using a quieter oil-free pumping system, flow controllers to study flowing atmospheric samples, and perhaps even electrically controlled gas taps. The other major hindrance to reliability of the instrument, particularly when using the Maxion laser, was the low quality of the cavity mirror mounts, which result in poor alignment stability. A simple way to improve this situation would be to use higher quality commercially available mirror mounts, whilst a more involved solution would be to instead use a monolithic cavity made of a low expansion ceramic.

The true utility of OF-CEAS lies in its ability to make rapid measurements, and a natural next step would be to implement realtime fitting of data in LabVIEW. The spectral region covered by this work meant that the presence of water often complicated the fitting analysis of the presented spectra, and this precluded the investigation of W-shaped residuals over the absorption peaks, that could indicate a degree of collisional narrowing. Improvement of the accuracy of concentration retrieval would require through investigation of this effect, i.e. by fitting different lineshape functions that account for collisional narrowing. The self-calibrating relative frequency scale in fact makes OF-CEAS a suitable technique for investigating this technique.

6.2 Extensions of linear cavity QCL OF-CEAS

This section outlines three possible extensions of the linear cavity QCL OF-CEAS methodology described in this work, all of which have the potential to extend the possible applications of the technique.

6.2.1 Broadly tuneable EC-QCL OF-CEAS

With a DFB-QCL, the maximum possible current tuning range in a single laser scan is around 1 cm^{-1}, slightly more if the temperature is scanned. If OF-CEAS were instead implemented with an external cavity QCL (EC-QCL), it may be possible to considerably increase the scan range, as QC structures have broad gain bandwidths (> 100 cm^{-1}). Broadly tuneable QCL OF-CEAS could be applied to the detection of trace atmospheric mid-IR broadband absorbers, for instance hydrocarbons like chlorofluorocarbons (CFCs) or benzene.

EC-QCLs work on the same principle as EC-DLs. A Fabry-Perot QCL is very strongly coupled by optical-feedback to an external cavity that includes a frequency-selective diffraction grating to produce single-mode output. EC-DL OF-CEAS has been successfully implemented in the visible [93], and in the near-IR spectral regions [84]; however neither of these devices had an enhanced tuning range compared to a DFB-DL, due to the limited mode-hop free tuning range of the EC-DLs used. Broadly tuneable mode-hop free EC-QCLs are available from Daylight Solutions at various mid-IR wavelengths, with a specified tuning range from 30 to 60 cm^{-1}.

Aside from the spectroscopic benefits, the effect of returning optical-feedback from a high finesse cavity on the linewidth and frequency of an EC-QCL is itself an interesting and novel experiment. EC lasers have much longer effective laser cavities and broader linewidths than DFB lasers, making them less sensitive to optical-feedback (Equation 3.10). Coupling optical-feedback back into the QCL waveguide is also demanding: calculations from a recent paper suggest for an

EC-QCL, around $23 \pm 8\%$ is returned [183]. However, experiments performed by Walker [206] already suggest that EC-QCLs are sufficiently sensitive to optical-feedback for OF-CEAS to work. An ICOS setup was built using a EC-QCL [Daylight Solutions, 21052-MHF], coupled to a V-shaped optical cavity, without optical isolation. No attempt was made to spatially mode-match the laser output to the optical cavity, which was then further aligned to excite high-order modes. Despite these steps, which would have reduced the coupling of optical-feedback back into the laser gain medium, the cavity output signal displayed persistent fringing periodic with the cavity $\Delta\nu_{\mathrm{FSR}}$, indicating that optical-feedback from the cavity was injection seeding the EC-QCL [206]. This observation strongly suggests that an EC-QCL coupled to a linear optical cavity with steps taken to maximize return of optical-feedback to the gain medium may well work as the basis for an OF-CEAS experiment.

A disadvantage of using an EC- rather than a DFB-QCL would be the decreased robustness of the laser and the frequency tuning mechanism, due to the required mechanical movement of the diffraction grating. Another consideration is the wavelength dependence of the cavity mirror reflectivity within the wide frequency scan. As accurate concentration retrieval would necessitate several ringdown calibrations measurements, given the experimental effort this would require, implementing the more complex but self-calibrating OF-CRDS technique may be more efficient.

6.2.2 Interband Cascade Laser OF-CEAS

The interband cascade laser (ICL) concept was proposed by Yang in 1995 [207] and extended by Meyer et al. [208]. The gain medium of a type-II ICL is depicted in Figure 6.1. Like in a QCL, an electron tunnels through an injection region into a quantum well in the conduction band, where it is trapped. However, unlike in a QCL, the electron then undergoes an interband transition, relaxing into

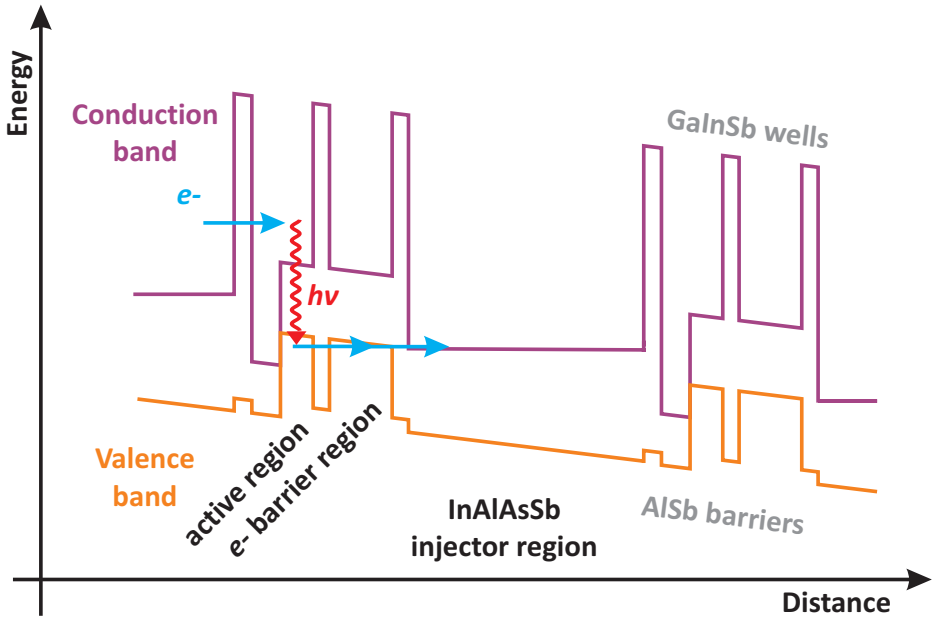

Figure 6.1: Schematic of the energy levels in a type-II ICL, adapted from [208].

the valence band by emitting a photon. Following this, the electron tunnels into the next quantum well, the thickness of which is engineered so that free carrier absorption owing to intervalence transitions is minimized at the lasing wavelength. Finally, the electron tunnels into the next injector region as part of a cascade [208].

Although proposed and implemented within three years of QCLs, ICL development has been much slower because design and fabrication of the gain medium is more complex. However, there are two distinct advantages of current ICL technology. The first is that ICLs do not have the fast phonon-scattering losses of QCLs, and additionally have suppressed Auger recombination through band-structure engineering. These properties result in higher operating temperatures, lower threshold currents, and better power conversion efficiency than QCLs. Their second advantage is access to the 2 to 4.5 µm spectral region, which is currently difficult to reach with QCLs due to band offset limitations. The fundamental vibrational transitions associated with the stretches of C−H, N−H, and O−H bonds of small molecules occur at around 3 µm, making this an important spectral region for trace gas sensing. The low power consumption and spectroscopic

properties of ICLs have already been usefully combined in the Sample Analysis at Mars instrument, currently deployed by NASA for in-situ measurements of methane isotopologues in the Martian atmosphere [2].

DFB-ICLs suitable for use in an OF-CEAS experiment are commercially available as off-the-shelf devices from Nanoplus (from 3 to 6 µm, with proven applicability to tuneable diode laser absorption spectroscopy [209]) and also from Maxion Technologies. Such lasers could very usefully be incorporated into an OF-CEAS experiment to create a low-power in-situ measurement device. Further, the effect of optical-feedback on ICLs has not been widely studied. The linewidth broadening parameter, β, of an ICL has been measured to be 0.71 [210], which suggests that ICLs will share the stability of QCLs to strong levels of optical-feedback, making a linear cavity OF-CEAS arrangement feasible.

6.2.3 Higher resolution multicomb linear cavity OF-CEAS

The spectral sampling resolution of traditional OF-CEAS instruments is limited by the $\Delta\nu_{\mathrm{FSR}}$ of the optical cavity (c. 0.01 cm^{-1}) and Hamilton has formally proposed the concept of multicomb OF-CEAS to overcome this [98]. This is adequate for pressure broadened absorption profiles that span 10 or more $\Delta\nu_{\mathrm{FSR}}$ and allow accurate fitting of Voigt lineshape functions, but not for low pressure regimes where line profiles are narrower and dominated by Doppler broadening. There are several advantages to working at lower pressure: overlapping of spectral features is reduced, and absorption profiles have Gaussian lineshapes. These could enable the detection of weak lines (e.g. those of isotopologues) in ambient air on an absorption free baseline and allow better spectral fitting and more accurate concentration retrieval.

Improved spectral sampling resolution could be achieved by sub-wavelength step-shifting of the cavity length, $L + \delta L$, by mounting one of the cavity mirrors on a PET, as in Figure 6.2. In this way, multiple "frequency combs" could be

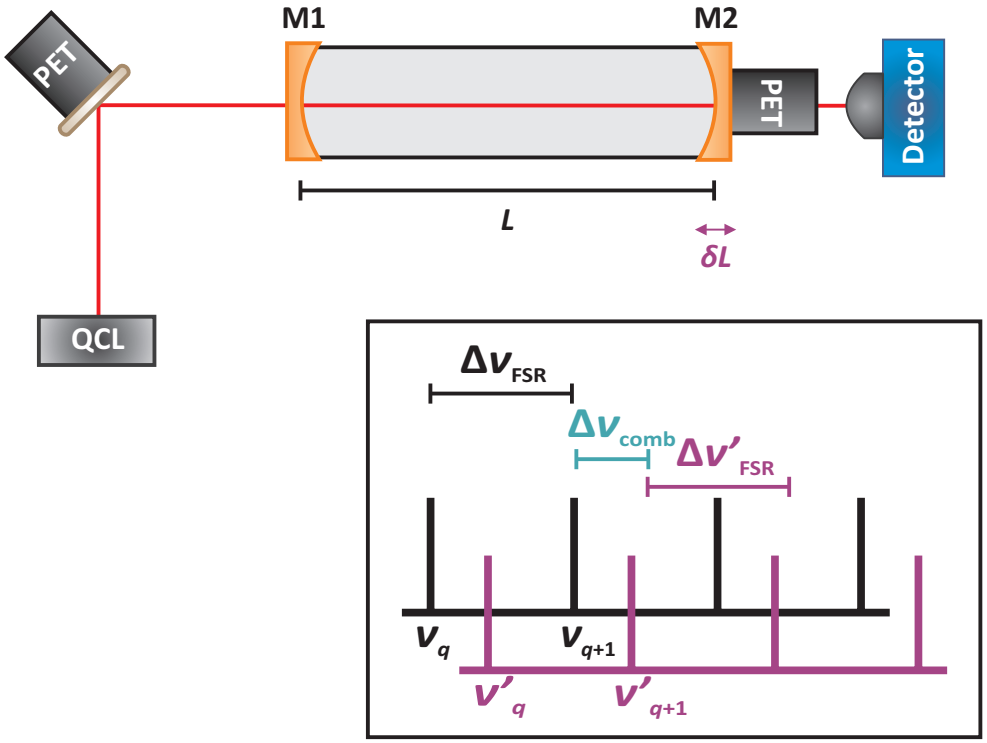

Figure 6.2: Schematic of linear cavity multicomb OF-CEAS.

successively accessed. Two such combs are shown schematically in Figure 6.2, where the parent comb (black) has an FSR denoted $\Delta\nu_{\mathrm{FSR}}$. The daughter comb, produced by a displacement δL of the cavity arm length, is shown in purple and has a free spectral range $\Delta\nu'_{\mathrm{FSR}}$, which is approximately $\Delta\nu_{\mathrm{FSR}}$. By Equation 2.15 the frequency displacement, $\Delta\nu_{\mathrm{comb}}$, between the frequencies of the first mode in the parent comb, ν_q, and the first mode in the daughter comb, ν'_q is given by:

$$\Delta\nu_{\mathrm{comb}} = \frac{qc}{2}\left[\frac{1}{L+\delta L} - \frac{1}{L}\right] \tag{6.1}$$

$$\approx \nu_q\left(\frac{\delta L}{L}\right) \tag{6.2}$$

The number of points across an absorption profile would be multiplied by the number of steps taken by the PET. The minimum step size of a PET is on the order of a pm; however at 1900 cm^{-1} a step size this small results in a $\Delta\nu_{\mathrm{comb}}$ less than the cavity bandwidth and therefore the optical-feedback reduced laser linewidth. A step size of around a nm would instead result in a $\Delta\nu_{\mathrm{comb}}$ on the

order of the laser linewidth (40 kHz), suggesting the spectral sampling resolution for a 75 cm cavity could theoretically be improved by up to a factor of 5000. However, reproducible scanning of the PET on a nm scale may be difficult, due to the need for a high-voltage low-noise driver and the natural hysteresis and memory effects of the ceramic. Acquiring so many spectra would also take a long time and be resource-heavy. A more realistic regime would be one in which the PET was stepped by ~ 0.2 µm to gain a factor of 20 for the spectral resolution, leading to around 20 points across a Doppler-broadened NO absorption profile at around 5 µm.

Hamilton's original proposal specified how multicomb V-cavity OF-CEAS could be implemented, and indicates that there may be several advantages to using a linear cavity for this experiment. The V-cavity must be setup to permit build-up of both even and odd cavity modes, so that the step modulation of the replication arm length does not perturb the optical-feedback phase. This introduces the alternation effect between the mode sets, leading to the necessity for ringdown calibrations for both even and odd modes with every step modulation of the cavity length. Changing the length of the replication arm will displace the node or antinode from the folding mirror and result in a different sinusoidal oscillation imposed on the baseline of each set of modes for each step, Section 3.3.3. So, this in fact necessitates a ringdown calibration for every single mode in each set for every single scan, effectively limiting the technique to OF-CRDS. Implemented with a linear cavity, all modes have a node on each mirror, so there is no alternation effect or baseline oscillation, enabling a single ringdown calibration per PET step.

OF-CEAS instruments have typically had cavity lengths of 40 cm or more, for the $\Delta\nu_{\mathrm{FSR}}$ to provide an adequate spectral sampling resolution. A secondary advantage of a multicomb system would be the prospect of a miniaturized OF-CEAS instrument, using a shorter cavity length, shorter laser to cavity beam path, with

a correspondingly reduced gas cell and total instrumental volume. The primary disadvantage of multicomb OF-CEAS would be the increased experimental complexity. Temporal resolution would also be lost, as the acquisition speed would be determined by the speed of the step-shift and consequent synchronization processes for phase matching, rather than the scan speed.

Appendix A

Evaluation of the sum in Equation 4.2

Defining $\omega t_z + \arctan\beta = \varphi$ for convenience, and using the compound angle formula:

$$\sin(A+B) = \sin A \cos B + \cos B \sin A, \tag{A.1}$$

allows the sum in Equation 4.2 to be rewritten as

$$\sum_{m=0}^{\infty} R^m \sin\left(\omega t_z + m\omega t_\mathrm{r} + \varphi\right) = \sin\varphi \sum_{m=0}^{\infty} R^m \cos\left(m\omega t_\mathrm{r}\right) + \cos\varphi \sum_{m=0}^{\infty} R^m \sin\left(m\omega t_\mathrm{r}\right). \tag{A.2}$$

These resulting sums may be evaluated by substituting in the trigonometric identities:

$$\cos x = \frac{\exp[\mathrm{i}x] + \exp[-\mathrm{i}x]}{2}, \tag{A.3}$$

$$\sin x = \frac{\exp[\mathrm{i}x] - \exp[-\mathrm{i}x]}{2\mathrm{i}}, \tag{A.4}$$

and summing as a geometric series, i.e:

$$\sum_{m=0}^{\infty} S^m = \frac{1}{1-S}. \tag{A.5}$$

This leads to:

$$\begin{aligned}
\sum_{m=0}^{\infty} R^m \sin\left(m\omega t_{\mathrm{r}}\right) &= \sum_{m=0}^{\infty} \frac{R^m}{2\mathrm{i}} \left(\exp\left[\mathrm{i}m\omega t_{\mathrm{r}}\right] - \exp\left[-\mathrm{i}m\omega t_{\mathrm{r}}\right]\right) && \text{(A.6)} \\
&= \frac{R\sin(\omega t_{\mathrm{r}})}{1+R^2-2R\cos(\omega t_{\mathrm{r}})}, && \text{(A.7)}
\end{aligned}$$

and

$$\begin{aligned}
\sum_{m=0}^{\infty} R^m \cos\left(m\omega t_{\mathrm{r}}\right) &= \sum_{m=0}^{\infty} \frac{R^m}{2} \left(\exp\left[\mathrm{i}m\omega t_{\mathrm{r}}\right] + \exp\left[-\mathrm{i}m\omega t_{\mathrm{r}}\right]\right) && \text{(A.8)} \\
&= \frac{1-R\cos(\omega t_{\mathrm{r}})}{1+R^2-2R\cos(\omega t_{\mathrm{r}})}. && \text{(A.9)}
\end{aligned}$$

Substituting these results back into Equation 4.2, and simplifying leads to an expression for the sum:

$$\begin{aligned}
&\sum_{m=0}^{\infty} R^m \sin\left(\omega t_z + m\omega t_{\mathrm{r}} + \arctan\beta\right) && \text{(A.10)} \\
&= \frac{\sin\varphi(1-R\cos[\omega t_{\mathrm{r}}]) + \cos\varphi(R\sin[\omega t_{\mathrm{r}}])}{1+R^2-2R\cos[\omega t_{\mathrm{r}}]} \\
&= \frac{\sin\varphi - R\left[\sin(\varphi)\cos(\omega t_{\mathrm{r}}) + \cos(\varphi)\sin(\omega t_{\mathrm{r}})\right]}{1+R^2-2R\cos(\omega t_{\mathrm{r}})} && \text{(A.11)} \\
&= \frac{\sin\varphi - R\sin(\varphi-\omega t_{\mathrm{r}})}{(1-R^2)+4R\sin^2(\omega t_{\mathrm{r}})}. && \text{(A.12)}
\end{aligned}$$

which leads directly to Equation 4.3.

Appendix B

Mode matching the QCL beam to the linear cavity

Considering the first cavity mirror, w_{cav} is taken as the object and (the unknown) w_{int} as the image. Equation 4.10 leads to

$$\frac{1}{f_{\mathrm{mirr}}} = \frac{-1}{z_2 - z_3} + \frac{1}{\left[\left(z_{\mathrm{R,cav}}/M^2\right)^2/\left(\frac{L}{2} - f_{\mathrm{mirr}}\right)\right] + \frac{L}{2}}, \tag{B.1}$$

and re-arranging gives $z_2 - z_3$ in terms of known parameters:

$$z_2 - z_3 = -\left[\frac{1}{f_{\mathrm{mirr}}} - \frac{1}{\left[\left(z_{\mathrm{R,cav}}/M^2\right)^2/\left(\frac{L}{2} - f_{\mathrm{mirr}}\right)\right] + \frac{L}{2}}\right]^{-1}. \tag{B.2}$$

Again using Equation 4.10 for the same optic, but considering instead w_{int} as the object and w_{cav} as the image yields

$$\frac{1}{f_{\mathrm{mirr}}} = \frac{2}{L} + \frac{1}{\left[\left(z_{\mathrm{R,int}}/M^2\right)^2/\left(-(z_2 - z_3) - f_{\mathrm{mirr}}\right)\right] - (z_2 - z_3)}, \tag{B.3}$$

which can be rearranged to give $z_{\mathrm{R,int}}$ as the subject:

$$z_{\mathrm{R,int}} = M^2\left\{\left[\left(\frac{Lf_{\mathrm{mirr}}}{L - 2f_{\mathrm{mirr}}}\right) + (z_2 - z_3)\right]\left[-(z_2 - z_3) - f_{\mathrm{mirr}}\right]\right\}^{1/2}. \tag{B.4}$$

From which w_{int} can be calculated, using Equation 2.9.

The magnification of the mode matching lens, with object w_{meas} and image w_{int}, is

$$\gamma_{\text{lens}} = \frac{w_{\text{int}}}{w_{\text{meas}}} = \left[\left[1 - z_1/f_{\text{lens}}\right]^2 + \left(\frac{z_{\text{R,meas}}}{f_{\text{lens}} M^2} \right)^2 \right]^{-1/2}, \tag{B.5}$$

which leads to the following expression for z_1:

$$z_1 = -f_{\text{lens}} \left[\gamma_{\text{lens}}^{-2} - \left(\frac{z_{\text{R,meas}}}{f_{\text{lens}} M^2} \right) \right]^{1/2}. \tag{B.6}$$

Equation 4.10 then leads to

$$\frac{1}{f_{\text{lens}}} = \frac{1}{z_1 + \left[\left(z_{\text{R,meas}}/M^2\right)^2 / \left(z_1 - f_{\text{lens}}\right) \right]} + \frac{1}{z_2}, \tag{B.7}$$

which re-arranged gives

$$z_2 = \left[\frac{1}{f_{\text{lens}}} - \frac{1}{z_1 + \left[\left(z_{\text{R,meas}}/M^2\right)^2 / \left(z_1 - f_{\text{lens}}\right) \right]} \right]^{-1}. \tag{B.8}$$

Combined with Equation B.2, this yields values for both z_1. and z_3.

Appendix C

Lines comprising the $R(3.5)$ transition in the $v = 1 \leftarrow 0$ vibrational band of NO

Term Symbol	Position / cm^{-1}	S / $\mathrm{cm}^{-1}/(\mathrm{molec\ cm}^{-2})$	Transition
$^2\Pi_{\frac{1}{2}}$	1890.707128	1.918×10^{-20}	$R(3.5)e$
	1890.707139	1.519×10^{-20}	
	1890.707219	1.199×10^{-20}	
$^2\Pi_{\frac{1}{2}}$	1890.718703	1.917×10^{-20}	$R(3.5)f$
	1890.718849	1.519×10^{-20}	
	1890.718852	1.198×10^{-20}	
$^2\Pi_{\frac{3}{2}}$	1890.912256	9.609×10^{-21}	$R(3.5)e$
	1890.912520	7.612×10^{-21}	
	1890.912695	6.006×10^{-21}	
$^2\Pi_{\frac{3}{2}}$	1890.912551	9.609×10^{-21}	$R(3.5)f$
	1890.912801	7.612×10^{-21}	
	1890.912978	6.006×10^{-21}	

Table C.1: The HITRAN listed lines comprising the $R(3.5)$ transition in the $v = 1 \leftarrow 0$ band of NO [9].

References

[1] E. Dlugokencky, L. Steele, P. Lang, and K. A. Masarie. Atmospheric methane at Mauna Loa and Barrow observatories: Presentation and analysis of in situ measurements. *Journal of Geophysical Research*, 100 (Dll):23103–23113, 1995. `http://www.agu.org/pubs/crossref/1995/95JD02460.shtml`. (page 1).

[2] C. Webster. Measuring methane and its isotopes $^{12}CH_4$, $^{13}CH_4$, and CHD_3 on the surface of Mars with in situ laser spectroscopy. *Applied Optics*, 44 (7):1226–1235, 2005. `http://www.opticsinfobase.org/abstract.cfm?id=82702`. (pages 1, 168).

[3] C. Wang and P. Sahay. Breath analysis using laser spectroscopic techniques: breath biomarkers, spectral fingerprints, and detection limits. *Sensors*, 9 (10):8230–8262, January 2009. `http://www.mdpi.com/1424-8220/9/10/8230`. (page 1).

[4] P. Werle. Tuneable diode laser absorption spectroscopy: recent findings and novel approaches. In *Infrared Physics and Technology, Proceedings of the 4th International Symposium on Monitoring of Gaseous Pollutants by Tunable Diode Lasers*, volume 37, pages 59–66, 1996. `http://www.sciencedirect.com/science/article/pii/1350449595001131`. (page 1).

[5] F. Tittel, G. Wysocki, A. Kosterev, and Y. Bakhirkin. Semiconductor laser based trace gas sensor technology: recent advances and applications. In M. EbrahiZadeh and I. Sorokina, editors, *Mid-Infrared Coherent Sources and Applications*, pages 467–493. Springer NATO Science Series, 2008. `http://link.springer.com/content/pdf/10.1007/978-1-4020-6463-0_15`. (page 1).

[6] P. Atkins and R. Friedman. *Molecular Quantum Mechanics*. Oxford University Press, fourth edition, 2005. (pages 3, 3, 6, 12).

[7] J. M. Hollas. *Modern Spectroscopy*. Wiley, fourth edition, 2004. (pages 3, 5, 7, 8).

[8] L. Rothman, C. Rinsland, A. Goldman, S. Massie, D. Edwards, J.-M. Flaud, A. Perrin, C. Camy-Peyret, V. Dana, J.-Y. Mandin, J. Schroeder, A. Mccann, R. Gamache, R. Wattson, K. Yoshino, K. Chance, K. Jucks,

L. Brown, V. Nemtchinov, and P. Varanasi. The Hitran Molecular Spectroscopic Database and Hawks (Hitran Atmospheric Workstation): 1996 Edition. *Journal of Quantitative Spectroscopy and Radiative Transfer*, 60(5): 665–710, November 1998. http://linkinghub.elsevier.com/retrieve/pii/S0022407398000788. (pages 4, 6).

[9] L. Rothman, I. Gordon, A. Barbe, D. Benner, P. Bernath, M. Birk, V. Boudon, L. Brown, A. Campargue, J.-P. Champion, K. Chance, L. Coudert, V. Dana, V. Devi, S. Fally, J.-M. Flaud, R. Gamache, A. Goldman, D. Jacquemart, I. Kleiner, N. Lacome, W. Lafferty, J.-Y. Mandin, S. Massie, S. Mikhailenko, C. Miller, N. Moazzen-Ahmadi, O. Naumenko, A. Nikitin, J. Orphal, V. Perevalov, A. Perrin, A. Predoi-Cross, C. Rinsland, M. Rotger, M. Šimečková, M. Smith, K. Sung, S. Tashkun, J. Tennyson, R. Toth, A. Vandaele, and J. Vander Auwera. The HITRAN 2008 molecular spectroscopic database. *Journal of Quantitative Spectroscopy and Radiative Transfer*, 110(9-10):533–572, June 2009. http://linkinghub.elsevier.com/retrieve/pii/S0022407309000727. (pages 5, 10, 70, 98, 130, 133, 177).

[10] W. Lamb. Theory of an Optical Maser. *Physical Review*, 134(6A):A1429–A1450, 1964. http://prola.aps.org/abstract/PR/v134/i6A/pA1429_1. (page 5).

[11] J. Olivero and R. Longbothum. Empirical fits to the Voigt line width: A brief review. *Journal of Quantitative Spectroscopy and Radiative Transfer*, 17(2):233–236, 1977. http://www.sciencedirect.com/science/article/pii/0022407377901613. (page 7).

[12] J. Humliĉek. Optimized computation of the Voigt and complex probability functions. *Journal of Quantitative Spectroscopy and Radiative Transfer*, 27 (4):437–444, 1982. http://www.sciencedirect.com/science/article/pii/0022407382900784. (page 7).

[13] P. Bouguer. *Essai d'Optique, sur la gradation de la lumiere*. Claude Jombert, Paris, 1729. (page 8).

[14] J. Lambert. *Photometria sive de mensura et gradibus luminis, colorum et umbrae*. Eberhardt Klett, Augsburg, 1760. (page 8).

[15] Beer. Bestimmung der Absorption des rothen Lichts in farbigen Flüssigkeiten. *Annalen der Physik und Chemie*, 86, 1852. (page 8).

[16] S. Welzel, F. Hempel, M. Hübner, N. Lang, P. Davies, and J. Röpcke. Quantum cascade laser absorption spectroscopy as a plasma diagnostic tool: an overview. *Sensors.*, 10(7):6861–900, January 2010. http://www.mdpi.com/1424-8220/10/7/6861. (page 9).

[17] F. Tittel, D. Richter, and A. Fried. Mid-Infrared Laser Applications in Spectroscopy. *Topics in Applied Physics: Solid-State Mid-Infrared Laser Sources*, 89:458–529, 2003. http://link.springer.com/chapter/10.1007/3-540-36491-9_11. (pages 10, 11).

[18] Y. Arita and P. Ewart. Multi-mode absorption spectroscopy. *Optics Communications*, 281(9):2561–2566, May 2008. http://linkinghub.elsevier.com/retrieve/pii/S0030401807013995. (page 10).

[19] G. Agrawal and N. Dutta. *Long-Wavelength Semiconductor Lasers*. Van Nostrand Reinhold, first edition, 1986. (pages 11, 12, 12, 46, 46, 46, 47, 47, 47, 48, 49, 52, 54, 54, 65, 65).

[20] L. Ciaffoni, R. Grilli, G. Hancock, A. J. Orr-Ewing, R. Peverall, and G. A. D. Ritchie. 3.5-μm high-resolution gas sensing employing a LiNbO3 QPM-DFG waveguide module. *Applied Physics B*, 94(3):517–525, November 2008. http://link.springer.com/10.1007/s00340-008-3291-0. (page 11).

[21] D. Richter, P. Weibring, and A. Fried. High-power, tunable difference frequency generation source for absorption spectroscopy based on a ridge waveguide periodically poled lithium niobate crystal. *Optics Express*, 15(2): 3163–3165, 2007. http://www.opticsinfobase.org/oe/abstract.cfm?uri=oe-15-2-564. (page 12).

[22] J. Faist, F. Capasso, D. Sivco, C. Sirtori, A. Hutchinson, and A. Cho. Quantum Cascade Laser. *Science*, 264(5158):553–556, 1994. http://www.sciencemag.org/content/264/5158/553.short. (pages 12, 12, 12, 82, 83, 92).

[23] C. Sirtori, P. Kruck, S. Barbieri, P. Collot, J. Nagle, M. Beck, J. Faist, and U. Oesterle. GaAs/Al[sub x]Ga[sub 1x]As quantum cascade lasers. *Applied Physics Letters*, 73(24):3486, 1998. http://link.aip.org/link/APPLAB/v73/i24/p3486/s1&Agg=doi. (page 12).

[24] C. Gmachl and F. Capasso. Recent progress in quantum cascade lasers and applications. *Reports on Progress in Physics*, 64(11):1533–1601, 2001. http://iopscience.iop.org/0034-4885/64/11/204. (pages 12, 85).

[25] J. White. Long optical paths of large aperture. *Journal of the Optical Society of America*, 32(5):285–285, 1942. (page 13).

[26] D. R. Herriott and H. J. Schulte. Folded Optical Delay Lines. *Applied Optics*, 4(8):883–889, August 1965. http://www.opticsinfobase.org/abstract.cfm?URI=ao-4-8-883. (page 13).

[27] C. G. C. Tarsitano and C. C. R. Webster. Multilaser Herriott cell for planetary tunable laser spectrometers. *Applied Optics*, 46(28):6923–6935, October 2007. http://www.opticsinfobase.org/abstract.cfm?id=142155. (page 13).

[28] V. Baev, T. Latz, and P. Toschek. Laser intracavity absorption spectroscopy. *Applied Physics B*, 69(3):171–202, 1999. http://dx.doi.org/10.1007/s003400050793. (page 14).

[29] G. Berden and R. Engeln, editors. *Cavity Ring-Down Spectroscopy: Techniques and Applications*. John Wiley & Sons, 2009. (pages 14, 36, 36, 38, 39, 124).

[30] J. H. Moore, C. C. Davis, and M. A. Coplan. *Building Scientific Apparatus*. Cambridge University Press, 2009. (pages 14, 15, 15, 18, 108, 108, 144).

[31] A. Bell. On the Production and Reproduction of Sound by Light. *American Journal of Science*, (XX):305–324, 1880. (page 16).

[32] A. Bell. Upon the Production of Sound by Radiant Energy. *The Philosophical Magazine and Journal*, (XI):510–528, 1881. (page 16).

[33] M. Viegerov. Eine Methode der Gasanalyse, Beruhend auf der Optisch-Akustischen Tyndall-Röntgenerscheinung. *Doklady Akademii Nauk SSSR*, (19):687–688, 1938. (page 16).

[34] F. J. M. Harren, G. Cotti, J. Oomens, and L. Hekkert. Photoacoustic Spectroscopy in Trace Gas Monitoring. In R. Meyers, editor, *Encyclopedia of Analytical Chemistry*, pages 2203–2226. John Wiley & Sons, 2000. (page 16).

[35] C. Haisch. Photoacoustic spectroscopy for analytical measurements. *Measurement Science and Technology*, 23(1):012001, January 2012. `http://stacks.iop.org/0957-0233/23/i=1/a=012001?key=crossref.cb3847f36a7413e2b8fcf20d5758adcc`. (page 16).

[36] B. A. Paldus, T. G. Spence, R. N. Zare, J. Oomens, F. J. Harren, D. H. Parker, C. Gmachl, F. Cappasso, D. L. Sivco, J. N. Baillargeon, A. L. Hutchinson, and A. Y. Cho. Photoacoustic spectroscopy using quantum-cascade lasers. *Optics Letters*, 24(3):178–80, February 1999. `http://www.opticsinfobase.org/ol/abstract.cfm?uri=ol-24-3-178`. (page 16).

[37] M. Hippler, C. Mohr, K. A. Keen, and E. D. McNaghten. Cavity-enhanced resonant photoacoustic spectroscopy with optical feedback cw diode lasers: A novel technique for ultratrace gas analysis and high-resolution spectroscopy. *The Journal of Chemical Physics*, 133(4):044308, July 2010. `http://jcp.aip.org/resource/1/jcpsa6/v133/i4/p044308_s1`. (pages 16, 79, 80).

[38] A. Kachanov, S. Koulikov, and F. K. Tittel. Cavity-enhanced optical feedback-assisted photo-acoustic spectroscopy with a 10.4 μm external cavity quantum cascade laser. *Applied Physics B*, 110(1):47–56, November 2013. `http://link.springer.com/10.1007/s00340-012-5250-z`. (page 16).

[39] A. A. Kosterev, Y. A. Bakhirkin, R. F. Curl, and F. K. Tittel. Quartz-enhanced photoacoustic spectroscopy. *Optics Letters*, 27(21):1902–4, November 2002. `http://www.opticsinfobase.org/ol/abstract.cfm?uri=ol-27-21-1902`. (page 16).

[40] G. Litfin, C. R. Pollock, R. F. Curl, and F. K. Tittel. Sensitivity enhancement of laser absorption spectroscopy by magnetic rotation effect. *The Journal of Chemical Physics*, 72(12):6602, 1980. http://link.aip.org/link/JCPSA6/v72/i12/p6602/s1&Agg=doi. (page 16).

[41] Y. Wang, M. Nikodem, and G. Wysocki. Cryogen-free heterodyne-enhanced mid-infrared Faraday rotation spectrometer. *Optics Express*, 21(1):740–755, 2013. http://www.opticsinfobase.org/abstract.cfm?URI=oe-21-1-740. (page 16).

[42] G. C. Bjorklund. Frequency-modulation spectroscopy: a new method for measuring weak absorptions and dispersions. *Optics Letters*, 5(1):15–17, 1980. http://www.opticsinfobase.org/abstract.cfm?id=7054. (page 17).

[43] G. Bonfiglioli and P. Brovetto. Principles of Self-Modulating Derivative Optical Spectroscopy. *Applied Optics*, 3(12):1417–1424, December 1964. http://www.opticsinfobase.org/abstract.cfm?URI=ao-3-12-1417. (page 17).

[44] E. I. Moses and C. L. Tang. High-sensitivity laser wavelength-modulation spectroscopy. *Optics Letters*, 1(4):115–117, October 1977. http://www.opticsinfobase.org/ol/abstract.cfm?uri=ol-1-4-115. (page 17).

[45] G. Hall and S. North. Transient laser frequency modulation spectroscopy. *Annual Review of Physical Chemistry*, 51:243–274, 2000. http://www.annualreviews.org/doi/pdf/10.1146/annurev.physchem.51.1.243. (page 17).

[46] J. Ye, L. Ma, and J. Hall. Ultrasensitive detections in atomic and molecular physics: demonstration in molecular overtone spectroscopy. *Journal of the Optical Society of America B*, 15(1):6–15, 1998. http://www.opticsinfobase.org/abstract.cfm?&id=35318. (pages 17, 40, 41).

[47] E. J. Moyer, D. S. Sayres, G. S. Engel, J. M. St. Clair, F. N. Keutsch, N. T. Allen, J. H. Kroll, and J. G. Anderson. Design considerations in high-sensitivity off-axis integrated cavity output spectroscopy. *Applied Physics B*, 92(3):467–474, August 2008. http://www.springerlink.com/index/10.1007/s00340-008-3137-9. (pages 19, 78).

[48] D. J. Hamilton and A. J. Orr-Ewing. A quantum cascade laser-based optical feedback cavity-enhanced absorption spectrometer for the simultaneous measurement of CH_4 and N_2O in air. *Applied Physics B*, 102(4):879–890, October 2011. http://www.springerlink.com/index/10.1007/s00340-010-4259-4. (pages 19, 43, 44, 77, 81, 102, 118, 131, 138, 138, 162).

[49] P. Gorrotxategi-Carbajo, E. Fasci, I. Ventrillard, M. Carras, G. Maisons, and D. Romanini. Optical-feedback cavity-enhanced absorption spectroscopy with a quantum-cascade laser yields the lowest formaldehyde detection limit. *Applied Physics B*, 110(3):309–314, February 2013. http:

//link.springer.com/10.1007/s00340-013-5340-6. (pages 19, 43, 44, 77, 118, 138, 138, 139, 162).

[50] D. Allan. Statistics of atomic frequency standards. *Proceedings of the IEEE*, 54(2):221–230, 1966. http://ieeexplore.ieee.org/lpdocs/epic03/wrapper.htm?arnumber=1446564. (page 20).

[51] W. J. Riley. *Handbook of Frequency Stability Analysis*. National Institute of Standards in Technology, 2008. http://tf.nist.gov/general/pdf/2220.pdf. (pages 20, 138).

[52] C. Fabry and A. Perot. Sur les franges des lames minces argentées et leur application a la mesure de petites épaisseurs d'air. *Annales de chimie et de physique*, 12(7):459–500, 1897. (page 21, 21).

[53] B. Saleh and M. Teich. *Fundamentals of Photonics*. John Wiley & Sons, Inc., first edition, 1991. (pages 21, 23, 26, 31, 34, 50).

[54] F. Jenkins and H. White. *Fundamentals of Optics*. McGraw Hill, 4th edition, 2001. (page 22).

[55] A. E. Siegman. *Lasers*. Oxford University Press, 1986. (pages 24, 24, 32, 49, 110).

[56] A. Siegman. Defining, measuring, and optimizing laser beam quality. *Proceedings of SPIE*, 1868:2–12, 1993. http://proceedings.spiedigitallibrary.org/data/Conferences/SPIEP/57005/2_1.pdf. (page 30).

[57] K. K. Lehmann and D. Romanini. The superposition principle and cavity ring-down spectroscopy. *The Journal of Chemical Physics*, 105(23):10263–10277, 1996. http://link.aip.org/link/JCPSA6/v105/i23/p10263/s1&Agg=doi. (pages 31, 33).

[58] J. Morville. *Injection des cavités optiques de haute finesse par laser à diode - Application à la CW-CRDS et à la détection de traces atmosphériques.* Doctoral thesis, Université Joseph Fourier, 2001. (pages 33, 35, 41, 65, 72).

[59] J. Morville, S. Kassi, M. Chenevier, and D. Romanini. Fast, low-noise, mode-by-mode, cavity-enhanced absorption spectroscopy by diode-laser self-locking. *Applied Physics B*, 80(8):1027–1038, May 2005. http://www.springerlink.com/index/10.1007/s00340-005-1828-z. (pages 33, 40, 43, 45, 56, 64, 64, 76, 118, 159).

[60] P. Laurent, A. Clairon, and C. Bréant. Frequency Noise Analysis of Optically Self-Locked Diode Lasers. *IEEE Journal of Quantum Electronics*, 25 (6):1131–1142, 1989. http://ieeexplore.ieee.org/xpls/abs_all.jsp?arnumber=29238. (pages 34, 41, 51, 54, 56, 60).

[61] G. Rempe, R. J. Thompson, H. J. Kimble, and R. Lalezari. Measurement of ultralow losses in an optical interferometer. *Optics Letters*, 17(5):363–365, March 1992. http://www.opticsinfobase.org/ol/abstract.cfm?uri=ol-17-5-363. (page 36).

[62] G. Brooker. *Modern Classical Optics*. Oxford University Press, 2003. (page 37).

[63] M. Born and E. Wolf. *Principles of Optics*. Cambridge University Press, seventh edition, 1999. (page 37).

[64] J. M. Herbelin, J. A. McKay, M. A. Kwok, R. H. Ueunten, D. S. Urevig, D. J. Spencer, and D. J. Benard. Sensitive measurement of photon lifetime and true reflectances in an optical cavity by a phase-shift method. *Applied Optics*, 19(1):144–147, January 1980. http://www.opticsinfobase.org/ao/abstract.cfm?uri=ao-19-1-144. (page 37).

[65] D. Z. Anderson, J. C. Frisch, and C. S. Masser. Mirror reflectometer based on optical cavity decay time. *Applied Optics*, 23(8):1238–1245, April 1984. http://www.opticsinfobase.org/ao/abstract.cfm?uri=ao-23-8-1238. (page 37).

[66] A. O'Keefe and D. A. G. Deacon. Cavity ring-down optical spectrometer for absorption measurements using pulsed laser sources. *Review of Scientific Instruments*, 59(12):2544–2552, 1988. http://link.aip.org/link/RSINAK/v59/i12/p2544/s1&Agg=doi. (page 38).

[67] D. Romanini and A. Kachanov. Diode laser cavity ring down spectroscopy. *Chemical Physics letters*, 270(5-6):538–545, 1997. http://www.sciencedirect.com/science/article/pii/S0009261497004065. (page 38, 38).

[68] B. A. Paldus, C. C. Harb, T. G. Spence, B. Wilke, J. Xie, J. S. Harris, and R. N. Zare. Cavity-locked ring-down spectroscopy. *Journal of Applied Physics*, 83(8):3991–3998, 1998. http://link.aip.org/link/JAPIAU/v83/i8/p3991/s1&Agg=doi. (page 39).

[69] Y. He and B. Orr. Ringdown and cavity-enhanced absorption spectroscopy using a continuous-wave tunable diode laser and a rapidly swept optical cavity. *Chemical Physics Letters*, 319(1-2):131–137, 2000. http://www.sciencedirect.com/science/article/pii/S000926140000107X. (page 39).

[70] S. S. Brown. Absorption spectroscopy in high-finesse cavities for atmospheric studies. *Chemical reviews*, 103(12):5219–38, December 2003. http://pubs.acs.org/toc/chreay/103/12. (page 39).

[71] A. Grant, S. O'Doherty, A. J. Manning, M. Athanassiadou, P. Simmonds, D. Young, and R. Derwent. Long-term atmospheric measurement and interpretation (of radiatively active trace gases). University of Bristol; Met Office, 2012. (page 39).

[72] Y. Chen, J. D. Kessler, K. K. Lehmann, and T. C. Onstott. Portable multiple laser continuous-flow NIR cavity-ringdown system for methane Isotopologues on Mars. In *ACS 2010*, 2010. (page 39).

[73] J. B. Paul, L. Lapson, and J. Anderson. Ultrasensitive absorption spectroscopy with a high-finesse optical cavity and off-axis alignment. *Applied Optics*, 40(27):4904–4910, September 2001. http://www.opticsinfobase.org/ao/abstract.cfm?uri=ao-40-27-4904. (page 40).

[74] T. Gherman and D. Romanini. Mode-locked cavity-enhanced absorption spectroscopy. *Applied Optics*, 10(19):1033–1042, 2002. http://www.opticsinfobase.org/oe/abstract.cfm?uri=oe-10-19-1033. (page 40).

[75] R. Grilli, G. Méjean, S. Kassi, I. Ventrillard, C. Abd-Alrahman, and D. Romanini. Frequency Comb Based Spectrometer for in Situ and Real Time Measurements of IO, BrO, NO_2, and H_2CO at pptv and ppqv Levels. *Environmental Science & Technology*, 46(19):10704–10710, October 2012. http://pubs.acs.org/doi/ipdf/10.1021/es301785h. (page 40).

[76] R. Grilli, M. Legrand, A. Kukui, G. Méjean, S. Preunkert, and D. Romanini. First investigations of IO, BrO, and NO_2 summer atmospheric levels at a coastal East Antarctic site using mode-locked cavity enhanced absorption spectroscopy. *Geophysical Research Letters*, 40(4):791–796, February 2013. http://doi.wiley.com/10.1002/grl.50154. (page 40).

[77] C. Bell, G. Hancock, R. Peverall, G. Ritchie, J. H. van Helden, and N. van Leeuwen. Characterization of an external cavity diode laser based ring cavity NICE-OHMS system. *Optics Express*, 17(12):9834–9839, June 2009. http://www.opticsinfobase.org/oe/abstract.cfm?uri=oe-17-12-9834. (page 41).

[78] A. Foltynowicz, J. Wang, P. Ehlers, and O. Axner. Distributed-feedback-laser-based NICE-OHMS in the pressure-broadened regime. *Optics Express*, 18(18):18580–18591, August 2010. http://www.opticsinfobase.org/oe/abstract.cfm?uri=oe-18-18-18580. (page 41).

[79] M. S. Taubman, T. L. Myers, B. D. Cannon, and R. M. Williams. Stabilization, injection and control of quantum cascade lasers, and their application to chemical sensing in the infrared. *Spectrochimica Acta Part A: Molecular and Biomolecular Spectroscopy*, 60(14):3457–3468, December 2004. http://www.sciencedirect.com/science/article/pii/S1386142504001258. (pages 41, 92).

[80] F. Schmidt. *Laser-based Absorption Spectrometry: Development of NICE-OHMS Towards Ultra-sensitive Traces Species Detection*. Doctoral thesis, Umeå Universitet, 2007. (page 41).

[81] F. Schmidt, A. Foltynowicz, W. Ma, and T. Lock. Doppler-broadened fiber-laser-based NICE-OHMS Improved detectability. *Optics Express*, 15(17):10822–10831, 2007. http://www.opticsinfobase.org/abstract.cfm?id=140815. (page 41).

[82] B. Dahmani, L. Hollberg, and R. Drullinger. Frequency stabilization of semiconductor lasers by resonant optical feedback. *Optics Letters*, 12(11):876–878, November 1987. http://www.opticsinfobase.org/ol/abstract.cfm?uri=ol-12-11-876. (pages 41, 51, 54).

[83] J. Morville, D. Romanini, A. Kachanov, and M. Chenevier. Two schemes for trace detection using cavity ringdown spectroscopy. *Applied Physics B: Lasers and Optics*, 78(3-4):465–476, February 2004. http://www.springerlink.com/openurl.asp?genre=article&id=doi:10.1007/s00340-003-1363-8. (pages 41, 55, 72).

[84] V. Motto-Ros, J. Morville, and P. Rairoux. Mode-by-mode optical feedback: cavity ringdown spectroscopy. *Applied Physics B*, 87(3): 531–538, April 2007. http://www.springerlink.com/index/10.1007/s00340-007-2618-6. (pages 42, 44, 80, 165).

[85] T. J. A. Butler, J. L. Miller, and A. J. Orr-Ewing. Cavity ring-down spectroscopy measurements of single aerosol particle extinction. I. The effect of position of a particle within the laser beam on extinction. *The Journal of Chemical Physics*, 126(17):174302, May 2007. http://jcp.aip.org/resource/1/jcpsa6/v126/i17/p174302_s1. (page 42).

[86] T. J. A. Butler, D. Mellon, J. Kim, J. Litman, and A. J. Orr-Ewing. Optical-Feedback Cavity Ring-Down Spectroscopy Measurements of Extinction by Aerosol Particles. *The Journal of Physical Chemistry A*, 113(16):3963–3972, 2009. http://pubs.acs.org/doi/abs/10.1021/jp810310b. (page 42).

[87] D. J. Hamilton, M. G. D. Nix, S. G. Baran, G. Hancock, and A. J. Orr-Ewing. Optical feedback cavity-enhanced absorption spectroscopy (OF-CEAS) in a ring cavity. *Applied Physics B*, 200(2):233–242, 2010. http://www.springerlink.com/index/158750364v11x505.pdf. (pages 43, 44, 61, 79, 80, 88).

[88] G. Maisons, P. Gorrotxategi Carbajo, M. Carras, and D. Romanini. Optical-feedback cavity-enhanced absorption spectroscopy with a quantum cascade laser. *Optics Letters*, 35(21):3607–3609, November 2010. http://www.opticsinfobase.org/ol/abstract.cfm?uri=ol-35-21-3607. (pages 43, 44, 77, 118, 131, 140, 162).

[89] A. G. V. Bergin, G. Hancock, G. A. D. Ritchie, and D. Weidmann. Linear cavity optical-feedback cavity-enhanced absorption spectroscopy with a quantum cascade laser. *Optics Letters*, 38(14):2475–2477, 2013. http://www.opticsinfobase.org/ol/abstract.cfm?uri=ol-38-14-2475. (pages 43, 44, 129, 161).

[90] D. Romanini, M. Chenevier, S. Kassi, M. Schmidt, C. Valant, M. Ramonet, J. Lopez, and H.-J. Jost. Optical-feedback cavity-enhanced absorption: a compact spectrometer for real-time measurement of atmospheric methane. *Applied Physics B*, 83(4):659–667, April 2006. http://www.springerlink.com/index/10.1007/s00340-006-2177-2. (pages 44, 131).

[91] R. Wehr, S. Kassi, D. Romanini, and L. Gianfrani. Optical feedback cavity-enhanced absorption spectroscopy for in situ measurements of the ratio ^{13}C:^{12}C in CO_2. *Applied Physics B*, 92(3):459–465, June 2008. http://www.springerlink.com/index/10.1007/s00340-008-3086-3. (page 44).

[92] I. Ventrillard-Courtillot, T. Gonthiez, C. Clerici, and D. Romanini. Multispecies breath analysis faster than a single respiratory cycle by optical-feedback cavity-enhanced absorption spectroscopy. *Journal of Biomedical Optics*, 14(6):064026, 2009. http://www.ncbi.nlm.nih.gov/pubmed/20059264. (page 44).

[93] I. Courtillot, J. Morville, V. Motto-Ros, and D. Romanini. Sub-ppb NO2 detection by optical feedback cavity-enhanced absorption spectroscopy with a blue diode laser. *Applied Physics B*, 85(2-3):407–412, July 2006. http://www.springerlink.com/index/10.1007/s00340-006-2354-3. (pages 44, 165).

[94] P. Cermak, M. Triki, A. Garnache, and D. Romanini. Optical-Feedback Cavity-Enhanced Absorption Spectroscopy Using a Short-Cavity Vertical-External-Cavity Surface-Emitting Laser. *IEEE Photonics Technology Letters*, 22(21):1607 – 1609, 2010. http://ieeexplore.ieee.org/xpls/abs_all.jsp?arnumber=5570899. (page 44).

[95] D. Romanini, J. Morville, and M. Chenevier. Laser device coupled to a cavity by optical feedback for detecting gas traces, 2004. (page 44).

[96] Ap2E. http://www.ap2e.com. (page 44).

[97] Subglacior Project. http://climateinitiative.pourunmondequichange.com/tag/subglacior/. (page 44).

[98] D. J. Hamilton. *On the development of absorption spectroscopy techniques using optical cavities and injection locking of visible and mid-IR semiconductor laser sources for the sensitive detection of trace atmospheric gases.* Doctoral thesis, University of Bristol, 2012. (pages 44, 88, 125, 168).

[99] S. G. Baran, G. Hancock, R. Peverall, G. A. Ritchie, and N. J. van Leeuwen. Optical feedback cavity enhanced absorption spectroscopy with diode lasers. *Analyst*, 134(2):243–249, 2009. (page 44).

[100] A. Schawlow and C. Townes. Infrared and Optical Masers. *Physical Review*, 112(6):1940–1949, 1958. (pages 45, 49).

[101] T. Maiman. Stimulated Optical Radiation in Ruby. *Nature*, (4736):493–494, 1960. (page 45).

[102] R. N. Hall, G. E. Fenner, J. D. Kingsley, T. J. Soltys, and R. Carlson. Coherant light emission from GaAs junctions. *Physical Review Letters*, 9 (9):366–369, 1962. (page 45).

[103] N. Holonyak and S. F. Bevacqua. Coherant (visible) light emission from Ga(As1xPx) junctions. *Applied Physics Letters*, 1(4):82–83, 1962. http://link.aip.org/link/APPLAB/v1/i4/p82/s1&Agg=doi. (page 45).

[104] M. I. Nathan, W. P. Dumke, G. Burns, F. H. Dill, and G. Lasher. Stimulated emission of radiation from GaAs p-n junctions. *Applied Physics Letters*, 1(3):62–65, 1962. http://link.aip.org/link/APPLAB/v1/i3/p62/s1&Agg=doi. (page 45).

[105] T. M. Quist, R. H. Rediker, R. J. Keyes, W. E. Krag, B. Lax, A. L. McWhorter, and H. J. Zeigler. Semiconductor maser of GaAs. *Applied Physics Letters*, 1(4):91–93, 1962. http://link.aip.org/link/APPLAB/v1/i4/p91/s1&Agg=doi. (page 45).

[106] G. Agrawal. Line narrowing in a single-mode injection laser due to external optical feedback. *IEEE Journal of Quantum Electronics*, 20(5):468–471, May 1984. http://ieeexplore.ieee.org/lpdocs/epic03/wrapper.htm?arnumber=1072420. (page 46).

[107] S. V. Gaponenko. *Introduction to Nanophotonics*. Cambridge University Press, 2010. (page 47).

[108] M. W. Fleming and A. Mooradian. Fundamental line broadening of single-mode (GaAl)As diode lasers. *Applied Physics Letters*, 38(7):511–514, 1981. http://link.aip.org/link/?APL/38/511/1&Agg=doi. (page 49).

[109] C. Henry. Theory of the linewidth of semiconductor lasers. *IEEE Journal of Quantum Electronics*, 18(2):259–264, February 1982. http://ieeexplore.ieee.org/lpdocs/epic03/wrapper.htm?arnumber=1071522. (page 49).

[110] S. Bartalini, S. Borri, P. Cancio, A. Castrillo, I. Galli, G. Giusfredi, D. Mazzotti, L. Gianfrani, and P. De Natale. Observing the Intrinsic Linewidth of a Quantum-Cascade Laser: Beyond the Schawlow-Townes Limit. *Physical Review Letters*, 104(8):083904, February 2010. http://link.aps.org/doi/10.1103/PhysRevLett.104.083904. (pages 49, 92).

[111] M. Osiski and J. Buus. Linewidth Broadening Factor in Semiconductor Lasers- An Overview. *IEEE Journal of Quantum Electronics*, QE-23(1):9–29, 1987. http://ieeexplore.ieee.org/xpls/abs_all.jsp?arnumber=1073204. (pages 50, 65).

[112] R. Lang and K. Kobayashi. External optical feedback effects on semiconductor injection laser properties. *IEEE Journal of Quantum Electronics*, 16(3):347–355, March 1980. http://ieeexplore.ieee.org/lpdocs/epic03/wrapper.htm?arnumber=1070479. (pages 50, 51).

[113] F. Favre and D. Le Guen. Spectral properties of a semiconductor laser coupled to a single mode fiber resonator. *IEEE Journal of Quantum Electronics*, 21(12):1937–1946, December 1985. http://ieeexplore.ieee.org/lpdocs/epic03/wrapper.htm?arnumber=1072600. (page 51).

[114] R. Tkach and A. Chraplyvy. Regimes of feedback effects in 1.5-m distributed feedback lasers. *Journal of Lightwave Technology*, 4(11): 1655 – 1661, 1986. http://ieeexplore.ieee.org/xpls/abs_all.jsp?arnumber=1074666. (page 53).

[115] N. Schunk and K. Petermann. Numerical analysis of the feedback regimes for a single-mode semiconductor laser with external feedback. *IEEE Journal of Quantum Electronics*, 24(7):1242–1247, 1988. http://ieeexplore.ieee.org/xpls/abs_all.jsp?arnumber=960. (pages 53, 103).

[116] M. Mazurenka, A. J. Orr-Ewing, R. Peverall, and G. A. D. Ritchie. Cavity ring-down and cavity enhanced spectroscopy using diode lasers. *Annual Reports Section C (Physical Chemistry)*, 101:42, 2005. http://xlink.rsc.org/?DOI=b408909j. (page 60).

[117] V. Motto-Ros, M. Durand, and J. Morville. Extensive characterization of the optical feedback cavity enhanced absorption spectroscopy (OF-CEAS) technique: ringdown-time calibration of the absorption scale. *Applied Physics B*, 91(1):203–211, February 2008. http://www.springerlink.com/index/10.1007/s00340-008-2950-5. (pages 61, 76, 80, 138).

[118] K. Libbrecht and J. Hall. A low-noise high-speed diode laser current controller. *Review of Scientific Instruments*, 64(8):2133–2135, 1993. http://ieeexplore.ieee.org/xpls/abs_all.jsp?arnumber=4991156. (pages 62, 93).

[119] Z. Tan, X. Long, K. Yang, and S. Wu. Spectral ripple effect in continuous-wave fold-type cavity ring down spectroscopy. *Journal of the Optical Society of America B*, 27(12):2727–2730, November 2010. http://www.opticsinfobase.org/abstract.cfm?URI=josab-27-12-2727. (page 64).

[120] Refractive Index Database. http://refractiveindex.info. (page 65).

[121] R. A. Toth, L. R. Brown, C. E. Miller, V. Malathy Devi, and D. C. Benner. Spectroscopic database of CO_2 line parameters: 4300-7000 cm^{-1}. *Journal of Quantitative Spectroscopy and Radiative Transfer*, 109 (6):906–921, April 2008. http://linkinghub.elsevier.com/retrieve/pii/S0022407307003512. (page 71).

[122] P. Nelson, S. Quigley, and M. Smith. Sources of atmospheric hydrocarbons in Sydney: A quantitative determination using a source reconciliation technique. *Atmospheric Environment*, 17(3):439–449, 1983. http://www.sciencedirect.com/science/article/pii/0004698183901178. (pages 73, 74).

[123] Y. Xiao, D. J. Jacob, and S. Turquety. Atmospheric acetylene and its relationship with CO as an indicator of air mass age. *Journal of Geophysical Research*, 112(D12):D12305, June 2007. http://doi.wiley.com/10.1029/2006JD008268. (page 73).

[124] Defra Air Quality Data. http://uk-air.defra.gov.uk. (pages 73, 73, 140, 150, 152).

[125] R. Yardley, J. Dernie, and P. Dumitrean. UK Hydrocarbon Network: Annual Report for 2011. AEA, 2012. (pages 73, 150).

[126] L. D. Le, J. D. Tate, M. B. Seasholtz, M. Gupta, T. Owano, D. Baer, T. Knittel, A. Cowie, and J. Zhu. Development of a rapid on-line acetylene sensor for industrial hydrogenation reactor optimization using off-axis integrated cavity output spectroscopy. *Applied Spectroscopy*, 62(1):59–65, January 2008. www.lgrinc.com/publications/acetylene.pdf. (page 73).

[127] *In Service Exhaust Emission Standards for Road Vehicles Seventeenth Edition*. Department for Transport, 2012. (page 73).

[128] F. M. Schmidt, O. Vaittinen, M. Metsälä, P. Kraus, and L. Halonen. Direct detection of acetylene in air by continuous wave cavity ring-down spectroscopy. *Applied Physics B*, 101(3):671–682, May 2010. http://www.springerlink.com/index/10.1007/s00340-010-4027-5. (page 76).

[129] B. A. Paldus, C. C. Harb, T. G. Spence, R. N. Zare, C. F. Gmachl, F. Capasso, D. L. Sivco, J. N. Baillargeon, A. L. Hutchinson, and A. Y. Cho. Cavity ringdown spectroscopy using mid-infrared quantum-cascade lasers. *Optics Letters*, 25(9):666–668, May 2000. http://www.opticsinfobase.org/ol/abstract.cfm?uri=ol-25-9-666. (page 77).

[130] A. A. Kosterev, A. L. Malinovsky, F. K. Tittel, C. Gmachl, F. Capasso, D. L. Sivco, J. N. Baillargeon, A. L. Hutchinson, and A. Y. Cho. Cavity ringdown spectroscopic detection of nitric oxide with a continuous-wave quantum-cascade laser. *Applied Optics*, 40(30):5522–5529, 2001. http://www.opticsinfobase.org/abstract.cfm?&id=65460. (page 77).

[131] M. R. McCurdy, Y. A. Bakhirkin, and F. K. Tittel. Quantum cascade laser-based integrated cavity output spectroscopy of exhaled nitric oxide. *Applied Physics B*, 85(2-3):445–452, July 2006. http://link.springer.com/10.1007/s00340-006-2365-0. (page 78).

[132] S. Welzel and P. Davies. Cavity enhanced absorption spectroscopy using room temperature quantum cascade lasers. *Geophysical Research Abstracts*, 11(EGU2009-12980), 2009. (pages 78, 84).

[133] B. L. Cummings. *Applications of infrared laser spectroscopy to breath analysis*. Doctoral thesis, University of Oxford, 2011. http://ethos.bl.uk/OrderDetails.do?uin=uk.bl.ethos.556283. (pages 78, 93, 124).

[134] G. N. Rao and A. Karpf. Extremely sensitive detection of NO2 employing off-axis integrated cavity output spectroscopy coupled with multiple-line integrated absorption spectroscopy. *Applied Optics*, 50(13):1915–24, May 2011. http://www.opticsinfobase.org/ao/abstract.cfm?uri=ao-50-13-1915. (page 78).

[135] J. Morville and D. Romanini. Sensitive birefringence measurement in a high-finesse resonator using diode laser optical self-locking. *Applied Physics B*, 74(6):495–501, April 2002. http://www.springerlink.com/Index/10.1007/s003400200854. (pages 79, 80).

[136] C. E. Tanner, B. P. Masterson, and C. E. Wieman. Atomic beam collimation using a laser diode with a self-locking power-buildup cavity. *Optics letters*, 13(5):357–9, May 1988. http://www.ncbi.nlm.nih.gov/pubmed/19745897. (pages 79, 80).

[137] R. Salter, J. Chu, and M. Hippler. Cavity-enhanced Raman spectroscopy with optical feedback cw diode lasers for gas phase analysis and spectroscopy. *The Analyst*, 137(20):4669–76, October 2012. http://pubs.rsc.org/en/Content/ArticleLanding/2012/AN/C2AN35722D. (pages 79, 80).

[138] G. Dixon, C. Tanner, and C. Wieman. 432-nm source based on efficient second-harmonic generation of GaAlAs diode-laser radiation in a self-locking external resonant cavity. *Optics Letters*, 14(14):731–3, July 1989. http://www.opticsinfobase.org/ol/abstract.cfm?uri=ol-14-14-731. (pages 79, 80).

[139] V. Motto-Ros. *Cavites de haute finesse pour la spectroscopie d'absorption haute sensibilite et haute precision: Application a l'etude de molecules d'interet atmospherique*. Doctoral thesis, Université Claude Bernard Lyon 1, 2005. (page 79).

[140] D. J. Hamilton. *Two attempts to demonstrate optical-feedback cavity ring-down spectroscopy with a linear cavity*. Master, University of Bristol, 2008. (pages 80, 81).

[141] D. King and R. Pittaro. Simple diode pumping of a power-buildup cavity. *Optics Letters*, 23(10):774–776, May 1998. http://www.opticsinfobase.org/ol/abstract.cfm?uri=ol-23-10-774. (page 81).

[142] F. Capasso. The staircase to flexibility. Interview by Joerg Heber. *Nature Materials*, 9(5):374–5, May 2010. http://www.ncbi.nlm.nih.gov/pubmed/20414212. (page 82, 82).

[143] L. Esaki and R. Tsu. Superlattice and Negative Differential Conductivity in Semiconductors. *IBM Journal of Research and Development*, 1970. (page 82).

[144] R. Kazarinov and R. Suris. Possible amplification of electromagnetic waves in a semiconductor with a superlattice. *Fizika i Tekhnika Poluprovodnikov*, 5(4):797–800, 1971. (page 82).

[145] C. Sirtori, F. Capasso, D. L. Sivco, A. L. Hutchinson, and A. Y. Cho. Mid-Infrared (8.5 um) Semiconductor Lasers Operating at Room Temperature. *IEEE Photonics Technology Letters*, 9(3):294–296, 1997. http://ieeexplore.ieee.org/xpls/abs_all.jsp?arnumber=556051. (pages 84, 84, 85).

[146] J. Faist, F. Capasso, C. Sirtori, D. L. Sivco, A. L. Hutchinson, and A. Y. Cho. Continuous wave operation of a vertical transition quantum cascade laser above T=80 K. *Applied Physics Letters*, 67(21):3057, 1995. http://link.aip.org/link/APPLAB/v67/i21/p3057/s1&Agg=doi. (pages 84, 92).

[147] J. Faist, F. Capasso, C. Sirtori, D. L. Sivco, A. L. Hutchinson, and A. Y. Cho. Vertical transition quantum cascade laser with Bragg confined excited state. *Applied Physics Letters*, 66(5):538, 1995. http://link.aip.org/link/APPLAB/v66/i5/p538/s1&Agg=doi. (page 84).

[148] J. Faist, C. Gmachl, F. Capasso, C. Sirtori, D. L. Sivco, J. N. Baillargeon, and A. Y. Cho. Distributed feedback quantum cascade lasers. *Applied Physics Letters*, 70(20):2670, 1997. http://link.aip.org/link/APPLAB/v70/i20/p2670/s1&Agg=doi. (page 85).

[149] K. Namjou, S. Cai, E. A. Whittaker, J. Faist, C. Gmachl, F. Capasso, D. L. Sivco, and A. Y. Cho. Sensitive absorption spectroscopy with a room-temperature distributed-feedback quantum-cascade laser. *Optics Letters*, 23(3):219–21, February 1998. http://www.opticsinfobase.org/ol/abstract.cfm?uri=ol-23-3-219. (page 85).

[150] Alpes offers CW and pulsed quantum cascade lasers, 2004. http://www.laserfocusworld.com/articles/2004/04/alpes-offers-cw-and-pulsed-quantum-cascade-lasers.html. (page 85).

[151] R. Köhler, A. Tredicucci, F. Beltram, H. E. Beere, E. H. Linfield, A. G. Davies, D. A. Ritchie, R. C. Iotti, and F. Rossi. Terahertz semiconductor-heterostructure laser. *Nature*, 417(6885):156–9, May 2002. http://www.nature.com/nature/journal/v417/n6885/abs/417156a.html. (page 86).

[152] J. Devenson, R. Teissier, O. Cathabard, and A. N. Baranov. InAsAlSb quantum cascade lasers emitting below 3 μm. *Applied Physics Letters*, 90(11):111118, 2007. http://link.aip.org/link/APPLAB/v90/i11/p111118/s1&Agg=doi. (page 86).

[153] H. Chou, M. Anwar, T. Manzur, J. Zeller, and A. K. Sood. Nitride THz GaN quantum cascade lasers. In *2011 International Semiconductor Device Research Symposium (ISDRS)*, volume 4, pages 1–2. Ieee, December 2011. ISBN 978-1-4577-1756-7. http://ieeexplore.ieee.org/lpdocs/epic03/wrapper.htm?arnumber=6135413. (page 86).

[154] T. Ive, K. Berland, M. Stattin, and T. Andersson. Design and Fabrication of Nitride Heterostructures for Intersubband Applications. In *2012 International Conference on Solid-State and Integrated Circuit (ICSIC 2012)*, volume 32, pages 62–66, 2012. http://www.ipcsit.com/vol32/012-ICSIC2012-D2009.pdf. (page 86).

[155] O. Malis, C. Gmachl, D. L. Sivco, L. N. Pfeiffer, A. M. Sergent, and K. W. West. The quantum cascade laser: A versatile high-power semiconductor laser for mid-infrared applications. *Bell Labs Technical Journal*, 10(3): 199–214, November 2005. http://doi.wiley.com/10.1002/bltj.20114. (page 86).

[156] J. P. Commin, D. G. Revin, S. Y. Zhang, A. B. Krysa, K. Kennedy, and J. W. Cockburn. High peak power λ~3.3 and 3.5 μm InGaAs/AlAs(Sb) quantum cascade lasers operating up to 400 K. *Applied Physics Letters*, 97 (3):031108, 2010. http://link.aip.org/link/APPLAB/v97/i3/p031108/s1&Agg=doi. (page 86).

[157] J. L. Zhang, X. Huang, C. F. Gmachl, V. Tokranov, and S. Oktyabrsky. Cascaded-transition Quantum Cascade laser. In *2012 Lester Eastman Conference on High Performance Devices (LEC)*, pages 1–4. IEEE, August 2012. ISBN 978-1-4673-2301-7. http://ieeexplore.ieee.org/lpdocs/epic03/wrapper.htm?arnumber=6410996. (page 86).

[158] G. Luo, C. Peng, S.-S. Pei, H. Lee, W.-Y. Hwang, B. Ishaug, and J. Zheng. Broadly wavelength-tunable external cavity, mid-infrared quantum cascade lasers. *IEEE Journal of Quantum Electronics*, 38(5):486–494, 2002. http://ieeexplore.ieee.org/xpls/abs_all.jsp?arnumber=998621. (page 86).

[159] R. Maulini, M. Beck, J. Faist, and E. Gini. Broadband tuning of external cavity bound-to-continuum quantum-cascade lasers. *Applied Physics Letters*, 84(10):1659, 2004. http://link.aip.org/link/APPLAB/v84/i10/p1659/s1&Agg=doi. (page 86).

[160] B. G. Lee, M. A. Belkin, R. Audet, J. MacArthur, L. Diehl, C. Pflugl, F. Capasso, D. C. Oakley, D. Chapman, A. Napoleone, D. Bour, S. Corzine, G. Hofler, and J. Faist. Widely tunable single-mode quantum cascade laser source for mid-infrared spectroscopy. *Applied Physics Letters*, 91(23): 231101, 2007. http://link.aip.org/link/APPLAB/v91/i23/p231101/s1&Agg=doi. (page 86).

[161] P. Q. Liu, K. Sladek, X. Wang, J.-Y. Fan, and C. F. Gmachl. Single-mode quantum cascade lasers employing a candy-cane shaped monolithic coupled cavity. *Applied Physics Letters*, 99(24):241112, 2011. http://link.aip.org/link/APPLAB/v99/i24/p241112/s1&Agg=doi. (page 86).

[162] P. Q. Liu, X. Wang, J.-Y. Fan, and C. F. Gmachl. Single-mode quantum cascade lasers based on a folded Fabry-Perot cavity. *Applied Physics Letters*, 98(6):061110, 2011. http://link.aip.org/link/APPLAB/v98/i6/p061110/s1&Agg=doi. (page 86).

[163] T. S. Mansuripur, S. Menzel, R. Blanchard, L. Diehl, C. Pflügl, Y. Huang, J.-H. Ryou, R. D. Dupuis, M. Loncar, and F. Capasso. Widely tunable mid-infrared quantum cascade lasers using sampled grating reflectors. *Optics*

Express, 20(21):23339–48, October 2012. http://www.opticsinfobase.org/oe/abstract.cfm?uri=oe-20-21-23339. (page 86).

[164] Mid-InfraRed Technologies for Health and the Environment. http://www.mirthecenter.org. (page 86).

[165] Alpes Lasers Quantum Cascade Laser User's Manual, Version 3.1.1. 2013. (page 90, 90).

[166] R. J. Walker, J. H. van Helden, J. Kirkbride, E. A. McCormack, M. T. Bell, D. Weidmann, and G. A. D. Ritchie. Rapid passage signals from a vibrationally excited target molecule: a pump and probe experiment with continuous wave quantum cascade lasers. *Optics Letters*, 36(24): 4725–4727, 2011. http://www.opticsinfobase.org/abstract.cfm?URI=ol-36-24-4725. (page 89).

[167] J. M. R. Kirkbride, S. K. Causier, E. A. McCormack, D. Weidmann, and G. A. D. Ritchie. Coherent transient spectroscopy with continuous wave quantum cascade lasers. *Physical Chemistry Chemical Physics*, 15(8):2684–91, February 2013. http://pubs.rsc.org/en/content/articlehtml/2012/cp/c2cp44116k. (pages 91, 100).

[168] J. Kim, M. Lerttamrab, S. L. Chuang, C. F. Gmachl, D. L. Sivco, F. Capasso, and A. Y. Cho. Theoretical and Experimental Study of Optical Gain and Linewidth Enhancement Factor of Type-I Quantum-Cascade Lasers. *IEEE Journal of Quantum Electronics*, 40(12):1663–1674, 2004. http://ieeexplore.ieee.org/xpls/abs_all.jsp?arnumber=1359974. (page 92).

[169] T. Aellen, R. Maulini, R. Terazzi, N. Hoyler, M. Giovannini, J. Faist, S. Blaser, and L. Hvozdara. Direct measurement of the linewidth enhancement factor by optical heterodyning of an amplitude-modulated quantum cascade laser. *Applied Physics Letters*, 89(9):091121, 2006. http://link.aip.org/link/APPLAB/v89/i9/p091121/s1&Agg=doi. (page 92).

[170] J. von Staden, T. Gensty, W. Elsässer, G. Giuliani, and C. Mann. Measurements of the alpha factor of a distributed-feedback quantum cascade laser by an optical feedback self-mixing technique. *Optics Letters*, 31(17):2574–6, September 2006. http://www.opticsinfobase.org/ol/abstract.cfm?URI=ol-31-17-2574&origin=search. (page 92).

[171] N. Kumazaki, Y. Takagi, M. Ishihara, K. Kasahara, A. Sugiyama, N. Akikusa, and T. Edamura. Detuning characteristics of the linewidth enhancement factor of a midinfrared quantum cascade laser. *Applied Physics Letters*, 92(12):121104, 2008. http://link.aip.org/link/APPLAB/v92/i12/p121104/s1&Agg=doi. (page 92).

[172] M. Yamanishi, T. Edamura, K. Fugita, N. Akikusa, and H. Kan. Theory of the intrinsic linewidth of quantum-cascade lasers: Hidden reason for the narrow linewidth and line-broadening by thermal photons. *IEEE Journal of*

Quantum Electronics, 44(1):12–29, 2008. http://ieeexplore.ieee.org/xpls/abs_all.jsp?arnumber=4397142. (page 92).

[173] H. Ganser, B. Frech, A. Jentsch, M. Manfred, C. Gmachl, F. Capasso, D. L. Sivco, J. N. Baillargeon, A. L. Hutchinson, A. Y. Cho, and W. Urban. Investigation of the spectral width of quantum cascade laser emission near 5.2 μm by a heterodyne experiment. *Optics Communications*, 197(1-3): 127–130, 2001. http://www.sciencedirect.com/science/article/pii/S0030401801014419. (page 92).

[174] D. Weidmann, L. Joly, V. Parpillon, D. Courtois, Y. Bonetti, T. Aellen, M. Beck, J. Faist, and D. Hofstetter. Free-running 9.1 µm distributed-feedback quantum cascade laser linewidth measurement by heterodyning with a $C^{18}O_2$ laser. *Optics Letters*, 28(9):704–706, 2003. http://www.opticsinfobase.org/ol/abstract.cfm?uri=ol-28-9-704. (page 92).

[175] R. Williams, J. Kelly, and J. Hartman. Kilohertz linewidth from frequency-stabilized mid-infrared quantum cascade lasers. *Optics Letter*, 24(24):1844–1846, 1999. http://www.opticsinfobase.org/abstract.cfm?id=63913. (page 92).

[176] PNNL refines and licenses laser sensors, 2010. http://www.pnl.gov/edo/newsletter/article.asp?id=651. (page 94).

[177] T. L. Myers, R. M. Williams, M. S. Taubman, C. Gmachl, F. Capasso, D. L. Sivco, J. N. Baillargeon, and a. Y. Cho. Free-running frequency stability of mid-infrared quantum cascade lasers. *Optics Letters*, 27(3): 170–2, February 2002. http://www.opticsinfobase.org/ol/abstract.cfm?id=67696. (pages 94, 100).

[178] Agilent Spectrum Analysis Basics. Agilent Technologies, 2006. (page 96).

[179] L. R. Brown, D. Chris Benner, J. P. Champion, V. M. Devi, L. Fejard, R. R. Gamache, T. Gabard, J. C. Hilico, B. Lavorel, M. Loete, G. C. Mellau, A. Nikitin, A. S. Pine, A. Predoi-Cross, C. P. Rinsland, O. Robert, R. L. Sams, M. A. H. Smith, S. A. Tashkun, and V. G. Tyuterev. Methane line parameters in HITRAN. *Journal of Quantitative Spectroscopy and Radiative Transfer*, 82(1-4):219–238, November 2003. http://linkinghub.elsevier.com/retrieve/pii/S0022407303001559. (page 98).

[180] C. E. Langley. *Development of Techniques for Trace Gas Detection in Breath*. Dphil, University of Oxford, 2012. (page 100).

[181] L. Ciaffoni, G. Hancock, J. J. Harrison, J.-P. H. van Helden, C. E. Langley, R. Peverall, G. A. D. Ritchie, and S. Wood. Demonstration of a mid-infrared cavity enhanced absorption spectrometer for breath acetone detection. *Analytical Chemistry*, 85(2):846–50, January 2013. http://pubs.acs.org/doi/abs/10.1021/ac3031465. (page 100).

[182] Private communciation between A.J. Orr-Ewing and G.A.D. Ritchie. (page 102).

[183] R. A. Brownsword and D. Weidmann. Intracavity widely-tunable quantum cascade laser spectrometer. *Optics Express*, 21(2):1581–92, January 2013. http://www.opticsinfobase.org/oe/abstract.cfm?uri=oe-21-2-1581. (pages 102, 166).

[184] D. Weidmann, K. Smith, and B. Ellison. Experimental investigation of high-frequency noise and optical feedback effects using a 9.7 microm continuous-wave distributed-feedback quantum-cascade laser. *Applied Optics*, 46(6): 947–53, February 2007. http://www.opticsinfobase.org/ao/abstract.cfm?uri=ao-46-6-947. (pages 103, 127).

[185] F. P. Mezzapesa, L. L. Columbo, M. Brambilla, M. Dabbicco, S. Borri, M. S. Vitiello, H. E. Beere, D. a. Ritchie, and G. Scamarcio. Intrinsic stability of quantum cascade lasers against optical feedback. *Optics Express*, 21(11): 13748, May 2013. http://www.opticsinfobase.org/abstract.cfm?URI=oe-21-11-13748. (page 103, 103).

[186] P. Mineault. Auto Gaussian & Gabor Fits (MATLAB), 2011. http://www.mathworks.co.uk/matlabcentral/fileexchange/31485-auto-gaussian-gabor-surface-fit. (page 108).

[187] S. A. Self. Focusing of spherical Gaussian beams. *Applied Optics*, 22(5):658–61, March 1983. http://www.opticsinfobase.org/ao/abstract.cfm?id=26503. (page 112).

[188] S.-i. Ohshima and H. Schnatz. Optimization of injection current and feedback phase of an optically self-locked laser diode. *Journal of Applied Physics*, 71(7):3114, 1992. http://link.aip.org/link/JAPIAU/v71/i7/p3114/s1&Agg=doi. (page 117).

[189] J. Osmundsen and N. Gade. Influence of optical feedback on laser frequency spectrum and threshold conditions. *IEEE Journal of Quantum Electronics*, 19(3):465–469, 1983. http://ieeexplore.ieee.org/xpls/abs_all.jsp?arnumber=1071857. (page 125).

[190] D. Weidmann, W. J. Reburn, and K. M. Smith. Retrieval of atmospheric ozone profiles from an infrared quantum cascade laser heterodyne radiometer: results and analysis. *Applied Optics*, 46(29):7162–71, October 2007. http://www.opticsinfobase.org/ao/abstract.cfm?uri=ao-46-29-7162. (page 129).

[191] C. Rodgers. *Inverse Methods for Atmospheric Sounding: Theory and Practice: Errata*. World Scientific, 2000. (page 130).

[192] P. L. Varghese and R. K. Hanson. Collisional narrowing effects on spectral line shapes measured at high resolution. *Applied Optics*, 23(14): 2376, July 1984. http://www.opticsinfobase.org/ao/abstract.cfm?id=27661. (page 135).

[193] R. Eng. Collisional narrowing of infrared water-vapor transitions. *Applied Physics Letters*, 21(7):303, 1972. http://link.aip.org/link/?APL/21/303/1&Agg=doi. (page 135).

[194] R. P. Wayne. *Chemistry of Atmospheres*. Oxford University Press, second edition, 1995. (pages 139, 149, 150).

[195] E. Maddy and C. Barnet. What are retrieval averaging kernels?, 2009. (page 141).

[196] J. H. Seinfeld. *Atmospheric Chemistry and Physics of Air Pollution*. John Wiley & Sons, first edition, 1986. (page 149).

[197] T. H. Risby and F. K. Tittel. Current status of midinfrared quantum and interband cascade lasers for clinical breath analysis. *Optical Engineering*, 49(11):111123, November 2010. http://opticalengineering.spiedigitallibrary.org/article.aspx?doi=10.1117/1.3498768. (page 150, 150).

[198] L. Gustafsson and A. Leone. Endogenous nitric oxide is present in the exhaled air of rabbits, guinea pigs and humans. *Biochemical and Biophysical Research Communications*, 181(2):852–857, 1991. http://www.sciencedirect.com/science/article/pii/0006291X9191268H. (page 150).

[199] K. Alving, E. Weitzberg, and J. M. Lundberg. Increased amount of nitric oxide in exhaled air of asthmatics. *The European Respiratory Journal*, 6(9):1368–70, October 1993. http://www.ncbi.nlm.nih.gov/pubmed/7507065. (page 150).

[200] Y. A. Bakhirkin, A. A. Kosterev, R. F. Curl, F. K. Tittel, D. A. Yarekha, L. Hvozdara, M. Giovannini, and J. Faist. Sub-ppbv nitric oxide concentration measurements using cw thermoelectrically cooled quantum cascade laser-based integrated cavity output spectroscopy. *Applied Physics B*, 82(1):149–154, November 2005. http://link.springer.com/10.1007/s00340-005-2058-0. (page 150).

[201] B. W. M. Moeskops, S. M. Cristescu, and F. J. M. Harren. Sub-part-per-billion monitoring of nitric oxide by use of wavelength modulation spectroscopy in combination with a thermoelectrically cooled, continuous-wave quantum cascade laser. *Optics Letters*, 31(6):823–5, March 2006. http://www.opticsinfobase.org/ol/abstract.cfm?uri=ol-31-6-823. (page 150).

[202] J. Mandon, M. Högman, P. J. F. M. Merkus, J. van Amsterdam, F. J. M. Harren, and S. M. Cristescu. Exhaled nitric oxide monitoring by quantum cascade laser: comparison with chemiluminescent and electrochemical sensors. *Journal of Biomedical Optics*, 17(1):017003, January 2012. http://www.ncbi.nlm.nih.gov/pubmed/22352669. (page 150).

[203] L. Dong, V. Spagnolo, R. Lewicki, and F. K. Tittel. Ppb-level detection of nitric oxide using an external cavity quantum cascade laser based QEPAS sensor. *Optics Express*, 19(24):24037–45, November 2011. http://www.opticsinfobase.org/oe/abstract.cfm?uri=oe-19-24-24037. (page 150).

[204] P. Kluczynski, S. Lundqvist, J. Westberg, and O. Axner. Faraday rotation spectrometer with sub-second response time for detection of nitric oxide using a cw DFB quantum cascade laser at 5.33 μm. *Applied Physics B*, 103(2):451–459, December 2010. http://link.springer.com/10.1007/s00340-010-4336-8. (page 150).

[205] M. Silva, D. Sonnenfroh, D. Rosen, M. Allen, and A. O'Keefe. Integrated cavity output spectroscopy measurements of NO levels in breath with a pulsed room-temperature QCL. *Applied Physics B*, 81(5):705–710, July 2005. http://www.springerlink.com/index/10.1007/s00340-005-1922-2. (page 150).

[206] R. J. Walker. *Quantum Cascade Laser Spectroscopy*. Doctoral thesis, University of Oxford, 2011. http://ora.ox.ac.uk/objects/uuid%3A28408b32-eb79-4c84-b4be-12b3a51b5efa. (page 166, 166).

[207] R. Q. Yang. Infrared laser based on intersubband transitions in quantum wells. *Superlattices and Microstructures*, 17(1):77–83, 1995. http://www.sciencedirect.com/science/article/pii/S0749603685710178. (page 166).

[208] J. Meyer, I. Vurgaftman, R. Q. Yang, and L. R. Ram-Mohan. Type-II and type-I interband cascade lasers. *Electronics Letters*, 32(1):45–46, 1996. http://ieeexplore.ieee.org/xpls/abs_all.jsp?arnumber=490720. (pages 166, 167, 167).

[209] P. Kluczynski, M. Jahjah, L. Nähle, O. Axner, S. Belahsene, M. Fischer, J. Koeth, Y. Rouillard, J. Westberg, A. Vicet, and S. Lundqvist. Detection of acetylene impurities in ethylene and polyethylene manufacturing processes using tunable diode laser spectroscopy in the 3-μm range. *Applied Physics B*, 105(2):427–434, July 2011. http://link.springer.com/10.1007/s00340-011-4645-6. (page 168).

[210] M. Lerttamrab, S. L. Chuang, R. Q. Yang, and C. J. Hill. Linewidth enhancement factor of a type-II interband-cascade laser. *Journal of Applied Physics*, 96(6):3568, 2004. http://link.aip.org/link/JAPIAU/v96/i6/p3568/s1&Agg=doi. (page 168).